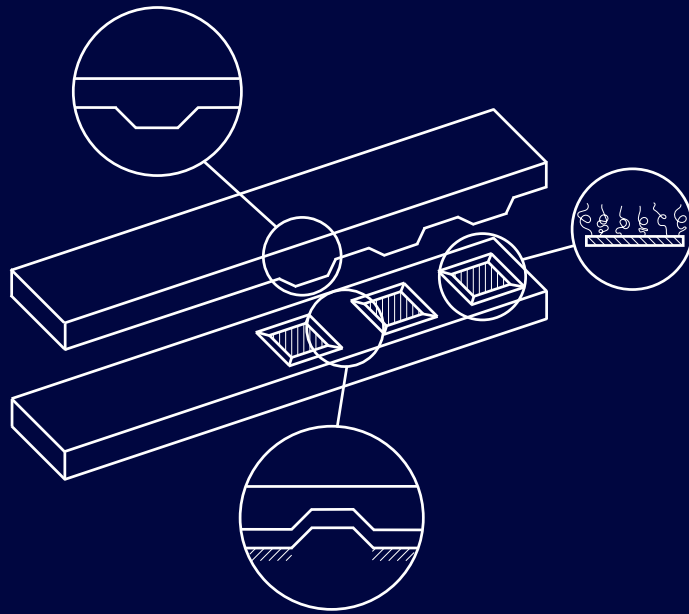


MECHANICS AND FAILURE OF STRUCTURED INTERFACES



Simon Heide-Jørgensen

Department of Engineering

Aarhus University

A dissertation submitted for the degree of

Philosophiae Doctor

August, 2019

ISBN: 978-87-7507-458-7
DOI: 10.7146/aulsps-e.339

AARHUS UNIVERSITY

PHD DISSERTATION

Mechanics and Failure of Structured Interfaces

Author:
Simon Heide-Jørgensen

Supervisor:
Michal K. Budzik

*A dissertation submitted in fulfillment of the requirements
for the degree of Philosophiae Doctor*

in the

Department of Engineering, Aarhus University

August, 2019

Abstract

This dissertation concerns heterogeneous, structured interfaces' mechanics and failure, in particular the load response, critical fracture energy and crack kinetics. During the project eight manuscripts have been prepared and submitted to scientific journals. Five of these are included here forming the main body of the dissertation. The topics of these include development and test of a new nano-adhesive based on polymer brushes to bond rubber and metal, a novel peel test specimen comprising a heterogeneous geometry, consequences of zones of weak adhesion, bridging of a support carrier in the bondline, and, macro- and micromechanical behavior of pillar-structured interfaces. Analytical modeling and numerical simulations backed up by experimental testing were used to study these, among others.

The following results and conclusions are drawn from the project.

- The nano-adhesive offers similar adhesion strength and quality as a common commercial binder-and-primer solution while having a bondline three orders of magnitude thinner.
- An additional length scale parameter (the elastic process zone size) have been introduced and its role in effective critical fracture energy has been recognized.
- Introducing zones of weak adhesion reduces joint performance. However, if a zone of strong adhesion at least the size of the elastic process zone exists, the joint recovers its full strength. The effective critical fracture energy can be calculated as the weighted sum of strong and weak adhesion zones within the elastic process zone.
- Rate effects from loading rate and crack velocity play a vital role when determining the energy release rate and might result in a conservative critical fracture energy.
- Pillar structured interfaces enhance critical fracture load and damage tolerance while slightly increasing the joint compliance.

Resumé

Denne afhandling undersøger effekten af strukturerede heterogene grænseflader på mekanikken og svigt af adhæsive samlinger med fokus på lastresponset, den kritiske brudenergi og revnekinetikken. Gennem projektet er otte artikler udarbejdet og indsendt til videnskabelige tidsskrifter. Af disse er fem inkluderet i afhandlingen. Artiklerne berører følgende emner: udvikling og test af en ny type nano-adhæsiv baseret på polymer børster til sammenføjning af gummi og metal, konsekvenserne ved områder med svag adhæsion, brodannelse af en støttebærer i adhæsiven og, slutteligt, de makro- og mikromekaniske egenskaber hos søjle- strukturerede grænseflader. Analytisk modellering, numerisk simulation og eksperimentelt arbejde er anvendt.

Følgende resultater og konklusioner er opnået gennem projektet:

- Nano-adhæsiven gav samme adhæsionsstyrke og -kvalitet som en typisk kommerciel adhæsiv.
- En ekstra længdeskalaparameter er blevet introduceret og dens rolle i den effektive kritiske brudenergi er blevet identificeret.
- Introduktion af områder med svag adhæsion reducerer samlingens præstation. Imidlertid, hvis området med stærk adhæsion er på størrelse med eller større end det elastiske procesområde, genopretter samlingen sin fulde styrke. Den effektive kritiske brudenergi kan beregnes som den vægtede sum af områderne med svag og stærk adhæsion i det elastiske procesområde.
- Rateeffekter stammende fra lastraten og revnehastigheden spiller en væsentlig rolle når energiudslipshastigheden skal bestemmes og kan give et unødvendigt, konservativt resultat.
- Søjle-strukturerede grænseflader forbedrer den kritiske brudlast og skadetolerancen samt øger samlingens eftergivelse.

Preface

This dissertation is submitted in partial fulfillment of the requirements for the degree of PhD from Aarhus University (AU). The research herein was conducted at the Department of Engineering in the Section of Mechanical Engineering at AU in the period of 1st September 2016 to 31st July 2019 under the supervision of Associate Professor Michal Kazimierz Budzik and at University of Pennsylvania during a fourth month research stay under supervision of Professor Kevin T. Turner. The project is part of the Molecular Adhesive for Strong and Durable Bonding of Rubber to Metal (MoAd) project funded by the Innovation Fund Denmark. The MoAd project is a multidisciplinary collaboration between AU represented by the Department of chemistry and the Department of Engineering including Section of Mechanical Engineering and Section of Chemical Engineering, AVK Gummi A/S and RadiSurf ApS. During the PhD additional funding was provided by IDAs og Berg-Nielsens Studie- og Støttefond, Aage og Johanne Louis-Hansens Fond, Augustinus Fonden and Knud Højgaards Fond, which are gratefully acknowledged.

The dissertation is structured as a collection of articles according to the guidelines of the Section of Mechanical Engineering. Furthermore, it follows the official rules and regulations stated by the Graduate School of Science and Technology (GSST) at AU. It consists of seven chapters starting with a broad introduction to the research field, followed by five article-based chapters each containing introduction, methods used, the author's contributions, key findings and reflections specific to the paper. Finally, the seventh chapter brings up a summary and an outlook tying up the dissertation.

Anyway, I hope you will find my work interesting.

Simon Heide-Jørgensen
Aarhus, Denmark
August, 2019

Declaration

I, Simon Heide-Jørgensen, declare that this dissertation titled, "Mechanics and Failure of Structured Interfaces" and the work presented in it are my own. I confirm that:

- This work was done wholly or mainly while in candidature for a research degree at this University.
- Where any part of this thesis has previously been submitted for a degree or any other qualification at this University or any other institution, this has been clearly stated.
- Where I have consulted the published work of others, this is always clearly attributed.
- Where I have quoted from the work of others, the source is always given. With the exception of such quotations, this thesis is entirely my own work.
- I have acknowledged all main sources of help.
- Where the thesis is based on work done by myself jointly with others, I have made clear exactly what was done by others and what I have contributed myself.

Acknowledgment

It has been a privilege studying at Aarhus University during my PhD. Through my work I have received support from several people to whom I am deeply grateful. First of all, I would like to express my deepest sense of gratitude to my supervisor Associate Professor Michal Kazimierz Budzik, without whom none of this would have been possible. I owe him a debt of gratitude for his invaluable guidance, encouragement and continuous support through the past years. His has inspired me to push on in times of despair and strive to greater levels.

I also thank all of my collaborators in the MoAD project in specific Rasmus Krag Møller, Kristian Birk Buhl, Mogens Hinge, Steen Uttrup Pedersen, Mikkel Kongsfelt and Kim Daasbjerg for their help and encouragement. I am grateful to my colleagues and fellow PhD students Kasper Ringgard, Dan Thomsen, Oliver Tierdad Filsoof, Emil Madsen and Frederik Foldager for being a source of inspiration and joy. I place on record, my sincere gratitude to Simon Peter Hald Skovsgård for academic discussions, useful suggestions and his unconditional support as a colleague and as a friend. I also place on record, my sense of gratitude to one and all who, directly or indirectly, have lent their help in venture.

Furthermore, I am grateful to Professor Kevin Thomas Turner for receiving me as a visiting scholar in his research group at the University of Pennsylvania. I would like to thank all the people in The Turner Research Group for welcoming me with open arms and making my stay enjoyable.

Last but not least, I would like to thank my family and friends for their love and support. I am especially grateful to my girlfriend Camilla who has given me unconditional love and support.

To each and every one of you, thank you

Publications

- [Paper 1] Heide-Jørgensen, Simon, et al. Efficient bonding of ethylene-propylene-diene M-class rubber to stainless steel using polymer brushes as a nanoscale adhesive. *International Journal of Adhesion and Adhesives*. Vol. 87 (2018): 31-41.¹
- [Paper 2] Heide-Jørgensen, Simon and Budzik, Michal K. Crack growth along heterogeneous interface during the DCB experiment, *International Journal of Solids and Structures*. Vol. 120 (2017): 278–291.²
- [Paper 3] Heide-Jørgensen, Simon, and Budzik, Michal K. Effects of bondline discontinuity during growth of interface cracks including stability and kinetic considerations. *Journal of the Mechanics and Physics of Solids*. Vol. 117 (2018): 1-21.³
- [Paper 4] Heide-Jørgensen, Simon, Teixeira de Freitas, Sofia and Budzik, Michal K. On the fracture behaviour of CFRP bonded joints under mode I loading: Effect of supporting carrier and interface contamination, *Composites Science and Technology*. Vol. 160 (2018): 97–110.⁴
- [Paper 5] Heide-Jørgensen, Simon, Michal K. Budzik, and Kevin T. Turner. "Mechanics and Fracture of Structured Pillar Interfaces. *Journal of the Mechanics and Physics of Solids*. Vol. 137 (2019).⁵

Contributions to other work:

- [**Contribution 1**] Budzik, Michal K., and Heide-Jørgensen, Simon. Branching and softening of loading path during onset of crack at elastic-brittle interface. *Mechanics of Materials*. Vol. 127 (2018): 1-13.⁶
- [**Contribution 2**] Buhl, Kristian Birk, et al. Highly Efficient Rubber-to-Stainless Steel Bonding by Nanometer-Thin Cross-linked Polymer Brushes. *Acs Omega*. Vol. 3.12 (2018): 17511-17519.⁷
- [**Contribution 3**] Røjkjær, Rasmus et al. Straight Forward Approach for Obtaining Relaxation-Recovery Data. *OSF*. doi:10.17605/OSF.IO/S6UPA (2018).⁸

Oral conference presentations:

- I** DCAMM 16th Internal Symposium, March 2017 Middelfart, Denmark
Title: Crack Growth Along Heterogeneous Interface During the DCB Experiment

- II** The 4th international conference on structural adhesive bonding, June 2017 Porto, Portugal
Title: Effects of interface heterogeneities on load response and R-curve

- III** The 6th World Congress on Adhesion and Related Phenomena (WCARP), February 2018 San Diego, USA
Title: Effects of bondline discontinuity during growth of interface crack

- IV** The 12th European Adhesion Conference and 4th Luso-Brazilian conference on Adhesion and Adhesives, September 2018 Lisbon, Portugal
Title: Nanoscale adhesive bonding system for EPDM rubber and stainless steel

- V** DCAMM 17th Internal Symposium, March 2019 Børkop, Denmark
Title: Fracture toughness of rubber/stainless steel bonding using nanothick adhesive

Contents

Abstract	iv
Resumé	vi
Publications and contributions	xi
Preface	x
1 Introduction	1
1.1 Adhesively Bonded Joints	3
1.1.1 Shear Lag Configuration	6
1.1.2 Double Cantilever Beam Configuration	7
1.1.3 Peel Configuration	12
1.1.4 Notes on Numerical Methods	14
1.2 Stochastic and Structured Interfaces	15
1.2.1 Beyond Homogeneous Bondlines	15
1.2.2 Inspiration from Metamaterials	18
1.3 Scope of Work	19
2 Paper 1 - On Rubber-Metal Bonding	25
2.1 Introduction	25
2.2 Method	25
2.3 Contribution	26
2.4 Finding	26
2.5 Reflection	27
3 Paper 2 - On Effective Critical Fracture Energy	39
3.1 Introduction	39
3.2 Method	39
3.3 Contribution	40
3.4 Finding	40
3.5 Reflection	41

4	Paper 3 - On Bondline Discontinuities and Kinetic Effects	57
4.1	Introduction	57
4.2	Method	57
4.3	Contribution	58
4.4	Finding	58
4.5	Reflection	59
5	Paper 4 - On Kissing-Bonds and Support Carriers	81
5.1	Introduction	81
5.2	Method	82
5.3	Contribution	82
5.4	Finding	82
5.5	Reflection	83
6	Paper 5 - On Pillar-Structured Interfaces	99
6.1	Introduction	99
6.2	Method	99
6.3	Contribution	100
6.4	Finding	100
6.5	Reflection	101
7	Summary and Outlook	123
7.1	Contributions to the Field	124
7.2	Perspective	127
7.3	Recommendation for Further Work	130

List of Abbreviations

ADCB	A symmetric D ouble C antilever B eam
BE	B oundary E lement
CAD	C omputer A ided D esign
CFRP	C arbon F iber R einforced P olymer
DCB	D ouble C antilever B eam
EPDM	E thylene P ropylene D iene M onomer
ERR	E nergy R elease R ate
FD	F inite D ifference
FE	F inite E lement
IRRAS	I nfra R ed R eflection A bsorption S pectroscopy
LFM	L inear F racture M echanics
MEMS	M icro- E lectro- M echanical S ystems
PDMS	P oly D i M ethyl S iloxane
PMMA	P oly M ethyl M eth A crylate
XPS	X -ray P hotoelectron S pectroscopy

Chapter 1

Introduction

Bonding is the action of joining two or more materials of different or similar types together by means of adhesive, heat, pressure or by chemical bonds. It is essential since it permits forming new materials or structures with enhanced properties from existing ones. As a consequence bonding can be found in a lot of places. For instance in nature, the inner shell layer of seashells, clam shells, mollusc shells and many others is made of nacre. Nacre consists of platelets of aragonite bonded together by an elastic bio-polymer. Aragonite is very strong but brittle whereas the elastic bio-polymer is not very strong but has substantial toughness. Bonded together they form a composite laminate,⁹ which is both strong and tough and, thus, far superior to each of the materials on their own. Another example is the gecko, whose feet contain a specific hierarchical structure, which permits it to bond to almost any surface through van der Waals forces. This gives it the ability to crawl on walls.¹⁰ Humans also benefit from bonding and have been doing so for a long time. Some of the oldest known man-made tools were bonded with birch bark pitch nearly 200,000 years ago by the Neanderthals.¹¹ By connecting different parts we were and are able to create structures and mechanisms with abilities far beyond the parts themselves.

Advances in chemistry and material science paved the way for the discovery of synthetic polymers in the late 19th century,¹² which led to the development of modern adhesives. By the mid-1900s a broad selection of synthetic adhesives such as phenol-formaldehyde, acrylic, polyurethane, epoxies, cyanoacrylates, among others, were commercially available promoting adhesive bonding for structural applications.¹³ Adhesive bonding is a special type of bonding where two substrates are jointed together by an intermediate layer. The layer is called the adhesive while the substrates often are referred to as adherends.

The synthetic polymers also gave birth to a new type of material: composite laminates. These advanced materials, which typically are stiff fibers

embedded in a softer, often polymeric, matrix, can achieve high stiffness-to-weight ratios. Since they rely on bonding to adhere the fibers and the different layers together, they are vulnerable to the same defects and failures as adhesive joints. For instance, interfacial heterogeneities leading to partial bonding between fiber and matrix can have severe consequences on the composite's performance¹⁴ and delamination where adhesion between two or more layers of the composite fails can lead to significantly reduction of load carry capacity and, in worst case, to catastrophic failure.^{15,16}

Common for all bonded joints is that they contain interfaces, material discontinuities and local highly stressed areas.¹⁷ How the interface region is structured greatly influences the mechanical behavior and how it should be treated theoretically. In Figure 1.1 is seen a schematic of a bonded joint with an interface region, depicted with dashed lines. The hatched area is the adhesive with thickness t . The white rectangle with height d and width s represents an area with different properties. Only a single area is depicted, however, many areas can be present. Depending on the thickness

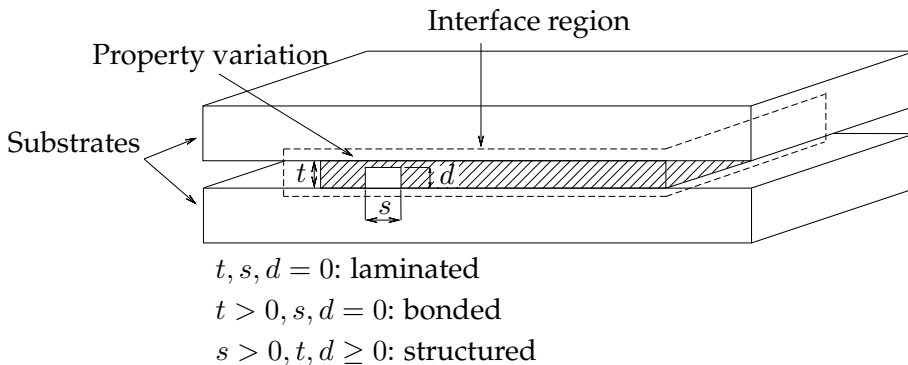


FIGURE 1.1: Bonded joint with two substrates and an intermediate adhesive layer (hatched) with thickness t . The white square with dimensions d, s in the adhesive layer represents a region of different properties. Three types of interfaces exist. 1) $t, d, s = 0$ is regarded as a laminated. 2) $t > 0, s, d = 0$ is bonded. 3) $s > 0, t, d \geq 0$ is structured

of the adhesive, the existence and dimensions of the property variation, three types of interface regions can be defined.

- $t, s, d = 0$: Laminated interface
- $t > 0, s, d = 0$: Bonded interface

- $s > 0, d, t \geq 0$: Structured interface

When the thickness of the bondline is zero and no property variations exist, the interface is regarded as laminated. This is the case for composite laminates where the resin is fused together with the fibers and as such the substrates are the source of adhesion. When treating laminates theoretically often no bondline is included and perfect bonding is assumed. Even though these interfaces are very interesting and have great potentials, they are out of the scope of the present dissertation and will not be covered here.

When the bondline has a finite thickness the interface is regarded as bonded. This is the case for adhesive joints where the bondline is comprised of the adhesive. Classically, the bondline is assumed to be homogeneous and uniform meaning that no property variation exists. When treating adhesive joints theoretically the bondline can either be included or neglected depending on the scenario and the approach taken. More on that later.

When a property variation is present and its dimensions are controlled the interface is regarded as structured. In that sense a joint containing defects is not regarded to have a structured interface. Property variations can be introduced to both laminated and bonded interfaces hence $t \geq 0$ and can either be restricted to the surface $d = 0, s > 0$ or have a spatial distribution across the interface $d, s > 0$. The variation can come from many different sources both material, physical or geometrical. These are the main scope and will be described in greater details later. First, the theoretical background for adhesive joints is presented since this constitutes the framework upon which this work is done.

1.1 Adhesively Bonded Joints

Adhesively bonded interfaces cover a broad selection of different joints and geometries. In Figure 1.2 are shown four common joint types a) single lap joint, b) double lap joint, c) scarf lap joint, and, d) butt joint. Each of these joint types results in different loading and stress types.

In order to analyze all the different joint types on a common basis, four main loading modes are established. The loading modes are illustrated in Figure 1.3 and cover a) tension, b) shear, c) cleavage, and, d) peel. Tension is produced by loading the joint perpendicular to the bondline along the mid-planes of the adherends. This is the idealized loading case for butt joints [Figure 1.2(d)] for which failure of the joint is solely depended on the

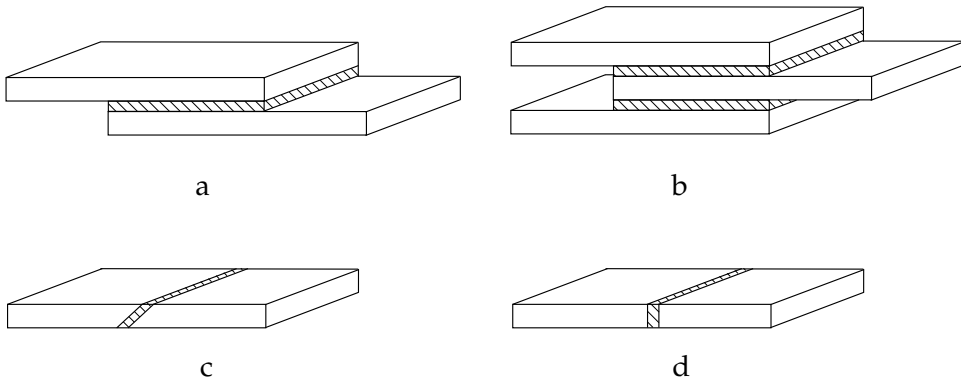


FIGURE 1.2: Four common adhesive joint types with the adhesives marked as hatched areas. a) Single lap joint. b) Double lap joint. c) Scarf lap joint. d) Butt joint.

strength of the adhesive. Shear is produced when the loading is parallel to the bondline through the mid-planes of the adherends. This results in the load being transferred as shear from the upper adherend to the lower adherend through the adhesive. This is the dominant loading mode for lap joints [Figure 1.2(a-b)]. Cleavage happens when tensile loading is applied perpendicular to the bondline at one end of the joint. This is the most severe type of loading since it is related to mode I failure, which is the dominant failure mode. In addition, the stresses tend to increase with the crack length for this type of loading. The fourth type is peeling. It is similar to cleavage as it is induced by a tensile load in one end of the joint. However, for it to be peeling at least one of the adherends has to be flexible such that it bends and aligns with the loading direction. This minimizes bending and causes the failure to be force driven. As cleavage this leads to an opening crack, however, the force does not scale with the crack length and, thus, does not change as the crack grows.

These idealized loading scenarios help identifying how the joint is affected by applied loads and, in relation to fracture mechanics, how it is going to fail. The three fracture mechanical failure modes are depicted in Figure 1.4 and consist of mode I) opening crack, mode II) sliding crack, and, mode III) tearing crack. Mode I arises from tension at the crack front and is related to cleavage and peel. The crack opening resulting from mode I weakens the joint causing further opening and, thus, often leads to catastrophic failure when it occurs. Mode II is caused by in-plane shearing of

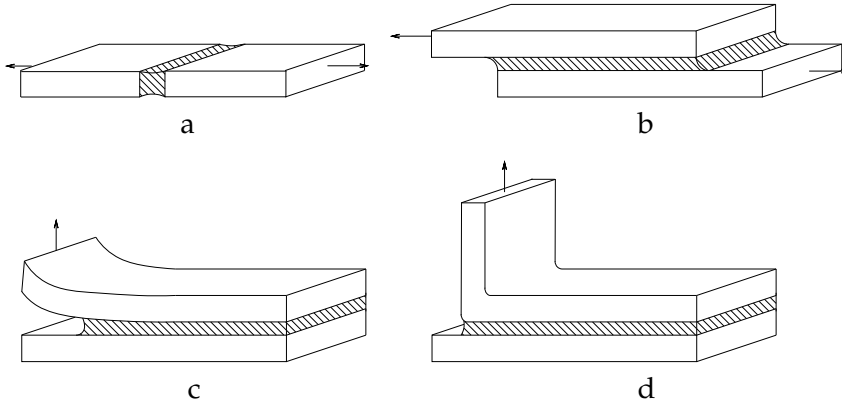


FIGURE 1.3: Four general loading types of adhesive joints. The hatched areas show the adhesive. a) tensile. b) shear. c) cleavage. d) peel.

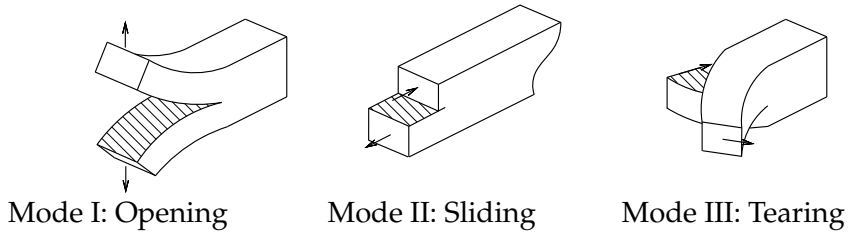


FIGURE 1.4: The three fracture modes corresponding to the three ways a force can propagate a crack: Opening, sliding and tearing.

the joint as is seen in Figure 1.3(b). Contrary to mode I, sliding does not weaken the joint. The joint strength is retained and might even increase due to effects such as crack shielding¹⁸ or friction. The last mode is caused by out-of-the-plane shearing and results in a tearing crack. Similar to sliding, this mode can result in shielding of the crack tip, which preserves or even increases the apparent fracture toughness of the joint. With these modes it is possible to identify the type of failure or crack growth the joint faces based on the applied loading. It is important to notice that the joint types, loading types and fracture modes all are idealized and simplified cases. In reality any joint or loading type may be a combination of several types. Similarly, several fracture modes may co-exist in a single joint causing what is known as mode-mixity. To account for the rich diversity in

joint geometries and loading scenarios a large variety of mechanical models have been developed through the last century. Several aspects of adhesive bonding had been explored earlier, however, much of the advances in methods and protocols of adhesive joints, especially in composite structures, began in the 1970s with Hart-Smith's work for NASA and the Primary Adhesively Bonded Structures Technology program implemented by the US Air Force.¹⁷ Here a brief overview of some of the theoretical developments in mechanical modeling of adhesive joints through the 1900s is given. The list is nowhere near complete or exhaustive, but is meant as a short introduction to the topic.

1.1.1 Shear Lag Configuration

The first model for bonded joints in the literature is the shear lag model proposed by Volkersen in 1938 (see Figure 1.5).¹⁹ The model describes a

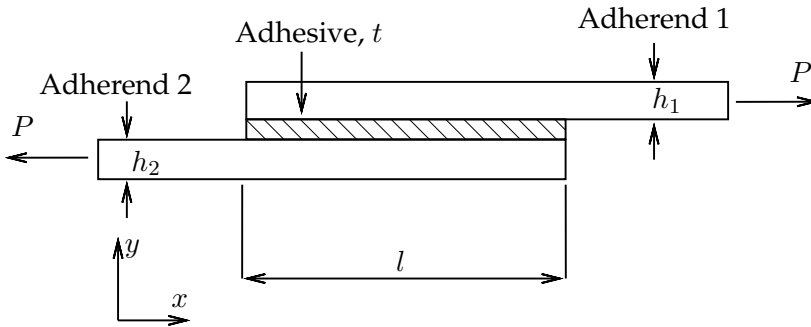


FIGURE 1.5: Schematics of the shear lag model. Adherend 1 is joined with adherend 2 through the intermediate adhesive layer. h_1, h_2, t are the thickness of adherend 1, adherend 2 and the adhesive, respectively. l is the overlap length and P is the applied force.

single lap joint and predicts the differential shear stress through the shear layer (adhesive) as stated in eq. (1.1).

$$\frac{d^2\tau}{dx^2} - \alpha^2\tau = 0 \quad \text{with} \quad \alpha = \sqrt{\frac{G}{t} \left(\frac{E_1 h_1 + E_2 h_2}{E_1 h_1 E_2 h_2} \right)} \quad (1.1)$$

where τ, E, G, h, t are shear stress in the adhesive, adherend elastic modulus, adhesive shear modulus, adherend thickness and adhesive thickness,

respectively. Subscripts 1, 2 denote the top and bottom adherend, respectively. The solution to eq. (1.1) has the following form.

$$\tau = A \cosh(\alpha x) + B \sinh(\alpha x) \quad (1.2)$$

The model did not take into account the bending effects resulting from the eccentric load path.²⁰ In 1944 Goland and Reissner extended the shear lag model by including the rotation and resulting moment.²¹ This enabled separation of the shear stress and the peel stress acting on the adhesive. In the 1970s the lap joint was revisited by Hart-Smith, who introduced plasticity of the adhesive.²² His analysis combined elastic peel stresses with plastic shear stresses distinguishing between regions of elasticity and regions of plasticity. This refinement of the lap joint model improved its ability to accurately describe the joint behavior and predict the failure.

1.1.2 Double Cantilever Beam Configuration

The double cantilever beam (DCB) seen in Figure 1.6 was developed to describe cleavage. It consists of two adherends of width b and thickness h with an intermediate layer of adhesive of thickness t . The initial crack has a length of a while the bonded part has a length of l . The load P is applied to adherends in the cracked end. While, this is the standard DCB different versions of it exist. If there is only one adherend or one of them is much stiffer (effectively rigid) it is called a single cantilever beam (SCB). If the two adherends are not identical it is called an asymmetric double cantilever beam (ADCB). Here we focus on the standard DCB.

The theoretical description of the DCB has been modified, extended and augmented to cover various effects. Its evolution with time is seen in Figure 1.7. The DCB was first proposed by Benbow and Roesler in 1956.²³ Originally, the DCB was developed as a method of measuring critical fracture energy or toughness of various materials. With tensile stresses perpendicular to the crack plane being dominant, the DCB offers almost pure mode I loading. Benbow and Roesler used simple beam theory to model the cracked parts of the adherends as cantilever beams. The governing equation for their model was:

$$EI \frac{d^4 w}{dx^4} = q \quad (1.3)$$

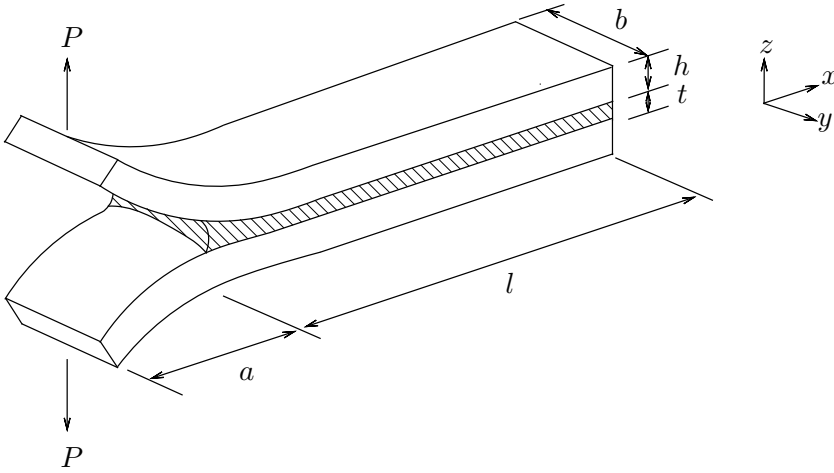


FIGURE 1.6: DCB configuration comprising two adherends of thickness h , width b , initial crack length a and intact length l . The intermediate adhesive layer of thickness t is hatched. The load P is applied in one end of the joint perpendicular to the bondline.

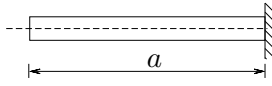
where q is a distributed load and I is the second moment of area. The homogeneous solution to eq. (1.3) is a polynomial of the form.

$$w = A\frac{1}{6}x^3 + B\frac{1}{2}x^2 + Cx + D \quad (1.4)$$

with A, B, C, D being constants of integration to be found through a boundary value problem. This model treated the intact part of the joint as completely rigid (through the clamped boundary conditions of the cantilevers: $a < x : w = 0$), which overestimated the stiffness of the joint.

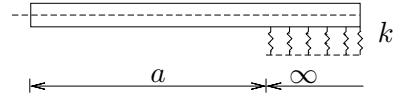
It turned out that a solution to this problem was already developed. In 1867 when working on longitudinal sleepers in railway engineering Winkler came up with the first beam on an elastic foundation model known as the Winkler foundation.^{24,25} In short, the model is a simple beam on a foundation, which acts as a series of linear springs. The foundation represents the material on which the beam is resting on. In 1973 Kanninen came up with the idea to represent the intact part of the DCB as a beam on the

1956: J.J. Benbow and F.C. Roesler



$$0 < x < a : EI \frac{d^4 w}{dx^4} = 0$$

1973: M.F. Kanninen

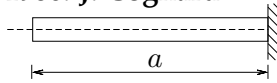


$$0 < x < a : EI \frac{d^4 w}{dx^4} = q$$

$$a < x < \infty : EI \frac{d^4 w}{dx^4} + kw = q$$

$$k = \left(\frac{2Eb}{t} \right)$$

1986: J. Cognard



$$0 < x < a : EI \frac{d^4 w}{dx^4} = q - \frac{EI}{\kappa AG} \frac{d^2 q}{dx^2}$$

1992: F.E. Penado

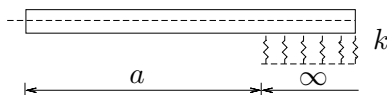


$$0 < x < a : EI \frac{d^4 w}{dx^4} = q$$

$$a < x < \infty : EI \frac{d^4 w}{dx^4} + kw = q$$

$$k = \frac{1}{\frac{1}{k_{adherent}} + \frac{1}{k_{adhesive}}}$$

2012: N.B. Salem et al.



$$0 < x < a : EI \frac{d^4 w}{dx^4} = q - \frac{EI}{\kappa AG} \frac{d^2 q}{dx^2}$$

$$a < x < \infty : EI \frac{d^4 w}{dx^4} - \frac{kEI}{\kappa GS} \frac{d^2 w}{dx^2} + kw = q$$

$$k_{adherent} = \frac{4Eb}{t}$$

$$k_{adhesive} = \frac{b}{t} \frac{E}{1 - \nu^2}$$

FIGURE 1.7: Time evolution of DCB

Winkler foundation as:

$$EI \frac{d^4 w}{dx^4} + kw = q \quad \text{with} \quad k = \frac{2Eb}{h} \quad (1.5)$$

The solution to Kanninen's model has the following form.

$$w = e^{\lambda x} [A \cos(\lambda x) + B \sin(\lambda x)] + e^{-\lambda x} [C \cos(\lambda x) + D \sin(\lambda x)]$$

$$\text{with} \quad \lambda = \left(\frac{k}{4EI} \right)^{\frac{1}{4}} \quad (1.6)$$

Kanninen formulated the foundation modulus k as the stiffness of part of the adherend replaced by it. Doing so provided a more accurate description of specimen stiffness compared to previous model. Furthermore, modeling the intact part of the joint provided valuable information about the region in front of the crack in particular the elastic process zone, λ^{-1} .²⁶ The elastic process zone is responsible for distributing tensile stress ahead of the crack. The model was intended for studying fracture specimens and, thus, did not include an adhesive layer. This would be added later.

In 1986 J. Cognard described wedge testing of adhesives using the DCB model. He replaced the simple beam theory by Timoshenko beam theory to account for the shearing adding it to the energy balance.²⁷ The governing equation for his model was:

$$EI \frac{d^4 w}{dx^4} = q - \frac{EI}{\kappa SG} \frac{d^2 q}{dx^2} \quad (1.7)$$

Where $\kappa = 5/6$ is the shear factor for rectangular beams and $S = hb$ is the cross-sectional area of the adherend. For applications such as the wedge test where there is no distributed load ($q = 0$) but a prescribed displacement, the solution to eq. (1.7) is essentially the same as that of the original DCB model. However, Timoshenko boundary conditions would be used in the boundary value problem.

In 1993 Penado extended Kanninen's work by including the adhesive.²⁸ As such the governing equation and the solution were the same but the foundation modulus was changed. Penado suggested that the intact part of the adherend below the neutral axis and the adhesive worked as springs

in series. Hence, the foundation modulus could be calculated as follows.

$$k = \frac{1}{\frac{1}{k_{adherend}} + \frac{1}{k_{adhesive}}} \quad (1.8)$$

The adherend stiffness was formulated like in the Kanninen model except Penado found that a factor of 4 correlated better when shear effects took place, hence.

$$k_{adherend} = \frac{4Eb}{h} \quad (1.9)$$

The stiffness of adhesive was found by considering the stress-strain relation in the adhesive layer. Assuming two-dimensional plane stress and no in-plane lateral strain in the adhesive Penado came up with the following expression for its stiffness.

$$k_{adhesive} = \frac{b E_{adhesive}}{t (1 - \nu^2)} \quad (1.10)$$

where ν is the Poisson's ratio. By coupling the adhesive with the response of the joint modeling of adhesive joints significantly improved. Now it was possible to assess how the thickness, width, stiffness etc. of the adhesive layer would effect the global behavior of the joint.

Recently, the foundation based model was revisited and further extended by N.B. Salem et al.²⁶ They rederived the model using Timoshenko beam theory together with the Winkler foundation, and later the Pasternak foundation. A more refined and accurate description of DCB specimens with thick adherends was obtained. Their model was formulated as follows.

$$EI \frac{d^4 w}{dx^4} - \frac{kEI}{\kappa GS} \frac{d^2 w}{dx^2} + kw = 0 \text{ with } k = E_{adhesive} \frac{(1 - \nu)}{(1 - 2\nu)(1 + \nu)} \frac{b}{t} \quad (1.11)$$

The two main differences between this model and the two previous foundation models were the middle term in eq. (1.11), which took shearing of the cross-section into account, and the formulation of the foundation modulus. The foundation modulus was determined as the stiffness of the adhesive under the three-dimensional plane strain assumption, hence it neglected the adherend. This is justified when the stiffness of the adherend is much higher than that of the adhesive. The solution to eq. (1.11) is of the

following form.

$$\begin{aligned}
 w &= P A e^{\lambda_1 x} + P B e^{\lambda_2 x} \\
 \phi &= P C e^{\lambda_1 x} + P D e^{\lambda_2 x} \\
 \text{with } C &= \left(\lambda_1 - \frac{k}{\kappa G S} \frac{1}{\lambda_1} \right) A \quad D = \left(\lambda_2 - \frac{k}{\kappa G S} - \frac{1}{\lambda_2} \right) B \\
 \text{and } \lambda_{1,2} &= \sqrt{\frac{1}{2} \left[\frac{k}{\kappa G S} \pm \sqrt{\left(\frac{k}{\kappa G S} \right)^2 - 4 \frac{k}{EI}} \right]}
 \end{aligned} \tag{1.12}$$

where ϕ is local beam rotation and A, B are constants to be determined through a boundary value problem.

The DCB is one of the most used configurations for mode I fracture testing since it is very flexible. As shown by the model variety the configuration can describe DCB tests, SCB tests, wedge tests, among others. It is easy to produce and test and data treatment and reduction are straight forward since all of the theoretical models have simple closed-form solutions. Even though the configuration is simple, one has to be aware of several aspects, i.e. root rotation of the adhesive, shearing of the adherends, stiffness of adhesive and adherends etc., when using the DCB. This is also reflected by the variations in the theoretical models.

1.1.3 Peel Configuration

The resemblance between cleavage and peel is remarkable, e.g. both fail in mode I and have similar loading conditions, but they are indeed quite different. Peeling is a special type of cleavage where at least one of the adherends is flexible, either due to limited thickness $I \propto h^3$ or due to low material stiffness, see Figure 1.8. The flexibility results in large deformations and rotations violating the infinitesimal strain theory, which the DCB is based on. With a low bending stiffness the load transfer is mainly driven by membrane forces where the adherend bends and aligns its neutral axis with the loading. As such peeling differs from the DCB configuration. A large body of work has been devoted to studying peeling. The first peel model recorded was proposed by Rivlin in 1944, a decade before the DCB, who formulated the fracture energy in terms of the force applied to the strip being peeled (often referred to as the film), the width of it and the

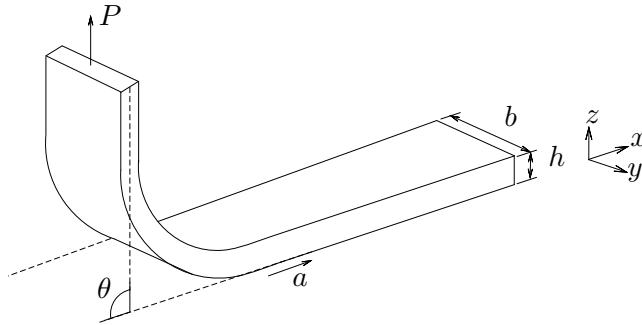


FIGURE 1.8: Peel configuration with a single flexible adherend of thickness h , width b and peeled length a . P is the applied force and θ is the peel angle that is the angle at which the adherend detaches.

angle of inclination of the substrate, which it was attached to.²⁹ He formulated the effective work of adhesion per unit area W , i.e. energy release rate (ERR), as stated by eq. (1.13).

$$W = \frac{P}{b} (1 - \cos \theta) \quad (1.13)$$

where P, b, θ are the applied force, width of the film and the peeling angle, respectively. Interestingly, the length of the film does not enter the expression. Hence, the geometrical effects are only related to the width.

The model was revisited in 1971 by Kendall who did an energetic analysis of the peel geometry.³⁰ Kendall identified all the energy terms, i.e. bending and stretching of the film, the potential energy of the external loading and the surface energy as seen in eq. (1.14).

$$\frac{dU_t}{da} = -b\gamma + P(1 - \cos \theta) + \frac{dU_B}{da} + \frac{P^2}{2bhE} \quad (1.14)$$

where $U_t, U_B, a, b, h, P, \theta$ are the total energy of the system, the bending energy, a peeled length of the film, film width, film thickness, the applied load and the peel angle, respectively. γ is the surface energy of the adhesive, which relates to the work of adhesion as follows $W = 2\gamma$. The last term in the equation is the elastic energy stored in stretching the film.

Assuming the bending energy to be constant doing peeling $\frac{dU_B}{da} = 0$ and the elastic energy to be negligible compared to the other energetic

terms, Kendall arrived at an expression very similar to Rivlin:

$$W = 2\gamma = 2\frac{P}{b}(1 - \cos \theta) \quad (1.15)$$

Again, the length of the peel arm does not influence the work of adhesion.

In 1997 Cook, Edge and Packham studied adhesion between rubber and steel through peeling.³¹ Their study led to a rederivation of the peel model to account for the behavior of rubber. Their expression differs from the two previous by not restriction the film to linear elastic.

$$W = \frac{P}{b}(\lambda_1 - \cos \theta) - W_{\lambda_1}h \quad (1.16)$$

where λ_1 , W_{λ_1} , h are stretching of the peel arm, strain energy of the rubber spend in stretching it to λ_1 and the film thickness, respectively. Note that the length of the peel arm implicitly enters the expression through the stretching.

Other developments in the peel model involve introduction of preload in 1997 by Barquins and Ciccotti,³² addition of backing to the film in 2005 by Piau et al.,³³ consideration of the film thickness in 2011 by Kendall et al.,³⁴ among others.³⁵

1.1.4 Notes on Numerical Methods

The presented models are based on analytical mechanics. Their main advantages are transparency, phenomenological insight and simple closed-form expressions. However, the latter is also their weakness. To be able to obtain closed-form solutions often assumptions and simplifications have to be made. Sometimes they are justified, other times more details or complexity are needed to fully describe the problem. When this is the case, numerical modeling can be the solution. The main focus of this dissertation is analytical mechanics but for completeness a very brief presentation of three numerical methods used with adhesive joints are included.

Many numerical methods for modeling bonded joints exist, here three common ones are presented. The methods include the finite element (FE) method, the boundary element (BE) method and the finite difference (FD) method.³⁶ The FE method is by far the most extensively used and was, to the author's best knowledge, applied to adhesively bonded joints for the first time in 1974 by Adams and Peppiatt.³⁷ However, the technique has been used for a range of different applications before that. The FE method

has a lot to offer in terms of analyzing complex geometry, including both geometrical and material non-linearities, and implementation of a broad selection of different damage and failure mechanics, e.g. cohesive zone modeling,³⁸ virtual crack closure technique,³⁹ extended FE modeling,⁴⁰ virtual crack extension,⁴¹ among others. By subdividing the geometry into smaller, simpler geometries, i.e. finite elements, the method transforms the analytical boundary value problem into a system of algebraic equations.

The BE method has features which makes it attractive in some regards.⁴² For instance, it provides very good resolution of the stress gradients found in front of crack and across interfaces, such as those found in bonded joints. Contrary to the FE method where the full domain is discretization, the BE method only needs discretization on the boundary. This makes meshing and remeshing easier and reduces computation time. It also automatically satisfies any far field assumptions, which reduces the part of the joint necessary to discretize. However, the implementation of BE is not as straightforward as the FE and can prove very challenging. As a result BE is far less used than FE.

Finally, the FD method is a direct method of obtaining an approximate solution to partial differential equations.³⁶ The FD method can be used when a differential equation is too complex to be solved analytical. Instead, a numerical solution can be obtained. The implementation of FD is fairly straight-forward making it attractive. However, complex geometries and boundary conditions could prove challenging. As a result the FE method is preferred when dealing with complex shapes and advanced material models.³⁶

1.2 Stochastic and Structured Interfaces

1.2.1 Beyond Homogeneous Bondlines

Common for the models just presented is that they treat the interface region as homogeneous, i.e. uniform without variations. However, most interface regions are in fact heterogeneous since property variations exist. This can be variations in physical properties such as roughness, stiffness, toughness, etc., or in chemical properties, e.g. wetting, adhesion, etc.^{43,44} and can either be unwanted (stochastic) or designed on purpose (structured).

Stochastic heterogeneities mainly originate from manufacturing processes making them an inevitable part of bonded joints. Examples of these are flaws in the bondline, defects on the surfaces or remaining by-products,

e.g. oil or release film, just to name a few.^{43,44} The dreaded kissing bond, which poses a serious treat to bonded structures and laminated composites and is very difficult to detect, also belongs to this category.⁴ Their severities may vary and, hence, need to be analyzed to assess if the integrity of the joint is affected. Since they are stochastic in nature analyzing them sometimes requires stochastic models.

Structured heterogeneities can result from design requirements of the joint or interface but can also be introduced purposely to alter the response. The latter is of great interest both research- and application-wise. It turns out that structured interfaces can have beneficial effects on the global response of the joint. One of the first to realize this was Kendall in 1975, when he created films of varying stiffness either geometrically through increased thickness or materially by reinforcing the film.⁴⁵ From peeling the stiffness variation was found to increase the apparent toughness and, thereby, retard the crack growth.

Other examples of how structured interfaces can affect the global response include Das Neves et al's work on mixed adhesive lap joints from 2009. They studied the effects of combining low and high temperature adhesives in a changing working environment.⁴⁶ They found that the best performance of the joint when operating from low to high temperatures was obtained with a ratio of low and high temperature adhesives of around a half.

In the experimental study of Budzik et al. from 2012 the effects of a structured interface in a single cantilever beam setup were investigated.⁴⁷ By introducing bands of strong and weak adhesion running parallel to the crack growth direction, causing the adhesive strength to vary along the crack front, the authors studied consequences on the joint's failure behavior in terms of load response and fracture energy. It was observed that the crack advanced in the weak zones while retarded in the stronger zones. From the classical rule of mixtures, the effective fracture energy of the joint was expected to depend linearly on the ratio of strong to weak zones. However, the authors found that this was not the case. Different modifications to the rule of mixtures were proposed, however, an empirical power-law expression was found to describe the effective fracture energy the best. Tailoring the bondline with bands of weak and strong adhesive permits tuning of the global, effective fracture energy of the joint.

Xia et al. expanded Kendall's work in a two part article where they first explored elastic contrast⁴⁸ and, secondly, adhesive heterogeneity.⁴⁹ In their

first paper from 2013 they peeled thin adhesive tapes reinforced systematically with PET patches, which locally increased the bending stiffness, from an epoxy layer. Through experimental and theoretical analyses the authors found that the varying bending stiffness led to fluctuations in the elastic bending energy, which raised the apparent toughness of the joint and, therefore, increased the critical fracture load by an order of magnitude. In the other part of their work from 2015, they dealt with variations in surface properties resulting in a heterogeneous adhesion. Specifically, they attached polydimethylsiloxane (PDMS) to a transparent film on which patterns of ink were made. The adhesion strength varied greatly between the bare regions and those with ink. Peeling the PDMS from the film revealed that adhesive heterogeneities offered a broad selection of different behaviors such as wavy peel front, complex corrugated shapes in the film, etc. Most importantly, it enabled asymmetric peeling where one direction was stronger than the other.

Cuminatto et al. proposed an analytical DCB model in 2015 for studying patterned interfaces containing channels of void through the bondline running perpendicular to the crack growth direction.⁵⁰ The model included both stretching, rotation and finite bondline length. They obtained valuable insight in structured interfaces such as those found in microelectronics and Micro-Electro-Mechanical Systems (MEMS) showing that the periodicity and width of adhesive bands controlled the debonding behavior turning it either stable or unstable.

Cordisco et al.'s work from 2016 in which the standard straight bondline of the DCB was replaced with a sinusoidal one.⁵¹ By controlling the amplitude and the wavelength of the sinusoidal structure they were able to increase damage tolerance and, for some specific combinations, increase the critical load at fracture as well.

Minsky and Turner's⁵² paper from 2017 showed that the dry adhesion of a post can be enhanced and tuned by structuring of the interface. By including a stiff core in a compliant shell they obtained a post with enhanced adhesion under normal loading but reduced strength in shear. Their study emphasized the benefits and applications of structured interfaces by showing both the enhancing properties but also the establishment of new functionalities.

Ranade et al. studied DCB specimens with localized zones of weak interfaces from 2018. A reverse R-curve trend was observed when the crack tip approached these interfaces followed by a rising R-curve behavior when it left the patterns.⁵³ A rule of mixtures was found to describe the

fracture energy.

1.2.2 Inspiration from Metamaterials

Metamaterials receive a lot of attention from different scientific communities. They are materials engineered from small, often repeated, assemblies to have specific properties or behaviors not found in naturally occurring materials. Origami where folds are added to a structure⁵⁴ and kirigami where cuts are added⁵⁵ are examples of how geometrical features can facilitate new materials properties. Advances in manufacturing technologies, e.g. 3D-printing, laser cutting, etc., help to promote metamaterials. Inspired by these, a branch of structured interfaces and metasurfaces seek to tailor the global response and the properties of bonded joints solely through geometrical manipulation of the interface region. The correct combination of size and shape of geometrical features in the interface region can result in enhanced joint performance or promote new functionalities. An example of this is the work of Hwang et al.⁵⁶ where the authors used structured cuts in a polymer film to generate zones of either high or low stiffness. By tuning the zones the peeling strength increased compared to a homogeneous film. In addition, anisotropic peel strength where one peel direction was much stronger than the other was achieved. Such functionality could be attractive for band-aid and transfer processes.

Nguyen et al. introduced outward dimples, inward dimples, outward grooves and inwards grooves features, as seen in Figure 1.9, to metal-composite DCB specimens using Selective Laser Melting (SLM).⁵⁷ From experimental and theoretical work they assessed the apparent fracture toughness of each structured interfaces. They found that the outward grooves increased the apparent fracture toughness with up to 50% compared to the homogeneous bonded interface. The grooves deflected the crack path increasing its length while shifting the failure from pure mode I to mode-mixity.

The list of studies on the subject is nowhere exhaustive or complete but helps to underline some of the benefits or drawbacks of having structured interfaces. It is clear that structuring of the interface can significantly affect, and potentially tune, many joint parameters. Ways of structuring the interface are nearly infinite and each may have a very different impact on the joint, hence needs carefully studying. A lot of effort has been put into researching structured interfaces, however, they are still far from fully understood and may still retain many secrets.

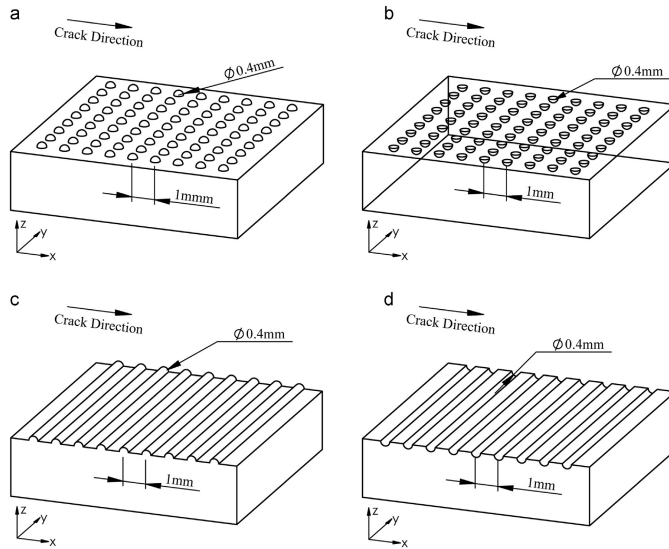


FIGURE 1.9: Interfacial features introduced by Nguyen et al. to study their impact on joint failure. a) Outward dimples. b) Inward dimples. c) outward grooves. d) Inward grooves. This figure is reproduced from reference 57.

1.3 Scope of Work

The scope of the project started as developing and testing a new type of polymer brush-based nano-adhesive for bonding rubber to metal in food and drinking water applications. The metal samples were restricted to 10×10 mm by the equipment used to apply the surface chemistry. To be able to test both the chemical composition of the adhesive on the surface and obtain the peel strength, a peel specimen containing three samples was designed. The metal samples were spaced out in the specimen and rubber was vulcanized on top facilitating bonding. This created a structured interface consisting of zones with adhesion separated by zones without adhesion, see Figure 1.10. As seen in the figure, the interface region contained several structured features: the fibril-like distribution of the polymer brushes, separation of the bonded zones and thickness variation of the rubber across the bonded regions. With cohesive failure in the rubber (as desired within the project) limited information about the interface was gained and it was hard to justify researching the rubber itself. However, the peel results were quite unusual compared to the standard peel tests since

the load response both oscillated, accelerated near the edges and contained snap-downs.

Two possible paths to investigate these phenomena were proposed. Either a refined numerical approach of the whole specimen including different models for describing the hyperelasticity, crack onset, propagation and damage, or an analytical approach where the problem was broken into smaller less complex pieces could be pursued. The numerical approach would allow full description of the specimen and the scenario but could easily end up being very complex and phenomenological details could get lost. The analytical approach would take small pieces of the problem at the time, and, thereby, lose some of the greater picture but could potentially provide valuable phenomenological insight and relate to more systems. The latter was chosen.

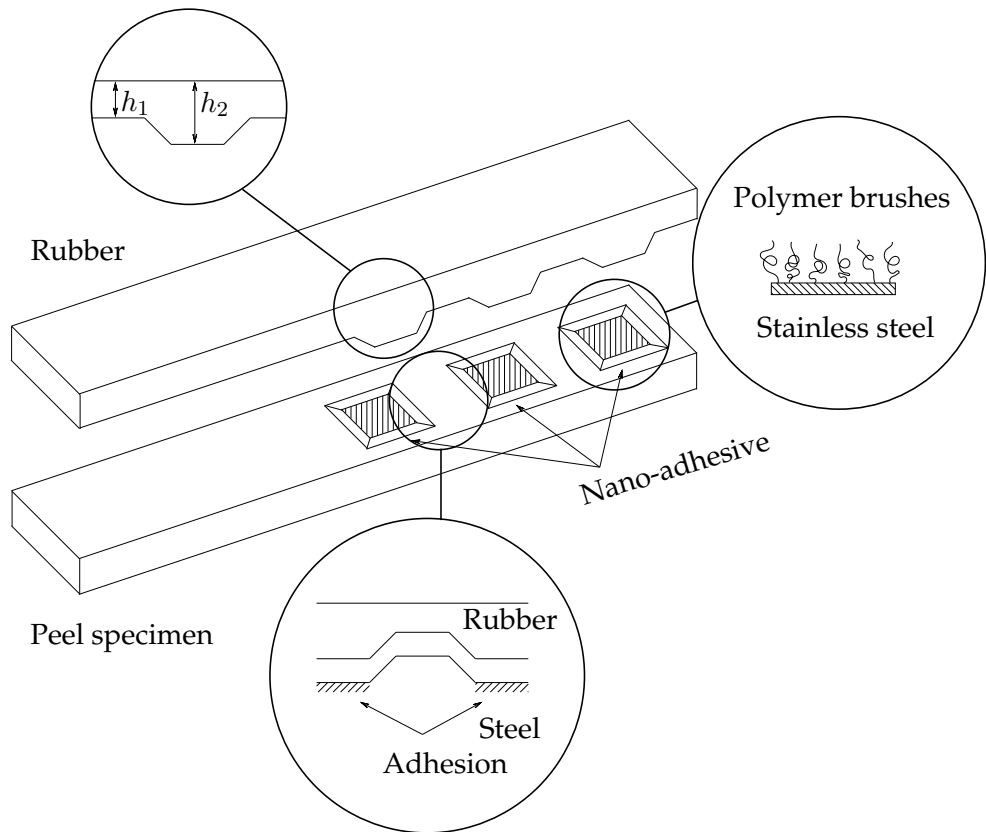


FIGURE 1.10: Peel specimen with nano-adhesive comprising a steel specimen, three samples with adhesion and a rubber part. Structuring of the interface are highlighted with close-ups. These include thickness variation of the rubber across the bonded zones, separation of the bonded zones and fibril-like distribution of the polymer brushes.

Research questions, such as the consequences of zones with adhesion separated by zones without, how the crack velocity and the load response are related for structured interfaces, etc., were pursued with an analytical approach supported by experimental and numerical work. This formed the scope of the present dissertation while its form is in accordance with the guidelines for a cumulative PhD dissertation proposed by the Department of Engineering. The following five chapters are each based on a manuscript either published or submitted during the PhD and contains a brief description including motivation for the work, methods used, the author's contributions, the main finding and reflections. In the seventh and final chapter the outcome of the dissertation is summarized and recommendations and ideas for future work are given.

Chapter 2 includes paper 1 concerning nano-adhesives. A new method of bonding Ethylene-Propylene-Diene M-class (EPDM) rubber to stainless steel through nano-scale polymer brushes is investigated. To be able to test both the chemistry and the mechanical properties, i.e. the adhesion strength and quality, without changing the specimen, a custom-made peel setup is developed. The specimens contain three distinct bonded zones making the bondline discontinuous and heterogeneous. Through experiments and theoretical data treatment the adhesion strength and quality is obtained and compared to a commercially available solution to validate the new nano-scale adhesive.

Chapter 3 includes the second article, which is the first solely pursuing structured interfaces. In it the impact of bands of low adhesion running perpendicular to the crack growth direction on load response and apparent fracture energy is studied. An analytical model is developed and used to explain experimental findings obtained using the DCB configuration.

Chapter 4 includes the third paper, which continues investigating interfacial heterogeneities running perpendicular to the crack propagation direction. This work explores the consequences of a single region of weak adhesion within the bondline by extending the analytical model from paper 2 with kinetic and rate-dependent mechanisms. These are used to describe the effects of the external loading rate and the crack velocity on the global response and critical fracture energy. The theoretical model is supported by experimental data.

Chapter 5 concerns the fourth paper, which also deals with heterogeneous adhesion but takes a slightly different direction. Kissing-bonds are introduced to composite DCB specimens comprising carbon fiber reinforced polymer (CFRP) adherends bonded together with an epoxy. The

epoxy contains a support carrier, normally regarded as a weakening factor, to control bondline thickness. The aim is to study how the kissing-bond is expressed in the load response and affects the fracture behavior. However, the carrier is found to trigger a bridging phenomenon, which greatly enhances the damage tolerance. Through experiments and theoretical modeling, including the model developed in the two previous papers, the impact of the kissing bond and the effects of the support carrier are predicted and described. The crack growth velocity and the loading rate are included in the failure analysis to determine the kinetic contribution to the ERR.

Chapter 6 contains the fifth and last paper, which is currently under review for *The Journal of the Mechanics and Physics of Solids*. A meta-material approach is taken in which the critical fracture load and damage tolerance is enhanced by pure geometric manipulation of the interface region. Pillars are introduced to the interface region in DCB and ADCB specimens, which were manufactured and tested. An extensive theoretical framework based around Euler-Bernoulli and Timoshenko beam theory including both micro- and macro-mechanical level is developed. With it key parameters and mechanisms responsible for the increased critical fracture load and the enhanced damage tolerance are identified and described.

Chapter 7 contains a short summary, an outlook putting the contributions and finding into perspective, and, finally, recommendations and ideas for future work based on the outcome of this project.

Chapter 2

Paper 1 - On Rubber-Metal Bonding

Efficient bonding of ethylene-propylene-diene M-class rubber to stainless steel using polymer brushes as a nanoscale adhesive¹

2.1 Introduction

Chemical migration from bonded interfaces between rubber and metal poses a hazard to the surroundings. This is of special concern in food and drinking water applications where contamination can be catastrophic. Motivated by this a new way of bonding EPDM rubber to stainless steel using a nanoscale adhesive composed of polymer brushes is sought. The chemical components involved and the minute amounts necessary for a nano-meter thick bondline are believed to minimize the risk of migration. To assess the nano-adhesive and compare it to existing solutions, equipment and standardized methods of both chemical and mechanical evaluation of the same sample are developed and tested.

2.2 Method

Chemically a grafting-from method is used to produce polymers a few nano-meter long at a steel surface. This is followed by a post-polymerization modification where peroxides are attached to the polymers to enhance and facilitate bonding. To validate the chemical composition ellipsometry, Infrared reflection absorption spectroscopy (IRRAS) and X-ray photoelectron

spectroscopy (XPS) are used. These techniques constrain the dimensions of the stainless steel samples to 10mm × 10mm, which is not suitable to mechanical evaluation.

To facilitate mechanical testing of the samples an aggregate allowing up to three samples to be mounted is designed and manufactured. The samples are equally spaced by 10 mm, which when the specimen is molded with rubber results in three separate and distinct bondlines. The aggregate is attached to a sled with low friction brass wheels. The sled allows for peel testing of the molded specimen in a universal testing machine. From peel testing the critical fracture energy (adhesive strength) of the specimens is determined and post-mortem scans of the fracture surfaces provided a measure of the bonding quality. Quantitatively the bonding quality is assessed as the ratio of cohesively failed area to the full bonded area. These two parameters – adhesive strength and adhesive quality – are used to benchmark the new bonding method to a common commercial binder-and-primer solution.

2.3 Contribution

The author's contributions include designing and manufacturing of the test setup and the components involved, carrying out the experiments and treating the data, theoretical modeling of the system and preparation of the manuscript.

2.4 Finding

The main finding of the work is that the nano-scale adhesive with a bondline three orders of magnitude thinner achieves equal adhesive strength and similar quality compared to a common commercial solution. This supports the use and further research of the system. Secondly, it is found that the setup developed permits both chemical and mechanical evaluation of the samples without any modifications, hence reducing risk of alterations. Such system is not report often, if at all, in the literature. Furthermore, the heterogeneous peel specimen provides more and better data by allowing three samples to be tested at each go and by forcing the crack towards the interface preventing peel arm failure, which is otherwise common when testing strong adhesives.

2.5 Reflection

Three phenomena were observed in the study 1) discontinuous load response, 2) acceleration of the crack near the edges of the bonded zones, and, 3) crack surface reconfiguration. Their origin and the roles of the material, i.e. hyperelasticity, strain-hardening, rate hardening, etc.,⁵⁸ and geometry, i.e. bondline separation, thickness variations,⁵⁹ are not fully understood. However, the structured interface is believed to contribute. To answer these questions the first two phenomena are pursued analytically in the following chapters where geometrical structuring of the interface and the influence of a finite bondline on crack velocity and load response are investigated. The crack reconfiguration is out of the scope of the dissertation but is dealt with in reference 6.



Efficient bonding of ethylene-propylene-diene M-class rubber to stainless steel using polymer brushes as a nanoscale adhesive



Simon Heide-Jørgensen^{d,1}, Rasmus Krag Møller^{b,1}, Kristian Birk Buhl^{c,1}, Steen Uttrup Pedersen^{a,c}, Kim Daasbjerg^{a,c}, Mogens Hinge^{b,a,*}, Michal K. Budzik^{d,1}

^a Department of Chemistry, Aarhus University, Langelandsgade 140, DK-8000 Aarhus C, Denmark

^b Department of Engineering, Aarhus University, Hångøvej 2, DK-8200 Aarhus N, Denmark

^c Interdisciplinary Nanoscience Center (INANO), Aarhus University, Gustav Wieds Vej 14, DK-8000 Aarhus C, Denmark

^d Department of Engineering, Aarhus University, Inge Lehmanns Gade 10, DK-8000 Aarhus, Denmark

ARTICLE INFO

Keywords:

Bonding
Nanoadhesive
Polymer brushes
Rubber
Steel

ABSTRACT

A novel approach to bond rubber to metal using nanometers thick polymer brushes in the interface is investigated. An atom transfer radical polymerization (ATRP) initiator is grafted to the surface of stainless steel (SS) and poly(glycidyl methacrylate) (PGMA) brushes are grown from the surface. Benzoyl peroxide (BPO) is drop casted on the polymer films before the samples are overmolded with ethylene-propylene-diene M-class (EPDM) rubber. For surface concentrations below $0.2 \mu\text{mol cm}^{-2}$ regions with adhesive failure were observed. Thermal infrared reflectance absorption spectroscopy (T-IRRAS) and X-ray photoelectron spectroscopy (XPS) show a conversion of oxirane groups after heating samples to 170°C .

A compression molding system designed to mold uncured rubber on modified SS samples and subsequently to perform peel tests of the rubber-steel specimens are presented. Four stages of crack propagation are identified in the peel data: 1) elastic loading, 2) stable crack propagation, 3) unstable crack propagation, and 4) loss of load carrying capacity. The novel nanometer thick bonding system was benchmarked against a commercial bonding system. Calculated peel energies are in good agreement with previously reported values and show no significant difference compared to a commercial bonding agent. Therefore, it is concluded that the novel bonding system applying only a nanometer thick surface immobilized polymer brush layer offers similar adhesion as existing micrometer thick primer adhesives.

1. Introduction

Bonding between rubber and metal components is important in scientific applications and in many industries, e.g. automotive, food, water, and aerospace [1–5]. Bonding can be achieved by mechanical fixation and/or chemical/physical adhesion. In many applications, bonding rubber to metal components enhances e.g. impact resistance, flexibility, and durability by obtaining hybrid-components combining the attractive properties of both metal and rubber [6–8]. However, designing and manufacturing of these hybrid components are challenging. Chemical methods of bonding rubber to metal include brass plating, vulcanization, or adhesion through primer and binder [9]. In brass plating (extensively used in the tire industry) cyanide and other additives are used, which may alter and degrade the rubber properties [10]. Industrially used adhesives rely on single or two-component

solvent based adherent that provide good and high strength adhesion [6,11–14]. The primer and binder are applied in several micrometer thick layers and migration may occur in certain applications. This may alter the rubber properties and raise health risks in specific applications like drinking water valves [9]. Recently, nanometer thick organic primers based on silane and thiol grafted organic layers were demonstrated to provide adhesion towards rubbers [15,16]. These nanometer-thick primers decrease the amount of hazardous chemicals used in the interface which, potentially, may migrate through the rubber into the surroundings.

Once the two materials are joined, a new challenge needs to be addressed. Within the multi-material structure misfits exist from a mechanical point of view. Rubber is both visco- and hyperelastic with roughly four orders of magnitude lower elastic modulus than that of steel [17]. Due to displacement field continuity hybrid components

* Corresponding authors.

E-mail addresses: hinge@eng.au.dk (M. Hinge), mibu@eng.au.dk (M.K. Budzik).

¹ These authors contributed equally to this work.

<https://doi.org/10.1016/j.ijadhadh.2018.09.006>

Accepted 19 September 2018

Available online 26 September 2018

0143-7496/© 2018 Elsevier Ltd. All rights reserved.

have stress gradients in the vicinity of edges and corners induced by the elastic misfits. This may alter the crack propagation after crack onset [18–21]. Furthermore, the elevated manufacturing temperatures (100–300 °C) along with the one order of magnitude difference in thermal expansion between rubber and metal introduces interfacial stresses [22]. The elastic moduli and thermal expansion differences could result in reduced load-carrying capacity of the joint and thereby reduce product lifetime and even lead to catastrophic failure. Existing evaluation procedures often decouple the chemical testing from the mechanical one [23,24]. In addition, samples tend to be prepared separately [25]. Thus, introducing a novel bonding agent along with a new evaluation procedure addressing both chemical and mechanical properties is critical.

This paper introduces and investigates novel nanometer thick polymer brushes as adhesion promoters between stainless steel and ethylene-propylene-diene M-class (EPDM) rubber. The polymer brushes are based on a “grafting from” procedure exploiting a surface grafted polymer initiator and followed by chemical post-polymerization modifications [26,27]. The surface immobilized polymer brush layer is characterized by ellipsometry, infrared reflection absorption spectroscopy (IRRAS) and X-ray photoelectron spectroscopy (XPS). Equipment and standardized methods allowing for both chemical and mechanical evaluation of the same sample are developed and applied for interfacial toughness testing.

2. Materials and methods

2.1. Materials

Dichloromethane (DCM), chloroform (CHCl₃), methanol (MeOH), acetonitrile (MeCN), and acetone were all HPLC grade. These solvents and 2-bromoisobutyl bromide (BIBB, 98%), 2,2'-bipyridine (BiPy, > 99%), triethylamine (TEA, > 99%), and sodium ascorbate (NaAsc, > 99%) were purchased from Sigma Aldrich. Cu^{II}Cl₂·2H₂O (99%) and benzoyl peroxide (BPO, > 97%) were obtained from Merck and Fluka, respectively. The chemicals were used as received without further purification. Glycidyl methacrylate (GMA, 99%, Sigma Aldrich) and methyl methacrylate (MMA, 99%, Sigma Aldrich) were passed through an aluminum oxide column to remove monomethyl ether hydroquinone (inhibitor).

Tetrabutylammonium tetrafluoroborate (Bu₄NBF₄) and 4-(2-hydroxyethyl)benzenediazonium tetrafluoroborate (HEBD) were synthesized according to standard procedures [28,29]. Stainless steel ASTM 316 plates (SS, Jensen Metal A/S, Denmark) 10 mm by 10 mm and 2 mm thick (Fig. 2a, item 4) were polished with a diamond suspension (Struers, grain size 9 μm) for 1 h and subsequently cleaned by sonication in Milli-Q water, acetone, and finally pentane for 10 min in each solvent. The plates were polished to obtain equal surface areas for proper comparing of the adhesive properties and to obtain a reflective surface for analytical purpose. EPDM shore 70 rubber (AVK Gummi A/S, Denmark, Tensile modulus 2.11 ± 0.04 MPa)² was applied throughout the study. A commercial bonding agent (denoted SS_{CBA}) was applied to the steel surfaces, annealed at 140 °C for 1 h according to a standard procedure from the supplier, and used as a reference when overmolded.

2.2. Immobilization/grafting of initiators for activators regenerated from electron transfer (ARGET) atom transfer radical polymerization (ATRP)

Unmodified SS substrates (denoted SS_{Blank}) were electrochemically grafted with HEBD using the protocol described elsewhere [28]. In short, SS_{Blank} was modified by potentiostatic electrolysis (−0.81 V vs

² The notation $xx \pm yy$ means average value \pm standard deviation throughout the manuscript.

SCE) for 300 s while stirring. The applied potential was selected to be 0.2 V more negative than the peak potential obtained in a cyclic voltammogram (*vide infra*). The hydroxyl surface grafted SS sample (denoted SS_{OH}; step 1 in Fig. 1) was rinsed in MeCN and sonicated in acetone for 10 min. Acylation was performed by immersion of SS_{OH} in DCM containing 0.5 M BIBB and 0.05 M TEA for 3 h at ambient (~22 °C) temperature (step 2 in Fig. 1) to produce the sample denoted SS_{Br}, followed by rinsing with DCM and sonication in acetone for 10 min.

2.3. Surface initiated (SI) ARGET ATRP

Surface initiated polymerization was performed in a Schlenk flask with 0.5 mL GMA (0.4 M) in 8.5 mL of 1:1 (v/v) Milli-Q water: MeOH. The solution was cooled to 0 °C and purged with argon for 10 min prior to addition of BiPy (12.4 mg, 8.8 mM), CuCl₂·2H₂O (6.8 mg, 4.4 mM), and NaAsc (7.0 mg, 3.9 mM) giving a final molar ratio of 2.2:1.1:1.0 for the three components. The Schlenk flask was closed with a rubber septum penetrated by four stainless steel clamps each holding one SS_{Br} sample. The flask was purged with argon for additionally 15 min before the four samples were lowered into the solution either for 1.5 or 3 h. After polymerization to obtain the corresponding SS_{PGMA} samples (step 3 in Fig. 1), these were rinsed in MeOH and water followed by sonication in acetone for 15 min.

2.4. Drop casting of BPO

Five CHCl₃ solutions with different BPO concentrations (≈0.4, 1, 2, 3, or 4 mM) were prepared. SS_{PGMA} samples were drop casted with 0.1 mL BPO solution by stepwise additions of 0.01 mL followed by CHCl₃ evaporation at ambient pressure and temperature. Surface concentrations (Γ^* of ≈ 0.04, 0.1, 0.2, 0.3, or 0.4 μmol cm^{−2}) on the samples (denoted SS_{PGMA}^{BPO}) were obtained.

2.5. Infrared reflection absorption spectroscopy

All SS_{PGMA} and SS_{PMMA} samples were analyzed by IRRAS using a Nicolet 6700 (Thermo Fisher Scientific) instrument for the recording of spectra. The Fourier transform infrared (FTIR) spectrometer was attached to an external module with a gold wire polarizer *p*-polarizing the incoming infrared light beam that after reflection on the sample was detected on a narrow band mercury–cadmium–telluride (MCT) detector (cooled with liquid nitrogen). All samples were irradiated using a grazing angle of 80° and the *p*-polarized reflectivity of the polymer film, $R_p(d)$, was divided with the reflectivity of the unmodified substrate, $R_p(0)$, and presented as IRRAS absorbance [$-\log(R_p(0)/R_p(d))$] after baseline correction using the OMNIC32 software. The spectral resolution was 4 cm^{−1} and number of scans was 100. All spectra were recorded at ambient temperature in dry air.

Thermal IRRAS (T-IRRAS) was recorded on samples installed in a ceramic sample holder heated by a nichrome alloy of nickel and chrome wire. The homebuilt furnace was controlled by a proportional-integral-derivative (PID) controller with a precision of ± 1 °C by adjusting the voltage output of the heat element. Each temperature level (25, 40, 60, 80, 100, 120, 140 and 170 °C) was kept constant for 2 min before IRRAS was recorded on the heated samples. After T-IRRAS, the samples were sonicated in acetone for 10 min.

2.6. X-ray photoelectron spectroscopy

XPS analysis was performed on the SS_{PGMA} and SS_{PMMA} samples using a Kratos Axis Ultra-DLD spectrometer (Kratos Analytical Ltd., Manchester, U.K.). Monochromated Al K α X-ray (150 W) with an analysis area of 300 μm × 700 μm was used. For survey spectra the analyzer was operated in the constant analyzer energy (CAE) mode (pass energy = 160 eV). Charge compensation was achieved with an electron

S. Heide-Jørgensen et al.

International Journal of Adhesion and Adhesives 87 (2018) 31–41

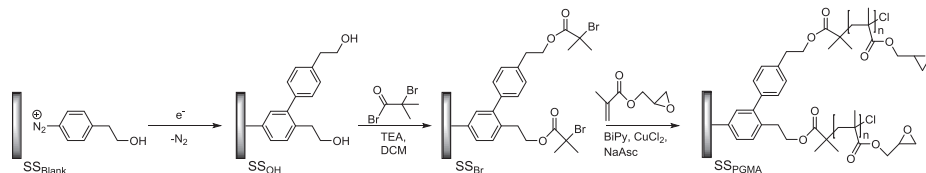


Fig. 1. Reaction protocol for accomplishing the electrografting, acylation, and ATRP of GMA on stainless steel.

flood gun. Binding energy of 285.0 eV (C–C/C–H components of C 1s peak) was used as reference. Spectral processing was performed by CasaXPS (v. 2.3.18, Casa Software Ltd. U.K.).

2.7. Ellipsometry

Dry film thickness (d) was measured using an ellipsometer (Dre, Germany) on the SS_{Blank} , SS_{OH} , SS_{Br} , SS_{PGMA} and SS_{PMMA} samples. All measurements were based on an 75° incidence angle. The ellipsometric parameters Δ and Ψ , where Δ is the phase and $\tan(\Psi)$ is the amplitude shifts upon reflection, were measured in air at ambient temperature. A complex refractive index was calculated from the measured Δ and Ψ values on SS_{Blank} . A three-layer optical model was applied consisting of a substrate (with a complex refractive index) determined for SS_{Blank} , an organic layer characterized only by its refractive index (assumed 1.55 and 0 for the real and imaginary parts, respectively) and thickness, and finally a layer of air to calculate the organic layer thickness [30,31]. Ellipsometric measurements were performed before and after each surface modification at three different positions on the samples from which average thicknesses and standard deviations were obtained.

2.8. Sample holder and loading

For compression molding and subsequent mechanical testing, a multipurpose sample holder (Fig. 2a; items 2–5) was fabricated allowing molding and testing of up to three samples at the same time. The sample holder itself (item 3; 77 mm by 20 mm and 5 mm thick) was manufactured in Toolox 44 steel with samples (item 4) equally separated giving a discontinuous bondline. Sample holders were loaded with two SS_{Blank} and one SS_{PGMA}^{BPO} samples or one SS_{Blank} and two SS_{CBA} samples. A steel back panel (item 5; 55 mm by 12 mm and 1.50 mm

thick) fastened with four M3 bolts locked the samples exposing 7.85 mm by 7.85 mm of the modified SS sample surface.

2.9. Compression molding

Two heating elements ($\varnothing 100$ mm) were placed in a 10 metric ton hydraulic press (Carver model #3912). On the lower heating element an aluminium (6060 alloy) mold part with a cavity (Fig. 2a, item 6) and two ejectors were bolted tight. A mating mold piston (item 1) was mounted on the upper heating element. Prior to molding the two parts were aligned and preheated to 170°C . A loaded sample holder and uncured EPDM rubber (item 2, approx. 77 mm by 20 mm and 6 mm thick) were placed in the mold cavity (77 mm by 20 mm and 20 mm deep). The mold was closed and a pressure of six metric ton (effective compression pressure of 384 bar) at 170°C was applied for 12 min. Rubber samples were post cured in an oven (Binder E28, Holm og Halby, DK) at 150°C for 4 h. Optimum process time and temperature for curing and post curing were given by the supplier. Post curing ensures a homogeneous rubber and removal of decomposition products ensuring uniform specimens.

2.10. Mechanical testing

After molding, the rubber-metal specimen (Fig. 2b, item 7) was mounted in a custom made translation sled (item 8). The sled was designed with six low friction brass wheels running in a custom made track allowing the sled to move only perpendicular (horizontal) to the load (vertical) making it suitable for 90° peeling. The peel tests were performed using a universal testing machine (Zwick 2005, Zwick GmbH & Co. KG, Ulm-Einsingen, Germany) with a 5kN load cell (5kN load cell Zwick/Roell, Zwick GmbH & Co. KG, Ulm-Einsingen, Germany). The

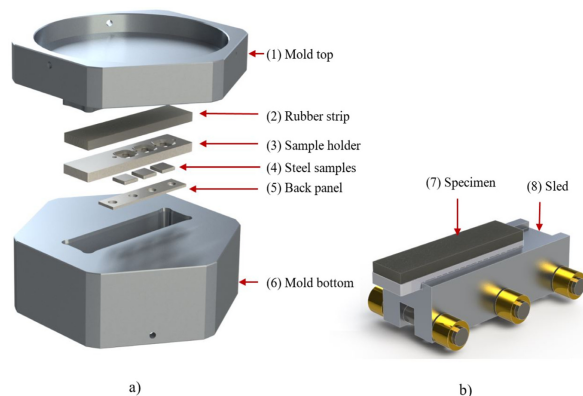


Fig. 2. Drawing showing the compression molding specimen consisting of the (a) mold itself (item 1 and 6) that comprises a rubber strip (item 2), a sample holder (item 3), up to three chemically modified samples (item 4) and a back panel (item 5) and the (b) six-wheeled sled (item 8) on which the test specimen (item 7) is mounted.

tracks were mounted to the machine base (Appendix, Fig. A1) and the cured rubber secured in the upper grip of the tensile tester. A preload of $F = N$ was applied at a rate of 1 mm s^{-1} . Subsequently, a peel test was performed at a constant displacement rate ($\dot{\delta} = 0.5 \text{ mm s}^{-1}$) and the sled translated during the test ensuring a peel angle (θ) of $\sim 90^\circ$. The peel tests concluded when full debonding of the rubber was achieved. The force (F) and the displacement (δ) were simultaneously acquired at 50 Hz. All tests were performed at $21 \pm 2^\circ \text{C}$ in ambient atmosphere.

2.11. 3D Scanning surface topography

To determine the type of failure after the peel test, 3D images of the fractured regions were obtained with a 3D micro/macroscope scanner (VR-3200, Keyence, Japan). Image analysis was performed using VR-3000 series Analyzer (Software v. 1.4.0.0, Keyence, Japan). The fractured area ascribed to cohesive failure [6] carrying rubber residues was measured manually. It is recognized that it is almost always possible to find residues on any fracture surface, making adhesive failure debatable, if enough sophisticated methods such as atomic force microscopy, depth-sensing nanoindentation or scanning electron microscope are used [32]. In the present case residues are limited to obvious rubber remainders detectable with the 3D micro/macroscope scanner. The area ratio between the cohesively failed areas and the initial bonded area (A_{total}), i.e. $A_r = \frac{A_{\text{cohesive}}}{A_{\text{total}}}$, was implemented as a quantitative measure of the bonding quality.

2.12. Data reduction

The Irwin-Kies method [33] was used to calculate the peel energy (P) which on the assumption that the width of the crack path (b) is constant [7,9] is described by Eq. (1):

$$P = (F/b)(\alpha - \cos(\theta)) - Wh \quad (1)$$

In this expression F is the applied peel force, h is the thickness of the rubber in the undeformed configuration, W is the strain-energy density function of the rubber, and $\alpha = 1 + \varepsilon$ is the peel arm stretch with ε denoting engineering strain. Neglecting the rubber extension during the peel process (thus, $\alpha = 1$ and $W = 0$ during crack growth) and assuming a peel angle of $\theta = 90^\circ$, Eq. (1) can be rewritten into Eq. (2) [34,35].

$$P = F/b \quad (2)$$

This equation is experimentally convenient since it relates the global quantity F to the local quantity P [10]. A Griffith's type of fracture criterion [36] was assumed at the crack onset and onwards, meaning that the crack is assumed only to propagate when P equals the fracture toughness, \mathcal{G} [37]. \mathcal{G} obtained from similar surface modifications are listed as average with standard deviation. The latter is

obtained as the mean of the maximum values of P calculated from Eq. (2) for all samples with a cohesive-to-adhesive failure ratio above 50% (i.e. $A_r \geq 0.5$) within each modification group (Appendix, Table A1). The following nomenclature will be used: R denotes the apparent resistance of the material against fracture, which is different from the material property fracture toughness (\mathcal{G}). Note that $R = \mathcal{G} = \text{constant}$, once the crack grows under steady-state conditions. This is represented by a dashed, horizontal line in Fig. 8.

3. Results

3.1. Preparation and characterization of SS_{OH} , SS_{Br} , SS_{PGMA} , and SS_{PMMA}

Fig. 3a shows the characteristic broad irreversible reduction wave of HEBD in a cyclic voltammogram recorded on a SS_{blank} sample. The wave having the peak potential, $E_{p,c}$ of -0.66 V vs SCE (sweep rate = 0.1 V s^{-1}) originates from the direct reduction of HEBD to afford after expulsion of N_2 from the corresponding aryl radicals, i.e. the grafting agents [28].

Fig. 3b shows the passivation of SS_{blank} by performing a potentiostatic electrolysis of HEBD. The distinct decrease seen in the current with time is caused by the reduction of HEBD and subsequent grafting and passivation of the electrode surface while producing SS_{OH} . Next, the SS_{OH} samples were converted via acylation reactions involving treatment with BIBB into radical initiators, i.e. SS_{Br} . These served as the initiator for SI polymerization reactions to produce SS_{PGMA} and SS_{PMMA} , respectively.

Ellipsometry performed on the electrografted SS_{OH} showed an average film thickness of $d = 4.2 \pm 0.4 \text{ nm}$. As expected the acylation provides a small increase of d by $0.2\text{--}0.8 \text{ nm}$ going to SS_{Br} . For the polymerized SS_{PGMA} and SS_{PMMA} samples d increases to $17\text{--}19 \text{ nm}$ after 1.5 h and for SS_{PGMA} up to $\sim 34 \text{ nm}$ after 3 h polymerization. Within a given polymerization batch (4 samples) the standard deviations were between 1–3 nm.

Fig. 4 depicts the IRRAS spectra of SS_{PGMA} and SS_{PMMA} samples with characteristic peaks appearing at $3000\text{--}2850 \text{ cm}^{-1}$ (m) from the C-H sp^3 bond stretch, 1736 cm^{-1} (s) from the C=O bond stretch of the unconjugated ester, $1490\text{--}1440 \text{ cm}^{-1}$ (m) from the C-H deformations (bending), and $1300\text{--}1050 \text{ cm}^{-1}$ from the C-O stretch of the ester, respectively. For the SS_{PGMA} sample a peak at 909 cm^{-1} is observed from out of plane C-H bending of the oxirane ring [38]. XPS survey spectra of SS_{PGMA} and SS_{PMMA} showed C and O components with a C/O ratio of 2.7 and 2.8, respectively (Appendix, Fig. A2 and Table A2), which are close to the theoretically expected 2.3 and 2.5 for PGMA and PMMA, respectively. A component at 200.0 eV was assigned to Cl 2p, attributed to the end-capped polymer chains [38].

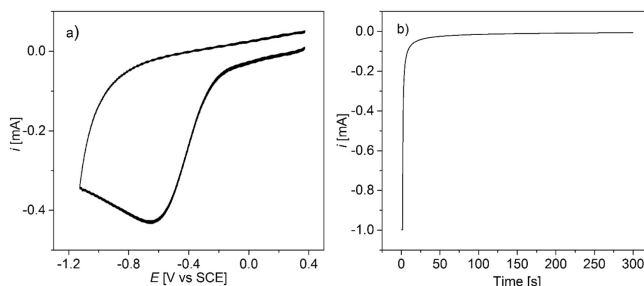


Fig. 3. a) Cyclic voltammogram recorded of 2 mM HEBD on SS_{blank} using a sweep rate = 0.1 V s^{-1} in $0.1 \text{ M Bu}_4\text{NBF}_4/\text{MeCN}$. b) Potentiostatic electrolysis; current vs time using an applied potential of $E_{p,c} = -0.2 \text{ V} = -0.86 \text{ V}$ vs SCE for 300 s in $0.1 \text{ M Bu}_4\text{NBF}_4/\text{MeCN}$.

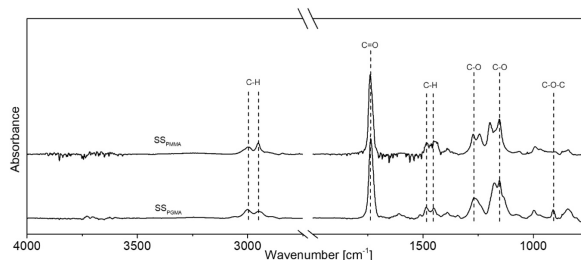


Fig. 4. IRRAS spectra of SS_{PGMA} and SS_{PMMA} samples.

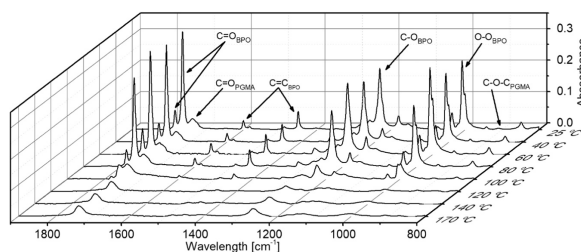


Fig. 5. T-IRRAS spectra of SS_{PGMA}^{BPO} recorded in the temperature interval 25–170 °C.

3.2. T-IRRAS of SS_{PGMA}^{BPO}

Fig. 5 shows the recorded IRRAS spectra of SS_{PGMA}^{BPO} from 25–170 °C. Characteristic peaks are observed at 1784 cm⁻¹ and 1764 cm⁻¹ (s) from the C=O stretch of the benzoyl group in BPO, at 1599, 1578, and 1450 cm⁻¹ (m) from the aromatic C=C stretch, 1230 cm⁻¹ from the C-O stretch of the ester, and 1008 cm⁻¹ from the O-O stretch of the peroxide [39]. As the temperature is elevated the peroxide peaks disappear, which shows the expected decomposition of BPO (1 h half-life time = 84 °C) [40], leaving at 120 °C only the characteristic PGMA peaks (see Fig. A3 in appendix for IRRAS spectra of SS_{Blank}^{BPO}).

Fig. 6 reports the average³ oxirane-to-carbonyl integral of the T-IRRAS analysis of a SS_{PGMA} sample (i.e. before application of BPO) and a SS_{PGMA}^{BPO} sample at 120, 140, 170 °C and, finally, after the thermal analysis and sonication. A distinct decrease in this ratio at the elevated temperatures is observed.

3.3. High-resolution XPS spectra of SS_{PGMA} and SS_{PGMA}^{BPO}

For SS_{PGMA} the high-resolution XPS shows five carbon components from the carbon atom in the backbone (H-C-C, 285.0 eV), the carbon atom adjacent to the ester group (C-C=O, 285.8 eV), the C-O component (286.7 eV), the carbon atoms in the oxirane ring (C-O-C_{ox}, 287.2 eV), and the carbon in the ester group (O-C=O, 289.1 eV) in agreement with literature reports [41,42]. After addition of BPO and heating, the deconvolution of C 1 s for the SS_{PGMA}^{BPO} sample showed a lowered surface composition of oxirane carbons (Appendix, Fig. A4 and Table A3). The ratio of the aliphatic carbons and carbons in the oxirane ring was determined to 1.30 before treatment and 2.55 after.

³ The error bar notation illustrates ± one standard deviation throughout the manuscript

3.4. Distribution of peroxide

Fig. 7 presents four SS_{PGMA} samples where one is untreated and three are drop coated with different amounts of BPO. Sample 2 (Fig. 7b) with a low surface concentration ($\Gamma \approx 0.04 \mu\text{mol cm}^{-2}$) shows an inhomogeneous BPO distribution as evidenced by the low reflection of light in areas with low amounts of crystals. Samples with $\Gamma \approx 0.4 \mu\text{mol cm}^{-2}$ and $\Gamma \approx 0.2 \mu\text{mol cm}^{-2}$ BPO show strong light reflection in areas with a high number of crystals (arrow, Fig. 7d).

3.5. Peel tests

High reproducibility, both quantitatively and qualitatively, was

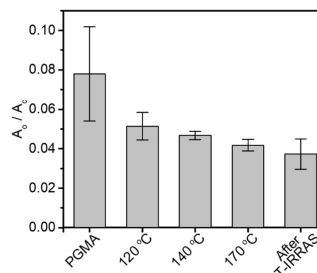


Fig. 6. Graph shows the average (and standard deviation) absorbance ratio of oxirane (A_{ox}) / carbonyl (A_C), determined by integration of the oxirane peak at 909 cm⁻¹ and the carbonyl peak at 1737 cm⁻¹ for SS_{PGMA}, SS_{PGMA}^{BPO} at three different temperatures, and SS_{PGMA}^{BPO} after the heating and subsequent sonication.

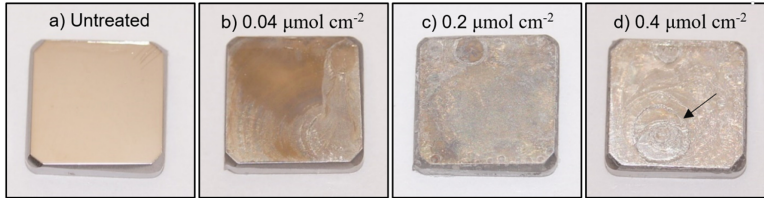


Fig. 7. Pictures of a SS_{PGMA} sample (10 mm by 10 mm) along with three SS_{PGMA}^{BPO} samples with increasing concentration of BPO going from left to right. The BPO was drop-casted on the plates in a chloroform solution (see experimental section).

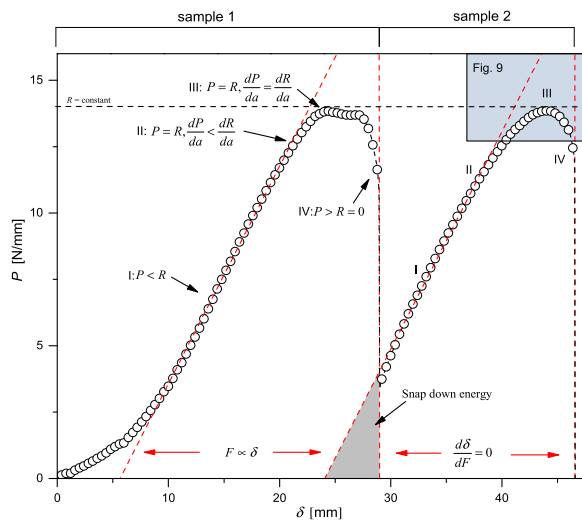


Fig. 8. The plot shows the load response during peeling of two samples. P is calculated from Eq. (2) with a width of $b = 7.85$ mm ($\gamma = 1$). The circles depict the experimental data, and the red, dashed lines show the elastic loading and the drop of load carrying capacity. The black, dashed line represents the fracture toughness of the rubber. The four stages of the crack evolution are marked on the plot for both samples. (For interpretation of the references to color in this figure legend, the reader is referred to the web version of this article).

observed for all peel tests of SS_{CBA} samples (Appendix, Table A4). SS_{blank}^{BPO} , SS_{PGMA} , and SS_{PMMA}^{BPO} samples showed no or weak adhesion causing no cohesive fracture (Appendix, Tables A5–7). Fig. 8 shows a representative peel test of two SS_{CBA} samples, where the peel energy is calculated from Eq. (2).

Initially, in the first stage (region I in Fig. 8) the loading is applied to the specimen. After an initially nonlinear response (probably due to the set-up alignment), the load increases proportionally with the applied displacement, $F \propto \delta$ (the oblique, dashed, red lines). During this stage the failure criterion is not met since P , which acts as the driving force of the crack propagation, is lower than the material's resistance against crack extension, R . As the loading increases the fracture criterion is met ($P = R$) and the crack initiates. This marks the second stage (region II) where the loading and the load response are governed by the crack initiation and a loss of linearity is evident, i.e. P competes against R . At this stage the local stability criterion, $dP/da \leq dR/da$ (the rate of change in P with respect to the crack extension, a , does not exceed the rate of change in R with respect to a), is satisfied and, hence, the crack

growth is a stable process. When the R curve rises, the driving force also has to increase to extend the crack further. Since P is rising, the R curve (a plot of R vs a) [37] is not flat, which is normally expected, cf. Eq. (2). This may, in particular, be associated with nonlinear elastic materials [43].

At stage 3 (region III), the crack starts to propagate and the maximum P is achieved. In the present configuration this stage is an inflection point, $dP/da = dR/da$, beyond which the rate of change of the driving force exceeds the slope of the R curve, $dP/da \geq dR/da$, and the crack growth becomes unstable.

In stage 4 (region IV) the crack velocity, assuming Motts analysis [44], approaches the Rayleigh speed of sound wave, $da/dt = c$ [45], as the resistance against crack extension is effectively reduced to zero, $R \approx 0$. This is reflected in the vertical drop in the force: $d\delta/dF = 0$ (the vertical, dashed, red lines). Noteworthy, the curve does not return to $P = 0$ which is due to elastic energy stored in the finite extension and the finite curvature of the rubber. At this stage, a snap-back phenomenon will normally release all the energy and both P and δ will go to

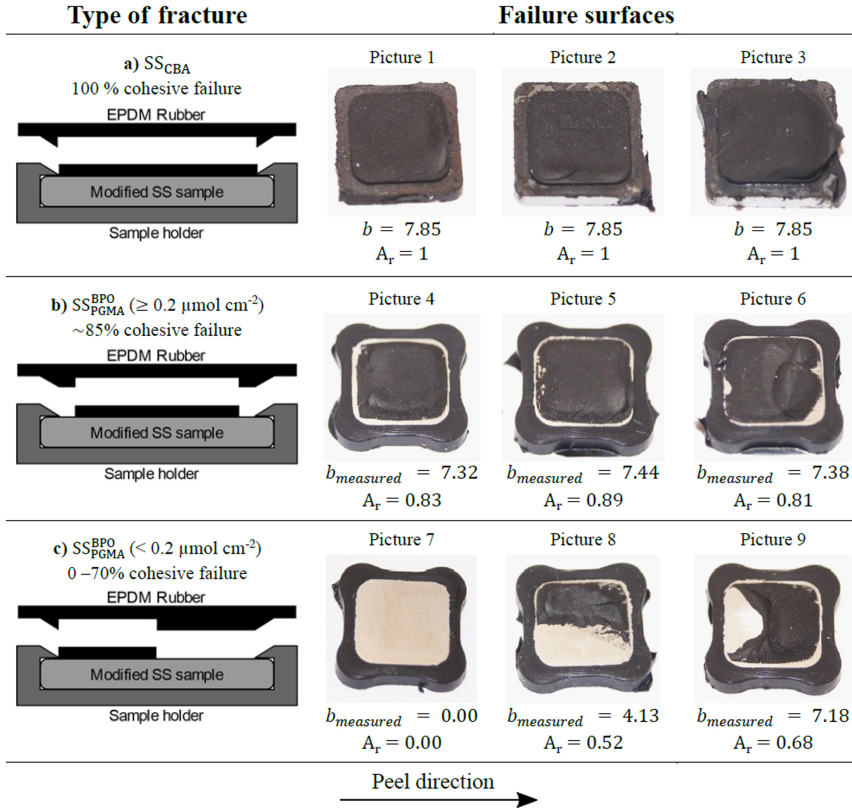


Fig. 9. Failure surfaces of various samples after peeling. a) SS_{CBA} samples with 100% cohesive fracture. b) SS_{PGMA}^{BPO} samples with the characteristic non-bonded strip along the edges. c) SS_{PGMA}^{BPO} samples with varying A_r .

zero. However, due to the constant displacement boundary condition introduced by the tensile machine the latter is prevented. As the crack reaches the second sample the load-carrying capacity is recovered and stages 1–4 are repeated. Clearly, the present geometry changes the crack growth process by changing the crack growth kinetics. To exclude some of the effects prior to peel testing, a rate-dependence test revealed no significant dependence in the loading range of $0.1\text{--}2.1 \text{ mm s}^{-1}$ of the rubber used (Appendix, Fig. A5). Therefore, the observed phenomena should be solely associated to the geometrical aspect of the crack growth process [46,47].

3.6. Analysis of the failed SS_{PGMA}^{BPO} and rubber surfaces

Fig. 9a–c shows the fractured surfaces after peel test. SS_{PGMA}^{BPO} samples for which $\Gamma \geq 0.2 \mu\text{mol cm}^{-2}$ revealed high cohesive-to-adhesive failure ratios ($A_r > 0.8$). Examinations of the peeled surfaces show that BPO modified samples always had an unbonded region along the edges of the sample holder (Fig. 9b, Picture 1–3), and full cohesive failure ($A_r = 1$) was therefore not achieved. SS_{Blank} samples were spray-painted

with a metallic adherent (See Appendix for procedure, denoted SS_{Paint}) to describe the effect. SS_{Paint} samples molded according to the standard procedure, demonstrated identical removal of the paint along the edges (Appendix, Fig. A6). The decrease in bond width ($b \rightarrow b_{\text{measured}}$) reduced the maximum peel force with roughly $\sim 20\%$ compared to SS_{CBA} ($A_r = 1$).

The size, shape, and position (relative to the peel direction) of the cohesively failed areas influence the maximum peel energies and therefore is the specific cohesive fracture width (b_{measured}) used to calculate it, cf. Eq. (2). Pictures 8 and 9 (Fig. 9c) show samples which obtained a maximum peel force of $F_{\text{max}} = 57 \text{ N}$ with $A_r = 0.52$ and $F_{\text{max}} = 96 \text{ N}$ with $A_r = 0.68$, respectively. The change in crack path width (perpendicular to the peel direction) causes the significant difference in F_{max} . The average $\dot{\gamma}$ values for SS_{PGMA}^{BPO} and SS_{CBA} were calculated to $12.2 \pm 1.3 \text{ N mm}^{-1}$ and $13.9 \pm 1.0 \text{ N mm}^{-1}$, respectively (See all entries in appendix, Table A1).

Fig. 10a shows a picture (left) and a 3D profile (right) of a failed rubber sample marked with four stages of the crack evolution. The crack locus (marked by the dashed lines to facilitate observations)

S. Heide-Jørgensen et al.

International Journal of Adhesion and Adhesives 87 (2018) 31–41

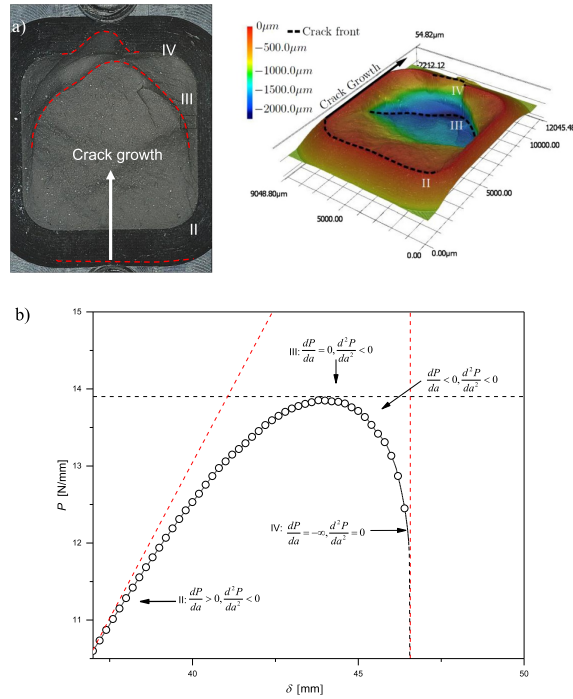


Fig. 10. Crack growth path. a) Picture (top left) and 3D profilometry (top right) of the ruptured rubber surface. Region II–IV indicates at which stage the crack is. The dashed lines mark the crack front, which narrows and develops into a parabolic shape as the crack initiates. b) Crack initiation and propagation regime of the experimental data where the circles show the data, the dashed red lines are the loading path and drop of load carrying capacity, respectively, and the dashed black line marks the fracture toughness.

changes during the crack propagation from an initial straight crack front (region II) into a parabolic shape (region III–IV). The 3D profile reveals that the crack deviates from the rubber-metal interface and grows ~2 mm into the rubber before returning towards the interface as the load carrying capacity is recovered by the next sample. Similar results of cracks deflecting into elastomers have previously been reported for cohesive failure [7,34]. At this stage a Kendall approach [48] for composite geometries could be adopted but this is out of the scope of the present study.

3.7. Critical peroxide concentration and dry film thickness

Fig. 11 shows the \mathcal{G}_c of SS^{BPO}_{PGMA} samples drop casted with different surface concentrations of BPO. The \mathcal{G}_c values were determined using $b_{measured}$ of each sample (Appendix, Table A1). A critical surface concentration (Γ_c) of $0.2 \mu\text{mol cm}^{-2}$ was found from Fig. 11. Samples with $\Gamma < 0.2 \mu\text{mol cm}^{-2}$ resulted in varying \mathcal{G}_c values while high and consistent \mathcal{G}_c values were obtained when $\Gamma \geq 0.2 \mu\text{mol cm}^{-2}$. SS^{BPO}_{PGMA} samples of $d = 10\text{--}35 \text{ nm}$ with peroxide concentrations above Γ_c all resulted in high A_r and \mathcal{G}_c . Hence, the results were independent of dry film thickness (Appendix, Table A1).

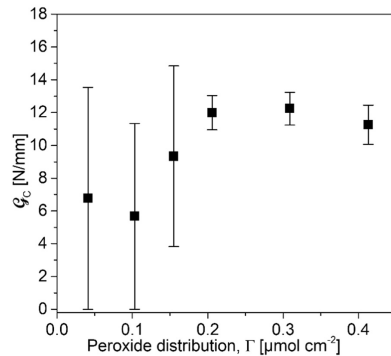


Fig. 11. Peel energies of SS^{BPO}_{PGMA} substrates treated with different concentrations of BPO.

S. Heide-Jørgensen et al.

International Journal of Adhesion and Adhesives 87 (2018) 31–41

Table 1
Average dry film thickness of SS_{OH}, SS_{Bt}, SS_{PGMA}, and SS_{PMMA} samples.

Modification	d (nm)
SS _{OH}	4.2 ± 0.4
SS _{Bt}	4.3 ± 0.4
SS _{PGMA} ^a	19.3 ± 8.5
SS _{PGMA} ^b	25.8 ± 8.2
SS _{PMMA} ^c	16.9 ± 0.3

^a 16 SS_{PGMA} samples polymerized for 1.5 h.

^b 8 SS_{PGMA} samples polymerized for 3 h.

^c 4 SS_{PMMA} samples polymerized for 1.5 h.

4. Discussion

4.1. Crosslinking of EPDM rubber and SS_{PGMA}

No adhesive strength was obtained between SS_{PGMA}^{BPO} samples and EPDM rubber. This stands in contrast to what is obtained between grafted SS_{PMMA} and bulk PMMA, where the adhesion was believed to be caused by entanglement of polymer brushes and the bulk polymer [49]. However, the high density polymer brushes [38] used in this work have low dry film thickness, i.e. low chain length, (Table 1) and entanglement is not expected [50]. Furthermore, PMMA and PGMA are very different from EPDM rubber in solubility characteristics and poor or no mixing is predicted [51,52]. The high peel energies obtained for SS_{PGMA}^{BPO} samples must therefore, be a result of cross-linking between the few upper nanometers of the brushes with EPDM rubber. This is supported by all the sample entries which show no correlation between the dry film thickness, A_T and \mathcal{E}_c .

The inclusion of SS_{PGMA}^{BPO} samples prove the significant role that oxirane groups play in the PGMA brushes. The alkoxy radicals formed in the decomposition of BPO can abstract hydrogen atoms in alpha or beta position to the oxygen atom in the oxirane ring, which is followed by a rearrangement to afford alpha keto radicals or unsaturated alkoxy radicals. Both mechanisms potentially crosslink the PGMA brushes and EPDM rubber, by, respectively, adding to olefins or forming allylic moieties in the polymer brushes [53,54].

T-IRRAS was employed to replicate the temperature conditions the samples were exposed to during molding/curing (Fig. 5). The measurements show a slight decrease in the oxirane-to-carbonyl relation once the SS_{PGMA}^{BPO} samples had been heated to 120 °C (Fig. 6). This indicates that a reaction takes place between free radicals and oxirane groups in the upper few nanometers of the brushes. Furthermore, the oxirane-to-carbonyl ratio keeps decreasing as the samples were heated to 170 °C (Fig. 5). This may be explained by the formed alcohol groups initiating a S_N2-like cross-linking mechanism within the PGMA brush matrix [55]. Deconvolution of C 1s high-resolution spectra (Appendix, Table A3) shows a partly disappearance of the oxirane ring, which is in line with the T-IRRAS experiments. The results substantiate a hypothesis of the involvement of the oxirane rings in the radical reactions.

4.2. Drop casting and peroxide distribution

SS_{PGMA} samples coated with different concentrations of BPO were studied to evaluate the effect of having different values of Γ (Fig. 7). The thickness of the drop casted films is roughly proportional to the solution concentration. However, the solvent's wettability of the substrate, evaporation rates, and capillary forces affects the distribution and homogeneity of the film [56]. Fig. 7 demonstrates that this manual drop casting method leaves areas with higher concentrations of BPO than others (crystals). Consequently, high concentrations, relative to the polymer brushes, are required to completely cover the surface with peroxide (Γ_c). A back-of-the-envelope calculation show that the BPO applied in the case of $\Gamma_c = 0.2 \mu\text{mol cm}^{-2}$ yields more than 100-fold

radicals upon thermal degradation than available oxirane groups with the assumption that the polymer density of the brushes is 1.00 g cm^{-3} , that only the upper 5 nm of the brushes react and 100% decomposition of BPO.

4.3. Specific crack path width

Fig. 9 reveals that A_T , in general, was lower for the SS_{PGMA}^{BPO} samples than for the reference SS_{CBA} samples due to the unbonded edge regions. The unbonded regions originate from the flow of hot, viscous rubber in between the sample and the sample holder during molding (Fig. 9, rubber is present outside the exposed surface area). The rubber drags off peroxide and decreases bonded area. The rubber samples clearly illustrate the same effect in interlocking and edge regions (Appendix, Fig. A6). The result is analogously transferred to removal of the peroxide, which explains the lack of the adhesion along the edges. The specific fracture width is therefore measured for each sample (b_{measured}). The commercial bonding agent does not experience this effect as the primer is strongly bonded to the SS surface before molding.

4.4. Evaluation of A_T and \mathcal{E}_c

Several SS_{PGMA}^{BPO} samples with low A_T resulted in high \mathcal{E}_c due to the position and shape of the cohesive failed area relative to the peel direction. Samples with less than $A_T \leq 0.5$ were, therefore, excluded from the calculation of the average fracture toughness. To determine the performance of the different SS_{PGMA}^{BPO} samples, A_T was used to estimate the reproducibility. SS_{PGMA}^{BPO} samples with BPO concentrations $\geq \Gamma_c$ turned out to give the most reliable results as high and consistent A_T were obtained. Correlating the average \mathcal{E}_c of SS_{PGMA}^{BPO} and SS_{CBA} with a previously reported fracture toughness of rubber, $\mathcal{E}_{c,\text{rubber}} = 13 \text{ N mm}^{-1}$ [34], through the Tukey's test indicated that the difference of the means is not significant at a 95% confidence interval. As such, there is no evidence against the different systems providing the same fracture toughness and, thus, the same adhesion. These findings do not permit assessment of the interfacial toughness since \mathcal{E}_c is dictated by the toughness of the rubber. It can therefore be concluded that the novel bonding systems offer the same bonding properties as the existing, reference bonding system while being only a few nanometers thick.

4.5. Crack evolution and stability during peel test

From Fig. 8, an undulating load response is seen. This is normally not the case in peel experiments where stable crack propagation ($dP/da = dR/da$) and a flat R curve are expected. From region II to III a softening of the load response is observed. A possible explanation for this is the competition between geometrical and material effects. For example, strain rate hardening of the material tends to enhance the crack propagation while the rate strengthening in the fracture process zone tends to retard the propagation of the crack [43]. Another contributor could be a geometrical transition of the crack front from an initial straight configuration to a parabolic, self-similar shape through a curvilinear reconfiguration as indicated in Fig. 10a [57,58]. It is recognized that several phenomena, including the effect of the Poisson's ratio and the anticlastic bending (since at the crack tip the curvature of bending $\neq 0$), is the origin of the transition [59–61]. Recently, it has been discovered that the crack initiates semi-circularly and by extension in the width direction attains a parabolic, semi-elliptical shape [61,62]. The curvilinear reconfiguration seems to be produced to accommodate the Poisson's ratio effects and through a local transition from plane strain conditions to plane stress conditions along the crack front causes of a softening behavior of the load response [62]. With a Poisson's ratio of nearly a half these effects are more dominant in rubber than in other materials and could contribute to the nonlinear load response observed from region II to III. Heterogeneities or discontinuities in the vicinity of the crack tip can lead to substantial

S. Heide-Jørgensen et al.

International Journal of Adhesion and Adhesives 87 (2018) 31–41

decreases in the resistance against crack extension [63]. As the crack tip approaches the end of the bonded area so does the elastic process zone (responsible for transferring stresses in front of the crack tip). When the elastic process zone length, λ^{-1} , exceeds the remaining bonded area and extends into the gap R is effectively reduced [63]. This leads to an excess of the strain energy, strain localization and ultimately stress magnification and acceleration of the crack [64,65]. This is consistent with recent findings where crack pinning (i.e. initiation, propagation and arrest) was achieved for the peel geometry by purposely patterning the bondline [46].

The instability occurring from region III to IV is thought to be partially driven by a decrease in R caused by the interaction between the process zone and the gap between the samples. Following Kanninen's approach [66], the elastic process zone length in the present case can be approximated by the bending formula to $\lambda^{-1} = \frac{h}{\delta^{3/4}} = \frac{6.5\text{mm}}{\delta^{3/4}} = 4.15\text{mm}$. The bonded area has a maximum length of 7.85 mm. Therefore, as the crack is roughly half way through the bonded region, R starts to decrease. The decrease is governed by the weighted sum of bonded area within the process zone $R = \mathcal{A}_c \left(\frac{L_{\text{bond}}}{r^{-1}} \right)$, where L_{bond} is the length of the bonded area within the process zone [63]. Since the process zone is proportional to the thickness of the rubber the changing locus may affect it and the related effects. The changing locus also contributes to the instability by gradually reducing the crack width and area as seen in Fig. 10a. R is a function of the crack surface area since it is, partly, determined by the number of chemical bonds broken in the rubber. Thus, a reduction of the width of the crack path results in a reduction of the resistance against crack extension. The fracture criterion states that the crack will grow when the peel energy equals the materials resistance against fracture. Therefore, a decrease in resistance against crack will lead to a lower peel energy, which is seen beyond the inflection point in Fig. 10b where $\frac{dP}{da} < 0 \wedge \frac{d^2P}{da^2} \leq 0$.

5. Conclusions

Nanometer thick surface immobilized polymer brushes of PGMA were grown from SS substrates to adhere EPDM rubber. BPO was added to the PGMA-rubber interface to enhance the concentration of radicals in the bonding region, once heated. Analysis by T-IRRAS and XPS confirmed that the oxirane side groups in the polymer film reacted upon heating with BPO on the surface. The interfacial toughness was assessed through peel testing while the reproducibility of adhesion was assessed by measuring the ratio of the cohesively failed area to the initial bonded area.

Softening of the load response and the unstable crack propagation were observed. The former observations were associated to the Poisson's effects and reconfiguration of the crack front and the latter to the elastic process zone interacting with the gap between the samples. Cohesive fracture within the rubber was consistently observed. This was supported by the fact that no significant difference in fracture toughness was found between SS samples modified with PGMA and BPO and the commercial bonding agent. The values were in good agreement with a previously reported fracture toughness of rubber. From this it was concluded that efficient bonding of EPDM rubber and metal with PGMA brushes as a nanoscale adhesive could be achieved with similar interfacial toughness as the commercial bonding agent.

Acknowledgements

Funding from the Innovation Fund Denmark (MoAd 5163-00005B) is gratefully acknowledged. The authors wish to thank AVK GUMMI A/S and RadiSurf ApS for helping and providing the materials used in the study.

Appendix A. Supplementary material

Supplementary data associated with this article can be found in the online version at doi:10.1016/j.ijadhadh.2018.09.006.

References

- [1] Van Ooij WJ. The role of XPS in the study and understanding of rubber-to-metal bonding. *Surf Sci* 1977;68:1–9.
- [2] Stevenson A. On the durability of rubber/metal bonds in seawater. *Int J Adhes Adhes* 1985;5:81–91.
- [3] Persson S, Goude M, Olsson T. Studying the cure kinetics of rubber-to-metal bonding agents using DMTA. *Polym Test* 2003;22:671–6.
- [4] Crowther BG. Rubber to metal bonding. Shawbury: ISmithers Rapra Publishing; 1996.
- [5] Gossot J. Bonding of rubber to metal by means of new chemical derivatives of rubber. *Rubber Chem Technol* 1950;23:281–91.
- [6] Sasidharan Achary P, Gouri C, Ramaswamy R. Reactive bonding of natural rubber to metal by a nitrile-phenolic adhesive. *J Appl Polym Sci* 2001;81:2597–608.
- [7] Ansarifard MA, Lake GJ. On the mechanics of rubber-to-metal bond failure. *J Adhes* 1995;53:183–99.
- [8] Crowther BG. Handbook of rubber bonding. Shawbury: ISmithers Rapra Publishing; 2001.
- [9] Cook JW, Edge S, Packham DE. The adhesion of natural rubber to steel and the use of the peel test to study its nature. *Int J Adhes Adhes* 1997;17:333–7.
- [10] Jayaseelan SK, Van Ooij WJ. Rubber-to-metal bonding by silanes. *J Adhes Sci Technol* 2001;15:967–91.
- [11] Jazenski PJ, Manino LG. Adhesive compositions comprising (a) halogenated polyolefin (b) aromatic nitroso compound and (c) lead salts. U.S. Patent 4,119,587, October 10, 1978.
- [12] Troughton FB, Kucera HW. Phenolic Resin Adhesion Promoters and Adhesive Compositions, and Bonding Method Employing same. U.S. Patent 5,162,156, November 10, 1992.
- [13] Auerbach RA, Berry DB. Adhesive compositions. U.S. Patent 5,036,122, July 30, 1991.
- [14] Rezaeian I, Zahedi P, Rezaeian A. Rubber adhesion to different substrates and its importance in industrial applications: a review. *J Adhes Sci Technol* 2012;26:721–44.
- [15] Gong P, Mori K, Oishi Y, Hotaka T. Direct adhesion between polymer plated metals and rubbers during vulcanization, Part 4 direct adhesion between polymer plated steel and peroxide crosslinked epdm during vulcanization. *Soc Rubber Sci Technol* 2003;76:154–9.
- [16] Wang F, Xu J, Luo H, Wang J, Wang Q. A new organofunctional ethoxysilane self-assembly monolayer for promoting adhesion of rubber to aluminum. *Molecules* 2009;14:4087–97.
- [17] Dundurs J. Edge-bonded dissimilar orthogonal elastic wedges under normal and shear loading. *J Appl Mech* 1969;36:650–2.
- [18] Bogy DB. Two edge-bonded elastic wedges of different materials and wedge angles under surface tractions. *J Appl Mech* 1971;38:377–86.
- [19] Suo Z, Hutchinson JW. Interface crack between two elastic layers. *Int J Fract* 1990;43:1–18.
- [20] Ye T, Suo Z, Evans AG. Thin film cracking and the roles of substrate and interface. *Int J Solids Struct* 1992;29:2639–48.
- [21] M. Liechti K, Liechti KM, Wu J-D. Mixed-mode, time-dependent rubber/metal debonding. *J Mech Phys Solids* 2001;49:1039–72.
- [22] He MY, Evans AG, Hutchinson JW. Crack deflection at an interface between dissimilar elastic materials: role of residual stresses. *Int J Solids Struct* 1994;31:3443–55.
- [23] Piveteau L-D, Gasser B, Schlapbach L. Evaluating mechanical adhesion of sol-gel titanium dioxide coatings containing calcium phosphate for metal implant application. *Biomaterials* 2000;21:2193–201.
- [24] Lane M, Liniger E, Lloyd JR. Relationship between interfacial adhesion and electrochromism in Cu metallization. *J Appl Phys* 2003;93:1417–21.
- [25] Mäkilä R, Paajanen L, Nurmi A, Kivistö A, Koskela K, Rowell R. Effect of chemical modification of wood on the mechanical and adhesion properties of wood fiber/polypropylene fiber and polypropylene/veneer composites. *Eur J Wood Wood Prod* 2001;59:319–26.
- [26] Min K, Gao H, Matyjaszewski K. Preparation of homopolymers and block copolymers in miniemulsion by ATRP using activators generated by electron transfer (AGET). *J Am Chem Soc* 2005;127:3825–30.
- [27] Hansson S, Östmark E, Carlmark A, Malmström E. ARGET ATRP for versatile grafting of cellulose using various monomers. *ACS Appl Mater Interfaces* 2009;1:2651–9.
- [28] Iruthayaraj J, Chernyy S, Lillithorup M, Ceccato M, Røn T, Hinge M, Kingshott P, Besenbacher F, Pedersen SU, Daasbjerg K. On surface-initiated atom transfer radical polymerization using diazonium chemistry to introduce the initiator layer. *Langmuir* 2011;27:1070–8.
- [29] Diget JS, Petersen HN, Schaarup-Jensen H, Sørensen AU, Nielsen TT, Pedersen SU, Daasbjerg K, Larsen KL, Hinge M. Synthesis of β -cyclodextrin diazonium salts and electrochemical immobilization onto glassy carbon and gold surfaces. *Langmuir* 2012;28:16828–33.
- [30] Tiberf F, Landgren M. Characterization of thin nonionic surfactant films at the silica/water interface by means of ellipsometry. *Langmuir* 1993;9:927–32.
- [31] Landgren M, Jonsson B. Determination of the optical properties of silicon/silica

S. Heide-Jørgensen et al.

International Journal of Adhesion and Adhesives 87 (2018) 31–41

- surfaces by means of ellipsometry, using different ambient media. *J Phys Chem* 1993;97:1656–60.
- [32] Chaudhury M, Pocius AV. Adhesion science and engineering-2-surfaces. Chemistry and applications. Elsevier Science BV; 2002.
- [33] Irwin GR, Kies JA. *Weld Res Suppl* 1954;193–8.
- [34] Ansarifar MA, Zhang J, Baker J, Bell A, Ellis RJ. Bonding properties of rubber to steel, aluminium and nylon 6,6. *Int J Adhes Adhes* 2001;21:369–80.
- [35] Lindley P. Ozone attack at a rubber-metal bond. *J Inst Rubber Ind* 1971;5:243–8.
- [36] Griffith AA, Eng M. VI. The phenomena of rupture and flow in solids. *Philos Trans R Soc Lond A* 1921;221:163–98.
- [37] Anderson TL. *Fracture mechanics: fundamentals and applications*. 3rd ed Lonon: CRC press; 2005.
- [38] Lillethorp M, Shimizu K, Plumeré N, Pedersen SU, Daasbjerg K. Surface-attached poly(glycidyl methacrylate) as a versatile platform for creating dual-functional polymer brushes. *Macromolecules* 2014;47:5081–8.
- [39] Bronze-Uhle ES, Batagin-Neto A, Xavier PHP, Fernandes NI, de Azevedo ER, Graeff CFO. Synthesis and characterization of melanin in DMSO. *J Mol Struct* 2013;1047:102–8.
- [40] Butala DN, Liang WR, Choi KY. Multiobjective dynamic optimization of batch free radical polymerization process catalyzed by mixed initiator systems. *J Appl Polym Sci* 1992;44:1759–78.
- [41] Barbey R, Laporte V, Alnabulsi S, Klok H-A. Postpolymerization modification of poly(glycidyl methacrylate) brushes: an XPS depth-profiling study. *Macromolecules* 2013;46:6151–8.
- [42] Mao Y, Gleason KK. Hot filament chemical vapor deposition of poly(glycidyl methacrylate) thin films using tert-butyl peroxide as an initiator. *Langmuir* 2004;20:2484–8.
- [43] Landis CM, Pardoën T, Hutchinson JW. Crack velocity dependent toughness in rate dependent materials. *Mech Mater* 2000;32:663–78.
- [44] Mott N. Brittle fracture in mild steel plates. *Engineering* 1948;165:16–8.
- [45] Abraham FF, Gao H. How fast can cracks propagate? *Phys Rev Lett* 2000;84:3113.
- [46] Hernandez E, Alfano M, Pulungan D, Lubineau G. Toughness amplification in copper/epoxy joints through pulsed laser micro-machined interface heterogeneities. *Sci Rep* 2017;7:16344.
- [47] Hwang D-G, Trent K, Bartlett MD. Kirigami-inspired structures for smart adhesion. *ACS Appl Mater Interfaces* 2018;10:6747–54.
- [48] Kendall K. Control of cracks by interfaces in composites. *Proc R Soc Lond Ser A* 1975;341:409–28.
- [49] Shimizu K, Malmos K, Holm AH, Pedersen SU, Daasbjerg K, Hinge M. Improved adhesion between PMMA and stainless steel modified with PMMA brushes. *ACS Appl Mater Interfaces* 2014;6:21308–15.
- [50] Gutowski WS. Interface/interphase engineering of polymers for adhesion enhancement: part I. Review of micromechanical aspects of polymer interface reinforcement through surface grafted molecular brushes. *J Adhes* 2003;79:445–82.
- [51] Troughton MJ. *Handbook of plastics joining: a practical guide*. 2nd ed Norwich: William Andrew; 2008.
- [52] Hansen CM. *Hansen solubility parameters: a user's handbook*. 2nd ed Boca Raton: CRC press; 2007.
- [53] Sabatino EC, Gritter RJ. The free-radical chemistry of cyclic ethers. V. β -hydrogen atom abstraction from epoxides and a thioepoxide. *J Org Chem* 1963;28:3437–40.
- [54] Wallace TJ, Gritter RJ. The free radical chemistry of cyclic ethers—IV. *Tetrahedron* 1963;19:657–65.
- [55] Kwak MJ, Kim DH, You JB, Moon H, Joo M, Lee E, Im SG. A sub-minute curable nanoadhesive with high transparency, strong adhesion, and excellent flexibility. *Macromolecules* 2018;51:992–1001.
- [56] Liu Y, Zhao X, Cai B, Pei T, Tong Y, Tang Q, Liu Y. Controllable fabrication of oriented micro/nanowire arrays of dibenzo-tetrahydrofulvalene by a multiple drop-casting method. *Nanoscale* 2014;6:1323–8.
- [57] Budzik MK, Jumel J, Shanahan ME. Antagonist adhesion effects due to variable substrate surface. *Soft Matter* 2012;8:8321–6.
- [58] Liechti K, Chai Y-S, Liang Y-M. Three-dimensional effects in interfacial crack propagation. *Exp Mech* 1992;32:218–24.
- [59] Nilsson K-F, Thesken J, Sindlear P, Giannakopoulos A, Stoäkers B. A theoretical and experimental investigation of buckling induced delamination growth. *J Mech Phys Solids* 1993;41:749–82.
- [60] Patinet S, Vandembroucq D, Roux S. Quantitative prediction of effective toughness at random heterogeneous interfaces. *Phys Rev Lett* 2013;110:165507.
- [61] Moberg A, Budzik MK, Jensen HM. Crack front morphology near the free edges in double and single cantilever beam fracture experiments. *Eng Fract Mech* 2017;175:219–34.
- [62] Budzik MK, Heide-Jørgensen S. Branching and softening of loading path during onset of crack at elastic-brittle interface. *Mech Mater* 2018;127:1–13.
- [63] Heide-Jørgensen S, Budzik MK. Crack growth along heterogeneous interface during the DCB experiment. *Int J Solids Struct* 2017;120:278–91.
- [64] Tadepalli R, Turner KT, Thompson CV. Effects of patterning on the interface toughness of wafer-level Cu-Cu bonds. *Acta Mater* 2008;56:438–47.
- [65] Cuminatto C, Parry G, Braccini M. A model for patterned interfaces debonding – application to adhesion tests. *Int J Solids Struct* 2015;75:122–33.
- [66] Kanninen M. An augmented double cantilever beam model for studying crack propagation and arrest. *Int J Fract* 1973;9:83–92.

Chapter 3

Paper 2 - On Effective Critical Fracture Energy

Crack growth along heterogeneous interface during the DCB experiment²

3.1 Introduction

Motivated by the findings in the previous chapter this contribution investigates the consequences of having structured zones of weak (effectively zero) adhesion running in bands perpendicular to the crack growth direction. The emphasis is placed on how the interaction between the stress distribution in front of the crack, i.e. the elastic fracture process zone, and the heterogeneities is reflected in the load response and how the critical fracture energy is affected.

3.2 Method

A series of DCB fracture tests are conducted on specimens with a soft, elastic adhesive providing a large elastic process zone. Zones of weak adhesion are included with different combinations of number of zones ranging from 0 up to 16 zones and zone sizes varying from 15% to 100% of the process zone length. To explain the experimental data a theoretical framework is established.

An analytical unit pattern model containing one band of strong adhesion and one band of weak adhesion is developed based on simple beam theory, the Winkler foundation and linear fracture mechanics (LFM). The

unit pattern offers phenomenological insight in the interaction between neighboring zones of strong and weak adhesion. More complex modeling is achieved by repeating the unit pattern model and semi-analytically solving it. This way any number and sizes of weak zones can be investigated. The multi-pattern model is used to compare and explain the experimental data.

The effective critical fracture energy of the joint is formulated as a function of the critical fracture energy of the strong zones and the weak zones and their volume fractions within the process zone (as a rule of mixtures).

3.3 Contribution

The author did theoretical modeling, parts of the experimental work and preparation of the manuscript.

3.4 Finding

It is found that smooth, steady-state crack propagation is replaced by an oscillating load response when the bonded interface is replaced by a structured interface. The behavior is explained by a change in the apparent critical fracture energy due to alterations of strong and weak adhesion within the process zone. Since the process zone originates from the crack tip, the strong-to-weak adhesion ratio within it changes as the crack propagates. The changes in the effective fracture energy are captured by a simple rule of mixtures. With it the model accurately predicts the experimental results.

In addition, it is found that large (relatively to the process zone) zones of strong and weak adhesion cause large oscillations in the load response, which are clearly visible in the experimental data. Smaller zones cause smaller oscillations to the point where the load response appears smooth. However, the small zones have the largest impact on the effective critical fracture energy substantially weakening the joint. This is accurately predicted by the proposed rule of mixtures.

Contrary to the findings of Budzik et al.,⁴⁷ who suggest a power-law rule of mixtures for describing the effective critical fracture energy for bands of weak adhesion running parallel to the crack growth direction, the apparent fracture energy for bands of weak adhesion running perpendicular to the crack growth direction is accurately predicted by a linear rule of mixtures.

3.5 Reflection

The behavior observed in Chapter 2 is successfully recreated with oscillations and snap-downs in the load response near the edges of the bonded zones. This indicates that geometry definitely plays a role.

In addition, it is of both great interest and concern, that the smallest heterogeneities have the largest impact on the adhesive strength of the joint since these are commonly introduced during manufacturing. The rule of mixtures proposed can be of potential help when assessing whether or not defects are crucial for a joint's integrity. However, it is reassuring that the rule of mixtures predicts almost maximum (theoretical) strength of the joint as long as there are no defects in an area the size of the process zone ahead of the crack.

It could be interesting to follow up with weak zones much larger than the process zone to see the effect. However, some sort of pseudo-dynamical approach is probably needed to take the crack acceleration through the weak zone and the resulting overshoot into account, e.g. as proposed recently by Taleb Ali et al.⁶⁰ In addition, it could be interesting to repeat some of the experiments with more brittle or stiff adhesives to see how the rule of mixtures apply.



Contents lists available at ScienceDirect

International Journal of Solids and Structures

journal homepage: www.elsevier.com/locate/ijsolstr

Crack growth along heterogeneous interface during the DCB experiment



Simon Heide-Jørgensen*, Michal K. Budzik*

Department of Engineering, Aarhus University, Inge Lehmanns Gade 10, Aarhus 8000, Denmark

ARTICLE INFO

Article history:
Received 8 November 2016
Revised 27 March 2017
Available online 11 May 2017

Keywords:
Adhesion
Composites
DCB
Fracture
Heterogeneities
Interfaces

ABSTRACT

Interface and bondline heterogeneities are inherent parts of laminated materials. Recently, these otherwise unwanted features are gaining importance enhanced by the surface patterning techniques. In the present contribution, a double cantilever beam adhesion experiment is performed on joints with patterned interfaces. Weak/strong adhesion bands perpendicular to the crack growth direction are produced along the bonded surfaces. A vast range of specimens with different but systematic weak/strong zone ratios is tested. A novel analytical model, including a rule of mixture scaling, is developed to gain phenomenological insights into the data obtained. Two specific cases are addressed: a single strong/weak transition and multiple transitions. The new model proves a very good agreement with the experimental data obtained for any configuration tested. The role of three length scale parameters, weak, strong and process zone sizes, and their interactions, are emphasized. For instance, once small (in comparison to the process zone size) weak/strong zones are present, a substantial decrease in the fracture energy is recorded. This observation may be of importance in understanding both natural (e.g. geckos feet) and industrial (laminated and bonded materials) bondline discontinuities including the role of fillers, voids or kissing bonds.

© 2017 Elsevier Ltd. All rights reserved.

1. Introduction

When dealing with adhesive bonding homogeneous, continuous bondlines are assumed to simplify the task of modeling and describing their behavior (Tsai et al., 1998; Blackman et al., 2003; Pedado, 1993; Fernlund and Spelt, 1991). For many applications these assumptions are justified and have been the cornerstones in the establishment of today's knowledge of adhesive bonding for a long time. While applicable to some problems, not all bonded joints satisfy these assumptions. In fact, most adhesive bonded joints involve either heterogeneity, discontinuity or, to some extent, both.

One place where the impact of adhesive heterogeneity is truly put on display is in the inner shell layer of seashells called nacre, a composite comprising aragonite and a biopolymer. Nacre is superior in toughness compared to conventional engineering material due to its brick-and-mortar-like micro-structure which allows material interfaces to slide and harden during loading (Espinosa et al., 2011). On a nano-scale, the heterogeneity is even more evident since the bondlines between the brick-like aragonite platelets are not homogeneous but constituted from truss-like nano-structures

(Jackson et al., 1988). Similar heterogeneous mechanical interfaces with nano- or micro-structures are seen in various materials, such as the trabeculae connecting the subarachnoid space with the pia mater in the human brain, the truss-like structures bridging the interfaces of short glass-fiber-reinforced polypropylene, and the fibril bridging occurring in polypropylene (Bertoldi et al., 2007), just to name a few. Such 'adhesive' heterogeneities are found in nature on multiple occasions (Gillies et al., 2014; Kwak and Kim, 2010).

Adhesive heterogeneity plays a vital role, though often unwanted, in structural bonding. Frequently, it is not taken into account since most structural joints are designed based on the assumption of homogeneity or methods (i.e. homogenization) leading to the use of effective, representative, homogeneous properties. However, multiple cases of heterogeneities associated with different industries (with electronics and aircrafts as the most prominent ones) have been reported in the literature. Examples are: varying bondline thicknesses, unbonded areas, encapsulated particles, voids and kissing bonds (Niklaus et al., 2000; Chester and Roberts, 1989; Kim, 2003; Spiering et al., 1995). These reports indicate that heterogeneities are inevitable in structural joints.

Since imperfections violate the assumptions of homogeneity, they could potentially lead to unpredictable joint behavior and, in the worst case, to premature catastrophic failure of the structure.

* Corresponding authors.

E-mail addresses: shj@eng.au.dk (S. Heide-Jørgensen), mibu@eng.au.dk (M.K. Budzik).

<http://dx.doi.org/10.1016/j.ijsolstr.2017.05.013>
0020-7683/© 2017 Elsevier Ltd. All rights reserved.

Kendall (1975a) demonstrated that the crack propagation is affected by heterogeneous interfaces by peeling rubber strips with varying thickness and elastic moduli, one compliant and one stiff, from a glass plate. Kendall observed a retardation of the crack as it reached an interface with a stiffer material. Likewise, he observed an acceleration of the crack as it reached an interface with a more compliant material. This showed that interfaces with different properties have a huge impact on the crack propagation by altering the kinetics of the crack. If a large content of imperfections is present, the crack keeps accelerating. This could potentially result in the failure mode, shifting from cohesive to adhesive failure, or in the joint rapidly failing due to extensive crack growth (Kendall, 1975b).

This stresses the importance of understanding heterogeneous bondlines, but may also suggest using heterogeneities as a way to further advance in the area of adhesive bonding. Understanding heterogeneous bonding may hold the key to new and better technologies, risk assessment, damage prevention, and more reliable structural joints. At least a few contributions have already been devoted to the study of heterogeneity. Pearce et al. (1998) investigated the impact of voids on adhesive bond performance experimentally and found that a void content above 25% of the total bondline area reduces the T-peel and the peel strength of honeycomb and affects the durability of the bond. Kim (2003) conducted a theoretical study on how bondline thickness variations affect the shear stresses in the classical lap joint. He found that the stresses increased drastically if the bondline was thinner in one end of the joint compared to the other. This just briefly underlines some of the extensive work conducted in the area of heterogeneous adhesive bonding (Budzik et al., 2012; 2013; da Silva and Lopes, 2009; Pardoen et al., 2005).

Modeling of heterogeneous adhesive joints proves challenging due to the stochastic nature of the imperfections and the variations in the bonding properties. One method widely used to accommodate this issue is to account for the heterogeneities in the bondline statistically (Van Straalen et al., 1998; Jumel, 2017). The method focuses on assessing the influence of random variables, such as imperfections, voids, temperature, ageing among others, on joint strength or toughness by describing their combined effect statically, often supported by a Weibull distribution (Arenas et al., 2010; Towse et al., 1999; Weibull, 1951). This approach has been reported to be in good agreement with experimental data and to take the weakening effects of heterogeneities into account (Bresson et al., 2013). While the stochastic methods provide design and optimization parameters, they do not yield any information on the mechanism leading to the shift in mechanical behavior. To gain this insight mechanical models of heterogeneous adhesive joints, either utilizing the finite element method (Fitton and Broughton, 2005; Matouš et al., 2008; Patinet et al., 2013) or based on an analytical approach (fewer in number), have been established (Olia and Rossettos, 1996; Yamada, 1987). Some of the more extensive contributions of the latter include the work of Xia et al. (2012; 2013; 2015). Inspired by the work of Kendall the authors investigated the enhancing effects of heterogeneities on peel strength of a thin film. Two types of heterogeneities were studied; (1) variation in thickness of the peeled arm (Xia et al., 2013), and (2) variation in the bonded surface adhesion (Xia et al., 2015). By exploiting two novel analytical models and experimental peel tests the authors concluded that heterogeneities in the film can enhance the peel strength.

Due to the complex nature of heterogeneities authors need to simplify the imperfections and reduce the problem to a representative unit cell model as a way to obtain exact, closed-form solutions.

Such an approach was attempted in a recent work by Cuminatto et al. (2015). The authors proposed a novel analytical model to ana-

lyze debonding of patterned, discontinuous interfaces in microelectronic and micro-electromechanical devices. The periodic model, resembling the wedge fracture test, is based on bands of adhesive and bands of void with the former modeled as two springs; a linear and a torsional similar to Pasternak (1954) foundation. Exploiting fracture mechanics and assuming that the first band of the adhesive is damaged, the authors determined the strain energy release rate based on the stored energies in the beam and in the bondline. By comparison with established continuous models of bonded joint, namely Cognard (1986) model and Penado (1993) model, the authors discovered that these classical models deviate from their patterned model in terms of crack length and strain energy release rate predictions.

In this paper an analytical model is derived in which a novel unit pattern formulation is used for an adhesive joint with patterned interface. The model is based on a compliance approach making it capable of describing various common mode I fracture experiments such as the wedge test and the double cantilever beam (DCB) setups, among others. The patterned interface is obtained by introducing bands of 'void' (or weak adhesion zones) perpendicular to the crack growth direction causing the bondline (which in the present context refers to the adhesive and interfaces between the adhesive and the adherends) to become discontinuous. Using the interface fracture mechanics combined with a rule of mixtures applied within the process zone, the effective fracture energy with respect to the discontinuous, patterned bondline is determined and from it the force-displacement plot and the strain energy release rate (SERR) are obtained. The novel model is compared to continuous, homogeneous models established in the literature to verify the convergence and to identify the improvement in accuracy. Finally, extensive experimental work based on the DCB test configuration is conducted to verify the model in terms of the force-displacement curves and to describe the behavior of adhesive joints containing a single to 16 inclusions, varying in size. Very good agreement between the analytical model and the experimental results is reported. Thanks to such extensive approach a systematic knowledge of the effects of small, large, single, and multiple voids is gained. We hope that the present contribution can be used in the evaluation and design of heterogeneous interfaces in a reliable, accurate and fast manner.

2. Theoretical framework

To gain phenomenological insights into the impact of bondline heterogeneities on joint behavior, an analytical model of the DCB specimen is developed. The model is first established as a unit pattern consisting of one band of the adhesive and one band of the void orientated perpendicular to the crack growth direction. From the formulation perspective, 'the adhesive' band is equivalent to the strong adhesion zones, while 'the void' is a specific case of the weak adhesion zone for which fracture energy is zero). Cyclic repetition of the unit pattern allows more advanced joint configurations to be examined through semi-analytical solution strategies.

2.1. Unit pattern model

The model is constituted from three segments as shown in Fig. 1. The DCB specimen is symmetric about the x-axis along the centerline of the adhesive layer so only half of the specimen is modeled. The first segment represents the debonded part and acts as the loading arm. As the joint debonds, the length of the unbonded part increases, hence the loading arm (and thereby the moment) increases at the crack tip. The two other segments make up the unit pattern, where the first segment mimics the adhesive layer and the second represents the void inclusion. In that respect, the present model deviates from the existing one

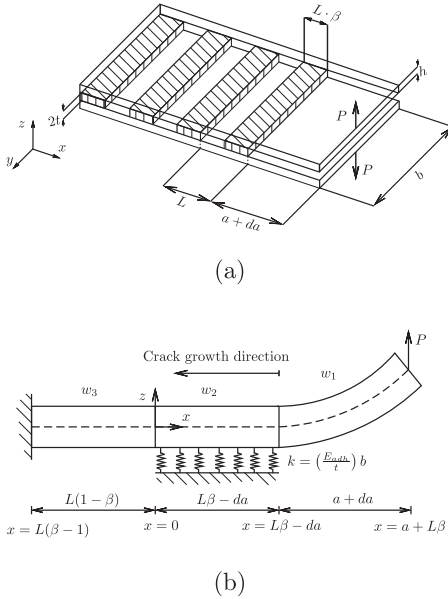


Fig. 1. The heterogeneous interface model. (a) The scheme of the heterogeneous adhesive double cantilever beam consisting of the bands of adhesive (hatched) with length $L\beta$ intermediated by bands of void with a length of $L(1-\beta)$. Other joint dimensions include the adherend thickness, h , width, b , adhesive thickness, $2t$, initial crack length, a , a crack extension of da , and an applied load, P . (b) Scheme of the unit pattern model comprising one band of adhesive modeled as a beam on an elastic foundation and one band of void modeled as a constrained beam and the unbonded part.

(Cuminatto et al., 2015) and captures the physical and geometrical characteristic parameters differently, as will be discussed in the following sections.

With a Cartesian coordinate system positioned at the interface between the adhesive and the void, the loading arm spans from $x = L\beta - da$ to $x = a + L\beta$. Here a is the initial unbonded length, da is the crack extension in the negative x -direction, L is the length of the unit pattern, and β is the degree of heterogeneity. The load is applied at $x = a + L\beta$ and the crack tip is positioned at $x = L\beta - da$ and moves with the propagation of the crack, i.e. as da increases. The adhesive part of the beam, which is represented by an elastic foundation, spans from $x = L\beta - da$ to $x = 0$, hence its span reduces as the crack grows. The segment containing void spans from the interface with the adhesive at $x = 0$ to $x = L(\beta - 1)$ where it is treated as encastre. Each beam segment is formulated differently and connected by imposing continuity conditions.

2.1.1. Beam segment I: debonded part

The first beam segment, which is represented by w_1 in Fig. 1, is a cantilever beam of length $l_1 = a + da$, which acts as the loading arm and represents the unbonded part of the joint. The cantilever is loaded with a concentrated force of P at the tip, $x = a + L\beta$. The length of the loading arm increases as the crack propagates and da , which is the crack extension, increases. In contrast to a regular cantilever beam, this segment does not have a built-in section

but is connected to the second beam segment through continuity conditions.

Based on the Euler–Bernoulli formulation, the governing equation for this segment is

$$\frac{d^2 w}{dx^2} = -\frac{M(x)}{EI} \quad (1)$$

The moment, $M(x)$, is defined by the length of the cantilever and the applied load. Substituting the moment in Eq. (1) with $M(x) = -P(a + L\beta - x)$ and performing the integration give the displacement equation of the beam, which yields

$$w_1 = \frac{P}{EI} \left(\frac{1}{2} L\beta x^2 - \frac{1}{6} x^3 + \frac{1}{2} a x^2 \right) + A_1 x + B_1 \quad (2)$$

where A_1 and B_1 are constants of integration determined through the continuity conditions between the beam segments I and II. It can be noted that the crack extension, da , does not explicitly enter Eq. (2). However, it affects the beam implicitly through x (the length of the beam segment is defined as $l_1 = a + da$). Evaluating the moment at the left end of the segment yields

$$M = -P(a + L\beta - x) \Big|_{x=L\beta-da} = -P(a + da) \quad (3)$$

Clearly, the larger the crack extension the larger the moment acting on the crack tip.

The continuity conditions for the first beam segment, which are used to determine the constants of integration, are

$$w_1 = w_2 \quad \text{for} \quad x = L\beta - da \quad (4)$$

$$\frac{dw_1}{dx} = \frac{dw_2}{dx} \quad \text{for} \quad x = L\beta - da \quad (5)$$

Since there is no distributed load acting on the first segment (the elastic foundation applies one on the second beam segment), there is no continuity of the fourth derivative between the segments. With two unknown constants of integration for the first segment, two equations of continuity are needed. The remaining two equations for the second and third derivative of the deflection are used for the second segment.

2.1.2. Beam segment II: bonded part with adhesive

The second segment represents the bonded part of the joint and has a length of $l_2 = L\beta - da$ which decreases as the crack propagates. This segment is modeled similarly to the Kanninen–Penado model (Kanninen, 1973; Penado, 1993); as a simple beam on a one-parameter elastic foundation as formulated by Winkler (1867). The governing equation for the segment in the absence of distributed loads yields

$$\frac{d^4 w}{dx^4} + 4\lambda^4 w = 0 \quad \text{where} \quad \lambda = \sqrt[4]{\frac{k}{4EI}} \quad (6)$$

where k is the stiffness of the foundation given by $k = (E_{ad}/t)b$ when the plain strain condition and the adhesive are assumed to be linear elastic with Young's modulus of E_{ad} . E is the elastic modulus of the substrates, I is the moment of inertia of the beam given by $I = \frac{bh^3}{12}$ and λ^{-1} is known as the wave length or the process zone length. This process zone should not be confused with the fracture process zone. The process zone in its present elastic foundation context is interpreted as a distance (from the crack tip) over which the positive peel stress is distributed. The general solution to Eq. (6) and to the deflection of the beam can be written in the form

$$w_2 = \cosh(\lambda x) [A_2 \cos(\lambda x) + B_2 \sin(\lambda x)] + \sinh(\lambda x) [C_2 \cos(\lambda x) + D_2 \sin(\lambda x)] \quad (7)$$

where A_2 , B_2 , C_2 and D_2 are constants of integration. Since this segment is placed between the two other segments, its solution solely depends on the continuity conditions. Differentiation of Eq. (7) leads to a significant number of terms which increases further when the differentiation is repeated several times. In order to limit the number of terms, the origo, $z, x = 0$, is placed at the left end of the segment. This causes all sine functions to be zero thus reducing the number of terms in the equations. Again, there is no continuity in the fourth derivative of the displacement between the second and third segment. The continuity conditions used to determine the constants of integration for the second beam segment are

$$\frac{d^2 w_1}{dx^2} = \frac{d^2 w_2}{dx^2} \quad \text{for} \quad x = L\beta - da \quad (8)$$

$$\frac{d^3 w_1}{dx^3} = \frac{d^3 w_2}{dx^3} \quad \text{for} \quad x = L\beta - da \quad (9)$$

$$\frac{d^2 w_2}{dx^2} = \frac{d^2 w_3}{dx^2} \quad \text{for} \quad x = 0 \quad (10)$$

$$\frac{d^3 w_2}{dx^3} = \frac{d^3 w_3}{dx^3} \quad \text{for} \quad x = 0 \quad (11)$$

These four equations enable determination of the four constants of integration while ensuring that the segments act as a continuous beam.

2.1.3. Beam segment III: bonded part with void

The third segment is modeled as a cantilever beam with a length of $l_3 = L(1 - \beta)$ and a built-in section on the left-hand side. Since the other end is positioned at $x = 0$, its coordinates will be negative and the left end is situated at $x = L(\beta - 1)$. The governing equation for the third segment is given by

$$EI \frac{d^4 w}{dx^4} = 0 \quad (12)$$

The general solution is of the form

$$w_3 = \frac{1}{6} A_3 x^3 + \frac{1}{2} B_3 x^2 + C_3 x + D_3 \quad (13)$$

where A_3 , B_3 , C_3 and D_3 are constants of integration, which are determined through a combination of boundary and continuity conditions. The built-in section at the left end does not allow for deflection or rotation, thus the boundary conditions read as

$$w_3 = 0 \quad \text{for} \quad x = L(\beta - 1) \quad (14)$$

$$\frac{dw_3}{dx} = 0 \quad \text{for} \quad x = L(\beta - 1) \quad (15)$$

The boundary conditions allow for determination of two of the four constants of integration. The remaining constants are found through continuity conditions between beam segments II and III.

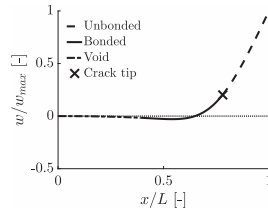
$$w_2 = w_3 \quad \text{for} \quad x = 0 \quad (16)$$

$$\frac{dw_2}{dx} = \frac{dw_3}{dx} \quad \text{for} \quad x = 0 \quad (17)$$

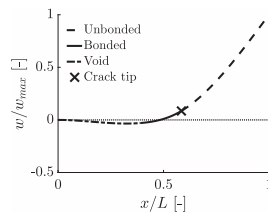
2.1.4. Fracture process

A linear fracture mechanics approach based on the Irwin–Kies compliance method (Irwin and Kies, 1997) is used to determine the SERR, \mathcal{G} . The SERR is defined as the difference between the potential energy of the external forces, V , and the internal strain energy, U , with respect to the change of crack surface area, A , hence

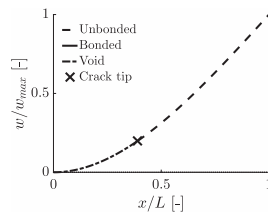
$$\mathcal{G} = \frac{d(V - U)}{dA} \quad (18)$$



(a)



(b)



(c)

Fig. 2. Displacement of the unit pattern model, comprising an unbonded, an adhesive and a void part as the crack propagates and the bondline fractures. (a) The displacement at crack onset, (b) the displacement when half of the bondline is debonded, and (c) the displacement as the bondline is completely fractured.

The compliance, C , of the specimen is defined as

$$C = \frac{\Delta}{P} \quad (19)$$

where Δ is the displacement at the load application point given as $\Delta = 1/2 w_1|_{x=L\beta+da}$ and P is the force at the tip of the loading arm. Combining Eq. (18) and Eq. (19) and assuming a straight crack front the expression of the SERR becomes

$$\mathcal{G} = \frac{P^2}{2b} \frac{dC}{da} \quad (20)$$

where b is the width of the specimen and da is the instantaneous crack length extension. With Griffith's (1921) type fracture criterion, the SERR at fracture is equivalent to the fracture energy, \mathcal{G}_c , of the adhesive. Finally, assuming that during propagation $\mathcal{G} = \mathcal{G}_c = \text{constant}$, it can be shown that the force and the displacement scales as $P \propto \Delta^{-1/2}$ (Budzik et al., 2012).

In Fig. 2(a)–(c) the displacements of the three segments at different stages of debonding: after loading (no fracture), half of the bondline fractured, and full debonding are seen. The figures indi-

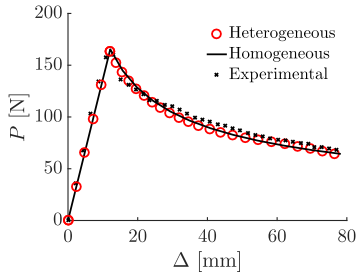


Fig. 3. Comparison of the homogeneous solution, the heterogeneous solution with no void included ($\beta = 1$) and DCB experimental results from a homogeneous joint. All of the solutions are in good agreement showing that the heterogeneous model converges to a homogeneous solution when the void goes toward zero.

cate continuity between all three segments through all stages. Furthermore, the first two figures, Fig. 2(a) and (b), show the characteristic behavior of an adhesive joint where a region of tension appears in the vicinity of the crack tip followed by a compressive zone. The span of the tensile region is defined as the process zone, λ^{-1} , and is a measure of how far in front of the crack tip the stress is distributed. In Fig. 2(c), once the adhesive is fully debonded, such characteristic behavior is absent and the model acts as a cantilever beam subjected to a tip load. This shows that the mechanical behavior of the model is valid for all stages of debonding from the crack initiation to full debonding. For verification similar plots were made for the shear forces and moments as derivatives of the deflection. The plots revealed that continuity was satisfied for these as well.

2.2. Verification and convergence

The novel model is verified with the well-established homogeneous model proposed by Kanninen (1973) (for a detailed derivation see Appendix A). The SERR for the homogeneous model is given by

$$G_{\text{homo}} = \frac{p^2}{2b} \frac{dC}{da} = \frac{p^2 (a^2 \lambda^2 + 2\lambda a + 1)}{\lambda^2 E I b} \quad (21)$$

where the variables are the same as for the heterogeneous model. Since the reference model has a homogeneous bondline, the novel model should converge to its solution as the length of the void tends toward zero, $L_{\text{void}} = L(1 - \beta) \rightarrow 0$. The theoretical predictions are furthermore compared with experimental results of a homogeneous adhesive joint as described later. In Fig. 3, the force-displacement plots for the homogeneous model, the heterogeneous model and the experiment are seen. The void inclusion in the novel model has been set to zero, i.e. $\beta = 1$, making the bondline homogeneous. It is evident from the figure that the novel model converges to the homogeneous solution when no void inclusion is present by both staying in good agreement. In addition, both models describe the experimental data (representative curve from 10 specimens tested) very well.

2.3. Multi-pattern model

With the unit pattern model being established and verified, a multi-pattern model is developed as a cyclic repetition of unit patterns. This allows for further investigation of more advanced joint configurations containing several inclusions. The multi-patterned model is established by combining n unit pattern models in a

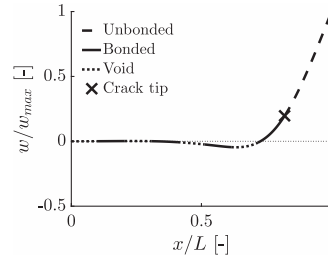


Fig. 4. Displacement of the multi-pattern model containing four strong bands, four weak bands and the unbonded part. It is evident that continuity between the different parts of the model exists and the process zone with a tensile and compressive zone is well-described.

cyclic manner. Since it is impossible to handle the model analytically, a semi-analytical approach is taken. The constants of integration are evaluated numerically and, subsequently, the analytical expressions are used to determine the displacement and the crack growth.

Analytical expressions of the displacements, Eqs. (2), (7) and (13), and the first, second and third derivatives of these are obtained. Based on the boundary conditions stated in Eqs. (14) and (15) and the continuity conditions in Eqs. (4)–(5), Eqs. (8)–(11) and Eqs. (16)–(17), a non-homogeneous matrix equations system is established in the form of

$$A\vec{x} = \vec{b} \rightarrow \vec{x} = A^{-1}\vec{b} \quad (22)$$

where A is an $n \times n$ matrix containing the coefficients in front of each constant of integration, \vec{x} is an n -row vector containing the constants of integrations, $\vec{x} = \{A_1, B_1, A_2, B_2, \dots, C_n, D_n\}$, \vec{b} is n -row vector containing the displacements, the shear forces and the moments of the segments with regard to the boundary and the continuity conditions, and n is the number of constants of integration in the particular model. The coefficients in A are obtained by evaluating the analytical expressions at the boundary and continuity points with respect to the involved segments. Replacing the expressions with one another, the combination of adhesive and void segments is freely chosen, e.g. instead of void segments, adhesive segments with different properties can be repeated. Solving the matrix equations system provides the constants of integration with which the displacements and the SERR are obtained as continuous functions. Composition of the model (the number and size of the adhesive and void bands) enters and affects the SERR through the constants of integration. In each iteration the fracture energy is evaluated based on the current crack length and the segment in which the crack tip is situated.

A customized MATLAB® (R2016a 9.0.0 64-bit, MathWorks, Massachusetts, USA) routine is developed to determine the constants of integration and calculate the force-displacement response of the n -pattern model. The multi-pattern model is governed by two parameters: the heterogeneity, β (the length ratio between adhesive and void), and the periodicity, n (the number of ‘voids’). Similarly to the unit pattern model the span of the adhesive is reduced as the crack propagates. Fig. 4 shows the deflection of the adherend from a multi-pattern model with heterogeneity of $\beta = 0.5$ and periodicity of $n = 4$. It is evident that the model imposes continuity between the segments exhibiting the characteristic behavior of a tension and a compression zone in the vicinity of the crack tip (as observed with the unit pattern model). This allows the process zone to span across the different strong and weak bands including the compressive zone. When examining the debonding be-

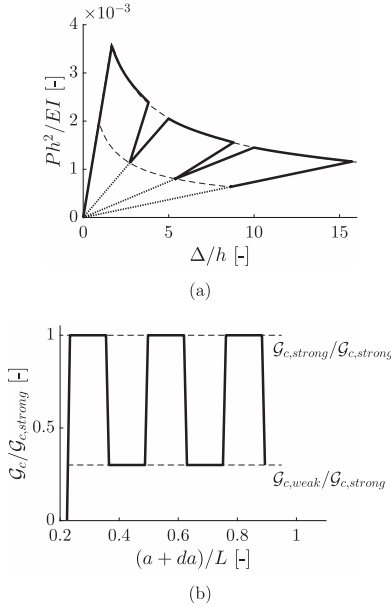


Fig. 5. Interface fracture behavior of the multi-pattern model during crack growth. (a) A normalized force–displacement plot showing how the load carrying abilities of the joint rapidly decrease as the crack tip reaches the weak zones, causing both the force and displacement to decrease. The none gradual reduction in load carrying capacity is caused by the none smooth transition in the fracture energy as shown in (b). The dashed lines indicate the upper and lower limits of the load carrying capacities (fracture energies) of the weak and the strong zones. The dotted lines show how each point on the curve is calculated as an independent compliance value based on the specific value of crack length. (b) The instantaneous fracture energy ($G_c/G_{c,strong}$) as a function of the crack length showing how the transition between upper and lower limits occurs discontinuously and stepwise (as it is seen at $(a+da)/L = 0.35, 0.5, 0.61, 0.75, 0.9$), which does not have any physical background.

avior of the multi-pattern model, the effects of varying interface adhesion are immediately visible in the force–displacement behavior. Fig. 5(a) shows a force–displacement plot obtained from the multi-pattern model with a periodicity of $n = 3$, a heterogeneity of $\beta = 0.5$. As the crack tip reaches the weak interface the fracture energy decreases leading to reduced load carrying capacity. This transition is visible on the force–displacement as rapid decreases in the force. Since the model is based on the compliance the loading and unloading paths follow the new position of the crack front calculated in each iteration. As it appears in Fig. 5(b) an upper and a lower limit (the fracture toughness of the strong and the weak zones, respectively) exist between which the instantaneous fracture energy changes. Indeed, the fracture energy evaluated at the crack tip ‘jumps’ between the values of the strong and the weak bonding depending on actual crack position. The model works properly according to the theory upon which it is derived. However, the sudden discontinuous changes observed in the force–displacement plot can take place only in situations where $\lambda^{-1} = 0$, viz. rigid–brittle adhesives. If void is included instead of a weak adhesive, the fracture energy would go to zero and the model would

break down when reaching such an interface. In order to further extend the model, a rule of mixtures is implemented in the multi-pattern model. Such an approach can correctly treat the case of $\lambda^{-1} > 0$. An effective parameter, in this case the fracture energy, will be involved. The commonly used rule of mixtures in mechanics of materials assumes that the elastic properties of the material are proportionally additive analog to springs acting in parallel (Voigt, 1889). This provides a simple linear relation between the fractions of the parameters and the resulting effective parameter. Assuming that the fracture energies of the strong and the weak adhesives act in parallel, the following rule of mixtures, as proposed by Budzik et al. (2013), is obtained

$$G_{c,eff} = f G_{c,s} + (1 - f) G_{c,w} \quad (23)$$

where $G_{c,eff}$ is the effective, instantaneous fracture toughness, $G_{c,s}$ is the fracture toughness for the strong zone, $G_{c,w}$ is the fracture toughness for the weak zone and f is the volume fraction of the strong adhesive given as

$$f = \frac{V_s}{(V_s + V_w)} \quad (24)$$

where V_s is the total volume of the strong zone and V_w is the total volume of the weak zone. The volume fraction is typically calculated for the total amount of the materials. However, in the present case, only a finite region in front of the crack tip related to the process zone (λ^{-1}) is affected by loading (Budzik et al., 2011; Jumel et al., 2011). It is therefore believed that only the affected part of the bondline contributes to the instantaneous fracture energy. As a result the fraction is calculated with respect to the length of the process zone and the strong/weak zones within it. Assuming that the process zone length is a constant (Eq. (6)) and that the widths of the different zones are identical, the fraction of strong to weak adhesion in the process zone can be written as

$$f = \frac{L_s}{(L_s + L_w)} = \frac{L_s}{\lambda^{-1}} = L_s \lambda \quad (25)$$

where $L_s = \sum_{n=1,2,\dots} l_{sn}$ is the sum of the lengths of the strong adhesion zones in the process zone and $L_w = \sum_{n=1,2,\dots} l_{wn}$ is the sum of the lengths of weak zones. Since the process zone originates from the moving crack tip, the process zone also moves equally. Hence, the ratio between the strong and weak zones within the process zone varies during the debonding as seen in Fig. 6(a) and (b). Combining Eq. (23) and Eq. (24) and assuming that the fracture energy of the weak zone is zero give the final form of the rule of mixtures that is implemented into the model. It yields

$$G_{c,eff} = G_{c,s} \cdot f = G_{c,s} \cdot \frac{L_s}{(L_s + L_w)} \quad (26)$$

The effective fracture energy has two limits: (1) when the length of the weak zone goes toward zero, the fracture toughness goes toward the homogeneous solution, hence $\lim_{L_w \rightarrow 0} G_{c,eff} \rightarrow G_{c,strong}$. (2) When the length of the weak zone goes toward infinity, the fracture toughness goes toward zero hence $\lim_{L_w \rightarrow \infty} G_{c,eff} \rightarrow 0$. Any fraction between 1 and 0 will produce an effective (strong/weak ‘composite’) fracture energy between zero and the fracture toughness of the strong adhesive. In each iteration, i.e. increase in crack length, of the semi-analytical routine, the current volume fraction of strong to weak adhesion in the process zone is assessed, and the instantaneous fracture energy is obtained from Eq. (26).

Fig. 7 shows the SERR for the multi-pattern model with the rule of mixtures implemented. It is clear that the rule of mixtures provides a gradual, continuous transition between the upper and lower limits of the effective fracture energy and that the discontinuous transitions observed in Fig. 5(b) are eliminated. The

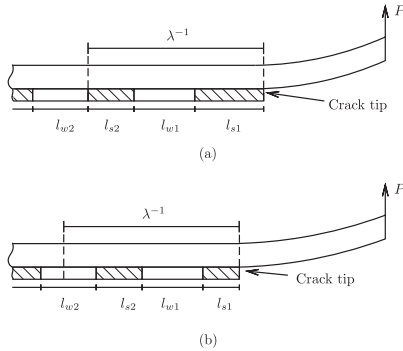


Fig. 6. Crack propagation of the multi-pattern model representing how the strong-to-weak zone ratio in the process zone, λ^{-1} , smoothly transits with respect to the crack front vicinity. (a) In this configuration, the process zone contains two strong bands and one weak band providing a ratio of $f = 2/3$. (b) The crack has propagated such that the process zone now contains one and a half strong bands and one and a half weak bands resulting in a ratio of $f = 1.5/3 = 1/2$.

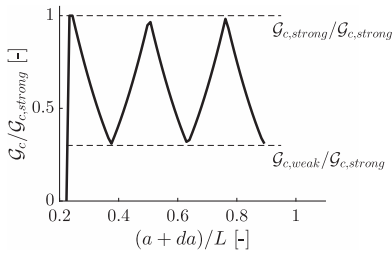


Fig. 7. The instantaneous fracture energy ($\bar{G}_c/\bar{G}_{c,s}$) as a function of the crack length of the multi-pattern model. A gradual transition between the upper and lower limits (dictated by the strong and weak zones) of the fracture energy is obtained by implementing a rule of mixtures in the multi-pattern model. The smooth transition of the fracture energy is reflected by gradual changes in the load carrying capacity of the joint.

gradual change in $\bar{G}_{c,eff}$ results in smooth transitions in the force-displacement plot, hence greatly improving the models physical consistency.

3. Experimental work

3.1. Material and processes

The experimental work follows two configurations. The first aims to investigate the impact of a single void in the bondline. The second aims to identify the effects of multiple heterogeneities. A mode I fracture test setup is used, based on the DCB experiment principles for obtaining force vs. displacement data. The specimen consists of two PMMA adherends (Fig. 8) of length $L_{specimen} = 200$ mm, width $b = 25$ mm and thickness $h = 8$ mm. The flexural rigidity, D , (the product of Young’s modulus, E , and the moment of inertia, $I = b \cdot h^3/12$) of the adherends was evaluated from a cantilever beam test leading to $D = 1.16 \pm 0.20 \text{ Nm}^2$.

A silicone adhesive (Bostik AB, Helsingborg, Sweden) is used to bond the two adherends with a layer of thickness $2t$. The elastic

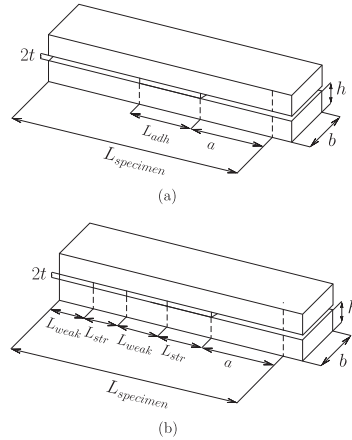


Fig. 8. Experimental specimen configurations with length $L_{specimen}$, width b , adherend thickness h and adhesive thickness $2t$. (a) Specimens used in the first set of experiments comprising two adherends bonded with a single intermediate band of adhesive with a length of L_{adh} surrounded by void and an initial crack length of a . (b) Specimens with an initial crack length of a used in both the first and the second set of experiments. The two adherends are bonded by an intermediate bondline consisting of periodically varying weak and strong bands. L_{str} denotes the length of the strong bands while L_{weak} represents the length of the weak bands. Depending on the experiments, the bondline contains from two up to and sixteen bands.

modulus of the adhesive is found to be $E_{adh} = 0.23 \pm 0.03 \text{ MPa}$ in room temperature, approximately $21 \pm 2^\circ\text{C}$, through tensile testing. Although it could be criticized, such material was chosen deliberately. With linear behavior over the entire $\sigma = f(\epsilon)$ and a large (of the order of magnitude once compared to e.g. pure – brittle epoxy adhesives) process zone length (λ^{-1}), it is suitable to study the effects of weak and strong interfaces in the bondline. In fact, systems with softer but tougher bondlines gain more attention offering improved damage tolerance and damping capabilities, among others.

The adherends are prepared both mechanically and chemically prior to applying the adhesive. After such surface treatment the void/weak adhesion regions are masked by a nonadhesive tape and the adhesive is applied to both adherends. To ensure a uniform thickness of the bondline, spacers of approximately 0.6 mm are inserted at the extremities of the bonded region. The adherends are carefully aligned and put under static pressure of approximately 100 N and set aside in room temperature $21 \pm 2^\circ\text{C}$ for at least 48 h of curing. Prior to the testing, each specimen is measured using a 3D macroscopic scanner (VR-3200, Keyence, Illinois, USA) to ensure that the exact dimensions for each specimen are used in the post-processing and analysis of the experimental data.

3.2. Specimens

In the first set of experiments, a single void inclusion is introduced as shown in Fig. 8(a). The degree of heterogeneity, β , in the bondline is defined here as the ratio of the area of adhesion to the area of void, hence $\beta = L_{adh}/(L_{specimen} - a)$. Thus $\beta = 1$ refers to a homogeneous bondline without voids. First, two specimens with one band of void and one band of adhesive are manufactured. Post-manufacturing measurements of the specimens reveal

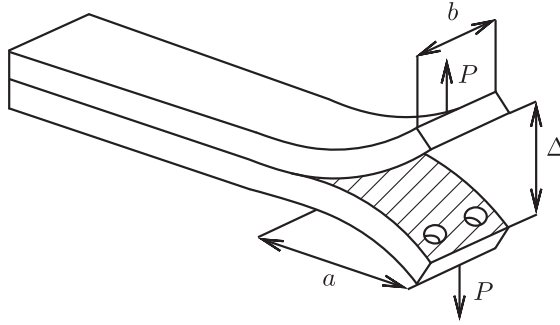


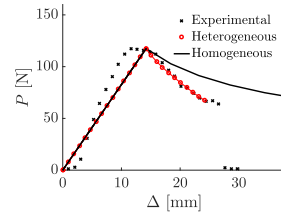
Fig. 9. Schematic of the double cantilever beam test configuration used where a represents the apparent crack length, b is the width of the specimen, P is the applied force and Δ is the crack tip opening displacement.

that they have an initial unbonded length of $a \approx 45.5 \pm 0.7$ mm, an adhesive thickness of $2t \approx 0.6 \pm 0.1$ mm and the fracture energy of $G_c \approx 1500 \pm 100$ J/m². The first specimen was bonded along $L_{adh1} = 61$ mm while the second has $L_{adh2} = 87$ mm. Since the length of the specimens is the same ($L_{specimen} = 200$ mm), the specimens have different degrees of heterogeneity, $\beta_1 = 0.43$ and $\beta_2 = 0.62$. Secondly, three specimens with two bands of strong adhesive separated by a single weak zone (similar to Fig. 8(b)) were prepared. For all three specimens the first band of strong adhesive has a length of $L_{str} = 40$ mm. The subsequent lengths of the weak bands are $L_{weak1} = 10$ mm, $L_{weak2} = 20$ mm and $L_{weak3} = 40$ mm. This results in heterogeneity ratios of $\beta_1 = 0.8$, $\beta_2 = 0.667$ and $\beta_3 = 0.5$.

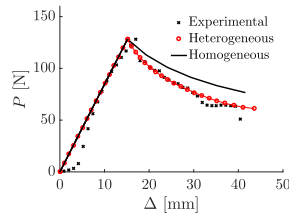
The second set of experiments investigates the effects of multiple strong/weak bands in the bondline, as seen in Fig. 8(b). The first weak zone is placed 20 mm from the initial crack front for all specimens. In this case the degree of heterogeneity is determined as the ratio of the area of the strong zones to the area of the weak zones, hence $\beta = L_{adh}/(L_{adh} + L_{void} - a)$. The periodicity, n , is defined as the number of unit patterns, i.e. one weak zone and one strong zone, in the bondline. Four batches of two specimens with varying periodicity are manufactured: $n_1 = 16$, $n_2 = 7$, $n_3 = 5$ and $n_4 = 4$ and respective heterogeneities $\beta_1 = 0.5$, $\beta_2 = 0.5$, $\beta_3 = 0.5$ and $\beta_4 = 0.667$. In the first batch referred to as 3W3S, the weak and strong zones of equal lengths are $L_{adh} = L_{void} = 3$ mm. In the second batch referred to as 6W6S, $L_{adh} = L_{void} = 6$ mm. In the third batch, referred to as 10W10S, the zones span over $L_{adh} = L_{void} = 10$ mm and in the fourth batch referred to as 10W20S, the strong adhesion zone is $L_{adh} = 20$ mm and the weak zone $L_{weak} = 10$ mm. The specimens have an adhesive thickness of $2t \approx 0.5 \pm 0.05$ mm and a fracture energy of $G_{c,s} \approx 900 \pm 100$ J/m². The weak adhesion zones are evaluated at $G_{c,weak} \approx 0$.

3.3. Data acquisition and post-processing

The fracture tests are conducted by installing the double cantilever beam specimen in a tensile machine (Zwick Z005, Zwick GmbH & Co. KG, Ulm-Eisingen, Germany) using a custom made fixture with a scheme of the DCB shown in Fig. 9. A preload of 1 N is applied before the displacement rate controlled load of $d\Delta/dt = 20$ mm min⁻¹ is applied to the tip of the top adherend. During the loading the opening displacement, Δ , and the applied force, P , are simultaneously acquired at a sampling rate of 50 Hz until full debonding.



(a)



(b)

Fig. 10. Comparison of the homogeneous model, the heterogeneous model and the first set of experiments comprising specimens with one single band of adhesive. A good agreement between the heterogeneous model and the experimental data is observed while the homogeneous model overestimates the joint strength. (a) Specimen with an adhesive band of $L_{adh} = 61$ mm and the predictions of the theoretical models, and (b) specimen containing a $L_{adh} = 87$ mm adhesive band.

4. Results and discussion

4.1. Single imperfection

The experimental results and the comparison with the two theoretical models are presented in Fig. 10(a) and (b). The crack propagates in the bondline until reaching the void leading to complete debonding. Since both the heterogeneous and the classical models share the same initial properties, identical linear relation is ex-

pected during loading. From the crack onset the two models behave differently. It is seen in both Fig. 10(a) and (b) that the homogeneous model overestimates the properties of the joint, which is reflected by higher force predictions, while the heterogeneous model predicts the experimental data accurately. This shows that introducing void in the bondline and hereby reducing its span also reduces the fracture strength of the joint. The weakening effect takes place even before the crack tip reaches the void, indicating that the effective fracture energy is affected by the vicinity of the crack. Furthermore, it seems as if the weakening effect induced is scaling with the size of the void. This is based on the fact that the first specimen which has the largest void, $\beta_1 = 0.43$, was weaker than the specimen with the smaller void, $\beta_2 = 0.62$. This effect is not captured by the conventional semi-infinite homogeneous models, but is described very well with the novel model presented. This indicates that using the conventional modeling technique may lead to overestimations of joint strength when imperfections are present in the bondline, especially near an edge where it would reduce the span of the bondline.

In Fig. 11(a)–(c) results for the (three) strong-weak-strong specimens are presented and compared to the unit pattern model. The force decreases as the crack reaches the void position just as for the unit pattern specimens. However, after the force has decreased, it slowly builds up again following the new compliance associated with the new crack position. The unit pattern model cannot, of course, describe this behavior since it only considers one band of the adhesive and one band of the void (this can be found sufficient for description of the joint behavior until the void is reached). In Fig. 11(a) a very good agreement between the experimental data for the 40 mm void and the unit pattern model is observed. Fig. 11(b), corresponding to the 20 mm void, shows that the analytical model stays in good agreement with the experimental results. However, instead of a decrease there is an increase in the force as the crack reaches the void. The same trend is observed for the 10 mm void, cf. Fig. 11(c). This is also found once $L_w \rightarrow 0$. The behavior is related to the boundary conditions set within the unit pattern model and displays the limits of the present model. Indeed, the controlling parameter is the process zone length. If the void (weak) zone is smaller than the process zone's length stiffening of the joint occurs due to the finite length effects. Since the process zone has a length of $\lambda^{-1} = 26$ mm and the first $L_w = 40$ mm, these effects are not visible since $L_w \lambda > 1$. The situation is changing for the second specimen with a void of 20 mm, and is clearly emphasized for the third specimen with only 10 mm of void since $L_w \lambda < 1$. As long as the void is large enough to contain the process zone, the unit pattern model describes the heterogeneous behavior very well. However, the unit pattern model was derived such that more advanced models could be established through the repetition of it, which would remove the finite length effects. In Fig. 12(a)–(c) the same experimental data is compared to a multi-pattern model simulating the joint configuration with two bands of adhesive and an intermediate band of void. All three figures show good agreement between the experimental data and the theoretical predictions. In contrast to the unit pattern model, the multi-pattern model is able to describe the crack propagation through the void inclusion. Importantly, the rule of mixtures implemented allows the model to describe the gradual loss and afterwards regain of the load carrying capacities as the crack propagates through the strong and the weak zones. The experimental data and the theoretical model display respectable agreement both before and after the crack has reached the weak zone.

4.2. Multiple imperfections

Recall that the specimens in the second experiment were manufactured by masking the bonded area, thus creating low adhesion

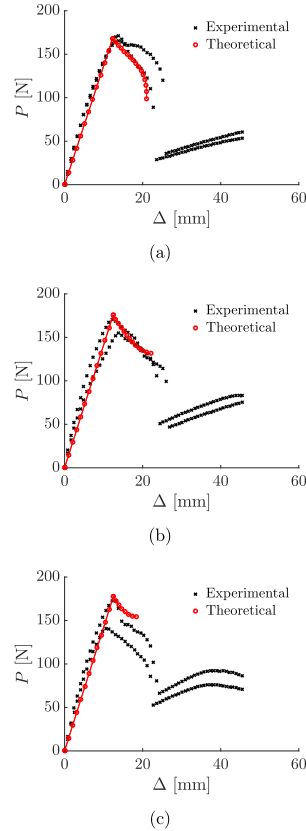


Fig. 11. Experimental results and comparison with the unit pattern model for specimens containing two bands of adhesive and an intermediate band of void. A very good agreement is observed, however, small void band edge effects appear. (a) Specimens with a $L_{\text{weak}} = 40$ mm void inclusion, (b) specimens with a smaller void inclusion of $L_{\text{weak}} = 20$ mm, and (c) specimens with the void inclusion of $L_{\text{weak}} = 10$ mm.

regions ($G_{c,w} \approx 0$). Since there is no actual void, the bondline is modeled as continuous using the beam on elastic foundation, Eq. (6), with zones of different fracture energies to simulate the varying adhesion. This will cause the crack to 'accelerate' and 'decelerate' depending on the position along the interface. In Fig. 13(a)–(c) the results obtained in the experiment are seen in which the 'standard' self-similar phase of the crack propagation (as associated with the crack propagation through homogeneous bondline or along homogeneous interface) has been replaced with oscillations. Clearly, the larger the bands of strong and weak adhesion, the larger the amplitudes and wave lengths of the force oscillations become. This is seen in Fig. 13(a) and (b) showing the results for 20 mm and 10 mm bands, respectively. As the zones shrink in size the oscillations become less pronounced, but a general accu-

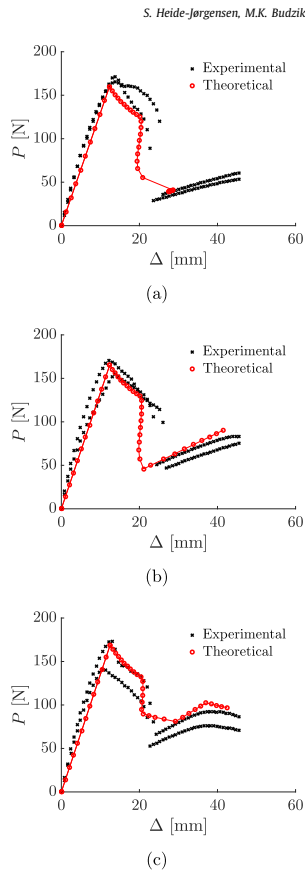


Fig. 12. Experimental results and comparison with the multi-pattern model for specimens containing two bands of adhesive and an intermediate band of void. A very good agreement is observed since the model is able to predict the drop in joint strength caused by the void inclusion while describing the subsequent recovering. (a) Specimens with a $L_{\text{weak}} = 40$ mm void inclusion, (b) specimens with a smaller void inclusion of $L_{\text{weak}} = 20$ mm, and (c) specimens with the void inclusion of $L_{\text{weak}} = 10$ mm.

mulative weakening effect seems to take place in the joint instead. This is supported by the oscillations being barely visible for the joints with band sizes of 6 mm and 3 mm, Fig. 13(c) and (d), but the overall joint properties being reduced and the failure occurring prematurely compared to the other specimens.

The figures further reveal that the assumption of fracture energies acting in parallel within the process zone holds well against the experimental data. The model mimics the characteristic oscillating behavior occurring when the adhesive bands are large. Moreover, it captures and describes the accumulative weakening effect once a significant number of small (compared to the process zone length) strong/weak zones is present. An interesting feature and addition to existing knowledge.

Finally, physical interpretation of the oscillating behavior is attempted using the adopted rule of mixtures. In Fig. 14 the force-displacement data from the 10W20S specimen is compared to the effective fracture energy with respect to crack front vicinity.

With a 20 mm strong band, the 26 mm process zone is almost fully developed, resulting in a maximum volume fraction of $f = L_s \lambda = 20/26 = 0.77$ and the largest fracture energy (for the discussed configuration) is obtained. This is visualized in point 1 in Fig. 14. The minimum volume fraction is obtained once the crack reaches the weak zone. In this case, all of the 10 mm weak zone stays within the process zone as shown in point 3 in Fig. 14. At this point, the volume fraction of the strong adhesive becomes $f = L_s \lambda = 16/26 = 0.62$. The difference between the two cases amounts to 24%. The transition happens gradually from point 1 to point 3 and the increase and the decrease are smooth.

The absence of oscillations and the lower resistance to fracture observed for the 3W3S specimens can also be explained using the principle of the volume fraction. Since both the strong and the weak bands equal 3 mm, $8 \frac{2}{3}$ bands are included within the process zone. Only $2/3$ of a band gradually transits from strong to weak and vice versa. The remaining 8 bands keep a constant composition of 50% strong and 50% weak within the process zone during the crack growth. In this case, 12 mm of strong zone and an equal fragment of weak zone are permanently within the process zone, hence only 2 mm varies between strong and weak. If the changing 2 mm is within the strong zone, the volume fraction becomes $f = L_s \lambda = 14/26 = 0.54$. On the other hand, if the 2 mm is contained in the weak zone, the volume fraction becomes $f = L_s \lambda = 12/26 = 0.46$. The difference between the upper and the lower limit of effective fracture energy for this specimen is approximately 17%, which is 7% less than the previous specimen. Compared to the volume fractions for the 10W20S, the fractions for the 3W3S are much smaller. In fact, the upper bound for the 3W3S is smaller than the lower bound of the 10W20S. Since the volume fraction determines the overall strength of the joint, this explains the general weakening effect observed for the small bands of adhesive, viz. the 3 mm and 6 mm bands.

5. Conclusions

We investigated, experimentally and analytically, effects of strong/weak adhesion bands running perpendicular to the crack growth direction during the mode I double cantilever beam (DCB) fracture experiment.

Transparent PMMA beams were bonded with an adhesive with a relatively large process zone (chosen deliberately to allow for variation of some important length scale parameters). By local masking of bonded surfaces, multiple experiments were designed and conducted, ranging from a single and up to 16 inclusions varying in size.

For data analysis, a novel, unit pattern based, analytical model for investigating patterned interfaces was derived. Based on the Euler-Bernoulli beam theory and the Winkler elastic foundation, simple but phenomenologically profound solutions were obtained for various cases. To describe the debonding of the bondline, an interface fracture mechanics approach based on the compliance method and a Griffith's type fracture criterion, was exploited. Especially, the force-displacement relation as an experimental outcome of the DCB experiment was of interest.

At first, through comparison with the existing solutions, we verified that the novel model converges to the homogeneous solution as the weak bands diminish. Both solutions, standard and novel, were in good agreement with the experimental data obtained for an assumed homogeneous DCB test setup. The situation changes once the single 'void' specimens were used. The homogeneous/continuous models such as Kanninen and Penado

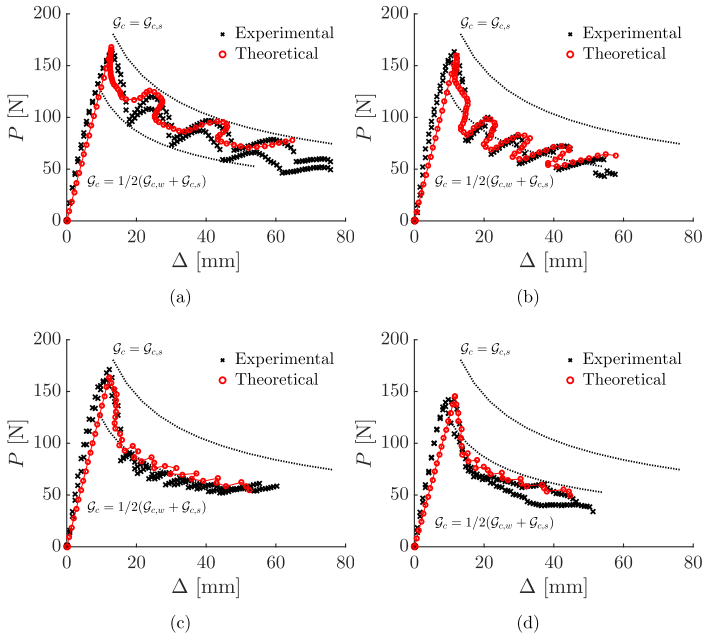


Fig. 13. Experimental data of specimens with multiple strong and weak bands compared to the multi-pattern model. An accumulative weakening effect is observed as the size of the bands decreases. This is visualized by the dotted lines representing the upper and lower limits of the fracture energy in the first experiment. The multi-pattern model describes the data well and a full correlation is reported. (a) Specimens containing four 20 mm strong bands and four 10 mm weak bands, (b) specimens with ten (five of each) equisized strong and weak bands of 10 mm, (c) Specimens containing a total of seven 6 mm bands equally divided between strong and weak, and (d) specimens with 8 strong and 8 weak bands all of 3 mm.

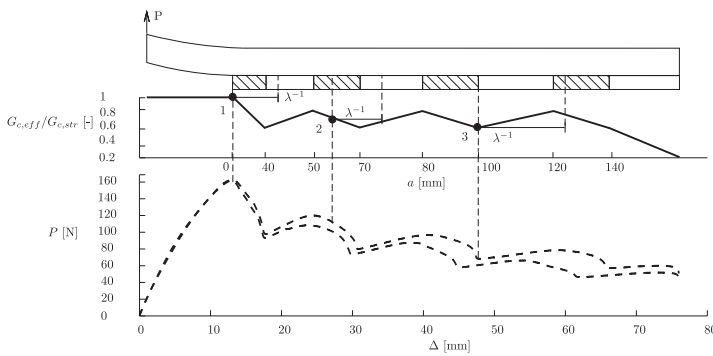


Fig. 14. The development in the SERR caused by changes in the strong-to-weak ratio in the process zone, visualized on the experimental data. It is evident that the transition, both for the model and for the data, happens smoothly.

(Kanninen, 1973; Penado, 1993) fail to recognize the weakening effect introduced by the ‘void’, while the novel model captured such behavior very well. The model describes successfully sudden drop of force, i.e. reduction in the joint’s load carrying capacity as the crack approaches the void. These experiments also demonstrated a huge impact of a single inclusion on fracture behavior with the crucial role of the process zone being emphasized.

Based on this observation, the model was further developed. A rule of mixtures (weighted fractions) was implemented to account for changing ratios of the process zone length and void content. The effective, instantaneous fracture energy depending on the ratio of strong to weak bands was obtained. Indeed, the multiple void inclusion experiments revealed an interesting behavior where the self-similar, stable, crack propagation phase is replaced by an oscillating behavior related to the crack crossing sharp transitions, i.e. strong/weak adhesion zones. This effect was more pronounced when the bands of strong and weak adhesives were within the range of magnitude of the process zone length. As their size decreased the oscillations became barely visible. However, a substantial, global, weakening of the joint is observed. All these effects are captured by the novel model demonstrating that the rule of mixtures implemented provides the desired physical background where the length scales associated with the dimensions of heterogeneity and the process zone are affecting the behavior of the joint.

The present study demonstrates that bondline/interface heterogeneities can significantly affect the behavior of the joint. When heterogeneities are small (size much smaller than the process zone size), the force vs. displacement curve is smooth and resembles a stable crack growth. Therefore, it may be tempting to estimate the ‘effective’ fracture energy and misinterpret it as properties of the ‘bulk’ (without the ‘voids’) bondline. By inverting the approach, if properties of a perfect/homogeneous material are known a priori, the difference between ‘measured’ and ‘perfect’ properties could be related to size and distribution of voids inside the bondline or along the interface. The effect of the small, ‘invisible’ voids presented is interesting, important and may be a crucial observation. Since it is deemed that real ‘homogeneous’ bondlines are filled with numerous inclusions and macro/micro voids of different origins, the results presented and their interpretation by using simple scaling can potentially lead to the evaluation of effects such as entrapped air or fillers in epoxy adhesives. This may also be of importance in explaining the reasons behind the hierarchical, discontinuous structure of the gecko’s feet. The model can also be used for designing an interface resulting in a certain, well defined, fracture energy, crack kinetics or similar. Finally, the model can be further extended to account for possible dynamic effects. In the present configuration, these were found to be of minor importance (flexible, damage tolerant bondline).

Acknowledgment

The authors would like to acknowledge the funding from the Innovation Fund Denmark through the MoAd (Molecular Adhesive for Strong and Durable Bonding of Rubber to Metal Surfaces) project.

Appendix A. Homogeneous model

A model for a homogeneous adhesive joint is derived based on the models proposed by Kanninen (1973) and Penado (1993).

The model is based on a cantilever beam representing the unbonded part of the specimen and a beam on an elastic foundation representing the bonded part, see Fig. A.15. The simplest theories are used, hence the beams are modeled using Euler–Bernoulli beam theory and the foundation is modeled as a Winkler foundation.

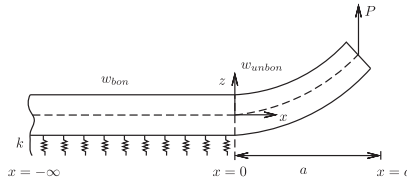


Fig. A15. Kanninen model of a homogeneous adhesive joint for fracture testing. The model comprises a cantilever beam representing the unbonded part and a beam on elastic foundation representing the bonded part. The crack tip is located at $x = 0$.

The displacement free part of the cantilever beam is given by

$$w_{unbon} = \frac{1}{6}A_1x^3 + \frac{1}{2}B_1x^2 + C_1 + D_1 \tag{A.1}$$

where A, B, C and D are constants of integration, which are determined through boundary and continuity conditions. The cantilever is tip loaded with a concentrated force, which provides the following boundary conditions

$$w'_{unbon} = 0 \text{ and } w''_{unbon} = -\frac{P}{EI} \text{ at } x = a \tag{A.2}$$

where the prime notation indicates differentiation with respect to x , E is Young’s modulus and I is the area moment of inertia. With the boundary conditions, the following constants are identified as

$$A_1 = -\frac{P}{EI} \tag{A.3}$$

$$B_1 = \frac{Pa}{EI} \tag{A.4}$$

The bonded part of the beam is modeled as an Euler–Bernoulli beam on a Winkler foundation as mentioned before. Full solution is in the form of

$$w_{bon} = e^{-\lambda x}(A_2 \cos(\lambda x) + B_2 \sin(\lambda x)) + e^{\lambda x}(C_2 \cos(\lambda x) + D_2 \sin(\lambda x)) \tag{A.5}$$

where λ is a constant based on the geometric and material properties of the beam and the adhesive assuming plane stress conditions. It is defined as

$$\lambda = \sqrt[4]{\frac{k}{4EI}} \text{ where } k = \left(\frac{E_{adhes}}{t_{adhes}}\right)b \tag{A.6}$$

where E_{adhes} is the elasticity of the adhesive, t_{adhes} is the thickness of it and b is the width of the specimen. Assuming that the model is semi-infinite in the negative direction and that this end is unaffected by the loading the following constants are determined as

$$A_2 = 0 \text{ and } B_2 = 0 \tag{A.7}$$

The remaining constants are determined through the continuity between the bonded and the unbonded part, which are stated as

$$w_{un} = w_{bond} \text{ at } x = 0 \tag{A.8}$$

$$w'_{un} = w'_{bond} \text{ at } x = 0 \tag{A.9}$$

$$w''_{un} = w''_{bond} \text{ at } x = 0 \tag{A.10}$$

$$w'''_{un} = w'''_{bond} \text{ at } x = 0 \tag{A.11}$$

where the primes indicate differentiation with respect to the spatial coordinate x . Since the foundation acts as a distributed load and the unbonded part is only loaded through a concentrated load, no continuity of the fourth derivative exists.

Using the four continuity equations, the remaining constants are found to be

$$C_1 = \frac{1}{2} \frac{1}{\lambda^2} \left(\frac{P}{EI} + \frac{\lambda Pa}{EI} \right) + 1/2 \frac{Pa}{\lambda EI} \quad (\text{A.12})$$

$$D_1 = \frac{1}{2} \frac{1}{\lambda^3} \left(\frac{P}{EI} + \frac{\lambda Pa}{EI} \right) \quad (\text{A.13})$$

$$C_2 = \frac{1}{2} \frac{1}{\lambda^3} \left(\frac{P}{EI} + \frac{\lambda Pa}{EI} \right) \quad (\text{A.14})$$

$$D_2 = \frac{1}{2} \frac{Pa}{EI\lambda^2} \quad (\text{A.15})$$

Inserting the six constants, Eqs. (A.3), (A.7), (A.12), (A.13), (A.14) and (A.15) into the governing Eqs. (A.1) and (A.5) provides the equations for the model, which yields

$$w(x) = \frac{P}{6EI\lambda^3} \begin{cases} (3a\lambda^3x^2 - \lambda^3x^3 + 6a\lambda^2x + 3\lambda a + 3\lambda x + 3) & 0 \leq x \leq a \\ 3e^{\lambda x}(\cos(\lambda x)a\lambda + a \sin(\lambda x)\lambda + \cos(\lambda x)) & -\infty \leq x \leq 0 \end{cases} \quad (\text{A.16})$$

To obtain an expression for the fracture toughness, the strain energy release rate is determined using the compliance method (Krenk, 1991). First, the compliance is determined as the crack opening, Δ , which, in this case, is the double displacement at the crack tip divided by the applied load, P . The crack opening is determined to be

$$\Delta = w_{unbond} \Big|_{x=a} = \frac{1}{3} \frac{Pa^3}{EI} + \frac{a}{2} \frac{1}{\lambda^2} \left(\frac{P}{EI} + \frac{\lambda Pa}{EI} \right) + 1/2 \frac{Pa^2}{\lambda EI} + 1/2 \frac{1}{\lambda^3} \left(\frac{P}{EI} + \frac{\lambda Pa}{EI} \right) \quad (\text{A.17})$$

The compliance of the model, C , is then calculated as Eq. (A.17) divided by the applied force, P , hence

$$C = \frac{\Delta}{P} = \frac{1}{6} \frac{2a^3\lambda^3 + 6a^2\lambda^2 + 6\lambda a + 3}{EI\lambda^3} \quad (\text{A.18})$$

The strain energy release rate, G , is then calculated using the compliance. The strain energy release rate yields

$$\mathcal{G} = \frac{P^2}{2b} \frac{dC}{da} = \frac{1}{2} \frac{P^2(a^2\lambda^2 + 2\lambda a + 1)}{\lambda^2 EI b} \quad (\text{A.19})$$

The strain energy release rate found in Eq. (A.19) is derived based on a force controlled test setup, which is the reason why the applied force is present. Both Δ and P are related through (A.18) and can be easily interchanged.

References

- Arenas, J.M., Narbón, J.J., Alía, C., 2010. Optimum adhesive thickness in structural adhesives joints using statistical techniques based on weibull distribution. *Int. J. Adhes. Adhes.* 30 (3), 160–165.
- Bertoldi, K., Bironi, D., Drugan, W., 2007. Structural interfaces in linear elasticity, part I: nonlocality and gradient approximations. *J. Mech. Phys. Solids* 55 (1), 1–34.
- Blackman, B.R., Hadavinia, H., Kinloch, A., Paraschi, M., Williams, J., 2003. The calculation of adhesive fracture energies in mode I: revisiting the tapered double cantilever beam (TDCB) test. *Eng. Fract. Mech.* 70 (2), 233–248.
- Bresson, G., Jumel, J., Shanahan, M.E., Serin, P., 2013. Statistical aspects of the mechanical behaviour of a paste adhesive. *Int. J. Adhes. Adhes.* 40, 70–79.
- Budzik, M., Jumel, J., Shanahan, M., 2011. Formation and growth of the crack in bonded joints under mode I fracture: substrate deflection at crack vicinity. *J. Adhes.* 87 (10), 967–988.
- Budzik, M.K., Jumel, J., Shanahan, M.E., 2012. Impact of interface heterogeneity on joint fracture. *J. Adhes.* 88 (11–12), 885–902.
- Budzik, M.K., Jumel, J., Shanahan, M.E., 2013. Adhesive fracture of heterogeneous interfaces. *Philos. Mag.* 93 (19), 2413–2427.
- Chester, R., Roberts, J., 1989. Void minimization in adhesive joints. *Int. J. Adhes. Adhes.* 9 (3), 129–138.
- Cognard, J., 1986. The mechanics of the wedge test. *J. Adhes.* 20 (1), 1–13.
- Cuminato, C., Parry, G., Braccini, M., 2015. A model for patterned interfaces debonding – application to adhesion tests. *Int. J. Solids Struct.* 75, 122–133.
- Espinosa, H.D., Juster, A.L., Latourte, F.J., Loh, O.Y., Gregoire, D., Zavattieri, P.D., 2011. Tablet-level origin of toughening in abalone shells and translation to synthetic composite materials. *Nat. Commun.* 2, 173.
- Fernlund, G., Speltz, J., 1991. Analytical method for calculating adhesive joint fracture parameters. *Eng. Fract. Mech.* 40 (1), 119–132.
- Fitton, M., Broughton, J., 2005. Variable modulus adhesives: an approach to optimised joint performance. *Int. J. Adhes. Adhes.* 25 (4), 329–336.
- Gillies, A.G., Henry, A., Lin, H., Ren, A., Shiu, K., Fearing, R.S., Full, R.J., 2014. Gecko toe and lamellar shear adhesion on macroscopic, engineered rough surfaces. *J. Exp. Biol.* 217 (2), 283–289.
- Griffith, A.A., 1921. The phenomena of rupture and flow in solids. *Philos. Trans. R. Soc. Lond. Ser. A Contain. Pap. Math. Phys. Character* 221, 163–198.
- Irwin, G.R., Kies, J., 1997. Critical energy rate analysis of fracture strength. *SPIE Milest. Ser.* 137, 136–141.
- Jackson, A., Vincent, J., Turner, R., 1988. The mechanical design of nacre. *Proc. R. Soc. Lond. B: Biol. Sci.* 234 (1277), 415–440.
- Jumel, J., 2017. Crack propagation along interface having randomly fluctuating mechanical properties during DCB test finite difference implementation—evaluation of GC distribution with effective crack length technique. *Compos. Part B: Eng.* 116, 253–265.
- Jumel, J., Budzik, M.K., Shanahan, M.E., 2011. Process zone in the single cantilever beam under transverse loading: part I: theoretical analysis. *Theor. Appl. Fract. Mech.* 56 (1), 7–12.
- Kanninen, M., 1973. An augmented double cantilever beam model for studying crack propagation and arrest. *Int. J. Fract.* 9 (1), 83–92.
- Kendall, K., 1975a. Control of cracks by interfaces in composites. In: *Proceedings of the Royal Society of London A: Mathematical, Physical and Engineering Sciences*, 341. The Royal Society, pp. 409–428.
- Kendall, K., 1975b. Transition between cohesive and interfacial failure in a laminate. In: *Proceedings of the Royal Society of London A: Mathematical, Physical and Engineering Sciences*, 344. The Royal Society, pp. 287–302.
- Kim, H., 2003. The influence of adhesive bondline thickness imperfections on stresses in composite joints. *J. Adhes.* 79 (7), 621–642.
- Krenk, S., 1991. Energy Release Rate of Adhesive Joints. University Aalborg, Department of Building Technology and Structural Engineering, Aalborg.
- Kwak, J.-S., Kim, T.-W., 2010. A review of adhesion and friction models for gecko feet. *Int. J. Precis. Eng. Manuf.* 11 (1), 171–186.
- Matouš, K., Kulkarni, M.G., Geubelle, P.H., 2008. Multiscale cohesive failure modeling of heterogeneous adhesives. *J. Mech. Phys. Solids* 56 (4), 1511–1533.
- Niklaus, F., Eriksson, P., Kalvesten, E., Stemme, G., 2000. Void-free full wafer adhesive bonding. In: *Proceedings of the Thirteenth Annual International Conference on Micro Electro Mechanical Systems (MEMS 2000)*. IEEE, pp. 247–252.
- Olia, M., Rossettos, J., 1996. Analysis of adhesively bonded joints with gaps subjected to bending. *Int. J. Solids Struct.* 33 (18), 2681–2693.
- Pardon, T., Ferracin, T., Landis, C., Delannay, F., 2005. Constraint effects in adhesive joint fracture. *J. Mech. Phys. Solids* 53 (9), 1951–1983.
- Pasternak, P., 1954. On a new method of analysis of an elastic foundation by means of two foundation constants. *Gos. Izd. Lit. Stroit. Arkhitekture. Moscow*.
- Patinet, S., Vandembroucq, D., Roux, S., 2013. Quantitative prediction of effective toughness at random heterogeneous interfaces. *Phys. Rev. Lett.* 110 (16), 165507.
- Pearce, F., Arnott, D., Camilleri, A., Kindermann, M., Mathys, G., Wilson, A., 1998. Cause and effect of void formation during vacuum bag curing of epoxy film adhesives. *J. Adhes. Sci. Technol.* 12 (6), 567–584.
- Penado, F., 1993. A closed form solution for the energy release rate of the double cantilever beam specimen with an adhesive layer. *J. Compos. Mater.* 27 (4), 383–407.
- da Silva, L.F., Lopes, M.J.A.C., 2009. Joint strength optimization by the mixed-adhesive technique. *Int. J. Adhes. Adhes.* 29 (5), 509–514.
- Spiering, V.L., Berenschot, J., Elwenspoek, M., Fluitman, J.H., 1995. Sacrificial wafer bonding for planarization after very deep etching. *J. Microelectromech. Syst.* 4 (3), 151–157.
- Towse, A., Potter, K., Wisnom, M., Adams, R., 1999. The sensitivity of a weibull failure criterion to singularity strength and local geometry variations. *Int. J. Adhes. Adhes.* 19 (1), 71–82.
- Tsai, M.Y., Oplinger, D.W., Morton, J., 1998. Improved theoretical solutions for adhesive lap joints. *Int. J. Solids Struct.* 35 (12), 1163–1185.
- Van Straalen, I.J., Wardenier, J., Vogeleesang, L., Soetens, F., 1998. Structural adhesive bonded joints in engineering—drafting design rules. *Int. J. Adhes. Adhes.* 18 (1), 41–49.
- Voigt, W., 1889. Ueber die beziehung zwischen den beiden elasticitätsconstanten isotroper körper. *Ann. Phys.* 274 (12), 573–587.
- Weibull, W., 1951. Wide applicability. *J. Appl. Mech.* 103, 293–297.
- Winkler, E., 1867. *Theory of elasticity and strength*. DominicusPrague, Czechoslovakia.

S. Heide-Jørgensen, M.K. Budzik/*International Journal of Solids and Structures* 120 (2017) 278–291

291

- Xia, S., Ponso, L., Ravichandran, G., Bhattacharya, K., 2012. Toughening and asymmetry in peeling of heterogeneous adhesives. *Phys. Rev. Lett.* 108 (19), 196101.
- Xia, S., Ponso, L., Ravichandran, G., Bhattacharya, K., 2013. Adhesion of heterogeneous thin films-I: elastic heterogeneity. *J. Mech. Phys. Solids* 61 (3), 838–851.
- Xia, S., Ponso, L., Ravichandran, G., Bhattacharya, K., 2015. Adhesion of heterogeneous thin films II: adhesive heterogeneity. *J. Mech. Phys. Solids* 83, 88–103.
- Yamada, S.E., 1987. Elastic/plastic fracture analysis for bonded joints. *Eng. Fract. Mech.* 27 (3), 315–328.

Chapter 4

Paper 3 - On Bondline Discontinuities and Kinetic Effects

Effects of bondline discontinuity during growth of interface cracks including stability and kinetic considerations³

4.1 Introduction

Motivated by the findings in the previous paper this contribution explores into structured interfaces with a single zone of weak adhesion. The focus is on crack propagation stability and kinetics of the joint. In specific, the crack growth velocity before and after the weak zone and how they affect ERR are studied

4.2 Method

DCB fracture tests are conducted on specimens to obtain the material fracture properties and get a baseline. Then a second series of experiments are performed on DCB specimens with interfacial heterogeneities in terms of a single band of low adhesion, referred to as the defect, running perpendicular to crack growth direction. The size of the defect is systematically increased from a fraction of the elastic process zone size to almost twice its size. These experiments are used to study how a single defect in the

bondline effects the joint performance. Special attention is paid to the load response and to the ERR.

To explain the phenomena observed experimentally the unit pattern model developed in the previous paper is extended to contain four parts: 1) loading arm, 2) 1st bonded zone, 3) defect zone, 4) 2nd bonded zone. The extension obviates the need for semi-analytical treatment.

As a further extension and to be able to quantify the effects of loading rate and crack velocity Griffith's generalized theory with time-dependent loading and displacement is used to obtain a rate form of the ERR. By rate form is meant, that in addition to the crack length and the displacement their derivatives with respect to time are included in the expression as well.

4.3 Contribution

The author contributed with parts of the experimental work: specimen manufacturing, test setup, testing and data treatment, deriving the theoretical model and analytical results, and, manuscript preparation.

4.4 Finding

The main finding of this contribution is that a single discontinuity in the bondline can significantly affect the load response and fracture behavior. The severity of the defect is governed by its size relative to the elastic fracture process zone length: $d\lambda$ and its position. When size ratio $d\lambda > 0.45$ a critical state is attained and the load response is significantly altered. The defect is found to cause the crack to accelerate as it approaches. The larger the defect the larger the acceleration.

The ERR, which is calculated based on the experimental data, is decomposed using the rate form into a static and a kinetic part. The former being the classical expression of critical fracture energy, i.e. assumed to be a material constant, while the latter depends on both the crack growth velocity and the loading rate. The sum of static and the kinetic part constitute the effective ERR, which is the one measured experimentally.

It is found that under the commonly presumed quasi-static condition the kinetic ERR part cannot be neglected. During crack onset the kinetic part causes the effective ERR to be approximately 15% lower than the static part, which is normally used as failure criterion. Hence, neglecting the kinetic could potentially results in a conservative estimation of the critical

fracture energy. As the crack starts to propagate the contribution from the kinetic part diminishes and the resistance against crack growth increases. This could explain the commonly observed rise in the R-curve during DCB tests.

4.5 Reflection

The results show that regions of weak adhesion can cause an acceleration of the crack as it approaches. The larger the region, the larger the acceleration. It is believed to be facilitated by a decrease in the R-curve caused by the elastic process zone reaching the weak adhesion and, similarly, to the previous paper reducing the apparent critical fracture energy.

It could be interesting to explore deeper into the rate form of the ERR and investigate the impact of loading rates, especially, in relation to the quasi-static assumption. It might be beneficial to design tests based on the rate form model to either minimizing or maximize the kinetic effects.



Contents lists available at ScienceDirect

Journal of the Mechanics and Physics of Solids

journal homepage: www.elsevier.com/locate/jmps

Effects of bondline discontinuity during growth of interface cracks including stability and kinetic considerations

Simon Heide-Jørgensen, Michal K. Budzik*

Aarhus University, Dept. Engineering, Inge Lehmanns Gade 10, 8000, Aarhus C, Denmark



ARTICLE INFO

Article history:

Received 18 July 2017

Revised 5 April 2018

Accepted 7 April 2018

Available online 12 April 2018

Keywords:

Crack growth rate

DCB

Discontinuity

Interface

 R curve

Stability

ABSTRACT

The effects of a single discontinuity/void on the mode I interface crack growth under a constant loading rate are investigated experimentally and analytically. To account for a co-existence of the void and the crack tip process zone, a new unit pattern model is derived. The crack growth path is composed from the three distinctive zones: (1) The initially bonded crack front vicinity region—carrying the majority of the loading—is of finite length and modelled as a series of elastic springs. (2) The discontinuity region is modelled as a simple beam not carrying any surface tractions. (3) The far field is of infinite length and represented with elastic springs. In this model, the constant loading rate boundary conditions are fully considered. Subsequently, the kinetic effects associated with the specimen geometry and the presence of the discontinuity are attempted using the generalized Griffith's theory. A very good agreement between the experimental and the analytical results is observed for both the load response and the R curves for all void-to-process zone length ratios. A new light and a more profound appraisal of the equilibrium paths are gained.

© 2018 Elsevier Ltd. All rights reserved.

1. Introduction

For layered materials reliability under mechanical loading constitute an important technical problem. Controlling material properties and structural response through design of their interfaces could be an interesting approach to address the problem and an important step towards fracture metamaterials. For example, in bonded joints and laminated composites structural response could be tuned to a desired behaviour, properties or damage tolerance. This, however, demands introduction of heterogeneities along the crack growth path. Heterogeneities are an inevitable part of layered materials and could be associated with one of the following groups: (1) 'Extrinsic' - associated with the geometry of the joint and materials used, and leading to stress gradients and stress singularities due to the presence of edges and corners (Adams and Peppiatt, 1974; Bogy, 1968; Dundurs, 1969; Goland and Reissner, 1944; Hart-Smith, 1973; Jensen, 2003; Reedy, 1993, 1990; Volkersen, 1938; Weißgraeber et al., 2016; Williams, 1952). (2) 'Intrinsic' - associated with the microscopic features of the materials such as chemical and physical variations in composition of the bondline and the adherends (das Neves et al., 2009; Sancaktar and Kumar, 2000). (3) Interfacial-related to the quality of the surfaces of the materials to be joined, e.g. unwanted technological flaws, remaining by-products, oils, dust or water, but also release films and kissing bonds (Hong and Boerio, 2007; Lengline et al., 2011; Olia and Rossettos, 1996). However, the variation in the surface properties could be introduced 'on demand', e.g. to fine tune properties like the fracture energy (Alfano et al., 2014; Budzik et al., 2013; Cuminatto et al., 2015; Davami et al., 2016; Xia et al., 2012).

* Corresponding author.

E-mail address: mibu@eng.au.dk (M.K. Budzik).

The presence of flaws and heterogeneities, including their location and size, affects the observed strength of the joint and the crack path (Cao and Evans, 1989) with the onset and the evolution of crack propagation being of central importance for assessment of failure and crucial to address reliability issues. A methodology frequently adopted to consider heterogeneities is based on statistical analysis of their effects (Bazant and Pang, 2006; Bresson et al., 2013; Towse et al., 1999). To extract the effective properties of a material containing flaws, a representative volume element modelling or homogenization and rules-of-mixtures techniques are used (Budzik et al., 2013; Eshelby, 1957; Gao and Rice, 1989; Mori and Tanaka, 1973). On the crack front scale, analyses based on perturbation theory as proposed by Rice (Gao and Rice, 1989) are used to explore crack front trapping phenomena (Mower and Argon, 1995). In the direct approach, the local crack front morphology is assessed (Budzik and Jensen, 2014; Chopin et al., 2011; Patinet et al., 2011; Patinet et al., 2014). Provided that the crack front morphology is known, through an inversed method, estimation of the resultant fracture toughness is possible (Dalmás et al., 2009). Considering the problem as an out-of-the-plane i.e. the plane perpendicular to the crack growth plane (or simply, as seen from the side of the fracture specimen), crack growth paths are deduced (Akisanya and Fleck, 1992).

The effect of locally varying surface adhesion has been analysed experimentally, analytically and numerically (Cuminatto et al., 2015; Jumel, 2017; Razavi et al., 2017). Recently, two closed-form analytical solutions were proposed, both using unit pattern models (Cuminatto et al., 2015; Heide-Jørgensen and Budzik, 2017). The strain energy release rate (ERR, \mathcal{G}) was elucidated for a joint containing a single and multiple discontinuities. The local variation in the surface energy along the crack growth path must affect the kinetics of the crack growth process. Effects of the induced unstable or non-smooth crack growth processes were not addressed arising some concerns. From one side, the bondline materials are frequently polymer based. A rate-dependence analysis of such materials shows that the stress at failure $\sigma \propto \dot{\epsilon}^{1/n}$, where $\dot{\epsilon}$ is the deformation rate and n is the hardening exponent (Arruda et al., 1995). In Landis et al. (2000) a competition between the strain rate hardening and the rate strengthening within the fracture process zone, arising from the increased crack velocity, was identified. In Blackman et al. (2012) the authors confirmed, experimentally and numerically, the dependence between \mathcal{G} , σ and $\dot{\epsilon}$. The effects of material rate dependence could be negligible under quasi-static conditions and are not expected unless $\dot{\epsilon}$ varies across few orders of magnitude. More importantly for the present study, according to the generalized Griffith's theory (Davidson and Waas, 2012; Griffith, 1921), the crack growth and the observed material resistance are governed by the critical fracture stress ('static' component) and a ratio between the loading and crack growth rates ('kinetic' part). The ERR is an outcome of these and as such the non-constant (rising or falling) R curve behaviour could be explained without taking into account the rate dependence of the materials. An efficient interface design tool can clearly benefit from taking the crack front and the loading kinetics into consideration.

In the present work, the effects of a single discontinuity/void introduced along the crack growth path during the mode I fracture experiment are analysed analytically and experimentally. The size of the discontinuity is systematically varied across different void-to-(crack front) process zone size ratios. It is found that the presence of the discontinuity, including the size and the position within the process zone, is manifested by undulations in the load response and the resistance curves. The otherwise steady-state crack growth is altered. This work aims to identify the phenomena and the length scales involved. The paper is structured as follows. At first, the experimental details including materials and methods are provided followed by a steady-state analysis of the fracture experiment. To gain a phenomenological and a quantitative insight, a new unit pattern model is proposed for analysis. Contrary to the previous work of the authors (Heide-Jørgensen and Budzik, 2017), using a reconstituted unit pattern model, the effect of the finite length of the bonded/contact zones and behaviour of the crack front in the vicinity of the void are studied in details. This enables a correct representation of the effects introduced by the constant displacement rate and the constant displacement boundary conditions including the snap-down behaviour in the load response curve. Fracture results are summarized and discussed within the framework of static analysis. For full comprehension, the double cantilever beam (DCB) test is further revised using the generalized Griffith's fracture theory to capture the effects of the loading and the crack growth rates. The accent is on the effects of a single void on the loading curve and the R curve for which a detailed theoretical discussion is proposed. Finally, remarks and conclusions are listed.

2. Materials and methods

The major part of the experimental work is performed under fracture mode I loading conditions. Displacement controlled experiments are conducted on adhesively bonded DCB specimens, half of the specimen being schematically shown in Fig. 1, to investigate the load response and the phenomena associated with interactions between the crack front and the vicinity of discontinuity.

2.1. Materials and preparation of specimens

Two transparent brittle PMMA (polymethyl methacrylate, supplied by Bayer®, Germany) adherends of width, $b \cong 25$ mm, thickness, $h \cong 8$ mm and Young's modulus, E , of 3.2 ± 0.3 GPa (estimated from a series of three point bending experiments) were bonded using a commercial acrylic adhesive (Bostik, Germany). The bondline material (Young's modulus E_b of ca. 0.5 MPa) was checked, by hysteresis loop testing, and found not to expose any significant irreversibility until failure under a tensile loading while maintaining a linear loading path.

Prior to bonding the PMMA adherends were sandblasted (aluminium oxide with average 100 μ m diameter), cleaned in an ultrasonic bath (water-isopropyl solution, at 35 kHz for 5 min) and rinsed in ethanol to remove any residues. Ten of the

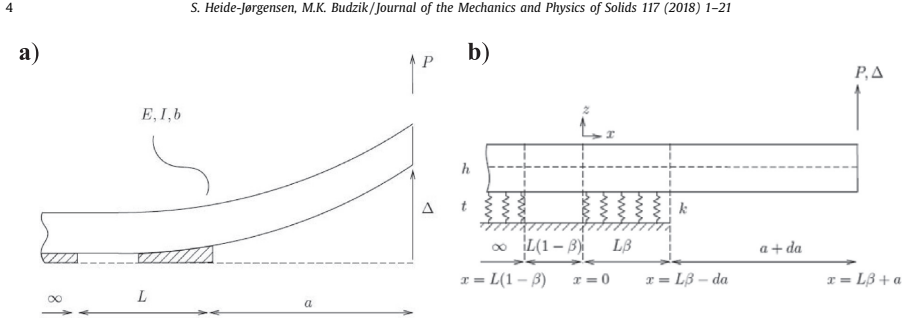


Fig. 2. (a) Schematic of the heterogeneous model. (b) Geometry and loading conditions for the model: a is the initial crack length, L is the length of the first unit pattern (one band of adhesive and one band of void), β is the ratio between the adhesive and void and da is the crack growth.

thus $C \equiv C_s$. Substituting C to Eqs. (1) to (2) yields:

$$G_I = 3 \frac{P}{bh} \sqrt[3]{\frac{P\Delta^2}{2bE}} \quad (3)$$

At fracture, the driving force equals the fracture energy, $G_I = G_{Ic}$, and the crack begins to grow. The linear relation between P and Δ , i.e. Eq. (1) bifurcates into a nonlinear one given by:

$$P = \gamma \Delta^{-1/2} \quad (4)$$

with $\gamma = 2b \sqrt[4]{\frac{h^3}{6} E G_{Ic}^{3/4}}$ where G_{Ic} is assumed constant during the steady-state propagation. Note, that the dimensional analysis of Eq. (4) leads to an insightful unit: $[\gamma] = N\sqrt{m} = J/\sqrt{m}$. Similarity to the stress intensity factor units is appealing and, effectively, γ can be treated as the fracture energy factor even though the physical interpretation is rather different. The present section will be treated as the basis for the experimental data reduction.

3. Unit pattern model of stick-slip crack growth

Following the experimental configuration an analytical model of the DCB specimen with a discontinuous, heterogeneous bondline is proposed. The physical model, shown in Fig. 2, comprises four parts: The loaded arm, the first bonded area, the (channelling through the width) void, and, finally, the second bonded area. The bondline, which is marked by the hatched areas, has a thickness of $2t$ and contains a void channelling perpendicular to the crack growth direction making it discontinuous and heterogeneous. The specimen is tip loaded by either a prescribed force, P , or by a prescribed displacement, 2Δ . The primary focus is on the two bonded zones and the intermediate band of the void. The unit pattern, comprising a band of void and a band of adhesive, is defined by the length L and the initial crack length a . To obtain a closed-form analytical solution and a phenomenological description of the crack growth process, the Euler-Bernoulli beam on the Winkler elastic foundation model is used.

3.1. Loading arm

The free part spans from the loading point, $x = L\beta + a$, to the crack tip, $x = L\beta - da$, and is modelled as a cantilever beam. At the crack tip the continuity requirements, up to C^3 , are held. The governing equation for the part is:

$$\frac{d^2w}{dx^2} = \frac{(\beta L + a - x)P}{EI} \quad (5)$$

where w is the vertical deflection of the beam along its neutral axis and β is the adhesive-to-void ratio.

3.2. First bonded zone

The bonded zone is represented by the Euler-Bernoulli beam on the Winkler elastic foundation (Hetenyi, 1979). The Winkler formulation is preferred over a more general one (e.g. Wieghardt's (Kerr, 1964)) and allows elastic loading and quasi-brittle crack growth to be analysed. The bonded zone is formulated from $x = 0$ to $x = L\beta - da$ and experiences length reduction during the crack growth - da . In the absence of the axial loading the differential governing equation for this part is:

$$\frac{d^4w}{dx^4} + 4\lambda^4 w = 0 \quad (6)$$

where $\lambda = \sqrt[4]{\frac{k}{4EI}}$ is the wave number, an inverse of which defines the process zone length. $k = m(\frac{E_p}{l})b$ is the foundation modulus describing the stiffness of the springs and is calculated based on the geometry and the material parameters of the adhesive. Constant m allows for arbitrary formulation of the stress/strain state at the crack tip (Cabello et al., 2016b). Assuming plane strain conditions $\lambda^{-1} \cong 23$ mm (details of λ^{-1} evaluation could be found in Appendix A). The elastic fracture process zone is deliberately extensive, i.e. $h\lambda < 1$, allowing for an (technically) easy and a systematic variation of the $d\lambda$ product. The first bonded zone is of length $> \lambda^{-1}$ (but $\leq 2\lambda^{-1}$), which is important due to the oscillating character of the solution to Eq. (6) and expected finite length effects (Kanninen, 1974). For further generalization, an elastic-plastic or a damage formulation could be also considered. This leads to a further complexity introducing a material driven softening and altering the chance of obtaining the exact analytical solution. In the present case such models of interfaces are unnecessary since the bondline is not dissipating the energy otherwise than through fracture. Moreover, the focus is on the expected geometrically induced structural softening due to the reduction of the load carrying area. Eq. (6) can be written in terms of the opening cohesive stress within the bondline, $\sigma(x)$. Then:

$$EI \frac{d^4 w}{dx^4} + b\sigma(x) = 0 \quad (7)$$

and the relation between the length scale parameter λ^{-1} and the cohesive stress becomes evident. The solution to the governing equation requires, as previously, C^3 conditions at the crack tip.

3.3. Discontinuity region

The discontinuity region is modelled by the Euler-Bernoulli beam, viz.:

$$EI \frac{d^4 w}{dx^4} = 0 \quad (8)$$

The length of the zone, associated to the length of the unit pattern and the adhesive-to-void ratio, spans from $x = 0$ to $x = L(\beta - 1)$. For the solution the boundary conditions are given as continuity with the surrounding parts.

3.4. Second bonded zone

The last zone is modelled similarly to the first bridging zone using:

$$\frac{d^4 w}{dx^4} + 4\lambda^4 w = 0 \quad (9)$$

Contrary to the first bridging zone, the second zone spans from $x = L(\beta - 1)$ to the far field, $x = -\infty$. The boundary value problem consists of the C^3 continuity with the unbonded part and the far field, which is assumed to be unloaded as $x \rightarrow -\infty$. The far field assumption can be justified by the fact, that the second bonded part of the specimens spreads over min. 65 mm $> 2\lambda^{-1}$.

3.5. Coupling

Obtaining the solution for each of the governing equations give the full description of the unit pattern model:

$$w(x, \beta) = \begin{cases} \frac{P(\frac{1}{2}L\beta x^2 + \frac{1}{2}ax^2 - \frac{1}{6}x^3)}{EI} + A_1 x + B_1 & \forall L\beta - da \leq x \leq L\beta + a \\ \cosh(\lambda x)(A_2 \cos(\lambda x) + B_2 \sin(\lambda x)) \\ + \sinh(\lambda x)(C_2 \cos(\lambda x) + D_2 \sin(\lambda x)) & \forall 0 \leq x \leq L\beta - da \\ \frac{1}{6}A_3 x^3 + \frac{1}{2}B_3 x^2 + C_3 x + D_3 & \forall L(\beta - 1) \leq x \leq 0 \\ e^{\lambda x}(C_4 \cos(\lambda x) + D_4 \sin(\lambda x)) & \forall -\infty \leq x \leq L(\beta - 1) \end{cases} \quad (10)$$

where $A_1, A_2, A_3, A_4, B_1, B_2, B_3, C_2, C_3, C_4, D_2, D_3, D_4$ are unknown constants to be determined through the boundary conditions stated earlier. Importantly, in the far field the solution experiences exponentially modulated decay, while within the zone of the finite length ($\cong 2\lambda^{-1}$) exponential growth toward the ends could be expected.

3.6. Crack growth

Previously described the Irwin-Kies method cf. Eq. (2) is used to evaluate the ERR. The compliance is obtained from Eq. (10) setting $w(x = L\beta + a) = \Delta$ (alternatively $\frac{\partial^3 w}{\partial x^3}(x = L\beta + a) = \frac{P}{EI}$ condition could be used for the force controlled conditions). As the crack begins to propagate the loading arm increases while the first bonded region decreases. Both effects contributes to the evaluated ERR, which effectively equates to $\mathcal{G}_I = \frac{1}{2} \frac{P^2}{b} (\frac{\partial C}{\partial a} - \frac{\partial C}{\partial(L\beta)})$. For the crack onset and steady-state

6

S. Heide-Jørgensen, M.K. Budzik / Journal of the Mechanics and Physics of Solids 117 (2018) 1–21

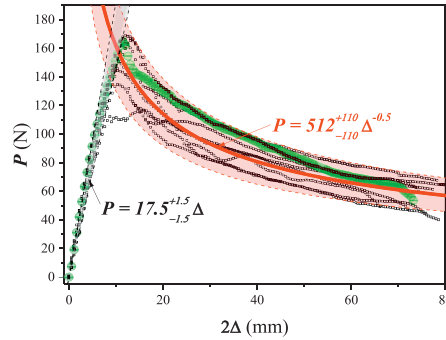


Fig. 3. The load response recorded during testing of the specimen without discontinuities. The dashed lines, and the corresponding shaded area between, indicate 99% confidence bounds for both, the loading and the crack growth stages.

growth a Griffith's type fracture criterion is implemented, i.e. the crack onsets and propagates under the assumption of the ERR being equal to the fracture energy:

$$\mathcal{G}_I = \mathcal{G}_{Ic} = \text{const.} \quad (11)$$

Value of \mathcal{G}_I is evaluated from Eq. (2) following an iterative crack growth routine implemented through a MATLAB (MATLAB R2016, MathWorks®, USA) script.

4. Interpretation of experimental results using static analysis

We begin by presenting results interpreted via the static models outlined in Sections 2.3 and 3. In specific, the experimentally recorded load response data and the evaluated driving forces and resistance curves are of interest.

4.1. Load response

In Fig. 3 test results corresponding to the ten DCB specimens without void are shown. The qualitative and the quantitative reproducibility appear very good. This is further supported by the post-mortem inspection of the fracture surfaces in which all the crack growth paths are found within the bondline layer.

The normal behaviour of the load response is observed. The initial, linear loading path bifurcates to a monotonic, positive value, negative slope steady-state crack growth path. The analytical data, obtained using Eq. (4) for the crack growth and Eq. (1) for the loading path, including 99% confidence bounds, are also plotted. Agreement between the analytical and experimental results seems very good. This applies when the data are treated as a population with the common mean value. However, a closer look into the behaviour on each of experimental curves (one of which is highlighted in Fig. 3) reveals an interesting feature. Once using the crack initiation value to find the mean curve for the entire population, such would remain closer to the lower bound in Fig. 3. Setting this observation aside, the loading path is sufficiently well described assuming the elastic bondline model and neglecting the effect of the through-the-thickness restraining of the adherends (Kanninen, 1973). This is further confirmed by the rather sharp transition at the expected bifurcation point (intersection between the loading $C(a)$ and crack growth $C(a, \mathcal{G}_{Ic} = \text{const.})$ paths).

In Fig. 4 (a–f) are presented the experimental and the analytical data for the bondlines with discontinuities of different sizes d . The size of the void is expressed as a non-dimensional product of $d\lambda$ (the ratio of void length to the process zone length). The analytical results (bold lines) are obtained taking the value of \mathcal{G}_{Ic} evaluated from a single (arbitrary chosen) experiment for each of the specific sizes of the void. A single experimental curve is followed closely by the analytical model with the second one verifying reproducibility of the observed phenomenon. To verify that each of the experiments is representative and reproducible (belongs to the same statistical population as the reference specimens) the confidence bounds (thin, dashed lines) as obtained for the reference specimens are plotted. The agreement between the experimental and the analytical results appears respectable for all the cases studied. For the small sizes of discontinuities: $d\lambda \cong 0.045$ and $d\lambda \cong 0.14$ (i.e. discontinuity size \ll the process zone size), Fig. 4(a) and (b) respectively, the steady-state crack growth path given by Eq. (4) is initially followed. Once the crack tip is affected by the presence of the discontinuity, which should be expected once the distance between the crack front and the void is within the range from λ^{-1} to $2\lambda^{-1}$, the strain localizes within the remaining band of the bonded zone and the applied force P decreases. Additional loading path evaluated by the means of the simple beam theory, Eq. (1), is added for $C(a + L - d - \lambda^{-1}) \cong C_\lambda$. The crack growth becomes unstable

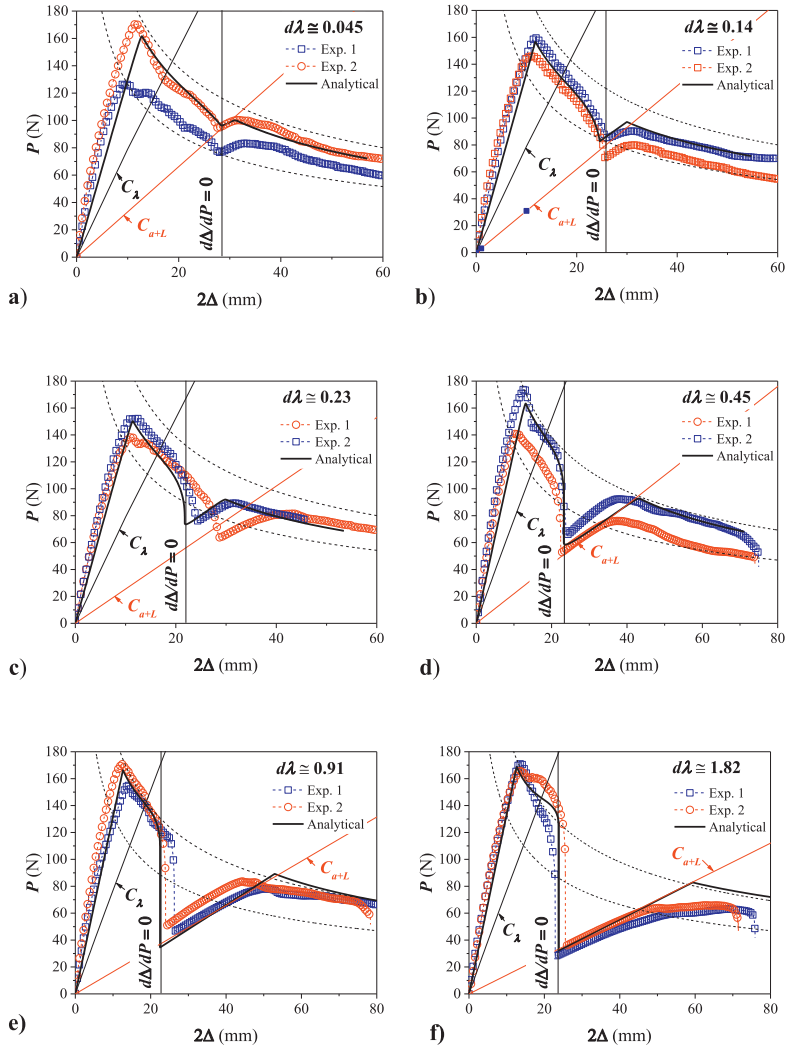


Fig. 4. Load response of the bondlines with different sizes of discontinuity: a) 1 mm, b) 3 mm, c) 5 mm, d) 10 mm, e) 20 mm, f) 40 mm. Analytical and experimental data from two specimens are presented.

(Bazant and Cedolin, 2010) while the critical state is attained once $\frac{d\Delta}{dP} = 0$ (the compliance is used to keep the ‘classical’ notation of the critical state). The associated vertical lines are added to Fig. 4. For the small sizes of ‘voids’ the stability could be easily restored by the presence of the second bonded zone. The secondary loading paths denoted as $C_{a+L} \equiv C(a+L)$, corresponding to the crack arrest position, viz. the end of the void, are added for illustration. For the intermediate sizes, $d\lambda \cong 0.23$ and $d\lambda \cong 0.45$ (i.e. discontinuity size < the process zone size), Fig. 4(c) and (d) respectively, a significant deviation

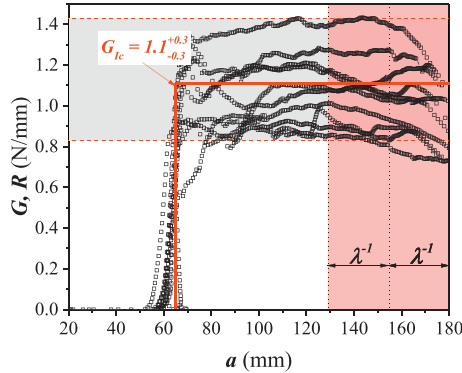


Fig. 5. Driving force and resistance curves obtained using Eq. (3) applied to data for the reference, homogeneous specimens. The red, bold line represents the overall average while the dashed, thin lines represent 99% confidence bounds. (For interpretation of the references to colour in this figure legend, the reader is referred to the web version of this article.)

from the power law relation, Eq. (4), is observed. For the case of $d\lambda \cong 0.45$ the experimental data becomes discontinuous near the critical state. The maximum acquisition rate used to record the data (10 Hz) is no longer sufficient. For the large ‘voids’ $d\lambda \cong 0.91$ and $d\lambda \cong 1.82$ (i.e. discontinuity size \geq the process zone size), Fig. 4(e) and (f) respectively, the discontinuity in the results becomes apparent. The size of the void is long enough to contain the entire process zone and the snap-down phenomena takes place. Subsequently, recovery along the linear loading path, with the new crack arrest position equal to the distance from the applied load to the second bonded zone, begins. The process continues until a new bifurcation point is reached. During the final stage the steady-state crack growth, viz. Eq. (4), is recorded. (For the case depicted in Fig. 4(f), the second bonded zone seems not long enough for a full recovery).

4.2. Driving force and resistance curves

In Fig. 5 are presented the G, R curves of the reference specimens obtained through Eq. (3). The statistical mean value of $G_{Ic} = 1.1$ N/mm is found (the bold, horizontal line) for $80 \leq a \leq 170$ mm consistently with the Griffith’s criterion. As in the case of the load response the 99% confidence bounds estimated are added for completeness.

After the loading, the crack growth process along homogeneous crack path can be characterized as stable. However, the rising R curve behaviour, with small fluctuations, is observed. The G_I increases until the distance between the crack front and the edge of the specimen approaches approx. $\lambda^{-1} - 2\lambda^{-1}$. Additional lines are added to represent the related region. Such effects are not captured by the present analysis, which necessarily predicts a constant value once $G_I = G_{Ic}$, c.f. Eq. (11). Due to the edge effects the R curves begin to descent (this being out of the scope for the present work). Note, that for each of the particular curves the initiation value is roughly 15% below the ‘peak’ value. In Fig. 6 (a–f) are shown the G, R curves for the specimens with bondlines containing discontinuities. The grey rectangle indicates the position and the length d of the void, while the red rectangle defines the distance from the void corresponding to the process zone size λ^{-1} . For clarity, the crack growth process until the crack arrest position is represented schematically using a ‘rolling ball’ example for the two of the characteristic cases.

Until reaching the crack onset threshold the cases depicted by Figs. 6 (a–c) resembles the one from Fig. 5. The experimental data proves a clear trend toward the rising R curve behaviour. From the analytical perspective, a linear, vertical, loading path bifurcates to the horizontal path of the crack growth stage. In contrary, for the remaining three (and specially the last two) cases - Fig. 6 (d–f), the analytical model predicts an increase in the R curve above the bifurcation point. Indeed, the growing crack reduces the length of the first bonded zone while the loading arm increases. The effective stiffness of the foundation is reduced. As a result the ERR increases (Cuminatto et al., 2015). Both, the experimental and the analytical results confirm this to be the case. A subsequent phenomenon observed, $\frac{dG_I}{da} < 0$, could be explained by the interaction between the two characteristic length parameters of the problem at hand. The crack front propagates in the vicinity of the void. For the smallest voids, Fig. 6(a) and (b), the process appears ‘continuous’ though not entirely smooth. A clear local minimum, a (pseudo) saddle point for which, in the present case $\frac{d^2G_I}{da^2} \rightarrow \infty$. The voids are effectively decreasing the load carrying area (Tadepalli et al., 2008a; Tadepalli et al., 2008b) and the regions for which $\frac{dG_I}{da} < 0$ are visible through all the cases (where $G_I \cong G_{Ic} = f(d\lambda)G_{Ic}$ and $f(d\lambda)$ is related to the area carrying the load, viz. fraction of the process zone with an embedded void). The position of the void may turn even more critical since the change of the void position with respect

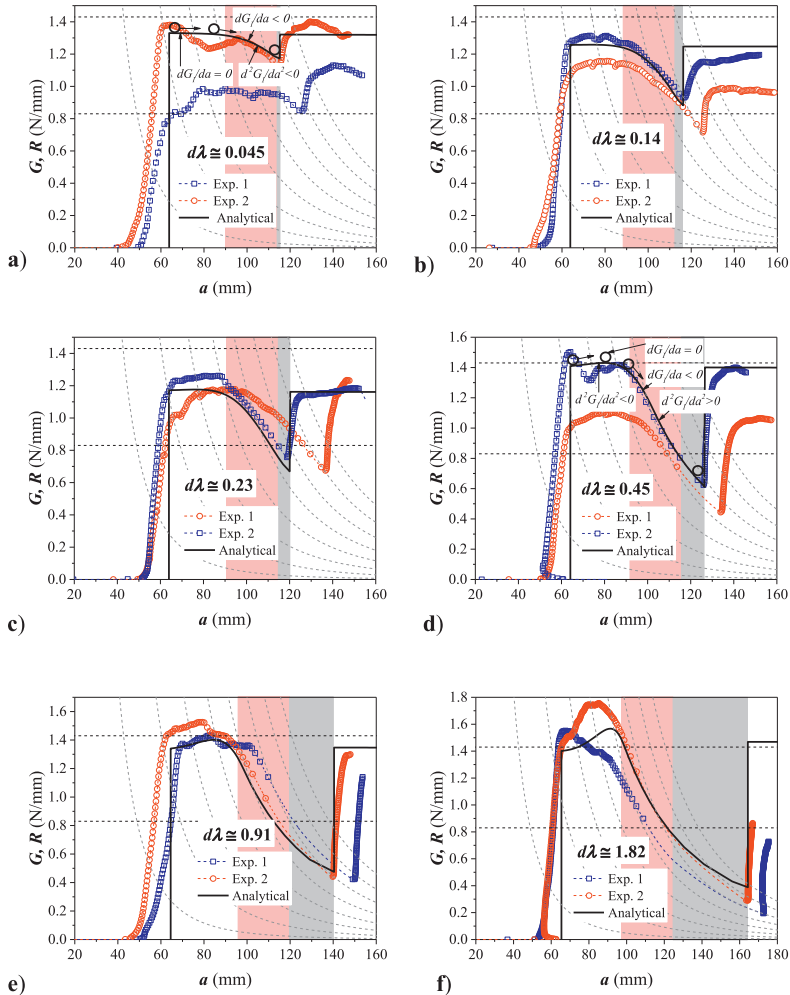


Fig. 6. The driving force, G , and the resistance, R , curves for the specimens with bondlines containing discontinuity, d , of different size: **a)** 1 mm, **b)** 3 mm, **c)** 5 mm, **d)** 10 mm, **e)** 20 mm, **f)** 40 mm. Analytical and experimental data from the two specimens are presented. The grey, shaded, regions correspond to the expected void positions and size while the red, shaded, regions correspond to the size of the process zone λ^{-1} . The grey, dashed lines represent the $G_I(a)$ equilibrium paths at fixed displacement BCs. The dashed, thin lines represent the G_{Ic} (see Fig. 5) 99% confidence bounds. (For interpretation of the references to colour in this figure legend, the reader is referred to the web version of this article.)

to the crack front position, from the far field to the crack tip, leads to an increase in the crack growth rate. The biggest effect (a local minimum of the curves) falls at the instance where the void becomes the crack tip. From the intermediate cases Fig. 6(c) and (d) the experimental results display a discontinuity near the void region. This is further emphasized for the large voids, Fig. 6(e) and (f). The experimental results could not be obtained for the void regions due to the finite rate of data acquisition. However, the trend of $G_I(a)$ is given by the analytical model.

To understand the lack of the snap-down behaviour and the non-zero values of the ERR once the crack enters the discontinuity, we inspect the stability condition under the prescribed displacement conditions. The elastic strain energy, for the linear elastic structures, within the small deformation theory and in absence of the body forces is given by: $U = \frac{1}{2}P\Delta$, together with Eq. (1) yields:

$$U = \frac{3EI\Delta^2}{2a^3} \quad (12)$$

Under the prescribed displacement condition the crack growth could be associated to the release of the elastic energy U . This yields:

$$\mathcal{G}_I = -\frac{1}{b} \frac{dU}{da} = \frac{3Eh^3\Delta^2}{8a^4} \quad (13)$$

The $\mathcal{G}_I(a)$ paths corresponding to Eq. (13) are plotted in Fig. 6(a–f) as grey, dashed lines (assuming: $2\Delta = 10\text{--}80$ mm with 10 mm steps—consistently with Fig. 4). As may be noted the equilibrium paths stay in a good, though not a perfect, agreement with the experimental results and the unit pattern model.

We return to the void vicinity region. Once the local maximum of the $\mathcal{G}_I(a)$ is reached, the energy is released following the stable path (the standard argument used for the displacement controlled loading $\frac{d\mathcal{G}_I}{da} \leq 0$ is always met, and inspecting $\frac{d(\mathcal{G}_{Iref} - \mathcal{G}_I)}{da} < 0$ we find the similar stable conditions). While, the $\frac{d\mathcal{G}_I}{da} = 0$ could be regarded as the equilibrium point for which the equilibrium path could be found, the critical state, according to the Lagrange-Dirichlet theorem (Bazant and Cedolin, 2010) is given by $\frac{d^2\mathcal{G}_I}{da^2} = 0$. The inflection point is found for all the cases starting from $d\lambda \cong 0.45$. The increase in the void size shifts the critical state to higher $\mathcal{G}_I(a)$ values, and shorter cracks a . A sufficiently large discontinuity, $d\lambda \geq 1$, provides the conditions for: a) the instantaneous crack growth (snap-through phenomenon) – this is altered by the prescribed displacement boundary conditions; b) the instantaneous drop in the ERR (snap-down) – which is altered by the presence of the second bonded zone, thus, $\Delta, P > 0$ and therefore $\mathcal{G}_I > 0$. In the DCB configuration, under the continuous loading, \mathcal{G}_I cannot experience neither snap-down nor snap-through phenomena. With the new ‘initial’ crack length, being the crack arrest position, the loading follows the vertical path until the $\mathcal{G}_I = R = \mathcal{G}_{Ic}$.

5. Crack growth rate and loading rate effects

Until now, the consequences of the bondline discontinuity were outlined using a quasi-static approach. Presented results suggest a more complex nature of the physical processes involved. Indeed, the variability of the crack growth path inevitably affects the crack growth kinetics and can hinder some information. In addition, the fact that the loading is applied in a continuous manner was ignored. These requests a complementary treatment and will be addressed next.

5.1. Crack growth during the DCB experiment: compliance approach

Consider the general loading case in which both the force and the displacement applied can vary over the time. The instantaneous crack front position, following Eq. (1), is given by:

$$a(t) = h \left[\frac{Eb\Delta(t)}{4P(t)} \right]^{\frac{1}{3}} \quad (14)$$

Using the Leibniz rule of differentiation, the crack growth rate can be found from:

$$\frac{da}{dt} = \frac{\partial a}{\partial \Delta} \frac{d\Delta}{dt} + \frac{\partial a}{\partial P} \frac{dP}{dt} \quad (15)$$

The substitution of Eq. (14) to Eq. (15) and further rearrangement yield:

$$\frac{da}{dt} = \frac{h}{3} \left(\frac{Eb\Delta}{4P} \right)^{\frac{1}{3}} \left(\frac{1}{\Delta} \frac{d\Delta}{dt} - \frac{1}{P} \frac{dP}{dt} \right) \quad (16)$$

Implementing Eq. (4) to Eq. (16):

$$\frac{da}{dt} \left(\gamma, \frac{d\Delta}{dt}, \Delta \right) = \dot{a} = \frac{h}{3} \left(\frac{Eb}{4\gamma} \right)^{\frac{1}{3}} \left[\Delta^{-1/2} \frac{d\Delta}{dt} - \Delta \frac{d(\Delta^{-1/2})}{dt} \right] \quad (17)$$

Finally, limiting the solution to the real (not conjugated) variables (which are found physically justified) a further rearrangement, and with $\frac{d\Delta}{dt} = \dot{\Delta}$, leads to:

$$\dot{a}(\gamma, \dot{\Delta}, \Delta) = \frac{h}{4} \left(\frac{Eb}{\gamma} \right)^{\frac{1}{3}} \dot{\Delta} \Delta^{-1/2} \quad (18)$$

Eq. (18) exposes a few interesting scaling relations of the steady-state crack growth during the DCB experiment, i.e. $\dot{a} \propto \Delta^{-1/2}$, $\dot{a} \propto \dot{\Delta}$ and finally $\gamma \propto (\frac{\dot{\Delta}}{a})^3$. Thus, it also relates the crack growth rate and the rate of separation to the fracture energy \mathcal{G}_{lc} since $\gamma \propto \mathcal{G}_{lc}^{3/4}$ and, thus, $\mathcal{G}_{lc} \propto (\frac{\dot{\Delta}}{a})^4$. Note, that the result gives a strong basis to deduce the increase of \mathcal{G}_{lc} with the increase of $\dot{\Delta}$. Clearly, the change in either \dot{a} or $\dot{\Delta}$ during the experiments must lead to different values of γ . Eq. (18) has an asymptotic character with the following material limits: 1) an infinitely tough interface: $\gamma \rightarrow \infty \therefore \frac{d\dot{a}}{d\dot{\Delta}} \rightarrow 0$, and 2) a void $\gamma \rightarrow 0 \therefore \frac{d\dot{a}}{d\dot{\Delta}} \rightarrow \infty$. For most of the known materials intermediate toughness values arise. The scope of the present work is yet another. Both, the effective fracture properties and the crack front growth rates are affected by the voids so that $\frac{\dot{\Delta}}{a}$ can significantly vary.

5.2. Continuous loading conditions: effective fracture energy

The scaling law given by Eq. (18) can be found very convenient for the data reduction since it is relying on the load response. Note, that after inserting Eq. (11) into Eq. (13) and further rearrangement yield:

$$a = \left(\frac{3 Eh^3}{8 \mathcal{G}_{lc}} \right)^{\frac{1}{4}} \Delta^{\frac{1}{2}} \quad (19)$$

The rate form equates to:

$$\dot{a} = \frac{da}{dt} = \frac{\partial \Delta}{\partial t} \frac{da}{d\Delta} = \frac{1}{2} \left(\frac{3 Eh^3}{8 \mathcal{G}_{lc}} \right)^{\frac{1}{4}} \dot{\Delta} \Delta^{-\frac{1}{2}} \quad (20)$$

yielding a result equivalent to Eq. (18). To further investigate the effect of continuous loading conditions we recall the generalization of the classical Griffith's theory (Davidson and Waas, 2012; Griffith, 1921). Differentiating Eq. (12) with respect to time, the chain rule yields:

$$\dot{U} = \frac{3}{2} EI \left(\frac{2 \dot{\Delta} \Delta}{a^3} - \frac{3 \Delta^2 \dot{a}}{a^4} \right) \quad (21)$$

Noting that the rate of the energy released during the crack growth amounts to $\mathcal{G}_I = -\frac{1}{b} \frac{dU}{da}$, Eq. (21) can be rearranged (full derivation is provided in Appendix B) and written as:

$$\mathcal{G}_I = \frac{EI}{b} \left[\left(\frac{9 \Delta^2}{2 a^4} \right) - \left(3 \frac{\dot{\Delta}}{a^3} \frac{\dot{a}}{a} \right) \right] = \hat{\mathcal{G}}_I - \check{\mathcal{G}}_I(\dot{\Delta}, \dot{a}) \quad (22)$$

where $\hat{\mathcal{G}}_I$ stands for the 'static' part and $\check{\mathcal{G}}_I(\dot{\Delta}, \dot{a})$ is the rate-dependent 'kinetic' part. For the dead load conditions, the $\Delta = \frac{P_0 b^2}{3EI}$ boundary condition could be used in Eq. (12) leading to $\mathcal{G}_I(\dot{P}, \dot{a})$. Importantly, the load response and the ERR observed experimentally are affected and dependent on both the crack velocity and the loading rate without considering non-linear, time or rate dependent, materials. An interesting interpretation is obtained by rewriting Eq. (22) in terms of U , i.e. Eq. (12). It reads:

$$\mathcal{G}_I = \frac{3}{b} \left[\frac{U}{a} - \left(3 \frac{\dot{\Delta}}{a} \right) \frac{U}{\Delta} \right] \quad (23)$$

The first term of Eq. (23) quantifies the release of the strain energy per unit of the cracked surface area and decreases during the crack growth. The second term amounts to the strain energy per applied displacement with $(3 \frac{\dot{\Delta}}{a})$ as a 'rate' weight factor and can increase providing $3 \frac{\dot{\Delta}}{a} > \frac{U}{\Delta}$. Another important form can be proposed for the rate controlled experiment once the force and the displacement are recorded. The explicit form of the boundary condition term, Eq. (1), can be recognized in Eq. (22) within the kinetic term. Hence:

$$\mathcal{G}_I = \hat{\mathcal{G}}_I - \check{\mathcal{G}}_I(\dot{\Delta}, \dot{a}) = \frac{3 Eh^3}{8} \left(\frac{\Delta^2}{a^4} \right) - \frac{P}{b} \left(\frac{\dot{\Delta}}{a} \right) \quad (24)$$

which significantly simplifies the experimental data treatment. The kinetic part could then be viewed as the 90°- peeling formula and, effectively, the role of the $(\frac{\dot{\Delta}}{a})$ - term is similar to the $(1 - \cos \theta)$ which in the peeling experiments accounts for the variation in the peel angle (Kendall, 1975). Completing and expanding the available analysis (Davidson and Waas, 2012) following, hypothetical, cases are deduced:

> Case 0: The prescribed displacement conditions $\dot{\Delta} \rightarrow 0$. The energy release rate, given by Eq. (23), indicates no crack growth and $\mathcal{G}_I = \hat{\mathcal{G}}_I$. Considering the first order (Taylor) expansion of the static part of the energy release rate around the crack arrest position a_0 gives:

$$\hat{\mathcal{G}}_I = \hat{\mathcal{G}}_{I0} + \frac{d\hat{\mathcal{G}}_{I0}}{da} (a - a_0) \quad (25)$$

Where $\hat{G}_{I0} = \hat{G}_I(a_0)$. From Eq. (13) $\frac{d\hat{G}_{I0}}{da} = -4\frac{\hat{G}_{I0}}{a_0}$ yielding:

$$\hat{G}_I = \hat{G}_{I0} - 4\frac{\hat{G}_{I0}}{a_0}(a - a_0) \quad (26)$$

Under the prescribed displacement conditions, the energy release rate can drop below the \hat{G}_I providing there is enough energy in the system to activate the crack growth (Lengline et al., 2011). An alternative interpretation of the decreasing energy release rate can be associated to the growth of the process zone, e.g. due to the viscous flow (Jumel et al., 2013).

> Case 1: The crack velocity is significantly higher than the loading rate, c.f. $\dot{\Delta} \gg \dot{a} \therefore \frac{\dot{\Delta}}{\dot{a}} \rightarrow 0$ (the ‘significantly higher’ could be linked to Eq. (25)):

$$\frac{\dot{\Delta}}{\dot{a}} \rightarrow 0 \wedge \mathcal{G}_I \rightarrow \hat{G}_I \quad (27)$$

The rate of work done by the external forces becomes negligible compared to the energy released by the crack growth. The crack growth eventually becomes unstable. In the present context, a crack travelling through the boundary between the bonded zone and the void experiences acceleration until the snap-down phenomena happens, as observed in Fig. 4. The loss of stability may cause the crack to accelerate approaching the Rayleigh speed of sound $\dot{a} = c$ (Abraham and Gao, 2000; Kanninen and Popelar, 1985) producing a speed wave and an additional energy.

> Case 2: The crack speed is significantly smaller than the loading rate: $\dot{\Delta} \gg \dot{a} \therefore \frac{\dot{\Delta}}{\dot{a}} \rightarrow \infty$. Within the present framework such conditions are not to be expected but can be forced by e.g. using the tapered (TDCB) geometries (Lof and Otten, 1974), patterning or soft adherends (transition to the peeling geometry). The kinetic term, Eq. (22), should not be ignored and the overall \mathcal{G}_I will be lowered.

> Case 3: The crack velocity and the loading rate are of the same order of magnitude and $\frac{\dot{\Delta}}{\dot{a}} = \text{const}$. The kinetic term will affect the total ERR. Eq. (22) can be further simplified providing that the term $\frac{\dot{\Delta}}{\dot{a}}$ becomes $\propto \frac{\dot{\Delta}}{\dot{a}}$ and for the specific case, once $\frac{\dot{\Delta}}{\dot{a}} = \frac{\Delta}{a}$, leads to:

$$\mathcal{G}_I = \frac{EI}{b} \left[\left(\frac{9}{2} \frac{\Delta^2}{a^4} \right) - \left(3 \frac{\Delta^2}{a^4} \right) \right] = \frac{3EI}{2b} \frac{\Delta^2}{a^4} = \frac{1}{3} \hat{G}_I \quad (28)$$

> Case 4: $\dot{\Delta} > \dot{a}$ and \dot{a} is increasing with time. Such situation will mark a departure from the steady-state process as long as the DCB specimen is considered. According to Eq. (20), the crack speed \dot{a} is decreasing if $\mathcal{G}_{Ic} = \text{const.} \forall a$. Following Eq. (22), the ERR increases from a lower value at the same rate as that of the crack growth.

> Case 5: $\dot{\Delta} > \dot{a}$ and \dot{a} is increasing to reach an asymptotic. Following Eq. (22), assuming $\dot{\Delta} = \text{const}$. \mathcal{G}_I will start at a low value and increases until reaching an asymptomatic value for which $\frac{\dot{\Delta}}{\dot{a}} = \text{const}$. Such a scenario can be observed during the DCB tests of composite materials and can be explained by the bridging phenomena between the crack faces or by using relatively flexible adherends.

> Case 6: $\dot{a} > \dot{\Delta}$ and $\frac{d\dot{a}}{da} < 0$ while $\dot{\Delta} = \text{const}$. Such conditions are expected the most common for the DCB and deemed as quasi-static (i.e. kinetic effects free). It is convenient to rearrange Eq. (22) by letting $\frac{\dot{\Delta}}{\dot{a}} = \frac{d\Delta}{da}$:

$$\mathcal{G}_I = \frac{EI}{b} \left[\left(\frac{9}{2} \frac{\Delta^2}{a^4} \right) - \left(3 \frac{\Delta}{a^3} \frac{d\Delta}{da} \right) \right] \quad (29)$$

The latter equation (the same applies to Eq. (22)) displays one of the major features of the generalized theory. The kinetic and the static effects balance each other once:

$$3 \frac{\dot{\Delta}}{\dot{a}} = \frac{U}{\Delta} \wedge \frac{d\Delta}{da} = \frac{3}{2} \frac{\Delta}{a} \quad (30)$$

which relates the secant and the tangent of the $\Delta(a)$ curve.

> Case 7: A steady-state DCB experiment. Note, that even if the displacement rate is controlled, $\dot{\Delta} = \text{const}$. the term $\frac{\dot{\Delta}}{\dot{a}}$ is expected to vary in agreement with Eqs. (16) or (20). Rearranging Eq. (20) leads to:

$$a = A\Delta^{\frac{1}{2}} \quad (31)$$

With $A = \left(\frac{3}{8} \frac{Eh^3}{\mathcal{G}_{Ic}} \right)^{\frac{1}{2}}$. Taking the power of 2 on both sides and upon further derivation:

$$\frac{d\Delta}{da} = 2A^{-2}a \quad (32)$$

leading to:

$$\mathcal{G}_I = \frac{EI}{b} \left[\left(\frac{9}{2} \frac{\Delta^2}{a^4} \right) - \left(6 \frac{\Delta}{a^2} A^{-2} \right) \right] \quad (33)$$

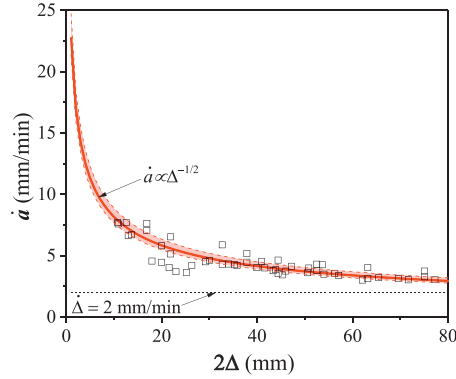


Fig. 7. Experimental and analytical crack growth rates for the reference specimens. The experimental data are obtained through Eq. (14) and denoted as squares, while Eq. (18) is used for the analytical curves—solid line (including 95% confidence bounds).

Eq. (32) increases with $\frac{d\Delta}{da} \propto a$ at rates lower than the decrease of $\frac{\Delta}{a^3}$ in Eq. (29). Assuming that the static criterion – the fracture energy is constant and behaves as indicated by the bold (horizontal) line in Fig. 5, then subtracting the kinetic part lead to an increase in \mathcal{G}_I during the crack growth. Thus, a rising R curve behaviour is predictable and an inherent property of the DCB experiment. In Eq. (33) the loading kinetic term is not represented explicitly however, it is accounted through the constant A , as coming from the analysis of Eq. (18), and the ratio $\frac{\dot{\Delta}}{a}$.

5.3. Mott's analysis of crack growth and crack arrest

Within the framework of the present study, due to the materials and the loading conditions used, the crack growth kinetic is not expected to significantly affect the results. However, for completeness, the elastodynamical definition of the energy balance equation will be used for a final presentation:

$$\mathcal{G}_I = -\frac{1}{b} \left(\frac{dU}{da} - \frac{dT}{da} \right) \quad (34)$$

with T being the kinetic energy due to the propagating crack speed wave. The generalization accounts for the possible effects introduced by the void, which can become significant depending on the system used. Adopting Mott's analysis (Kanninen and Popelar, 1985) for crack speeds small compared to the speed of the sound in the elastic body, the kinetic energy, per unit width, is given by:

$$T = \frac{1}{2} \rho \dot{a}^2 \iint \left(\frac{dw}{da} \right)^2 dx dz \quad (35)$$

where ρ is the mass density and w is the quasi-static displacement, as given by Eq. (10).

Reviewing the kinetic considerations, the Griffith's criterion is proposed as a special case of Eq. (22) in which $\frac{\dot{\Delta}}{a} = 0$. Under this condition the ERR attains a maximum value and, thus, at crack initiation $\mathcal{G}_I = \hat{\mathcal{G}}_I = \mathcal{G}_{Ic}$. Immediately after the crack onsets the Griffith's theory is no longer valid and the recorded experimental data displays the relation $\mathcal{G}_I = \hat{\mathcal{G}}_I - \tilde{\mathcal{G}}_I(\dot{\Delta}, \dot{a})$, which quantitatively is lower than the fracture energy \mathcal{G}_{Ic} . It becomes evident that, the loading rate and the presence of a void can affect the composition of the ERR. Finally, a possible experimental pitfall should be outlined. The simultaneous, separate, measurement of the kinetic and the static parts of the ERR is impossible. Both components are related through the same set of dependent variables, which reduces to the macroscopic force and the displacement. The analytical results presented so far were necessarily displaying the equivalent $\hat{\mathcal{G}}_I$ behaviour, i.e. at the lowered value since the experimental data were, effectively, representing the cumulated effect of both the kinetic and the static parts i.e. \mathcal{G}_I .

5.4. Results and discussion

5.4.1. Homogeneous bondline

For the homogeneous bondlines, the evaluation of the ERR including decoupling to the static and the kinetic parts can be performed by applying Eq. (33) to the experimental data providing the crack growth kinetic is known. In Fig. 7 the crack growth rate obtained by testing the reference samples is presented. Experimental \dot{a} curves are obtained by using

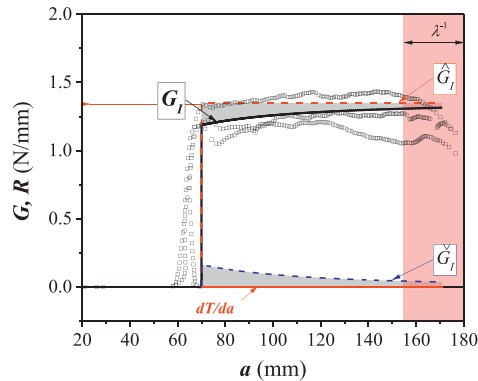


Fig. 8. The energy release rate according to the generalized theory. The analytical curves are obtained through Eq. (33).

the forward finite difference scheme: $\dot{a} \cong \frac{a_{i+1} - a_i}{\delta t}$ where the discrete crack positions, a_i , are found by applying Eq. (14) to the experimental data. (As explained in Appendix A, estimation of a using Eq. (4) may be imprecise, however for small increments, i.e. $\lim_{\delta t \rightarrow 0} \frac{\delta a}{\delta t}$ the effect of the estimation method becomes negligible). The total time was calculated from $\dot{\Delta}$ and discretised as: $\delta t = f(\Delta_{i+1} - \Delta_i)$ by applying the rule of $(\Delta_{i+1} - \Delta_i) = \max. 1 \text{ mm}$ if necessary. The analytical results, obtained using Eq. (18), including the 95% bounds (according to the previously found variation of the fracture energy factor γ), are also presented.

The agreement between the experimental and the analytical data is very good. Recalling that the loading rate was $\dot{\Delta} = 2 \text{ mm/min}$ shows that the ratio $\frac{\dot{\Delta}}{a}$ remains within the order magnitude for the most of the experiment. In such conditions, the crack front wave speed energy, T is expected as minuscule, $a \ll c$. In Fig. 8 are presented the three representative, experimental data sets and the analytical data obtained through Eq. (33). The kinetic and the static parts are plotted together with the driving force.

The analytical results, accounting for the continuous loading conditions, appear different from the previous ones given by the static analysis, c.f. Fig. 5. A significant qualitative improvement is observed with the rising R curve behaviour fully represented. The $G_I(a) \equiv R$ becomes a monotonic, positive function with a positive slope and $\frac{d^2 G_I}{da^2} (0 \forall a) a_0$. Importantly, accounting for the loading kinetic enables the 'static' material constant (average from all the data) G_{Ic} to be evaluated. In the present case this value, associated to \hat{G}_I , is higher (>15%) than the result of the static analysis using a 'standard' data reduction. This can be interpreted as a 'performance gain' and can significantly improve efficiency and robustness of layered materials. The crack growth kinetic contribution, dT/da completes the presented data. The effect is negligible.

5.4.2. Effects of voids

Crack growth rates for specimens with different discontinuity sizes, $d\lambda$, are presented in Fig. 9 (a–f).

The experimental (points) and the analytical (bold line) data, including the confidence bounds, are plotted. The model predicts crack growth rates correctly for all the cases studied. For sizes of voids amounting to ca. 4.5% and 14% of the process zone length, Fig. 9(a) and (b) respectively, acceleration in the vicinity of the void is visible. After reaching the crack arrest position, the crack begins to grow along the second bonded zone and the crack growth rates become similar to the one of the reference specimens. For the intermediate cases - (voids occupying ca. 23% and 45% of the process zone length), Fig. 9(c) and (d), the growth rate is initially similar to the preceding case. Once the void position is reached the crack growth rate increases. Providing the void is large/long enough (note, that the situation would require a very high loading rates), the maximum crack growth rate can attain the speed of sound in the material (for the acrylic materials $c = 1400 - 2000 \text{ m/s}$). Such values demand a very small time/displacement steps within the range of the electric noise of the present apparatus. The crack rate drops to zero and the crack arrests at the second bonded zone. Following the second crack onset, the growth rate returns to the values corresponding to the one of the homogeneous interface. The experimental data are found to show a slightly different trend, with a more gradual increase in the crack speed. This is deemed as the effect of the compliance approach used to estimate a and the straining of the fracture process zone interpreted as an increase in the 'effective' crack length. Similar phenomena are emphasized for the large voids (void occupies ca. 91% and 182% of the process zone length), Fig. 9(e) and (f). Note, that at the end of the crack growth stage, Figs. 9(d–f), the edge effects i.e. limit of the bonded zone and the associated crack acceleration are visible. The phenomenon is similar to that of a sufficiently large void and could be captured by the present model upon extension by an additional unit of the pattern.

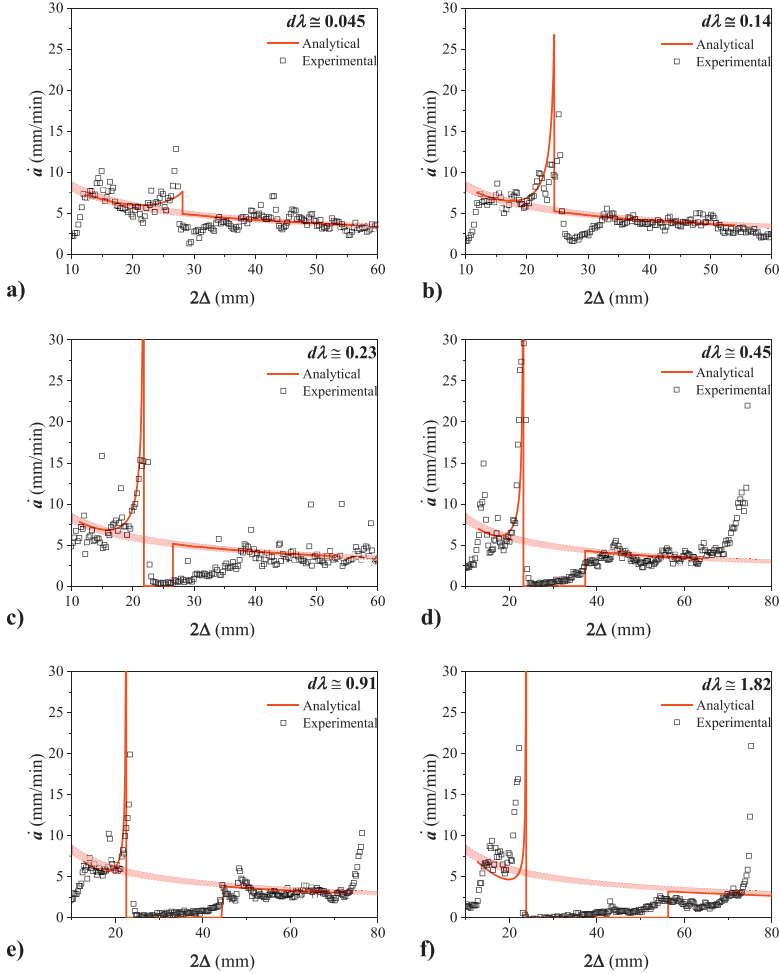


Fig. 9. The crack growth rates along the paths with voids. Presented are analytical data obtained using the unit pattern model and the experimental data evaluated by Eq. (14). Presented cases (a)–(f) corresponds to different sizes of voids, d , introduced to a bondline defined by the elastic process zone of length λ^{-1} . The dashed lines are obtained from Eq. (18) and corresponds to the reference specimens. The red, shaded, region marks the 95% confidence bounds. (For interpretation of the references to colour in this figure legend, the reader is referred to the web version of this article.)

5.4.3. Driving force and resistance curves

The driving force and the resistance curves for the specimens with voids are presented in Fig. 10(a–f). The resultant G_I , static \hat{G}_I and kinetic \tilde{G}_I components of the ERR are shown together with the kinetic energy release rate, dI/da , and the representative experimental data. The decomposition of the G_I is performed using Eq. (29) incorporated in the unit pattern model. As in the static case, for the two most specific cases the crack growth process is visualized using the ‘rolling ball’ example. Since the kinetic effects are now incorporated, the ERR paths (thin, solid lines) are obtained by considering $G_I(\frac{d\Delta}{dt}) \propto \frac{\Delta}{a^3}$ with $\frac{\Delta}{a} \propto \Delta^{\frac{1}{2}}$ and will be used through the data set to follow.

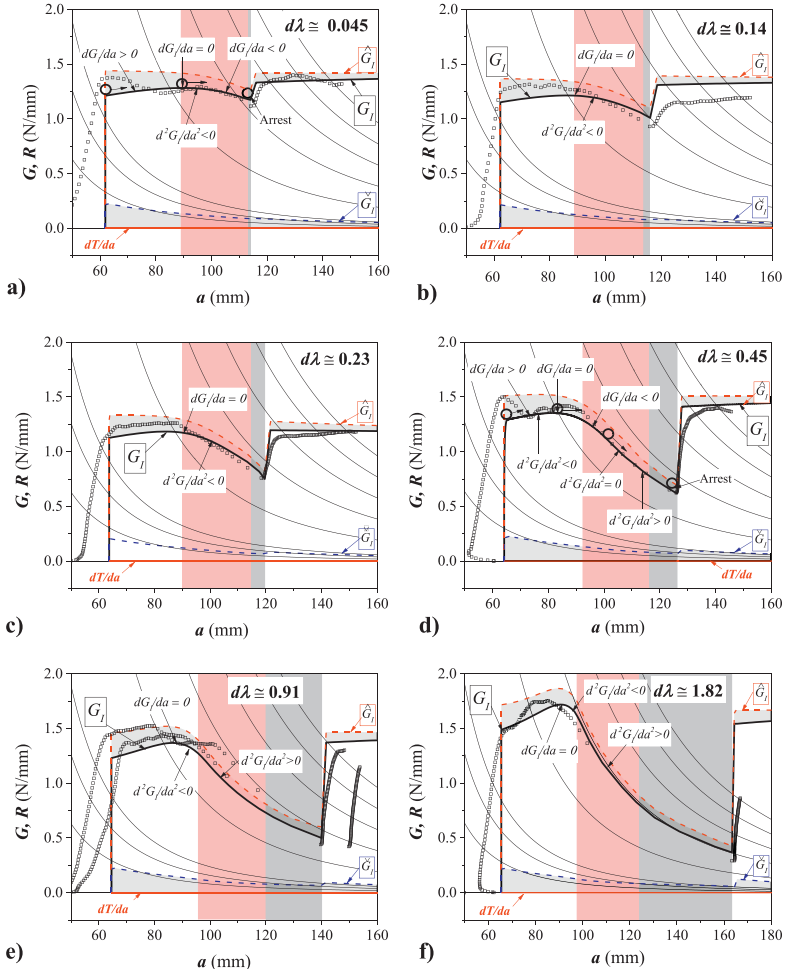


Fig. 10. The energy release rate components according to the kinetic analysis. Presented are the experimental and analytical data for the cases with different, increasing from (a) to (f), sizes of voids.

While the curves may appear similar to the one obtained by the static analysis—Fig. 6, the qualitative differences are significant and demands a more detailed discussion.

> 'Small' $d\lambda$: Fig. 10(a–c)

The rising R behaviour is emphasized. Contrary to the static analysis results, in which initially $\frac{dG_I}{da} = 0$, accounting for the loading kinetics leads to $\frac{dG_I}{da} > 0$. The crack growth process is initially stable. At a distance λ^{-1} from the void a local maximum, $\frac{dG_I}{da} = 0 \wedge \frac{d^2G_I}{da^2} < 0$ is attained denoting the unstable equilibrium condition. The material resistance gradually vanishes and further crack growth leads to instability, however, the critical state $\frac{d^2G_I}{da^2} = 0$ is not achieved and $\frac{dR}{da} > \frac{dG_I}{da}$. The process attains the minimal energy state at the crack arrest position marking the beginning of the second bonded zone.

> Large $d\lambda$: Fig. 10 (d–f)

Initially, the slope $\frac{dG_I}{da} > 0$ but higher than in previous cases. In addition, the effect increases with the size of the void. A local maximum is clear and the local curvature $\frac{d^2G_I}{da^2}$ increases with the size of the void. Once the local maximum is overcome, $\frac{dR}{da} = \frac{dG_I}{da}$ and $\frac{d^2G_I}{da^2}$ changes sign from the negative to the positive. A critical state exists, after which the G_I curve follows the derived (un)loading paths (thin, solid lines) with $\frac{dR}{da} = \frac{dG_I}{da}$ being maintained until the crack arrest position. The existence of the critical state suggests a snap-down behaviour, and in reality the load carrying capacity of the bondline material is lost. Considering the initial bonded zone to be longer a metastable path would become evident. The effect brought by taking the loading kinetic into account further emphasizes this finding. The loading kinetics shift the unstable equilibrium, $\frac{dG_I}{da} = 0$, and the critical state, $\frac{d^2G_I}{da^2} = 0$, points to longer cracks. Finally, the analytical model predicts a gradual decrease of the load carrying area, i.e. $G_I \equiv G_{Ieff}$ in the vicinity of the void, and this effect seems to be dominating over the changes in \tilde{G}_I .

Bringing the results into future perspective, it seems of practical importance and interest to design interfaces following the discovered ERR paths. The results suggest that to maximize the fracture toughness it is desirable to include larger/longer voids, preferably of the size close to the maximum used in the present study, c.f. $d \sim 2\lambda^{-1}$. It seems enough to use the bonded zones of the length $\lambda^{-1} - 1.5\lambda^{-1}$. Such a design guarantees a local stability, $\frac{dG_I}{da} > 0$, while the 'global' state resembling a metastable one. In the present case the crack speed wave energy effects were found not to play significant role, however a short discussion is given in Appendix C.

6. Conclusions

Effects of discontinuity along the crack growth path during mode I DCB experiment under continuous loading conditions are analysed experimentally and analytically and a new unit pattern model is derived. The model is composed of four regions. The first region represents the loaded arm of the double cantilever beam specimen. The second region represents the bondline or the interface of finite size/length and is modelled as a beam on an elastic foundation. The third region corresponds to the discontinuity, where the interface traction forces are not carried. The final region represents the remaining part of the interface/bondline and is modelled as a semi-infinite homogenous elastic foundation. It is found that the presence of a void in front of the growing crack affects the composition of the process zone region, leading to a variation in the crack growth rate. Moreover, the steady-state analysis showed that the DCB configuration introduces some ambiguity to the interpretation of the recorded energy release rate with the kinetic effects being ignored. The crack growth process is reconsidered adopting the generalized Griffith's fracture theory and, for completeness, taking into account the crack speed wave effects. To verify and validate the model, a series of double cantilever beam experiments are conducted, evaluating the effect of the void size. The load response curves are used to yield the kinetic and the static part of the energy release rate. Experimental and analytical results are compared for the load response and the driving force curves and following conclusions are drawn:

> Loading kinetics

Under presumed quasi-static conditions, the loading kinetics cannot be neglected. In the present case, using a relatively low loading rate, it is found that the loading kinetics effect amounts to approx. 15% of the total energy release rate. Consequently, one of the important findings concerns the estimation of the fracture energy defined as the material constant. The kinetic model shows that the values obtained experimentally by means of the (standard) static analysis could be (unnecessarily) conservative. The finite rate of loading used during the standardized DCB or TDCB experiments lead to lower values of the estimated fracture energy. The present study exposes this value to be affected by the test conditions. An attempt is made to translate the experimental results into static fracture energy. The fracture energy, estimated by using the new model, was found to be approx. 15% higher compared to the standard static analysis. This may be of fundamental importance for a more robust and efficient design. In addition, the loading kinetic explains the characteristic, rising, R curve behaviour. This observation is consistent with the existing literature (Davidson and Waas, 2012). Accounting for the loading kinetic effect is necessary for a correct and profound interpretation of the crack growth along the discontinuous path. Specifically, the (unstable) equilibrium points, $\frac{dG_I}{da} = 0$ and $\frac{d^2G_I}{da^2} > 0$ and the critical state points $\frac{d^2G_I}{da^2} = 0$ are revealed and shifted when compared to the standard, static model. The proposed model predicts the existence and the position of critical state points and the appropriate design of the interfaces avoiding or inducing instabilities.

> Role of process zone

During growth of the crack, the length (and the area) of the effective load carrying fracture process zone changes. A gradual increase or decrease in G_{Ic} is observed depending on the composition of the load carrying zone but also on the position of the void. The existence and the position of the equilibrium, and the critical state points depend on the ratio between the void and the fracture process zone sizes. For $d\lambda < 0.45$ the critical point is not attained. For $d\lambda > 0.45$ the critical state point appears once the distance between the crack front and the void lies within $(0.5\lambda^{-1} : \lambda^{-1})$. The exact position can be analytically derived.

> Role of voids

The size and the effect of the void should be recognized as inherently connected to the characteristic length scale of the material/structure – in the present case, the process zone. The size of the process zone defines the ‘size’ of the void. Obtained results suggest the introduction of an additional limits for a safe use and design of interface materials containing unwanted flaws. It is deduced that for maximum toughness it is enough if the bonding length slightly exceeds the process zone length. Subsequently, it is profitable to leave an unbonded zone of a length exceeding the length of the process zone. A ‘quasi’ metastable state is introduced for which the ERR is maximum.

The relatively simple model proposed indicates possible directions for future studies of interface heterogeneities and their effects. Our results highlight a number of observations that may aid the development of a more fundamental theory of the controllable structural response and damage tolerance by designing interfaces. For instance, the model can be used for designing interfaces for a specific equilibrium path, or as an additional requirement for the bondline design allowing full recovery from the unstable crack growth. Finally, the results presented should aid a better understanding and evaluation of the ‘kissing bonds’ - a big obstacle for the more efficient use of laminated materials including composites and adhesive joints.

Appendix A. Length of process zone λ^{-1}

In the present study, due to the materials used, $E_a \ll E$, the restraining of the adherend (Kanninen, 1973) can be neglected and the elastic foundation wave number equates to:

$$\lambda = \sqrt[4]{\frac{k}{4EI}} = \sqrt[4]{\frac{m E_a b}{4 t_a EI}} \tag{A.1}$$

The inverse of the wave number, λ^{-1} , is the length of the elastic (fracture) process zone ahead of the crack tip. The coefficient m defines the stress state at the crack tip. Specifically, with ν_a being the Poisson’s ratio of the bondline material:

- a) $m = 1/(1 - \nu_a^2)$ for the in-plane plain strain condition and plane stress conditions in the transverse direction (two dimensional plane strain state) (Krenk, 1992),
- b) $m = (1 - \nu_a)/[(1 - 2\nu_a)(1 + \nu_a)]$ if the plain strain condition is assumed in both out-of-plane and in-plane directions (three dimensional plane strain state) (Jumel et al., 2011),
- c) $m = 1$ for the plane stress condition in all directions (Chow et al., 1979).

More complex interpretations of m are also possible (Cabello et al., 2016a), but as such, the authors failed to find a comprehensive experimental analysis proving superiority of any of the model. In the present study $\nu_a = 0.45 \pm 0.02$ according to the product data sheet. Using the three aforementioned methods for evaluating m yields the following values for the length of the process zone: $\cong 25.5$ mm for the plane stress, $\cong 23.2$ mm for the 2D plane strain and $\cong 19.3$ mm for the 3D plane stress, independently of the crack length. To decide which of stress states prevails, the reference specimens were used to determine the λ^{-1} experimentally. The first procedure, described in (Ben Salem et al., 2013) inspects the crack front vicinity region in situ - Fig. A1. (a), during the crack growth using the digital image correlation (DIC) technique (Vic2D, Correlated Solutions, USA). In specific, the deflection along the neutral axis of the adherends is extracted. Assuming that in the far field the difference between the adherends deflection is zero (consistently with the theory), an intersection between the deflection lines is sought and compared to the actual, known, position of the crack front. The second method, named compliance

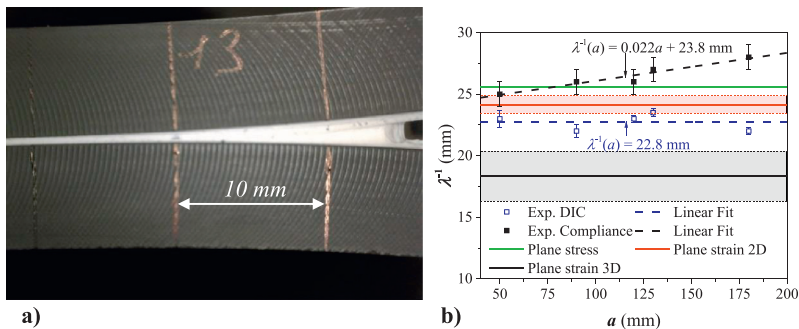


Fig. A1. (a) The crack front vicinity during the steady-state growth. (b) The process zone length during the crack growth.

relates to the effective crack length approach. The experimentally obtained force and displacement, $P = f(a)$, $\Delta = f(a)$ are inserted into Eq. (1) and the effective crack length, a_{eff} is elucidated. Then, $\lambda^{-1} \cong a_{eff} - a$ (Blackman et al., 2005) with a being macroscopic length of the crack (as seen in Fig. A1. (a)). In Fig. A1. (b) are given the experimental results - average from 10 reference specimens for a given crack length together with standard deviation. Included in the figure are also the analytical predictions - including variation in the Poisson's ratio (indicated, when relevant, by bounded, shaded regions) of the adhesive and assuming different stress state conditions at the crack tip as previously discussed.

The DIC evaluation yields $\lambda^{-1} = 22.8$ mm independent of the crack length. A different picture is displayed by the compliance method. The process zone length increases during the crack growth, which could indicate a progressive yielding process, viscous flow or other source of energy dissipation. However, the classical assumption used for estimating the length of the process zone in the DCB geometries: as the difference between the estimated crack front position and the real position, may be imprecise, specifically once $E_a \ll E$. For such material systems the ratio $\frac{a_{eff}}{a}$ should be expected constant during the crack growth (Budzik et al., 2011). Using this approach, which amounts to extrapolating a linear fit and finding an intercept point, viz. $\lambda^{-1}(a = 0)$ results in $\lambda^{-1} = 23.8$ mm consistently with the DIC measurements once taking into account the standard deviation. Clearly, in the present case, the full 3D plane strain assumptions leads to an overestimated stiffness and the process zone length is short compared to the experimental results. The plane stress conditions appears in better agreement, however, in this case the bondline appears too 'soft'. The 2D plane strain assumption, yielding $\lambda^{-1} \cong 23.2$ mm, seems the most appropriate. Ever since, the 2D plane strain condition was assumed for the analytical model.

Appendix B. Derivation of rate dependent energy release rate

The elastic strain energy is given by $U = \frac{1}{2}P\Delta = \frac{1}{2}C^{-1}\Delta^2$ in which $C^{-1}(a)$. The rate form of U is:

$$\frac{dU}{dt} = \frac{\partial U}{\partial \Delta} \frac{d\Delta}{dt} + \frac{\partial U}{\partial a} \frac{da}{dt} \tag{A.2}$$

Dividing both sides by $\frac{da}{dt}$ one gets:

$$\frac{dU}{da} = \frac{\partial U}{\partial \Delta} \frac{d\Delta}{da} + \frac{\partial U}{\partial a} \tag{A.3}$$

By definition, under the displacement controlled conditions, $G_I \stackrel{def}{=} -\frac{1}{b} \frac{dU}{da}$ yielding:

$$G_I = -\frac{1}{b} \left(\frac{\partial U}{\partial a} + \frac{\partial U}{\partial \Delta} \frac{d\Delta}{da} \right) \tag{A.4}$$

Taking $U = \frac{3}{4} \frac{E\Delta^2}{a^3}$ leads directly to Eq. (29).

Appendix C. Effect of crack speed wave

In Fig. C1 evaluation of the kinetic energy released during the crack growth process, dT/da is plotted for the different $d\lambda$ studied.

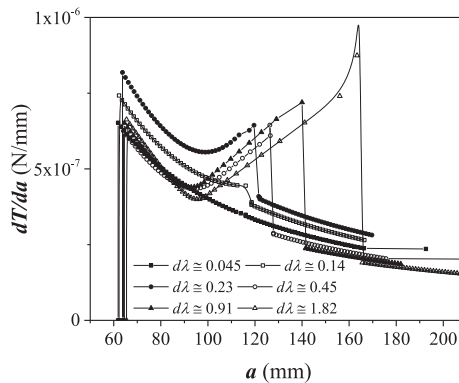


Fig. C1. Evaluation of the crack speed wave effect.

The presence of a void significantly affects the kinetic energy release rate. The results are qualitatively appealing (Lawn, 1993). However, quantitatively, the effects are insignificant and could be ignored in the present case but not in general. From the available literature (Kalthoff et al., 1977) where a similar DCB configuration was used with different materials, i.e. epoxy adhesive bondline (with $E \propto 10^3 E_a$ of the acrylic adhesive used at present) the crack front velocity of $\dot{a} \cong 10^{\frac{21}{5}}$ was found to affect the G_I . This being $10^3 - 10^4$ higher than the speed recorded at the present. However, an order of magnitude increase in the dT/da is induced by the void and with different materials being used this could lead to a failure or significantly affect G_I .

Supplementary materials

Supplementary material associated with this article can be found, in the online version, at doi:10.1016/j.jmps.2018.04.002.

References

- Abraham, F.F., Gao, H.J., 2000. How fast can cracks propagate. *Phys. Rev. Lett.* 84, 3113–3116.
- Adams, R.D., Peppiatt, N.A., 1974. Stress analysis of adhesive-bonded lap joints. *J. Strain Anal.* 9, 185–196.
- Akisanaya, A.R., Fleck, N.A., 1992. Analysis of a wavy crack in sandwich specimens. *Int. J. Fract.* 55, 29–45.
- Alfano, M., Pini, S., Chiodo, G., Barberio, M., Pironi, A., Furgiuele, F., Groppetti, R., 2014. Surface patterning of metal substrates through low power laser ablation for enhanced adhesive bonding. *J. Adhes.* 90, 384–400.
- Arruda, E.M., Boyce, M.C., Jayachandran, R., 1995. Effects of strain-rate, temperature and thermomechanical coupling on the finite strain deformation of glassy-polymers. *Mech. Mater.* 19, 193–212.
- Bazant, Z.P., Cedolin, L., 2010. *Stability of Structures: Elastic, Inelastic, Fracture and Damage Theories*. World Scientific Publishing Co. Pte. Ltd., Singapore.
- Bazant, Z.P., Pang, S.D., 2006. Mechanics-based statistics of failure risk of quasibrittle structures and size effect on safety factors. *Proc. Natl. Acad. Sci. USA* 103, 9434–9439.
- Ben Salem, N., Budzik, M.K., Jumel, J., Shanahan, M.E.R., Lavelle, F., 2013. Investigation of the crack front process zone in the Double Cantilever Beam test with backface strain monitoring technique. *Eng. Fract. Mech.* 98, 272–283.
- Blackman, B.R.K., Kinloch, A.J., Paraschl, M., 2005. The determination of the mode II adhesive fracture resistance, $G(II)$, of structural adhesive joints: an effective crack length approach. *Eng. Fract. Mech.* 72, 877–897.
- Blackman, B.R.K., Kinloch, A.J., Rodriguez-Sanchez, E.S., Teo, W.S., 2012. The fracture behaviour of adhesively-bonded composite joints: effects of rate of test and mode of loading. *Int. J. Solids Struct.* 49, 1434–1452.
- Bogy, D.B., 1968. Edge-bonded dissimilar orthogonal elastic wedges under normal and shear loading. *J. Appl. Mech.* 35, 460–466.
- Bresson, G., Jumel, J., Shanahan, M.E.R., Serin, P., 2013. Statistical aspects of the mechanical behaviour of a paste adhesive. *Int. J. Adhes. Adhes.* 40, 70–79.
- Budzik, M., Jumel, J., Shanahan, M.E.R., 2011. Adhesive compliance effect in mode I separation: profilometry approach. *Int. J. Adhes. Adhes.* 31, 135–145.
- Budzik, M.K., Jensen, H.M., 2014. Perturbation analysis of crack front in simple cantilever plate. *Int. J. Adhes. Adhes.* 53, 29–33.
- Budzik, M.K., Jumel, J., Shanahan, M.E.R., 2013. Adhesive fracture of heterogeneous interfaces. *Philos. Mag.* 93, 2413–2427.
- Cabello, M., Zurbitu, J., Renart, J., Turon, A., Martínez, F., 2016a. A general analytical model based on elastic foundation beam theory for adhesively bonded DCB joints either with flexible or rigid adhesives. *Int. J. Solids Struct.* 94–95, 21–34.
- Cabello, M., Zurbitu, J., Renart, J., Turon, A., Martínez, F., 2016b. A general analytical model based on elastic foundation beam theory for adhesively bonded DCB joints either with flexible or rigid adhesives. *Int. J. Solids Struct.* 94–95, 21–34.
- Cao, H.C., Evans, A.G., 1989. An experimental study of the fracture-resistance of bimaterial interfaces. *Mech. Mater.* 7, 295–304.
- Chopin, J., Prevost, A., Boudaoud, A., Adda-Bedia, M., 2011. Crack front dynamics across a single heterogeneity. *Phys. Rev. Lett.* 107, 144301.
- Chow, C.L., Woo, C.W., Sykes, J.L., 1979. Determination and application of cod to epoxy-bonded aluminum joints. *J. Strain Anal. Eng.* 14, 37–42.
- Cuminatto, C., Parry, G., Braccini, M., 2015. A model for patterned interfaces debonding–application to adhesion. *Int. J. Solids Struct.* 75–76, 122–133.
- Cuminatto, D., Barthel, E., Vandembroucq, D., 2009. Crack front pinning by design in planar heterogeneous interfaces. *J. Mech. Phys. Solids* 57, 446–457.
- das Neves, P.J.C., da Silva, L.F.M., Adams, R.D., 2009. Analysis of mixed adhesive bonded joints Part I: theoretical formulation. *J. Adhes. Sci. Technol.* 23, 1–34.
- Davami, K., Jiang, Y., Cortes, J., Lin, C., Shaygan, M., Turner, K.T., Bargatin, I., 2016. Tuning the mechanical properties of vertical graphene sheets through atomic layer deposition. *Nanotechnology* 27, 1–8.
- Davidson, P., Waas, A.M., 2012. Non-smooth mode I fracture of fibre-reinforced composites: an experimental, numerical and analytical study. *Phil. Trans. R. Soc. A* 370, 1942–1965.
- Dundurs, J., 1969. Discussion: "Edge-bonded dissimilar orthogonal elastic wedges under normal and shear loading". *J. Appl. Mech.* 36, 650.
- Eshelby, J.D., 1957. The determination of the elastic field of an ellipsoidal inclusion, and related problems. *Proc. Roy. Soc. Lond. A* 241, 376–396.
- Gao, H., Rice, J.R., 1989. A first-order perturbation analysis of crack trapping by arrays of obstacles. *J. Appl. Mech.* 11, 828–836.
- Goland, M., Reissner, E., 1944. The stresses in cemented joints. *J. Appl. Mech.* 11, A17–A27.
- Griffith, A.A., 1921. The phenomena of rupture and flow in solids. *Philos. Trans. R. Soc. London A* 221, 163–198.
- Hart-Smith, L.J., 1973. Adhesive-bonded single-lap joints. *NASA CR-112236*.
- Heide-Jørgensen, S., Budzik, M.K., 2017. Crack growth along heterogeneous interface during the DCB experiment. *Int. J. Solids Struct.* 120, 278–291.
- Hetenyi, M., 1979. *Beams on Elastic Foundation*. The University of Michigan Press, Ann Arbor.
- Hong, S.G., Boerio, F.J., 2007. Adhesive bonding of oil-contaminated steel substrates. *J. Adhes.* 32, 67–88.
- Jeenjithkaew, C., Guild, F.J., 2017. The analysis of kissing bonds in adhesive joints. *Int. J. Adhes. Adhes.* 75, 101–107.
- Jensen, H.M., 2003. Crack initiation and growth in brittle bonds. *Eng. Fract. Mech.* 70, 1611–1621.
- Jumel, J., 2017. Crack propagation along interface having randomly fluctuating mechanical properties during DCB test finite difference implementation – Evaluation of G_c distribution with effective crack length technique. *Compos. B: Eng.* 116, 253–265.
- Jumel, J., Budzik, M.K., Shanahan, M.E.R., 2011. Beam on elastic foundation with anticlastic curvature: application to analysis of mode I fracture tests. *Eng. Fract. Mech.* 78, 3253–3269.
- Jumel, J., Chauffaille, S., Budzik, M.K., Shanahan, M.E.R., Guitard, J., 2013. Viscoelastic foundation analysis of Single Cantilevered Beam (SCB) test under stationary loading. *Eur. J. Mech. A-Solid* 39, 170–179.
- Kalthoff, J.F., Winkler, S., Beinert, J., 1977. Influence of dynamic effects in impact testing. *Int. J. Fract.* 13, 528–531.
- Kanninen, M., 1973. An augmented double cantilever beam model for studying crack propagation and arrest. *Int. J. Fract.* 9, 83–92.
- Kanninen, M.F., 1974. Dynamic analysis of unstable crack-propagation and arrest in DCB test specimen. *Int. J. Fract.* 10, 415–430.
- Kanninen, M.F., Popelar, C.H., 1985. *Advanced Fracture Mechanics*. Oxford University Press, New York.
- Kendall, K., 1975. Thin-film peeling – elastic term. *J. Phys. D Appl. Phys.* 8, 1449–1452.
- Kerr, A.D., 1964. Elastic and viscoelastic foundation models. *J. Appl. Mech.* 31, 491–495.
- Krenk, S., 1992. Energy-release rate of symmetrical adhesive joints. *Eng. Fract. Mech.* 43, 549–559.
- Landis, C.M., Pardo, T., Hutchinson, J.W., 2000. Crack velocity dependent toughness in rate dependent materials. *Mech. Mater.* 32, 663–678.
- Lawn, B.R., 1993. *Fracture of Brittle Solids*, Second ed. Cambridge University Press, Cambridge.

- Lengline, O., Toussaint, R., Schmittbuhl, J., Elkhoury, J.E., Ampuero, J.P., Tallakstad, K.T., Santucci, S., Maloy, K.J., 2011. Average crack-front velocity during subcritical fracture propagation in a heterogeneous medium. *Phys. Rev. E* 84.
- Lof, C.J., Ottens, H.H., 1974. Compliances of a tapered DCB specimen configurations by a finite element method. *Eng. Fract. Mech.* 6, 573–585.
- Mori, T., Tanaka, K., 1973. Average stress in matrix and average energy of materials with mis-fitting inclusions. *Acta Metall.* 21, 571–574.
- Mower, T.M., Argon, A.S., 1995. Experimental investigations of crack trapping in brittle heterogeneous solids. *Mech. Mater.* 19, 343–364.
- Olia, M., Rossetto, J.N., 1996. Analysis of adhesively bonded joints with gaps subjected to bending. *Int. J. Solids Struct.* 33, 2681–2693.
- Patinet, S., Frelat, J., Lazarus, V., Vandembroucq, D., 2011. Propagation of planar crack fronts in heterogeneous brittle materials of finite dimensions. *Mech. Ind.* 12, 199–204.
- Patinet, S., Vandembroucq, D., Hansen, A., Roux, S., 2014. Cracks in random brittle solids: from fiber bundles to continuum mechanics. *Eur. Phys. J.-Spec. Top* 223, 2339–2351.
- Razavi, S.M.J., Ayatollahi, M.R., Esmaili, E., da Silva, L.F.M., 2017. Mixed-mode fracture response of metallic fiber-reinforced epoxy adhesive. *Eur. J. Mech. A/Solids* 65, 349–359.
- Reedy Jr., E.D., 1993. Free-edge stress intensity factor for a bonded ductile layer subjected to shear. *J. Appl. Mech.* 60, 715–720.
- Reedy Jr., E.D., 1990. Intensity of the stress singularity at the interface corner between a bonded elastic and rigid layer. *Eng. Fract. Mech.* 36, 575–583.
- Sancaktar, E., Kumar, S., 2000. Selective use of rubber toughening to optimize lap-joint strength. *J. Adhes. Sci. Technol.* 14, 1265–1296.
- Tadepalli, R., Turner, K.T., Thompson, C.V., 2008a. Mixed-mode interface toughness of wafer-level Cu–Cu bonds using asymmetric chevron test. *J. Mech. Phys. Solids* 56, 707–718.
- Tadepalli, R., Turner, K.T., Thompson, C.V., 2008b. Effects of patterning on the interface toughness of wafer-level Cu–Cu bonds. *Acta Mater.* 56, 438–447.
- Towse, A., Potter, K.D., Wisnom, M.R., Adams, R.D., 1999. The sensitivity of a Weibull failure criterion to singularity strength and local geometry variations. *Int. J. Adhes. Adhes.* 19, 71–82.
- Volkersen, O., 1938. *Nietkraftverteilung in zugbeanspruchten nietverbindungen mit konstanten, Luftfahrtforschung*, pp. 15–41.
- Weißgraber, P., Hell, S., Becker, W., 2016. Crack nucleation in negative geometries. *Eng. Fract. Mech.* 168, 93–104.
- Williams, M.L., 1952. Stress singularities resulting from various boundary conditions in angular corners of plates in extension. *J. Appl. Mech.* 20, 145–154.
- Xia, S., Ponso, L., Ravichandran, G., Bhattacharya, K., 2012. Toughening and asymmetry in peeling of heterogeneous adhesives. *Phys. Rev. Lett.* 108, 1–5.

Chapter 5

Paper 4 - On Kissing-Bonds and Support Carriers

On the fracture behavior of CFRP bonded joints under mode I loading: Effect of supporting carrier and interface contamination⁴

5.1 Introduction

With offset in an academic discussion at a conference the authors from Aarhus University and Delft University started a collaboration to study kissing bonds in composite joints. The collaboration benefited from Aarhus University's existing knowledge on similar structured interfaces and Delft University's extensive experience with manufacturing composite joints containing kissing bonds.

The joints studied comprise of carbon fiber reinforced polymer (CFRP) adherends bonded with an epoxy. A support carrier normally regarded as a weakening factor is used to control the bondline thickness. The scope, which is to measure the severity of a kissing bond on load carrying capacity and effective critical energy, changes as the support carrier, which is a polymer lattice, is found to trigger a bridging phenomenon altering the fracture behavior of the joint completely. Hence, the aim of the work becomes to investigate both the impact of the kissing bond and understand the effects of the support carrier in the bondline.

5.2 Method

First, homogeneous DCB specimens are manufactured of CFRP adherends bonded with an epoxy containing a polymer lattice and tested in mode I. These specimens serve as a baseline and to acquire fracture properties and behavior in terms of load response. Then, a second set of DCB specimens containing kissing bonds are produced and tested under the same conditions.

The analytical model proposed and extended in papers 2 and 3 is further extended with laminate theory to include the correct stiffness of the CFRP adherends. The rate form ERR presented in paper 3 is used to analyze the consequences of the kinetic effects of the kissing bond. In addition, an effective model of the ERR contribution from the lattice is proposed and combined with the rate form ERR to explain the experimental observations.

5.3 Contribution

The author contributed with parts of the experimental work in terms of testing and data treatment, theoretical modeling and simulation, and, preparation of the manuscript.

5.4 Finding

The main findings are twofold. First, the presence of a kissing bond destabilizes the fracture process by causing both crack acceleration and loss of load carrying capacity. The rate form of the ERR reveals a contribution on the fracture process from kinetic effects, especially at crack onset. The effects are small but non-negligible. This is already observed in papers 2 and 3 for similar defects. However, both the adhesive and the adherends are three orders of magnitude stiffer than in the previous studies. This significantly reduces the size of the process zone. Yet the analytical model still predicts the results accurately, which shows its robustness.

Second, the support carrier in the bondline is found to have a significantly positive impact on the effective fracture energy by triggering a bridging phenomenon. This leads to a rise in the R-curve by altering the failure mechanism and a significantly contribution to the ERR is observed. As a consequence the load response deviates from the expected power-law path and becomes almost flat.

5.5 Reflection

It seems like the mechanism governing the failure of structured interfaces where zones of weak or no adhesion exist is independent of the stiffness of the joint (three orders of magnitude tested here) and can be predicted accurately by the proposed model. The model should, of course, be investigated across an even larger order of magnitude.

The lattice support carrier in the bondline significantly enhances the damage tolerance of the joint by triggering a bridging phenomena constraining the cracked surfaces and retarding the crack. In the present study an effective way of modeling this behavior is implemented. An analytical model of the mechanism could greatly increase the understanding of the phenomenon. It could also be interesting to study different types of lattices to optimize the enhancement and to tailor the joint response.



On the fracture behaviour of CFRP bonded joints under mode I loading: Effect of supporting carrier and interface contamination

Simon Heide-Jørgensen^a, Sofia Teixeira de Freitas^{b,*}, Michal K. Budzik^{a,**}

^a Aarhus University, Dept. Engineering, Inge Lehmann's Gade 10, 8000, Aarhus C, Denmark

^b Delft University of Technology, Fact. Aerospace Engineering, Kluyverweg 1, 2629 HS Delft, The Netherlands

ARTICLE INFO

Article history:

Received 27 December 2017

Received in revised form

13 February 2018

Accepted 18 March 2018

Available online 20 March 2018

Keywords:

Bonding

Bridging

Composites

DCB

Kissing bonds

Lattice material

Rising *R* curve

ABSTRACT

This paper addresses the fracture behaviour of bonded composite plates featuring a kissing bond along the crack growth path. Double cantilever beam (DCB) experiments are carried out under a displacement controlled loading condition to acquire the load response. The experimental data are collected and analysed analytically for specimens with and without kissing bond. The following aspects are observed and discussed: effect of the adhesive carrier film, non-smooth crack growth and rising *R* curve. An analytical model taking into account the aforementioned effects is proposed. The kissing bond leads to unstable crack growth resulting in a loss of the load carrying capacity. The presence of the knit carrier in the adhesive film results in the crack growth process characteristic for the stick-slip phenomena and a significant increase of the resistance to fracture of the bondline by triggering a bridging phenomenon. The model shows a very good agreement with the experimental data. A sound understanding of the fracture process is gained enabling analysis and prediction of the effects of kissing bonds and supporting carrier.

© 2018 Elsevier Ltd. All rights reserved.

1. Introduction

A robust design of layered materials requires a profound understanding of failure phenomena associated with delamination, debonding and interface fracture being the most critical [1]. Evaluation of crack propagation is of central importance for the assessment of failures, the reliability and the damage tolerance of materials and structures [2–4]. Within multilayer materials, bondlines and interfaces are often assumed to be homogeneous. Analytical solutions are proposed for a variety of material systems and fracture modes [5–9]. The cohesive zone framework [10,11] is successfully adopted, implemented and exploited numerically [12–15]. However, the failure of layered materials can be affected by the presence of local heterogeneities along the crack growth path [16–19]. For composite materials the danger of trapping air, dust, release film or other contamination is high and can lead to premature failure e.g. due to change in the crack front locus [20]. The presence of voids in which no physical bonding between two

surfaces exists, could be detected by means of non-destructive methods. However, frequently, the contamination leads to a so-called 'kissing bond' where a physical continuity allows for the energy waves to propagate but the mechanical resistance is very low. A considerable number of studies used non-destructive testing methods to address the existence of kissing bonds [21–24]. Contributions addressing the mechanical behaviour of joints containing a kissing bond under mechanical load are less numerous. E.g. in Ref. [25] kissing bonds were prepared inside a composite/epoxy adhesive double lap joints. The effects on the load carrying capacity were not investigated. A significant amount of contributions addressing the effect of voids present along an interface, exists. An elasticity method was developed to study the bending and elucidate mechanical properties of laminated panels containing imperfections [26]. An approach utilizing layerwise formulation and representing bondline as an interface with discontinuity of the displacement field was adopted and validated using the finite element method [27]. A multiscale cohesive failure model investigating microheterogeneities was investigated in Ref. [28]. The process of decohesion along the imperfect interface was studied within the cohesive zone model framework [29]. In Ref. [30], a cohesive zone model was developed to investigate crack growth under the mixed-mode fracture conditions from a circular

* Corresponding author.

** Corresponding author.

E-mail addresses: S.TeixeiraDeFreitas@tudelft.nl (S. Teixeira de Freitas), mibu@eng.au.dk (M.K. Budzik).

inclusion. These works indicated a significant effect of the void on the local stress distribution. The Rice and Gao perturbation approach [31,32] can be used to elucidate fracture properties of the material with the local flaw as well as to deduce the shape of the crack front [33–36]. The perturbation approach was included and further developed to study circular and arbitrary shape inclusions or imperfection bands running parallel to the crack growth direction [17,35]. An interesting and relevant case could be envisaged once the flaw runs parallel to the crack front through the entire width of the structure. Potentially, the channelling void may turn the steady-state crack growth into an unstable process. In Ref. [37] an array of discrete soldered bands was analysed in two dimensions (2D) within the cohesive zone modelling framework. Effects of the crack front plasticity on interactions between the bands were elucidated. Recently, two analytical solutions were proposed for the mode I debonding along an interface with voids [38,39]. First results suggest a crucial effect of heterogeneities on stability of the crack growth process and the load carrying capacity. These aspects are yet to be investigated for composite materials.

In this work, the effect of a channelling through an interface kissing bond/contamination introduced to the crack growth path on the fracture behaviour of a bonded composite plates is

investigated experimentally and analysed theoretically. The bond-line consists of an epoxy film adhesive with an embedded polymer carrier resembling a 2D lattice material. Double cantilever beam (DCB) experiments are performed under quasi-static loading conditions. The aim of the study is to characterize the fracture behaviour of composite bonded structures with a kissing bond under mode I opening load.

2. Experimental procedure

2.1. Materials

2.1.1. Composite plates

The Carbon Fibre Reinforced Polymer (CFRP) plates used in this study are manufactured from unidirectional prepreg consisting of the thermoset epoxy resin HexPly 8552 in combination with AS4 carbon fibre (Hexcel Composites, Cambridge, UK). The curing of the composite plates was performed in an autoclave for 120 minutes at 180°C and 7 bars pressure. While curing, the surface of the composite plates was in contact with a Fluorinated Ethylene Propylene Copolymer release film (FEP Copolymer A 4000 clear red, Airtch Europe, Niederkorn, Luxembourg). Each plate used for the DCB

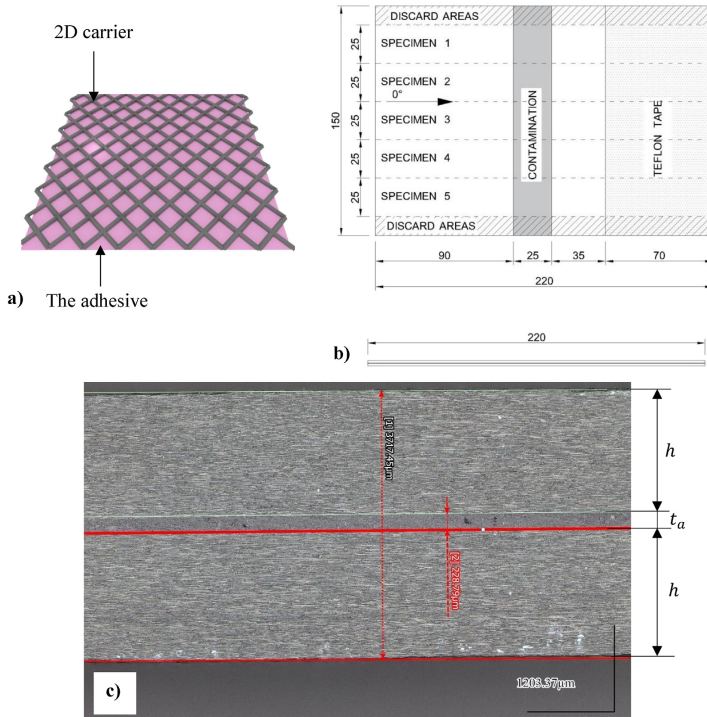


Fig. 1. (a) Schematic representation of the adhesive system AF163-2K. (b) Bonded composite DCB panel with the contamination strip (dimensions in mm). (c) Characteristic dimensions of the composite plate and the bondline.

experiment consisted of a unidirectional CFRP laminate with 10 plies $[0^{\circ}]_{10}$ resulting in the thickness $h = 1.8 \pm 0.05$ mm (the average \pm standard deviation). The modulus of elasticity of the plate along the fibre direction $E_1 \approx 100 \pm 10$ GPa was evaluated from a series of the three-point bending experiments. In a through-the-thickness direction the value of $E_2 \approx 10$ GPa was adopted from Ref. [40].

2.1.2. The bondline

The adhesive used for bonding composite plates was in the form of the epoxy film AF163-2K (3M Netherlands B.V., Delft, Netherlands) with a supporting, knitted, carrier. The carrier is used to maintain the thickness of the adhesive bondline while curing. Fig. 1 (a) shows a schematic representation of the adhesive system. The carrier consists of a two-dimensional, diamond-celled lattice knit of nylon fibres of $t = 40 - 50$ μ m diameter. The cured epoxy adhesive is characterized by the Young's modulus $E_a \approx 1.1$ GPa and a stress at failure (the epoxy without the carrier) $\sigma_f \approx 48$ MPa [40].

2.2. Specimens preparation

2.2.1. Surface pre-treatment and contamination

Prior to bonding the surfaces of the adherends were subjected to a surface pre-treatment consisting of two steps: 1) cleaning with PF-QD solution and 2) UV-ozone treatment. The PF-QD (PT Technologies Europe, Cork, Ireland) is a cleaning solvent for surface cleaning and degreasing [41]. Surfaces were wiped with a cloth soaked with PF-QD. The UV-ozone treatment was performed using an in-house apparatus consisting of 30 W UV-lamps with a sleeve of natural quartz (UV-Technik, Wümbach, Germany) – wave lengths were approximately 184.9 nm and 253.7 nm. Samples were treated for 7 minutes at a distance of 40 mm from the UV-lamps [42–45]. After the surface pre-treatment some of samples were contaminated with a band of a 'kissing bond' or a 'weak bond'. The contamination consisted of applying the release agent MARBOTE 227/CEE (Marbocote Ltd, Middlewich, UK). The composite surface was wiped with a cloth impregnated with the release agent and left to dry for 15 minutes. This procedure was repeated six times at the contamination strip area. Weight measurements of samples before and after the contamination showed a contamination weight of approximately $0.12 \mu\text{g}/\text{mm}^2$. In a previous study [44], contact angle measurements on composite surfaces with the exact same surface treatment showed an average of $40.9^{\circ} \pm 5.6^{\circ}$ angle on the surface after pre-treatment (PF-QD + UV/ozone) and $110.5^{\circ} \pm 0.7^{\circ}$ after contamination.

2.2.2. Bonded specimens

DCB coupons were manufactured by bonding two composite plates. The bonding process consisted of a secondary bonding, meaning that the composite plates were bonded after being cured. The bonding curing cycle was performed in an autoclave for 90 minutes at 120°C and 3 bars pressure with the contamination strip being applied along ca. 20 – 25 mm of the 220 mm length, on the surface of one of the CFRP adherends. Fig. 1 (b) shows an example of the bonded test panels (with contamination). Five specimens were cut from the bonded panels to the desired dimensions of 25 mm in width and 220 mm in length. Subsequently the adhesive thickness $t = 0.24 \pm 0.04$ mm was measured with the optical microscopy – see Fig. 1 (c).

Fig. 2 shows an example of the ultrasonic C-scan of the contaminated specimens before testing (squitter C-scan, 10 MHz frequency, crystal diameter 10 mm, water nozzle 8 mm diameter, scanned every 1 mm, 10 dB damping, no filters). The Teflon[®] tape area of the pre-crack is clearly visible, however, a more regular signal could be expected. Due to the wet environment in which the

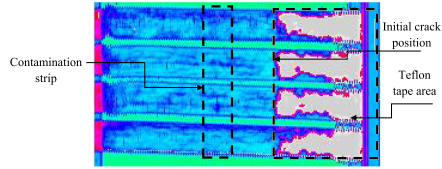


Fig. 2. Ultrasonic C-scan of the contaminated DCB specimens [46].

scanning takes place, a water penetration from the free edges is observed at the areas of the Teflon[®] insert. No defect can be detected in the area of the contamination strip. This confirms the presence of a 'kissing bond' inside DCB specimens.

2.3. DCB test

The experimental configuration is presented in Fig. 3. DCB specimens were installed in an universal testing machine (Zwick/Roell Z050, Zwick/Roell, Germany) and tested under displacement rate controlled conditions: $\frac{d\Delta}{dt} = \dot{\Delta} = 10$ mm/min. The applied force, P , and the specimen tip displacement, 2Δ , were recorded simultaneously at 10 Hz acquisition rate and used for the data reduction.

2.4. In-situ and post-mortem observations

The crack growth process was tracked from the side using a 5 megapixel resolution optical macro/microscope (Dino, ProLite, The Netherlands) at 1 Hz acquisition rate. To investigate features of fracture surfaces a wide area, three-dimensional measuring macroscope and a fringe projection scanner (Keyence VR-3200, Japan) were used. The scanner is characterized by < 100 nm out-of-the-plane resolution with up to a 200×200 mm² measuring area.

3. Analytical model

It is postulated that the composition of the bondline i.e. the epoxy adhesive and the 2D grid, requires an analytical model to be decomposed accordingly.

3.1. Steady-state model of debonding

The physical model is based on the kinematic assumptions of

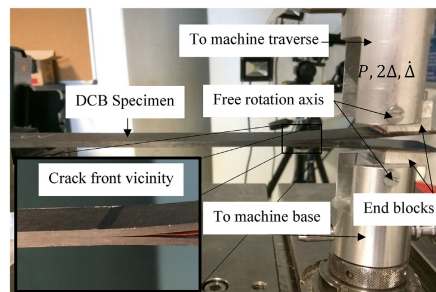


Fig. 3. The DCB experiment.

simple beam theory, e.g. in which the effects of the shear forces (thickness $h < a$, with a being the instantaneous crack length) are neglected. Considering half of the symmetric specimen (from the boundary condition at the loaded tip) the compliance of the specimen read as:

$$C = \frac{\Delta}{P} = \frac{a^3}{3E_1I} \quad (1)$$

where $I = \frac{bh^3}{12}$ is the second moment of the beam cross section area. The product E_1I expresses the effective bending rigidity assuming cylindrical bending of the laminated plate [47]. Using the Irwin-Kies compliance formula [2], the mode I Energy Release Rate (ERR), i.e. the driving force, can be expressed as:

$$\mathcal{G}_I = \frac{P^2}{2b} \frac{dC}{da} \quad (2)$$

The effect of the finite compliance of the loading system is in the present case neglected. Substituting eq. (1) into eq. (2) yields:

$$\mathcal{G}_I = 3 \frac{P}{bh} \sqrt{\frac{P\Delta^2}{2bE_1}} = \frac{1}{6E_1h^3} \left(\frac{Pa}{b}\right)^2 \quad (3)$$

The Griffith's fracture criterion is assumed once the driving force equals the fracture energy $\mathcal{G}_I = \mathcal{G}_{Ic}$, denoting the onset of the crack. Assuming $\mathcal{G}_{Ic} = \text{const.}$ eq. (3) is solved for a and introduced to eq. (1) revealing that at the crack onset, the linear relation between P and Δ bifurcates into a nonlinear one:

$$P = \gamma \Delta^{-1/2} \quad (4)$$

with $\gamma = 2b\sqrt{\frac{h^3E_1}{3}\mathcal{G}_{Ic}^3/4}$. Eq. (4) provides a power law for the steady-state, self-similar crack growth process and can be conveniently used to extract the fracture energy by a simple allometric function curve fitting. Interchanging the dependent variable in eq. (3) through eq. (1), viz. $P \rightarrow \Delta$, and upon further rearrangement the instantaneous crack length is given by:

$$a = \left(\frac{3}{8} \frac{E_1h^3}{\mathcal{G}_{Ic}}\right)^{\frac{1}{4}} \Delta^{\frac{1}{2}} \quad (5)$$

The second scaling is revealed - during the DCB experiment the crack position $\sim \Delta^{\frac{1}{2}}$. We introduce the crack growth rate in the form:

$$\dot{a} = \frac{da}{dt} = \frac{\partial a}{\partial \Delta} \frac{d\Delta}{dt} = \frac{1}{2} \left(\frac{3}{8} \frac{E_1h^3}{\mathcal{G}_{Ic}}\right)^{\frac{1}{4}} \Delta^{-\frac{1}{2}} \quad (6)$$

Eq. (6) seems of fundamental importance revealing an inherent effect of crack growth and loading rates on the fracture energy,

$\mathcal{G}_{Ic} \sim \left(\frac{\dot{a}}{a}\right)^4$. The elastic strain energy is given by $U = \frac{1}{2}P\Delta =$

$\frac{1}{2}C^{-1}\Delta^2$. The rate form of U can be obtained by using the chain rule:

$$\frac{dU}{dt} = \frac{\partial U}{\partial \Delta} \frac{d\Delta}{dt} + \frac{\partial U}{\partial a} \frac{da}{dt} \quad (7)$$

With $U = \frac{3}{8} \frac{E_1h^3\Delta^2}{\mathcal{G}_{Ic}}$:

$$\dot{U} = \frac{3}{2}E_1I \left(\frac{2\Delta}{a^3} - \frac{3\Delta^2\dot{a}}{a^4}\right) \quad (8)$$

where $\dot{U} = \frac{dU}{dt}$. Under the displacement controlled conditions

$\mathcal{G}_I \stackrel{\text{def}}{=} -\frac{1}{b} \frac{dU}{da}$ yielding:

$$\mathcal{G}_I = \frac{1}{b} \left(\frac{\partial U}{\partial a} - \frac{\partial U}{\partial \Delta} \frac{d\Delta}{da}\right) \quad (9)$$

leading to:

$$\mathcal{G}_I = E_1h^3 \left[\left(\frac{3}{8} \frac{\Delta^2}{a^4}\right) - \left(\frac{1}{4} \frac{\Delta}{a^3} \frac{d\Delta}{da}\right) \right] = \mathcal{G}_{Is} - \mathcal{G}_{Ik}(\dot{\Delta}, \dot{a}) \quad (10)$$

The result, with \mathcal{G}_{Is} being the static part and $\mathcal{G}_{Ik} = f(\dot{\Delta}, \dot{a})$ being the kinetic part, refers to the generalization of the Griffith's fracture theory [48,49]. Simplifying eq. (5) to a more convenient form:

$$a = \psi \Delta^{\frac{1}{2}} \quad (11)$$

with $\psi = \left(\frac{3}{8} \frac{E_1h^3}{\mathcal{G}_{Ic}}\right)^{\frac{1}{4}}$, subsequently, taking the power of 2 on both sides and upon further derivation yields:

$$\frac{d\Delta}{da} = 2\psi^{-2}a \quad (12)$$

which upon substitution to eq. (9) leads to an alternative form of eq. (10):

$$\mathcal{G}_I = \frac{E_1I}{b} \left[\left(\frac{9}{2} \frac{\Delta^2}{a^4}\right) - \left(6 \frac{\Delta}{a^2} \psi^{-2}\right) \right] \quad (13)$$

Eq. (13) exposes an inherent property of the DCB set-up for which the driving force is expected to rise during the experiment with the asymptote of a quasi-static fracture energy \mathcal{G}_{Ic} . As such, the recorded experimentally measured \mathcal{G}_I , though directly related, cannot be treated as the intrinsic material property. While, quantitatively, the effect is not expected as dominating (for the present case the ratio $\frac{\mathcal{G}_{Ik}}{\mathcal{G}_{Is}}$ is evaluated to max. 10%) it highly affects qualitative interpretation. Following the 'standard' analysis, $\mathcal{G}_I = \mathcal{G}_{Is}$ viz. eq. (3), once $\mathcal{G}_I = \mathcal{G}_{Ic}$, the crack growth is essentially a 'critical state' process viz. $\frac{d\mathcal{G}_I}{da} = 0$. During the DCB experiment, the presence of the kinetic component, $\mathcal{G}_I = \mathcal{G}_{Is} - \mathcal{G}_{Ik}$ viz. eq. (10) indicates the process to be stable: $\frac{d\mathcal{G}_I}{da} > 0$ and $\frac{d\mathcal{G}_I}{da} < 0$ and may explain the reason behind a rising resistance curve as often observed when testing layered materials [50,51].

3.2. Non-smooth debonding

The core of the analytical model is shared with the one used in Ref. [39] and, thus, some details are omitted in the following presentation. A cantilever beam is attached to a unit pattern model at the crack tip following Fig. 4.

The governing equation of the Euler-Bernoulli beam, following Pagano's model [5], reads:

$$E_1I \frac{d^4w}{dx^4} + b\sigma(x) = 0 \quad (14)$$

where σ represents the cohesive stress inside the bondline. $\sigma = 0$ for the unbonded zone(s) and $\sigma \neq 0$ for the bonded zones. Due to the finite rigidity of the interface a process zone of length $\lambda^{-1} = \sqrt{\frac{4E_1I}{k}}$ exists ahead of the crack tip for which the $\sigma(x) > 0$. Since $\frac{E_1}{E_2} = \frac{1}{10}$ the foundation constant k will be associated solely to the bondline material, i.e. $k = m\left(\frac{E_2}{l}\right)b$, where m allows for an arbitrary

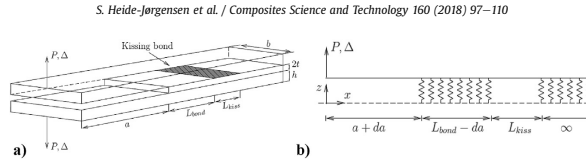


Fig. 4. The model of the beam on interface with the kissing bond. a) Illustration of the DCB specimen with a kissing bond. b) Schematics of the kissing bond model.

interpretation of the crack front stress state [52,53]. In the present case, the plane strain conditions are assumed at the crack tip [54] leading to $\lambda^{-1} \cong 2.4 \text{ mm}$. The model can be extended to account for the cohesive tractions exhibited by the composite plate [52]. In this case, the foundation modulus needs to be redefined as $k_t^{-1} = k^{-1} + k_c^{-1}$ with k_c^{-1} reflecting the transverse stiffness of the composite material. The model is then subdivided into a free part (cantilever), a first bonded zone of length L_{bond} , a kissing bond zone of length L_{kiss} , and a second bonded zone spreading to infinity. The region from the first to the second bonded zone constitutes the unit pattern which can be incorporated as a loop used repeatedly during the crack growth. The solution for each of the governing equations give the full description of the unit pattern model:

$$w(x, \beta) = \begin{cases} \frac{P(\frac{1}{2}L\beta x^2 + \frac{1}{2}ax^2 - \frac{1}{6}x^3)}{E_1 I} + C_1 x + C_2 & \forall 0 \leq x \leq a + da \\ \cosh(\lambda x)(C_3 \cos(\lambda x) + C_4 \sin(\lambda x)) \\ \quad + \sinh(\lambda x)(C_5 \cos(\lambda x) + C_6 \sin(\lambda x)) & \forall a + da \leq x \leq a + L_{bond} \\ \frac{1}{6}C_7 x^3 + \frac{1}{2}C_8 x^2 + C_9 x + C_{10} & \forall a + L_{bond} \leq x \leq a + L_{bond} + L_{kiss} \\ e^{\beta x}(C_{11} \cos(\lambda x) + C_{12} \sin(\lambda x)) & \forall a + L_{bond} + L_{kiss} \leq x \leq \infty \end{cases} \quad (15)$$

where $C_1, C_2, C_3, C_4, C_5, C_6, C_7, C_8, C_9, C_{10}, C_{11}, C_{12}$ are unknown constants to be determined through the four boundary conditions, i.e. $w(x=0) = \Delta, \frac{dw}{dx}(x=0) = 0, w(x=\infty) = 0, \frac{dw}{dx}(x=\infty) = 0$, and C^3 continuity conditions (continuity of displacement field, rotation, strain and shear forces) between each of the zones. In this model a is the initial crack length, da is the instantaneous crack growth and β is the ratio defined as $\beta = \frac{L_{kiss}}{L_{bond} + L_{kiss}}$. Importantly, in the far field the solution experiences exponentially modulated decay while within the zone of the finite length ($\cong 2\lambda^{-1}$) exponential growth toward the ends could be expected [52,55]. The model is implemented through a script written in Matlab® (v.2016b, MathWorks, USA) in which the continuous loading conditions are reproduced and the snap-back behaviour, viz. $d\Delta < 0$, is penalized. The ERR is then obtained through eq. (9).

3.3. Bridging

The bridging phenomena is considered an efficient way of increasing the fracture energy of composite materials. Different models are proposed to account for the fibre bridging between the cracked surfaces [6,56–59]. Since, in the present case, the composite adherends are bonded the bridging is not expected once the

crack locus is cohesive within the bondline, i.e. the bridging due to the fibres closing the cracked faces is an unlikely event. However, the physical composition of the bondline, i.e. the adhesive and the polymer carrier induces a bridging component between the two bonded surfaces which proved an efficient way of increasing the total ERR defined as:

$$\mathcal{E}_{It} = \mathcal{E}_I + \mathcal{E}_b \quad (16)$$

where \mathcal{E}_I refers to the ERR from eq. (13) and \mathcal{E}_b is the ERR due to bridging. In the present case, the bridging will 'effectively' be defined by:

$$\mathcal{E}_b = \frac{\mathcal{E}_{cp}}{b} \int_{a_0}^{a_0 + l_{bz}} f(a) da \quad (17)$$

where \mathcal{E}_{cp} is the energy at failure associated with the carrier (at this stage we will not decide the failure mode of the carrier) viz. a constant, which can be deduced from the experimental data. a_0 is the crack length at which the bridging phenomenon begins (most likely the initial crack length) and l_{bz} is a self-similar length of the bridging zone evaluated from the experimental data once the steady-state process begins. The definite integral formulation accounts for a cumulative effect from increasing the length of bridging zone during the crack growth. In general, an arbitrary, non-dimensional, function $f(a)$ of the crack position can be used as a kernel of the integral. In the present case $f(a)$ is assumed a constant, and thus, \mathcal{E}_b increase linearly until the full length of the bridging zone is established, $\mathcal{E}_b \sim \int_{a_0}^{a_0 + l_{bz}} 1 da \equiv l_{bz}(a)$. From that moment, l_{bz} is treated as an inherent property related to the bridging phenomena and further increase of the crack length will result in a steady-state process for which $l_{bz} = \text{const.} \cdot \frac{d\mathcal{E}_b}{da} = 0$. Equivalently, at the front of the bridging zone the carrier film needs

102

S. Heide-Jørgensen et al. / Composites Science and Technology 160 (2018) 97–110

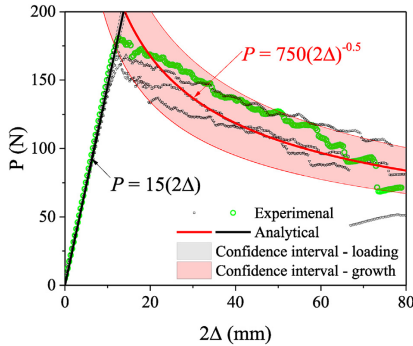


Fig. 5. The load response curves for the specimens without kissing bond. The experimental and the analytical data are plotted with the 95% confidence bounds.

to fracture or peel from the adherend. Finally, once the distance between the crack tip and the kissing bond $< l_{bz}, l_{bz}$ decreases and so will be \mathcal{S}_b as stated by eq. (17). The effect of the formation and the diminishment of the bridging zone on the ERR can be described as follows:

$$\begin{aligned} \mathcal{S}_b &= 0 \quad \forall a \leq a_0 \\ \frac{d\mathcal{S}_b}{da} &> 0 \quad \forall a \rightarrow a_0 + l_{bz} \\ \frac{d\mathcal{S}_b}{da} &= 0 \quad \vdash \quad \mathcal{S}_b = \text{const.} \quad \wedge l_{bz} = \text{const.} \\ \frac{d\mathcal{S}_b}{da} &< 0 \quad \forall l_{bz} > l - a \end{aligned} \tag{18}$$

where l is the distance between the load application point and the end of the bonded zone.

Within the scope of the present study the fracture energy of the kissing bond region was not evaluated. It is deemed (though not verified) that within this region the bonding is mainly due to very weak van der Waals interactions. Specimens with a (full) kissing bond pre-treatment felt apart under handling. Therefore, within the kissing bonds, values of $k = 0$ and $\mathcal{S}_{lc} = 0$ were adopted when necessary.

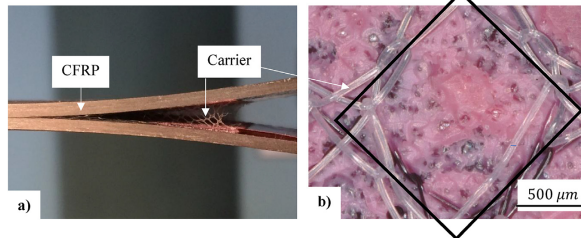


Fig. 6. Bridging of the cracked faces due to the embedded net. (a) An image taken during the DCB experiment. (b) A microscopic view of the fracture surface with the characteristic diamond-celled feature of the embedded net.

4. Results and discussion

4.1. Continuous interface

In Fig. 5 the load response during debonding of composite plates is presented. Results correspond to specimens with continuous interfaces – without the kissing bond. The experimental (points) and the analytical (lines) data corresponding to the steady-state model are presented. The analytical data provides the initial compliance of the system, eq. (1) (black line and a shaded area representing 95% confidence bounds) and the crack growth path, eq. (4) (red line with the shaded area referring to 95% confidence bounds).

During loading the experimental and the analytical data exhibit a similar, linearly increasing trend. The agreement is very good. Once the fracture threshold is attained, i.e. $\mathcal{S}_1 = \mathcal{S}_{lc}$, the linear path bifurcates to a nonlinear one and $P \sim \Delta^{-0.5}$. The crack growth stage begins. The analytical curve characterizing this stage is obtained by fitting an allometric function with the fixed power coefficient of -0.5 to all the experimental data. The coefficient of determination obtained $R^2 \cong 0.95$, suggests a very good correlation between the analytical and experimental data, however, a clear, systematic, deviation can be noticed. To facilitate this observation one of the experimental series is highlighted. In specific, the onset of the crack growth, as indicated by the experimental data, initiates from the analytical lower bound and tends, almost linearly, to the upper bound. This indicates a rising trend of the R curve. In the final stage, the trend is reversed and the curve begins to move towards the lower bound. The crack front is approaching the end of the crack growth path, which remains out of the scope of the present study. The more detailed analysis of this behaviour can be found in Refs. [52,60].

4.1.1. Crack locus and crack growth path

Fig. 6 shows details of the crack growth process (a) and a representative microscopic view of the fracture surface presenting a unit cell of the carrier (b).

From Fig. 6 (a) it is apparent that the crack growth is hindered by the bridging phenomena introduced by the knit carrier of the adhesive. Importantly, the crack growth is of cohesive nature, i.e. within the adhesive material, for all the specimens tested. The appearance of the fracture surface is presented in Fig. 6 (b) where the (pink) epoxy phase coexists with the knitted structure of the carrier.

In Fig. 7 a three-dimensional (3D) representation of the fracture surface is presented. In Fig. 7 (a) the crack growth paths for both of the specimen adherends (denoted by + and -) are shown. In Fig. 7

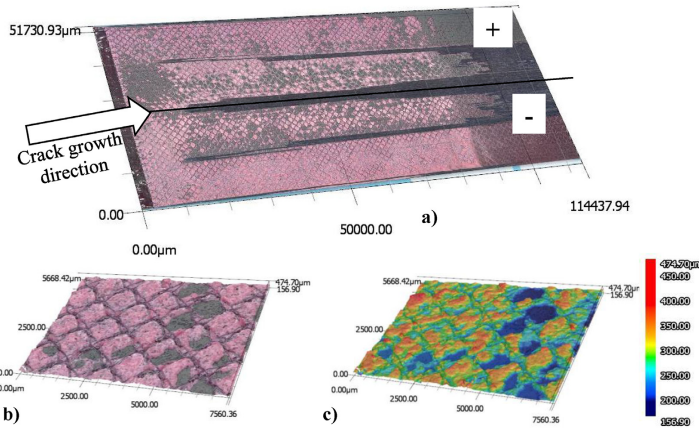


Fig. 7. Details of the fracture surfaces obtained by a scanning microscope. (a) Optical scan of the entire fracture surface for both adherends (+ and -). (b) Optical and magnified view of the fracture surface with visible features of the embedded net. (c) A 3D representation of (b). The scale is given in μm .

(b) and (c) a more detailed view of an arbitrary region of the crack growth path is presented.

The fractography reveals a specific pattern of the carrier grid. It is becoming evident that two fracture processes take place simultaneously. At first, the crack grows inside the epoxy phase. The crack tip does not propagate through the filament phase c.f. Fig. 6 (b), instead it propagates along the interface between the epoxy and the carrier grid. Consider following scenarios: 1) the carrier remains bonded to one of the adherends as the crack propagates cohesively, and 2) the carrier remains attached to both adherends. In the first case, the entire process of crack growth is driven by the epoxy phase. The presence of the carrier is affecting the composition of the crack growth path, however such effect is expected to be relatively small (this will be followed at the later stage). The latter case, depicted in Fig. 6 (a), is found for most of the specimens tested and enables the bridging between two adherends. The additional, unexpected, dissipation process functionalized through the bridging can, potentially, severely affect the strain energy release process.

4.1.2. Driving force and resistance curves

In Fig. 8 the driving force/resistance curves are plotted. Results of three experiments, \mathcal{G}_i^{exp} , are plotted as points. The analytical results are presented as lines - dashed and solid. Plotted are: the total ERR, \mathcal{G}_t c.f. eq. (16), together with the bridging, \mathcal{G}_b c.f. eq. (17) and the static, \mathcal{G}_{Is} , and the kinetic, \mathcal{G}_{Ik} , components of \mathcal{G}_i c.f. eq. (10).

To facilitate the discussion a schematic representation of the fracture process is provided in Fig. 9

During the first stage, denoted as (1) in Figs. 8 and 9, a process zone of length λ^{-1} is created and crack driving force increases until $\mathcal{G}_i = R = \mathcal{G}_t$. R is used to denote the resistance of the structure against crack extension which differs from the fracture energy, \mathcal{G}_t , assumed as a material constant under static loading conditions. As expected, the loading kinetic effect is quantitatively not dominating, however non-negligible. However, it is due to the loading kinetic, eq. (13), and the bridging, eq. (17), effects, that the

horizontal path, i.e. $\mathcal{G}_i = R$, should not be expected and is replaced by a linearly increasing path – stage (2). The bridging effect, \mathcal{G}_b^{exp} , is estimated from experiments as a difference between the analytically obtained ERR, i.e. related to fracture of the epoxy phase, \mathcal{G}_t , and the ERR calculated using eq. (3) applied to the experimental force and displacement data. A bridging energy threshold is equated to $\mathcal{G}_{cp} \cong 1 \text{ N/mm}$. The corresponding bridging zone spreads over $l_{bz} \cong 20 \text{ mm}$, which is found consistent with the macroscopic observations, Fig. 6 (a). Once the bridging zone is fully developed - l_{bz} becomes constant, a steady-state process is expected – stage (3). Note that due to the loading kinetic effect during stage (3) i.e. $\frac{d\mathcal{G}_i}{da} > 0$ the process is stable.

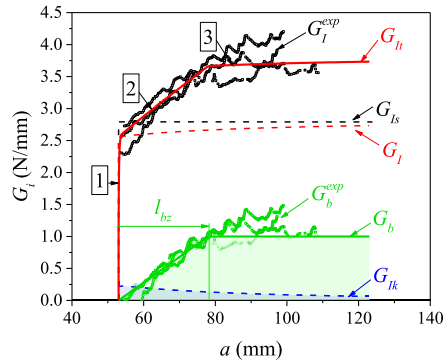


Fig. 8. The driving force/resistance curves. The experimental and analytical results are plotted. \mathcal{G}_t^{exp} and \mathcal{G}_b^{exp} represents the total and the bridging component of ERR obtained from the experimental data. The analytical, total ERR \mathcal{G}_{tot} is composed from static \mathcal{G}_{Is} , kinetic \mathcal{G}_{Ik} and bridging \mathcal{G}_b components.

104

S. Heide-Jørgensen et al. / Composites Science and Technology 160 (2018) 97–110

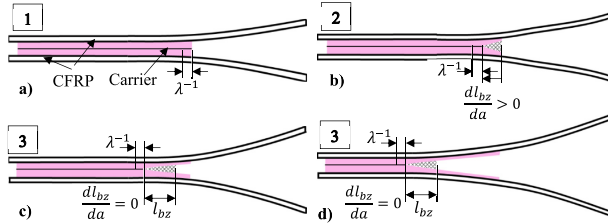


Fig. 9. Proposed description of the fracture process. (a) The configuration at the crack onset. (b) The crack growth through the bonding is assisted by creation of a bridging zone. (c)–(d) The bridging zone reaches a characteristic, self-similar, length l_{bz} . Numbers refer to stages indicated in the text and Fig. 8.

4.2. Discontinuous interface

In Fig. 10 the load responses of the specimens with the kissing bond are presented. The experimental and the analytical data are depicted. Confidence bounds, as obtained from the data for specimens without the kissing bond, are used.

The initial, linear loading path is similar to the specimens without the kissing bond. The loading path bifurcates to the steady-state crack growth stage near the lower bound values. As previously, the load response does not follow the steady-state trend but, instead, rises above it. The situation changes once $2\Delta \approx 30\text{ mm}$. The crack front approaches the kissing bond position. The crack rate increase, $\frac{da}{dP} \rightarrow \infty$, due to the edge effect and, eventually, the crack snaps through the kissing bond to the arrest position, $a \rightarrow a + L_{kiss}$. This process is captured as a snap-down, i.e. $\frac{da}{dP} = 0$. Subsequently, the loading and the crack initiation stages are repeated followed by a steady-state crack growth process.

4.2.1. Crack locus and crack growth path

In Fig. 11 a stereoscopic view of the crack growth path of the specimen with the kissing bond is presented.

The difference between the (strongly) bonded and the kissing bond zones is clearly visible. The strongly bonded zone shares the

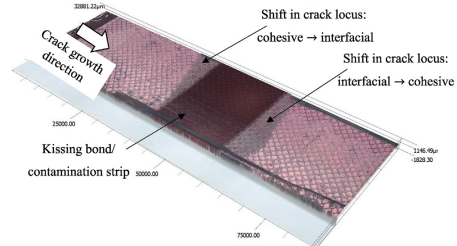


Fig. 11. A 3D image of the fracture surface of one of the adherends with kissing bond along the crack growth path. The scale is given in μm .

same features as observed for the ‘continuous’ specimens. The crack propagated cohesively revealing the characteristic structure of the embedded carrier. Along the kissing bond crack propagated in the adhesive manner – along the composite/adhesive interface. The proximity of the kissing bond zone revealed areas of finite length, indicated by arrows in Fig. 11, that could be related to shift in the crack locus from the cohesive, inside the bondline for the strongly adhering zones, to the interfacial, along the composite/adhesive interface, along the contaminated area. In Fig. 12 the

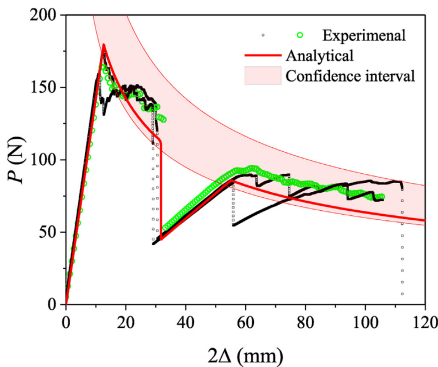


Fig. 10. The load response curves for the specimens with 20 mm kissing bond. The experimental (points) and the analytical (lines) data are plotted with the 95% confidence bounds.

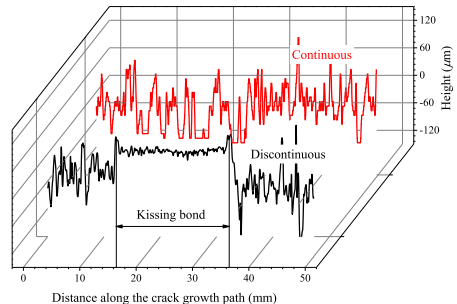


Fig. 12. Comparison of the fracture surface profiles for specimens with and without kissing bond. The profiles were taken along a straight line along the crack growth path.

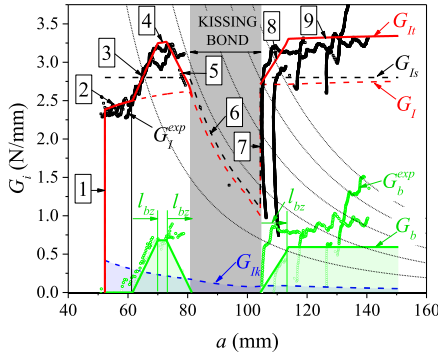


Fig. 13. The driving force/resistance curves for the specimens with a kissing bond along the crack growth path. G_t^{exp} and G_b^{exp} represents the total and the bridging component of ERR obtained from the experimental data. The analytical, total ERR G_t^a is composed from static, G_{Is} , kinetic, G_b , and bridging, G_b , components. The thin, parallel lines, running from the top to the right of the graph, represent the release of the elastic energy due to the snap-down phenomena.

$\approx 37 \mu\text{m}$ for the cohesive fracture surface, while $R_a \approx 3 \mu\text{m}$ for the kissing bond area. The values express an average from the three specimens with the three height profiles taken from each of specimens along the crack growth direction.

4.2.2. Driving force and resistance curves

In Fig. 13 the driving force/resistance curves are shown for the discontinuous bondline cases. The experimental and the analytical data are plotted. A grey rectangle is added to denote the size and the position of the kissing bond. Thin, dashed lines represents release of the elastic energy due to the kissing-bond induced snap-down phenomena. The family of curves is then obtained by assuming different values of \mathcal{E}_{Ic} and continuous loading conditions.

During loading, stage (1) in Fig. 13, the crack driving force increases following a vertical path providing no crack growth occurred. Once the adhesive fracture energy threshold is attained, the crack begins to grow – (2). Note, that contrary to the previous results the bridging does not occurred immediately after onset of the crack and the crack grows following eq. (13), c.f. \mathcal{E}_I . Indeed, the beginning and the end of the bridging process were not controlled. The post-mortem inspection revealed that for the discussed case the carrier remained initially attached to one of the adherends. After ca. 10 mm the cohesive crack growth develops into a process assisted by the bridging – (3). From this stage the fracture process deviates strongly from the one observed for the specimens without the contamination. To facilitate discussion chosen stages of the fracture process are schematically depicted in Fig. 14 (a)-(d) with the numbers referring to Fig. 13.

A similar bridging law is used as for the continuous bondline specimens. However, the length of the bridging zone, as estimated from the experimental data, is now limited to $l_{bz} \approx 7 \text{ mm}$ due to the finite size of the bonded zone of ca. 25 mm. Indeed, provided that the crack grew for ca. 10 mm without the bridging, only 15 mm remains for building and diminishing of the bridging zone. An

height profile of the fracture surface, for arbitrarily chosen line along the crack growth direction, are presented. Specimens with (discontinuous) and without (continuous) kissing bond are compared.

A difference exists between the cohesive and the adhesive fracture zones. Along the kissing bond a mirror like surface is produced. In contrary, along the cohesive fracture surface, surface profile oscillations become apparent. The arithmetic mean deviation of the profile, i.e. the roughness parameter R_a equates to

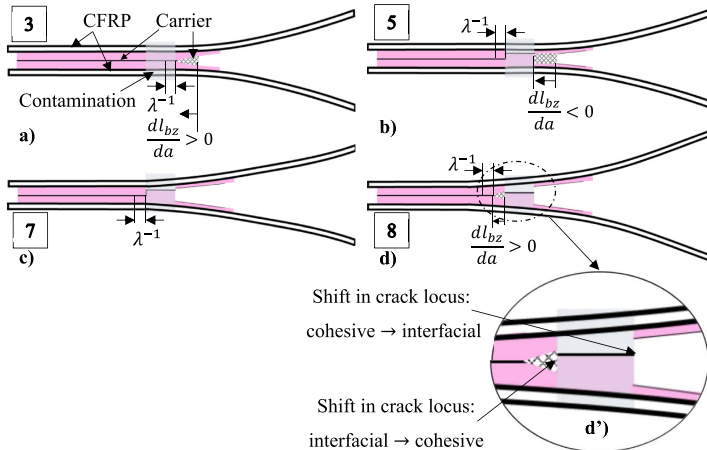


Fig. 14. Chosen aspects of the fracture process of contaminated specimens. (a) The build-up of the bridging zone. (b) The bridging zone length decreases due to the vicinity of the kissing bond. (c) The crack front attains crack arrest position. (d) The crack growth from the arrest position incorporating bridging. (d') A detail of (d) showing a crack growth path in the vicinity of contamination. Numbers refer to stages indicated in Fig. 13.

106

S. Heide-Jørgensen et al. / Composites Science and Technology 160 (2018) 97–110

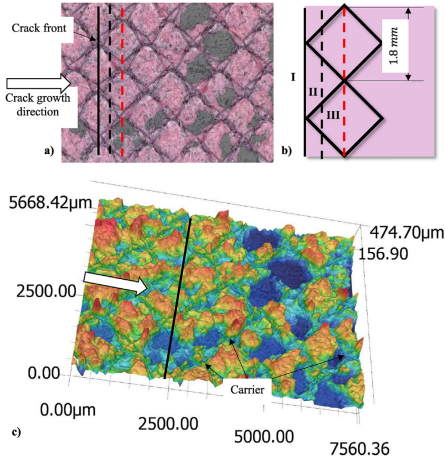


Fig. 15. Details of the crack growth path morphology obtained from 3D scanning. (a) Top view of the fracture surface presenting the orientation of the crack front and the propagation direction. (b) Simplified representation of the crack growth path and the unit cell structure of the embedded carrier. (c) Topography of the crack growth path.

approximately 3 mm transition zone between the increasing and the decreasing stages – (4) is allowed. First, the crack front process zone, defined by λ^{-1} , and later the bridging zone, defined with l_{bz} , are affected by the finite size of the bonded region. While $\lambda^{-1} < l_{bz}$, the process zone is responsible for transferring most of the external loading, i.e. $\mathcal{S}_I > \mathcal{S}_b$. Once attaining the kissing bond position $\frac{da}{da} < 0$, $\mathcal{S}_{It} > R \lambda \frac{d\mathcal{S}_a}{da} < 0$ - the crack accelerates, viz. (5) and Fig. 14 (b). Eventually, the load carrying capacity is lost. According to Fig. 10, the snap-down phenomenon takes place with the crack front arresting at the new position denoting the end of the kissing bond, viz. $\frac{da}{da} = 0$: $a \rightarrow a + L_{kiss}$. Since the process is instantaneous (at least in respect to the loading rate, viz. $\dot{a} \gg \Delta$) the loading conditions are equivalent to setting $\Delta = const.$ in eqs. (3) and (10). The model follows the force and the displacement data, including the snap-down data from Fig. 10, applied via eq. (3), which are non-zero and continuous along the snap-down owing to the analytical nature of the solution. Consequently, a stable crack driving force

equilibrium path - stage (6) in Fig. 13, is obtained. At the crack arrest position, a new loading path nucleates – (7), Fig. 14 (c). Once $\mathcal{S}_{It} = R$ the loading path bifurcates to the crack growth path but this time the crack growth is assisted by building of the bridging zone – (8), Fig. 14 (d). As a consequence of a series of events (5)–(8) the crack locus shifts twice as schematically shown in Fig. 14 (d') and as implied already from the crack growth path, c.f. Fig. 11. Once the bridging zone is developed the crack begins to propagate in a steady-state manner – (9). It can be observed that one of the curves reaches the level of the specimen without the contamination. On average the effects seem to be smaller. However, at this stage we cannot provide any quantitative reason behind this phenomena. The bridging process was neither designed nor controlled and as such this behaviour could be of stochastic nature. The process described summarizes the main part of the present study. However, during the steady-state process an oscillatory *R* curve character is witnessed, Figs. 8 and 13, which, potentially, makes a steady-state fracture energy an inadequate failure criterion.

5. Oscillating *R* curve: an ad-hoc interpretation of effects due to the carrier lattice structure

5.1. Surface morphology

The primary role of the knitted carrier used within the bondline is to assure a homogeneous and a consistent/reproducible bondline thickness. One of the important findings of the present study reveals a, potentially, huge impact of the carrier on the macroscale fracture resistance. In reality, the presence of the carrier changed the fracture process on both, the macro- and the microscales. The situation depicted in Fig. 6 (a), i.e. the large-scale bridging must at some stage lead to either ripping/fracture or peeling of the carrier lattice from the adhesive phase and, hence, enhancing the damage tolerance of the joint. In Fig. 15 a detailed view of the fracture surface obtained using the 3D scanning technique is presented. In Fig. 15 (a) a top view is given from which a clear distinction between the carrier and the epoxy adhesive can be made. In Fig. 15 (b) a schematic representation of the cell structure of the carrier is proposed. Fig. 15 (c) reveals the complex topography of the fracture surface.

As the available data are unsystematic and due the complexity of processes involved [61–63], which demands a detailed and a separate treatment, a refined quantitative analysis will be pursued in a future study. At present, however, a qualitative explanation will be attempted.

5.2. Peeling of the carrier

Consider a straight front crack propagating through the growth

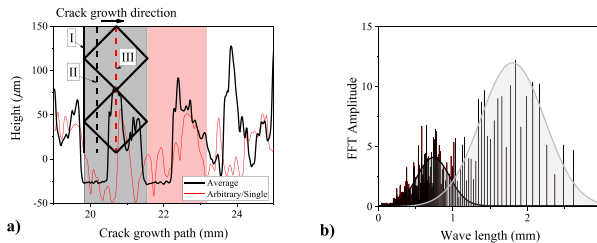


Fig. 16. Surface profiles along the crack front direction. I, II, III refer to the straight crack front position in respect to the lattice grid and consistent with Fig. 15.

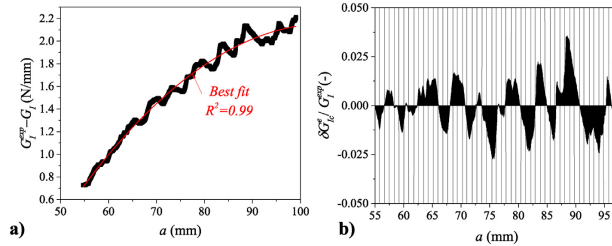


Fig. 17. (a) The difference between the experimental and the analytical energy release rate for one of the specimens. (b) The normalized residuals of the energy release rate.

path from position I to position III as schematically presented in Fig. 15 (a) and (b). Taking a straight-line cut, the fraction occupied by the adhesive is $f = \frac{l_a}{l_a + l_f}$, with l_a being the line length associated to the adhesive and l_f the length associated to the carrier. In Fig. 16 (a) the height profiles taken along the crack front direction are presented. The results correspond to a single specimen but are representative and reproducible. A thin line illustrates a surface profile along a single, arbitrary path while a bold line is obtained by averaging the height profile along the straight crack front.

It is assumed that the minimum observed from the average height profile is expected once the crack front position corresponds to position I in Fig. 15 (b) (minimum number of knots). For a better illustration, two unit cells of the grid are added to Fig. 16 (a) with the shaded regions showing the characteristic length of the grid. At this stage a remark must be made that the carrier cells are not always regular nor consistently distributed, c.f. Figs. 6 (b) and 15 (a). A Fast Fourier Transform (FFT) is applied to the profile height for the data gathered along the fracture surface to decide whether or not the periodicity can be associated to the carrier (micro)structure. The results in the form of the FFT amplitude as a function of the wave length are presented in Fig. 16 (b). Two normal distributions are recognized. The mean wave length of the first distribution yields 0.81 mm while for the second, a value of 1.79 mm is found. This values clearly coincide with the half and the full length of the characteristic dimension of the unit cell.

When considering a straight crack front travelling through a single cell upon passing the knot position, viz. I → II, the fraction of the lattice $(1 - f)$ doubles. Subsequently, f remains constant until position III is reached - Figs. 15 (b) and 16 (a). However, providing that the number of cells along the crack front is high enough, ca. 15 cells in the present case, position III can be treated as equivalent to position I. Indeed, the agreement between the reported averaged height profile and the size of the grid appears convincing with the fracture surface experiencing a clear periodicity. To elucidate a possible effect of composition of the material along the crack front the effective fracture energy of the bondline (omitting the bridging effect) could be defined as [64,65]:

$$\mathcal{G}_{lc}^e = f \mathcal{G}_{la} + (1 - f) \mathcal{G}_{lf} \quad (19)$$

where \mathcal{G}_{la} and \mathcal{G}_{lf} refer to the fracture energy of the adhesive phase and fracture energy of the interface between the filament and the adhesive. Eq. (20) holds once assuming that the mechanical ERR expressed by components of \mathcal{G}_l coincides with the surface energy following the original assumption of Griffith's fracture theory. From Fig. 15 (a) $f \cong 0.9$ once the straight crack front goes through the knots and $f \cong 0.8$ elsewhere. This agrees with

calculations where each arm of the grid is assumed of ca. $2t$ thickness. Substituting such values to eq. (19) shows that oscillations in \mathcal{G}_l^e of order $10^{-2} - 10^{-1}$ could, at least to some extend, be associated with the pattern revealed by the fracture surface. In Fig. 17 (a) the difference between the experimental ERR and the analytical prediction of the fracture energy is given.

Since the bridging and the loading kinetic effects occurred, the data are fitted with the quadratic polynomial function using a least square method to give a trendline and to extract the ERR residuals. In Fig. 17 (b) the ERR residual, i.e. $\delta \mathcal{G}_{lc}^e = (\mathcal{G}_{lc}^{exp} - \mathcal{G}_l) - \mathcal{G}_l^e$, with \mathcal{G}_l^e being the expected (statistical) ERR, normalized by the experimental data are presented. Lines with the spacing resembling that of the unit cell are also provided. Once the residuals are plotted against the estimated crack length, a , an oscillating character is revealed. This observation coincides with eq. (19) and can be associated to the lattice-trapping characteristic. The period of the oscillations appears in an encouraging agreement with the size of the cell. However, contrary to eq. (19), which suggests a square wave lattice modulation with a jump at knot positions the experimental data clearly resembles a smoother wave pattern.

5.3. Fracture of the lattice

Following [66] the geometric parameters attributed to the lattice/grid structure are: the shape of the cell - diamond in the present case, the characteristic length of a single cell $l \cong 1.7 - 2$ mm and the shape and the characteristic length scale of the cell wall - thickness/diameter $t \cong 40 - 50$ μm . From Fig. 8 we noticed that the growth of the bridging zone, l_{bz} , is altered once $\mathcal{G}_b \cong 1$ N/mm, which is now assumed to equate to the remote tensile loading (bending and shear contributions should be negligible due to relatively flexible microstructure of the lattice) applied to the lattice material. The calculated fracture stress $\sigma_f \cong 50$ MPa, using the fraction f as estimated before but with the adhesive being replaced by an hole, seems reasonable and is close to the fracture stress of the epoxy adhesive phase once cured [40]. From an existing study

[66] it is recognized that $\sigma_f \propto C \left(\frac{2t}{l}\right)^2 \sigma_{TS}$ with $C = \text{const.}$ depending on the type of the unit cell and σ_{TS} being the tensile strength of the cell material. Taking $\sigma_{TS} = 800$ MPa as an average value for the

Nylon material (matweb.com) and equating $\left(\frac{2t}{l}\right)^2 \cong 0.4 (10^{-3})$ leads to $C \cong 0.4$ which stays in respectable agreement with the results reported for similar lattice systems [66–68]. Once the remote loading achieves σ_f one of the cells breaks. Recalling that the loading conditions do not allow for the snap-back behaviour, therefore the energy released can be attributed to the partial

unloading of the otherwise strained lattice structure. Subsequently, the complex composite/adhesive/lattice system is loaded again but in the meantime a new crack surface is created and the bridging zone restored. Leaving limitations of the proposed interpretation (due to e.g. neglecting the local variation in toughness [17,69,70], interactions with the remaining length scale parameters of the problem including the effect of the crack front shape [71–73], the adhesive process zone size, the increasing bridging zone size or the straining/restraining of the net material) aside, the deduced sequence explains an oscillating character of events visible in Fig. 17.

5.4. Trapping component of the ERR

The analysis provided indicates a possibility that the oscillating character of the *R* curve can be induced by the carrier used inside the bondline. To broaden the analysis, due to an apparent similarity between an atomic scale fracture [74,75] and the structure of the carrier, a lattice model is adopted. The effects mentioned at the end of Section 5.3, i.e. an outcome of the complexity of the material and the process, and standing behind the simplicity of the proposed explanation will lead to the smoothing of a square-wave function given by eq. (19). An empirical, quasi-equilibrium, crack resistance energy function can be introduced:

$$\mathcal{G}_c^e = \mathcal{G}_l + \mathcal{G}_b + \delta \mathcal{G}_L(a) \cos\left(\frac{2\pi l}{a} F^{-1}\right). \quad (20)$$

where $\delta \mathcal{G}_L(a)$ is a modulating trapping component related to the failure of lattice structure of the carrier and *F* is a function accounting for e.g. effect of the lattice structure inhomogeneity, straining of the lattice etc. As can be observed from Fig. 17 (b), the amplitude of the normalized ERR, thus $\delta \mathcal{G}_L(a)$, increases during the crack growth. The physical argument being that during the DCB experiment the force, *P*, decreases, cf. eq. (4), while fracturing or peeling of an unit cell of the carrier require a critical and constant value of the applied stress/force. The increase in the period of the oscillation, $\sim \left(\frac{l}{a}\right) F$, can be explained using the argument remaining in the spirit of the previous one. Since, viz. eq. (5), $\Delta \sim a^2$ increasing the load to the lattice failure level requires $\frac{d\Delta}{da} > 0$. The oscillating character indicates healing once the crack is trapped by the lattice and coalescing when the crack advances [2,76]. The

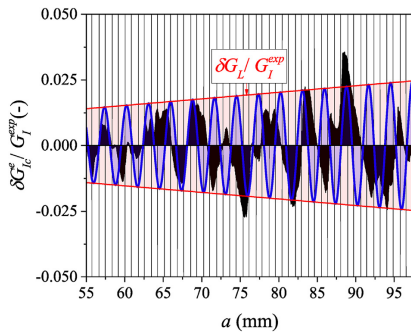


Fig. 18. Oscillating *R* curve with the lattice trapping component.

normalized lattice trapping component $\delta \mathcal{G}_L(a) \cos\left(\frac{2\pi l}{a}\right) / \mathcal{G}_I^{exp}$ is added to the previous results and shown in Fig. 18 as a continuous, bold (blue) line.

Even though a mismatch between the experimental and the analytical data exists the proposed model enables a correct estimation of a crucial lower and upper fracture thresholds. Indeed, eq. (20) exposes the following bounds:

$$\left. \begin{aligned} \mathcal{G}_{Ic}^{e+} &= \mathcal{G}_l + \mathcal{G}_b + \delta \mathcal{G}_L(a) \\ \mathcal{G}_{Ic}^{e-} &= \mathcal{G}_l + \mathcal{G}_b - \delta \mathcal{G}_L(a) \end{aligned} \right\} \quad (21)$$

which are added to Fig. 18 as bold (red) lines. Finally, it can be concluded that although the macroscopic response is present the macroscopic response of the specimen remains associated mainly to the effective fracture energy of the adhesive.

6. Conclusions

Debonding of composite plates containing kissing bonds along the crack growth path bonded with an epoxy adhesive with a carrier film is investigated experimentally and analytically. The load response data are collected and used to extract fracture properties. A rising *R* curve behaviour is revealed and associated to the loading kinetic effect and a bridging phenomenon. Contrary to the recognized fibre bridging phenomena expected during the delamination process of Fibre Reinforced Polymers [6,21,23,56,58], in the present case the bridging is induced by the two-phase composition of the bondline. The macroscopic camera observation reveals that the epoxy adhesive phase plays the role of matrix material for the second phase – 2D lattice material/grid. A significantly increased resistance to fracture of the bonded system is reported. This can be of fundamental importance for designing enhanced fracture toughness and damage tolerance facilitated through bridging of a 2D lattice material. Finally, using 3D fractography the characteristic lattice pattern is recognized on the fracture surface. An efficient analytical model is postulated in which the effects of the loading, the kissing bond and the bridging are incorporated. A complex fracture process is discovered allowing the following conclusions to be drawn.

- The presence of a kissing bond destabilizes the fracture process. In the present case, due to the size of the imperfection, $L_{kiss} > \lambda^{-1}$, the crack propagates in a non-smooth manner.
- The carrier used inside the bondline is found to, effectively, become a second and important phase of the bonding system. Two length scale parameters responsible for transfer of the load between the CFRP plates are recognized: 1) the process zone associated to the epoxy phase and 2) the bridging zone associated with the carrier. Due to the carrier, the resistance to fracture increases significantly by triggering a bridging phenomenon. The topic of using reinforcing materials in the form of lattices inside the adhesive layer can be of an importance for future adhesives with higher resistance to fracture and better damage tolerant. However, this demands further theoretical and experimental investigations.
- The complex fracture process is attempted analytically. The proposed model captures the effect of the loading rate, the kissing bond and uses bridging concept to explain the effect of the lattice/carrier material within the bondline.

Acknowledgments

The authors would like to thank 3M Netherlands B.V.

(Netherlands) for supplying the adhesive material.

This work is partly financed by the Netherlands Organisation for Scientific Research, project number 14366.

Appendix A. Supplementary data

Supplementary data related to this article can be found at <https://doi.org/10.1016/j.compscitech.2018.03.024>.

References

- [1] T.C. Triantafyllou, L.J. Gibson, Failure mode maps for foam core sandwich beams, *Mater. Sci. Eng.* 95 (1987) 37–53.
- [2] B.R. Lawn, *Fracture of Brittle Solids*, second ed., Cambridge University Press, Cambridge, 1993.
- [3] A. Chambolle, G.A. Francfort, J.J. Marigo, When and how do cracks propagate? *J. Mech. Phys. Solid.* 57 (2009) 1614–1622.
- [4] D. Leguillon, Strength or toughness? A criterion for crack onset at a notch, *Eur. J. Mech. Solid.* 21 (1) (2002) 61–72.
- [5] N.J. Pagano, Stress fields in composite laminates, *Int. J. Solid Struct.* 14 (5) (1978) 385–400.
- [6] Z. Suo, G. Bao, B. Fan, Delamination R-curve phenomena due to damage, *J. Mech. Phys. Solid.* 40 (1) (1992) 1–16.
- [7] J. Jumel, M.K. Budzik, N. Ben Salem, M.E.R. Shanahan, Instrumented end notched flexure – crack propagation and process zone monitoring. Part I: modelling and analysis, *Int. J. Solid Struct.* 50 (2) (2013) 297–309.
- [8] J. Jumel, N. Ben Salem, M.K. Budzik, M.E.R. Shanahan, Measurement of interface cohesive stresses and strains evolutions with combined mixed mode crack propagation test and Backface Strain Monitoring measurements, *Int. J. Solid Struct.* 52 (2015) 33–44.
- [9] F. Ozdil, L.A. Carlsson, Beam analysis of angle-ply laminate mixed-mode bending specimens, *Compos. Sci. Technol.* 59 (6) (1999) 937–945.
- [10] G.I. Barenblatt, Equilibrium cracks formed on a brittle fracture, *Dokl. Akad. Nauk SSSR* 127 (1) (1959) 47–50.
- [11] D.S. Dugdale, Yielding of steel sheets containing slits, *J. Mech. Phys. Solid.* 8 (2) (1960) 100–104.
- [12] M.F.S.F. de Moura, J.P.M. Gonçalves, A.G. Magalhães, A straightforward method to obtain the cohesive laws of bonded joints under mode I loading, *Int. J. Adhesion Adhes.* 39 (2012) 54–59.
- [13] H. Khoramishad, M. Hamzenezjad, R.S. Ashofteh, Characterizing cohesive zone model using a mixed-mode direct method, *Eng. Fract. Mech.* 153 (2016) 175–189.
- [14] B.F. Sørensen, E.K. Gamstedt, T.K. Jacobsen, Equivalence of J integral and stress intensity factor approaches for large scale bridging problems, *Int. J. Fract.* 104 (4) (2000) L31–L36.
- [15] E.K. Gamstedt, T.K. Jacobsen, B.F. Sørensen, Determination of cohesive laws for materials exhibiting large scale damage zones – from R-Curves for wedge loaded DCB specimens to cohesive laws, *Solid Mech. Appl.* 97 (2002) 349–352.
- [16] O. Lengline, R. Toussaint, J. Schmitzbuhl, J.E. Elkhoury, J.P. Ampuero, K.T. Talkad, S. Santucci, K.J. Maloy, Average crack-front velocity during subcritical fracture propagation in a heterogeneous medium, *Phys. Rev. E* 84 (3) (2011).
- [17] L. Legrand, S. Patinet, J.B. Leblond, J. Frelat, V. Lazarus, D. Vandembroucq, Coplanar perturbation of a crack lying on the mid-plane of a plate, *Int. J. Fract.* 170 (1) (2011) 67–82.
- [18] K. Kendall, Control of cracks by interfaces in composites, *P. Roy. Soc. Lond. A Mat.* 341 (1627) (1975) 409–428.
- [19] F. Condoico, P.D. Zavattieri, L.G. Hector, A.F. Bower, On the mechanics of sinusoidal interfaces between dissimilar elastic-plastic solids subject to dominant mode I, *Eng. Fract. Mech.* 131 (2014) 38–57.
- [20] E. Martin, D. Leguillon, C. Lacroix, A revisited criterion for crack deflection at an interface in a brittle bimaterial, *Compos. Sci. Technol.* 61 (12) (2001) 1671–1679.
- [21] R.C. Tighe, J.M. Dulieu-Barton, S. Quinn, Identification of kissing defects in adhesive bonds using infrared thermography, *Int. J. Adhesion Adhes.* 64 (2016) 168–178.
- [22] T. Kundu, A. Maji, T. Ghosh, K. Maslov, Detection of kissing bonds by Lamb waves, *Ultrasonics* 35 (8) (1998) 573–580.
- [23] D.W. Yan, B.W. Drinkwater, S.A. Neild, Measurement of the ultrasonic nonlinearity of kissing bonds in adhesive joints, *Ndt&E Int* 42 (5) (2009) 459–466.
- [24] M. Perton, A. Blouin, J.P. Monchalin, Adhesive bond testing of carbon-epoxy composites by laser shockwave, *J. Phys. D Appl. Phys.* 44 (3) (2011).
- [25] C. Jeonjikaew, F.J. Guild, The analysis of kissing bonds in adhesive joints, *Int. J. Adhesion Adhes.* 75 (2017) 101–107.
- [26] J.B. Cai, W.Q. Chen, G.R. Ye, Effect of interlaminar bonding imperfections on the behavior of angle-ply laminated cylindrical panels, *Compos. Sci. Technol.* 64 (12) (2004) 1753–1762.
- [27] R. Alvarez-Lima, A. Diaz-Diaz, J.F. Caron, S. Chataigner, Enhanced layerwise model for laminates with imperfect interfaces – Part I: equations and theoretical validation, *Compos. Struct.* 94 (5) (2012) 1694–1702.
- [28] K. Matos, M.G. Kulkarni, P.H. Geubelle, Multiscale cohesive failure modeling of heterogeneous adhesives, *J. Mech. Phys. Solid.* 56 (4) (2008) 1511–1533.
- [29] A. Needleman, An analysis of decohesion along an imperfect interface, *Int. J. Fract.* 42 (1) (1990) 21–40.
- [30] P. Feraren, H.M. Jensen, Cohesive zone modelling of interface fracture near flaws in adhesive joints, *Eng. Fract. Mech.* 71 (15) (2004) 2125–2142.
- [31] H. Gao, J.R. Rice, A first-order perturbation analysis of crack trapping by arrays of obstacles, *J. Appl. Mech.* 11 (1989) 828–836.
- [32] M.K. Budzik, H.M. Jensen, Perturbation analysis of crack front in simple cantilever plate peeling experiment, *Int. J. Adhesion Adhes.* 53 (2014) 29–33.
- [33] M. Vasoya, V. Lazarus, L. Ponson, Bridging micro to macroscale fracture properties in highly heterogeneous brittle solids: weak pinning versus fingering, *J. Mech. Phys. Solid.* 95 (2016) 755–773.
- [34] V. Lazarus, Perturbation approaches of a planar crack in linear elastic fracture mechanics: a review, *J. Mech. Phys. Solid.* 59 (2) (2011) 121–144.
- [35] M. Vasoya, A.B. Unni, J.B. Leblond, V. Lazarus, L. Ponson, Finite size and geometrical non-linear effects during crack pinning by heterogeneities: an analytical and experimental study, *J. Mech. Phys. Solid.* 89 (2016) 211–230.
- [36] V. Lazarus, J.B. Leblond, In-plane perturbation of the tunnel-crack under shear loading I: bifurcation and stability of the straight configuration of the front, *Int. J. Solid Struct.* 39 (17) (2002) 4421–4436.
- [37] V. Tvergaard, J.W. Hutchinson, Analyses of crack growth along interface of patterned wafer-level Cu-Cu bonds, *Int. J. Solid Struct.* 46 (18–19) (2009) 3433–3440.
- [38] C. Cuminatto, G. Parry, M. Braccini, A model for patterned interfaces debonding – application to adhesion tests, *Int. J. Solid Struct.* 75–76 (2015) 122–133.
- [39] S. Heide-Jørgensen, M.K. Budzik, Crack growth along heterogeneous interface during the DCB experiment, *Int. J. Solid Struct.* 120 (2017) 278–291.
- [40] S.T. de Freitas, J. Sinke, Failure analysis of adhesively-bonded metal-skin-to-composite-stiffener: effect of temperature and cyclic loading, *Compos. Struct.* 166 (2017) 27–37.
- [41] <http://www.paintservices.com/pf-pd/>.
- [42] J.A. Poulis, J.C. Cool, E.H.P. Logtenberg, Uv/ozone cleaning, a convenient alternative for high-quality bonding preparation, *Int. J. Adhesion Adhes.* 13 (2) (1993) 89–96.
- [43] R. Oosterom, T.J. Ahmed, J.A. Poulis, H.E.N. Bersee, Adhesion performance of UHMWPE after different surface modification techniques, *Med. Eng. Phys.* 28 (4) (2006) 323–330.
- [44] S.T. de Freitas, M.D. Banea, S. Budhe, S. de Barros, Interface adhesion assessment of composite-to-metal bonded joints under salt spray conditions using peel tests, *Compos. Struct.* 164 (2017) 68–75.
- [45] J.A. Poulis, Small Cylindrical Adhesive Bonds, Technical University Delft, The Netherlands, 1993.
- [46] S.T. de Freitas, D. Zarouchas, H. Poulis, The use of acoustic emission and composite peel tests to detect weak adhesion in composite structures, *J. Adhes.* <https://doi.org/10.1080/00218464.2017.1396975>.
- [47] J.N. Reddy, *Mechanics of Laminated Composite Plates and Shells: Theory and Analysis*, second ed., CRC Press, Boca Raton, 2004.
- [48] A.A. Griffith, The phenomena of rupture and flow in solids, *Phil. Trans. Roy. Soc. Lond.* 221 (1921) 163–198.
- [49] P. Davidson, A.M. Waas, Non-smooth mode I fracture of fibre-reinforced composites: an experimental, numerical and analytical study, *Phil. Trans. R. Soc. A* 370 (2012) 1942–1965.
- [50] A. Okada, I.N. Dyson, A.J. Kinloch, Subcritical interlaminar crack-growth in fiber composites exhibiting a rising R-curve, *J. Mater. Sci.* 30 (9) (1995) 2305–2312.
- [51] D. Sen, M.J. Buehler, Structural hierarchies define toughness and defect-tolerance despite simple and mechanically inferior brittle building blocks, *Sci. Rep.-UK* 1 (2011).
- [52] M.F. Kanninen, Dynamic analysis of unstable crack-propagation and arrest in dcB test specimen, *Int. J. Fract.* 10 (3) (1974) 415–430.
- [53] M. Cabello, J. Zurbitu, J. Renart, A. Turon, F. Martínez, A general analytical model based on elastic foundation beam theory for adhesively bonded DCB joints either with flexible or rigid adhesives, *Int. J. Solid Struct.* 94–95 (2016) 21–34.
- [54] S. Krenk, Energy-release rate of symmetrical adhesive joints, *Eng. Fract. Mech.* 43 (4) (1992) 549–559.
- [55] M.K. Budzik, J. Jumel, M.E.R. Shanahan, An in situ technique for the assessment of adhesive properties of a joint under load, *Int. J. Fract.* 171 (2) (2011) 111–124.
- [56] M.M. Shokrieh, M. Salamat-talab, M. Heidari-Rarani, Dependency of bridging traction of DCB composite specimen on interface fiber angle, *Theor. Appl. Fract. Mech.* 90 (2017) 22–32.
- [57] S.P. Fernberg, L.A. Berglund, Bridging law and toughness characterisation of CSM and SMC composites, *Compos. Sci. Technol.* 61 (16) (2001) 2445–2454.
- [58] B.F. Sørensen, T.K. Jacobsen, Large-scale bridging in composites: R-curves and bridging laws, *Compos. Part A-App. S* 29 (11) (1998) 1443–1451.
- [59] A.J. Brunner, B.R.K. Blackman, J.G. Williams, Calculating a damage parameter and bridging stress from G(I,C) delamination tests on fibre composites, *Compos. Sci. Technol.* 66 (6) (2006) 785–795.
- [60] M.F. Kanninen, Augmented double cantilever beam model for studying crack-propagation and arrest, *Int. J. Fract.* 9 (1) (1973) 83–92.
- [61] I. Quintana-Alonso, N.A. Fleck, Damage tolerance of a sandwich panel

- containing a cracked square lattice core, *J. Sandw. Struct. Mater.* 12 (2) (2010) 139–158.
- [62] I. Quintana-Alonso, S.P. Mai, N.A. Fleck, D.C.H. Oakes, M.V. Twigg, The fracture toughness of a cordierite square lattice, *Acta Mater.* 58 (1) (2010) 201–207.
- [63] X.D. Cui, Z.Y. Xue, Y.M. Pei, D.N. Fang, Preliminary study on ductile fracture of imperfect lattice materials, *Int. J. Solid Struct.* 48 (25–26) (2011) 3453–3461.
- [64] R. Tadepalli, K.T. Turner, C.V. Thompson, Mixed-mode interface toughness of wafer-level Cu–Cu bonds using asymmetric chevron test, *J. Mech. Phys. Solid.* 56 (2008) 707–718.
- [65] R. Tadepalli, T.K. Turner, C.V. Thompson, Effects of patterning on the interface toughness of wafer-level Cu–Cu bonds, *Acta Mater.* 56 (3) (2008) 438–447.
- [66] L.J. Gibson, M.F. Ashby, *Cellular Solids: Structure and Properties*, Kbh, Nota, 2016.
- [67] I.Q. Alonso, N.A. Fleck, Compressive response of a sandwich plate containing a cracked diamond-celled lattice, *J. Mech. Phys. Solid.* 57 (9) (2009) 1545–1567.
- [68] F. Lipperman, M. Ruykin, M.B. Fuchs, Fracture toughness of two-dimensional cellular material with periodic microstructure, *Int. J. Fract.* 146 (4) (2007) 279–290.
- [69] S. Patinet, D. Vandembroucq, A. Hansen, S. Roux, Cracks in random brittle solids: from fiber bundles to continuum mechanics, *Eur. Phys. J. Spec. Top.* 223 (11) (2014) 2339–2351.
- [70] S. Patinet, D. Vandembroucq, S. Roux, Quantitative prediction of effective toughness at random heterogeneous interfaces, *Phys. Rev. Lett.* 110 (16) (2013).
- [71] M.K. Budzik, J. Jumel, M.E.R. Shanahan, On the crack front curvature in bonded joints, *Theor. Appl. Fract. Mech.* 59 (1) (2012) 8–20.
- [72] K.F. Nilsson, On growth of crack fronts in the dcb-test, *Compos. Eng.* 3 (6) (1993) 527–546.
- [73] L.J. Yu, B.D. Davidson, A three-dimensional crack tip element for energy release rate determination in layered elastic structures, *J. Compos. Mater.* 35 (6) (2001) 457–488.
- [74] R. Thomson, C. Hsieh, V. Rana, Lattice trapping of fracture cracks, *J. Appl. Phys.* 42 (8) (1971), 3154–&.
- [75] R. Thomson, Pinning of cracks by dislocations, *Bull. Am. Phys. Soc.* 18 (3) (1973), 394–394.
- [76] D. Maugis, Sub-critical crack growth, surface energy and fracture toughness of brittle materials, in: R.C. E.A.G. Bradt, D.P.H. Hasselman, F.F. Lange (Eds.), *Fracture Mechanics of Ceramics*, Springer, Boston, MA, 1986.

Chapter 6

Paper 5 - On Pillar-Structured Interfaces

*Mechanics and Fracture of Structured Pillar Interfaces
(Currently under review in Journal of the Mechanics
and Physics of Solids)*

6.1 Introduction

The previous chapters deal with structured interfaces containing surface regions of weak adhesion. This contribution extends upon that and includes a metamaterial-inspired approach by adding a micro-structure to the bondline. The work is heavily inspired by the work done in the Turner group and is started during the author's stay at University of Pennsylvania. It is also to some degree inspired by the bridging phenomena from the previous chapter. Therefore, the micro-structure is design in the spirit of large-scale crack surface bridging in hope of enhancing the joint performance.

6.2 Method

ADCB and DCB specimens are cut from Polymethyl methacrylate (PMMA). First regular, homogeneous specimens are produced and fracture tested to obtain a reference data set and to determine the material properties. Then, specimens with structured interfaces containing pillars bridging the two adherends are produced and tested under similar conditions. The height

of the pillars is systematically varied while the width and the inter-pillar spacing are kept constant.

Twofold theoretical work is conducted to explain the experimental observations. First, numerical modeling based on FE is done to describe the field quantities of the specimens, in particular, the stress distribution in and around the pillars. Second, an analytical model based on Timoshenko beam theory and Winkler foundation formulation is derived. Both macro-mechanical (joint level) and micro-mechanical (pillar level) aspects are described and coupled. The former describes the overall behavior of the DCB by homogenizing the structured interface and using effective properties. From LFM the macro-mechanical ERR is obtained. The micro-mechanical approach describes the failure of a single pillar based on the macro-mechanical loading. Combining both models provides an effective way of predicting the global behavior of the specimen in terms of load response, compliance, crack position etc., while the detailed failure and critical fracture load depending on the pillar geometry is acquired.

6.3 Contribution

The author contributed with experimental work comprising specimen design and manufacturing, test setup and conduction and data treatment, theoretical modeling in terms of establishing the FE code, running it and analyzing the data, derivation of the analytical model, and, finally, manuscript preparation.

6.4 Finding

It is found that structuring the interface with pillars improved the dissipated energy (during fracture) significantly, irrespectively of the pillar sizes, by disrupting the crack propagation. Both critical fracture load and the compliance of the DCB increase with increasing pillar aspect ratio. No significant difference is found between the DCB and the ADCB indicating that mode-mixity does not significantly affect this result. However, the pillars reduce shearing of the interface with increasing pillar aspect ratio, thus reduce the mode-mixity.

The theoretical models describe the behavior very well making them ideal tools for designing and optimizing structured interfaces. To summarize, it is possible to tune the fracture properties (effective critical fracture

energy) of the joint by structuring the interface and, hereby, introducing heterogeneities in the specimen.

6.5 Reflection

Including a micro-structure to the interface region seems promising as a significant enhancement of critical fracture load is obtained in the present study. As future studies a softer, less brittle material can be used and its response compared to that of PMMA to see if these observations and theoretical predictions hold for soft materials as well. Opposite, elastic-plastic materials able to undergo strain-hardening can be used to trigger constrain effects and thereby enhancing dissipation in the pillars even further.⁶¹

Another thing could be to change the geometry of the pillars. Here the simplest geometry is used and shows great potential. Different shapes and geometries might enhance these effects further or simply cause other functionalities. Similarly, the pillars are purely two dimensional, it could be of great interest to expand it into three dimensions, e.g. by creating multiple rows of pillars.

Finally, the ADCB specimens provide mode-mixity to some extent, however, the shear contribution is rather small. It could be interesting to increase the shearing or even test the structure in pure shear to see if the mechanism changes significantly.

Journal of the Mechanics and Physics of Solids 137 (2020) 103825



Contents lists available at ScienceDirect

Journal of the Mechanics and Physics of Solids

journal homepage: www.elsevier.com/locate/jmps

Mechanics and fracture of structured pillar interfaces

Simon Heide-Jørgensen^a, Michal K. Budzik^{a,b,*}, Kevin T. Turner^c

^a Mechanical Engineering Section, Department of Engineering, Aarhus University, Aarhus, Denmark

^b iMAT - Centre for Integrated Materials Research, Aarhus, Denmark

^c Department of Mechanical Engineering and Applied Mechanics, University of Pennsylvania, Philadelphia, PA, USA



ARTICLE INFO

Article history:

Received 24 May 2019

Revised 9 December 2019

Accepted 10 December 2019

Available online 12 December 2019

Keywords:

Mechanical metamaterials

Architected materials

Toughness

Heterogeneities

Finite element analysis

ABSTRACT

Material architecture and geometry provide an opportunity to alter the fracture response of materials without changing the composition or bonding. Here, concepts for using geometry to enhance fracture resistance are established through experiments and analysis of the fracture of elastic-brittle, polymer specimens with pillar-structures along the fracture plane. Specifically, we investigate the fracture response of double cantilever beam specimens with an array of pillars between the upper and lower beams. In the absence of pillars, unstable crack growth and rapid catastrophic failure occur in the double cantilever specimens tested in displacement control. Introducing pillars at the interface by removing material via laser cutting yields a discontinuous interface and leads to a more gradual fracture process and an increase in the work of fracture. The pillar geometry affects the failure load and, notably, increasing the slenderness of the pillars leads to higher critical failure loads due to greater load sharing. The effect of pillar geometry on fracture is established through experiments and analysis, including analytical modeling and finite element simulations. An analytical model that includes the macro-scale response of the beam and the micro-scale response of the pillars is presented and describes the key effects of pillar geometry on fracture response.

© 2019 Elsevier Ltd. All rights reserved.

1. Introduction

High stiffness, strength and toughness are desired properties of materials in structural applications. While obtaining two of the three properties simultaneously, e.g. stiffness and toughness (e.g. elastic-ductile materials) or strength and stiffness (e.g. ceramics) are rather easy, achieving high strength, toughness and stiffness is challenging (Ashby and Johnson, 2010). For instance, increasing the strength can lead to brittleness, which reduces toughness and damage tolerance. Controlling the internal geometry can potentially assist in achieving all three properties simultaneously by altering the fracture process, failure modes, or crack growth paths. Especially, for brittle materials affecting the critical unstable crack growth can enhance damage tolerance. Mechanical metamaterial is a class of materials in which mechanical properties are determined by the internal geometry of the material rather than by the composition or atomic bonding. Lattice materials are common examples (Heide-Jørgensen et al., 2018b; Messner, 2016; Ostoja-Starzewski, 2002) and have gained attention due to their exceptional properties, notably high stiffness per weight. The advances in mechanical metamaterials in recent years have been driven by progress in digital manufacturing techniques that allow for fabrication of materials with complex internal geometry

* Corresponding author at: Mechanical Engineering Section, Department of Engineering, Aarhus University, Aarhus, Denmark.

E-mail addresses: mibu@eng.au.dk (M.K. Budzik), kturner@seas.upenn.edu (K.T. Turner).

<https://doi.org/10.1016/j.jmps.2019.103825>

0022-5096/© 2019 Elsevier Ltd. All rights reserved.

via additive, subtractive and selective manufacturing processes (Bertoldi et al., 2017; Glassmaker et al., 2007; Minsky and Turner, 2017; Ortiz and Boyce, 2008; Rayneau-Kirkhope and Dias, 2017; Walia et al., 2015; Wegst et al., 2015; Yang et al., 2018; Zhao et al., 2014). Mechanical analysis and simulation have been equally important providing the ability to design internal geometry and architecture to realize specific properties. The use of geometry has also received substantial interest from the adhesion community where geometrical features have been exploited to control toughness of interfaces (Autumn and Gravish, 2008; Chaudhury et al., 2015; Del Campo et al., 2007; Heide-Jørgensen et al., 2018a; Murphy et al., 2009; Xue et al., 2017; Yao and Gao, 2006). One outcome of the work to design dry adhesives with high adhesion strength is an adhesion scaling law (Bartlett et al., 2012), which suggests that the critical fracture force is proportional to the square root of the ratio between system compliance and contact area. This law was recently revisited and generalized to account for the case of progressive failure (Mojdehi et al., 2017).

The objective of this work is to understand the fracture behavior of structured interfaces consisting of an array of pillars. The high-level goal is to identify strategies to improve the toughness of the material through geometric control. We fabricated, tested, and analyzed structured double cantilever beam (DCB) specimens including symmetric geometries where the pillar region is subjected mainly to the uniaxial loading (i.e. mode I) and asymmetric geometries with a small contribution of in-plane shear stress (i.e. mixed-mode I/II) to failure. Through laser cutting of elastic-brittle Plexiglas® (i.e. PMMA) sheets the slenderness of the pillars is varied systematically while their intermediate distances are kept constant. The specimen behavior is analyzed using comprehensive analytical formulation and finite element analysis. Good agreement between the analytical model, experimental results, and numerical simulations is reported. More specifically, we detail the relationship between the long-range structural response of the specimen and the short-range micro-mechanical response of the pillar structure. The results indicate that the pillar-like geometries can be used to increase the critical fracture load and improve damage tolerance while minimally affecting the stiffness. Due to the geometrical nature of the enhancements, the conclusions are expected to remain valid over a range of different length scales and, therefore, be relevant for a number of different applications. Potentially, new or additional insights can be gained into: fracture in polymers via crazing and fibrillation phenomena, i.e. slender micro-structures with negligible bending stiffness, which could benefit from the load sharing mechanism (Deblieck et al., 2011; Geim et al., 2003; Neggens et al., 2015); the role of geometrical parameters in fracture of composites incorporating fibre bridging (Yao et al., 2016a; 2016b); nature inspired material architectures (Abid et al., 2019; Chung and Chaudhury, 2005; Grossman et al., 2019; Huang and Li, 2013). The results may provide insight into more complex, truss-like, structures (Hutchinson and Fleck, 2005; 2006; Wadley et al., 2003) and their behavior within confined or constrained zones of multi-materials including load transfer in sandwich materials with lattice-like cores. Finally, further directions toward adhesive bonding toughening can be deduced (Maloney and Fleck, 2018; 2019).

2. Materials and methods

2.1. Specimen

DCB specimens with a total length $L = 160$ mm, a load application point 10 mm from the end, width $b = 3$ mm, lower beam thickness of $h = 20$ mm, and top beam thickness of 20 or 30 mm were examined (Fig. 1). The specimens were laser cut (flatbed laser cutter, 10.6 μ m wavelength, CO₂ gas, 40W laser used at 80% power, 10 mmmin⁻¹ speed, Ten High, China) from 3 mm thick, extruded sheets of poly(methyl methacrylate) (PMMA) with a Young's modulus of $E^* \approx 2.7$ GPa, Poisson's ratio $\nu = 0.33$ (adopted from product data sheet) and a fracture energy of $G_c \approx 0.25$ N mm⁻¹ (see Appendix A1 for details on material property determination). Three types of specimens were tested: (1) reference PMMA DCB specimens; (2) DCB specimens with a pillar-like pattern along the interface (referred to as symmetric specimens) and (3) DCB specimens with a thicker top beam and a pillar-like pattern along the interface (referred as asymmetric specimens).

The reference [used mainly to estimate the fracture energy of PMMA (see Appendix A1)] and symmetric specimens had $h = 20$ mm for both the top beams and bottom while the asymmetric specimens had a top beam of thickness 30 mm, yielding a top-to-bottom thickness ratio of $\alpha = 30/20 = 1.5$. Both, symmetric and asymmetric specimens had, if not stated otherwise, an initial crack length $a = 90$ mm as defined in Fig. 1(a). The pillars constituting the bondline had a constant width $d = 1$ mm, a constant spacing of $s = 1$ mm, while their height was varied: $t = 1, 3, 5, 9$ mm. For each pillar height, three specimens for a total of twelve were manufactured and tested. To control the crack and ensure failure at the interface between the two substrates, the laser cutter (35% power, 100 mm⁻¹) was used to etch a line of approximately 250 μ m depth [measured using a 3D scanning microscope (Keyence VR3200, Japan)] along the middle of the specimen (Fig. 2). To relieve stress concentrations at the base of the pillars, fillets of $R \approx 200$ μ m were introduced. Failure originating from the corners was not observed during the experiments.

2.2. Testing

Each specimen was mounted using custom-made grips in a universal testing machine (Zwick/Roell Z050, Zwick/Roell, Germany). The tests were performed at a constant displacement rate of 3 mmmin⁻¹. Crosshead and force data were acquired simultaneously at a rate of 50Hz.

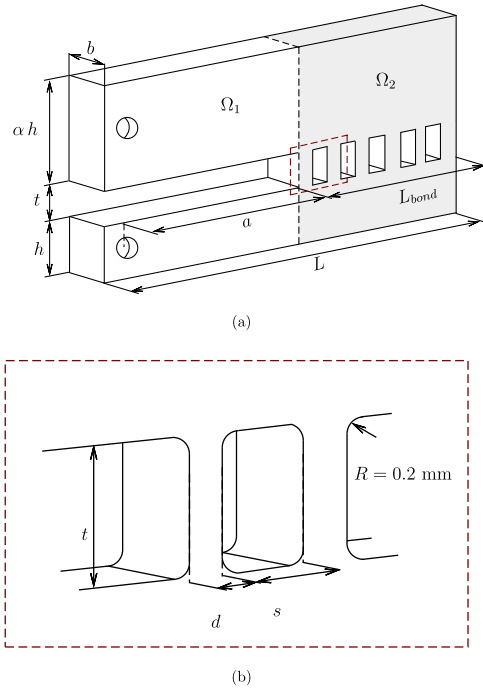


Fig. 1. Schematic of the specimens with unbonded region Ω_1 and bonded region Ω_2 . a) Specimen dimensions comprising length L , width b , initial crack length a , bonded length L_{bond} , beam thickness h , pillar height t and top-to-bottom thickness ratio α . b) Close-up of the pillars at the bondline with width d and spacing s .

3. Finite element analyses

A finite element analysis of the specimen geometries was programmed in Python (v. 2.7.3, Python Software Foundation) and solved using Abaqus (Abaqus/CAE 18.21.41, Dassault Systèmes, France). The geometry is modeled using four-noded, plane strain elements (plane strain conditions are assumed, since for most of the cases the relevant non-dimensional group of parameters: b/d ; $t/d \approx 1$) with reduced integration and a linear elastic, isotropic material model. The model and mesh are depicted in Fig. 3.

The top and bottom beams are modeled separately and connected with a surface-to-surface contact along the interface. The lower loading point is fixed and a load is applied to the upper loading point. During post-processing, the displacement at loading point and the stresses σ_{yy} and σ_{xy} at the middle of the pillars, as indicated by the thick line in Fig. 3, are obtained. The mesh density in the pillar region is higher compared to the rest of the model. A convergence study showed that it is feasible to use a global mesh seed of 0.5 mm and a local mesh seed of 30 μm for the pillars. This provided a maximum of 732,530 elements in the model and 33 elements across the width of each pillar.

4. Theoretical framework

4.1. Macro-mechanical model

The focus of this section is on developing a relatively simple and intuitive model for interpretation of the macroscopic behavior of the specimen in terms of substrate properties and effective interface properties of the pillar region. This approach neglects the geometrical details of the interface by treating it as homogeneous with spatially averaged properties.

4

S. Heide-Jørgensen, M.K. Budzik and K.T. Turner / Journal of the Mechanics and Physics of Solids 137 (2020) 103825

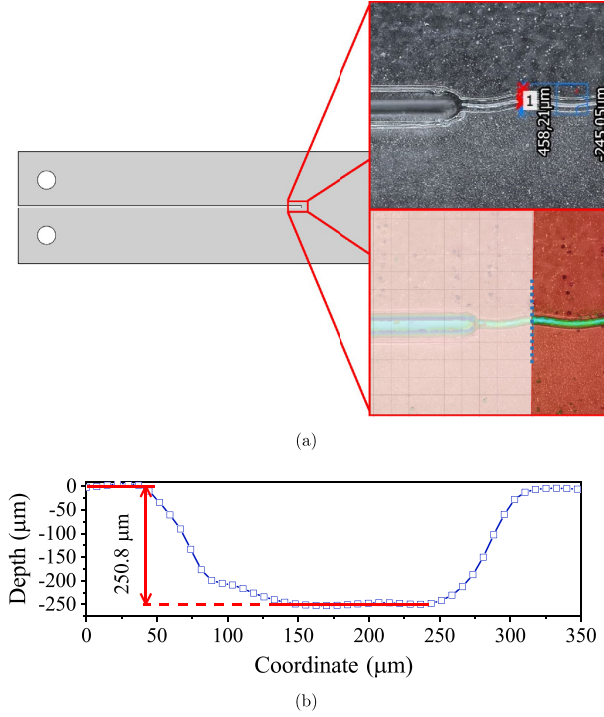


Fig. 2. Image and measured profile of the crack tip of the reference specimen. a) Region of interest marked on a schematic of the reference specimen. The two close-up images show, from top to bottom, an optical image of the crack tip region with the etched line and a topographic measurement of the same area. b) Height profile along the dashed, blue line in a). The depth of the etched trench is approximately 250 μm. (For interpretation of the references to color in this figure legend, the reader is referred to the web version of this article.)

The model is assumed to be under a prescribed force, P , loading, however, this is easily changed to a prescribed displacement if required. For the beams, Timoshenko theory is used while the pillar interface is represented as a Winkler foundation - recently reviewed (Dillard et al., 2018). Use of a beam theory framework that includes shear to represent the beam is deemed necessary due to the beam aspect ratio $\min(a/h) = 6$ for which the internal shear effects cannot be neglected. The Winkler foundation that describes the interface region cannot account for shear stresses, however, allows the model to remain simple and intuitive.

The model (Fig. 1) is then divided into two regions 1) the free/unbonded region (Ω_1) and the interface/bonded region (Ω_2), both connected through continuity conditions.

The equilibrium equations of the Timoshenko beam on the Winkler foundation (Salem et al., 2013) are:

$$\frac{dM}{dx} + V = 0 \quad \frac{dV}{dx} - kw = 0 \quad (1)$$

with:

$$M = EI_{\beta} \frac{d\varphi}{dx} \quad V = \kappa GA_{\beta} \left(\frac{dw}{dx} - \varphi \right) \quad \text{with } \beta = t, b \quad (2)$$

where M , V , w , and k are bending moment, shear force, deflection, and foundation modulus, respectively, and φ , E , I_{β} , κ , G , and A_{β} are rotation, elastic modulus, moment of inertia, shear coefficient, shear modulus, and the cross-sectional area, respectively. The subscript β either takes t for top or b for bottom such that $I_t = (ah)^3 b/12$ and $I_b = h^3 b/12$. For a rectangular, homogeneous and isotropic beam the cross-sectional area, shear coefficient and shear modulus are $A_{top} = ahb$ and $A_{bot} = hb$, $\kappa \approx 5/6$ (Ye, 2003), and $G = E/2(1 + \nu)$ with ν being the Poisson's ratio.

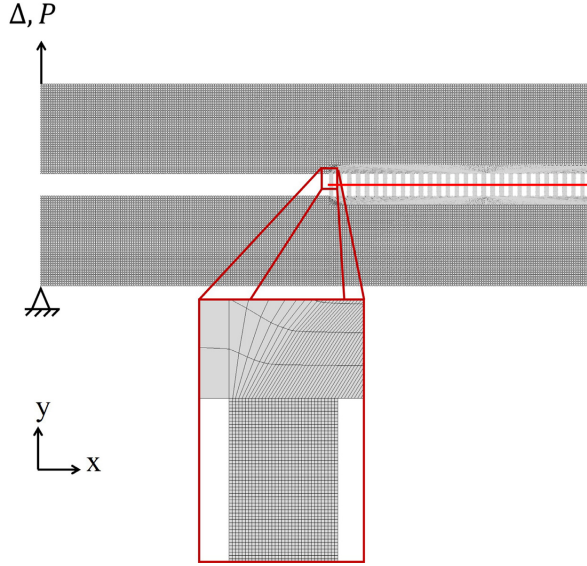


Fig. 3. FEA model of a double cantilever beam configuration with an array of pillars at the interface. The close-up of the first pillar shows details of the mesh. The configuration is loaded at the end with Δ while the reaction force, P , is acquired at the same point. Stresses, σ_{yy} and σ_{xy} , are extracted along the interface denoted by the red line. (For interpretation of the references to color in this figure legend, the reader is referred to the web version of this article.)

4.1.1. Interface region homogenization

Instead of a discrete formulation of the interface (Heide-Jørgensen and Budzik, 2017), which would lead to over-complicated derivation, at present this region is regarded as continuous with a representative unit cell consisting of a pillar with length d and a spacing of length s . The foundation modulus is taken as the resulting stiffness of the unit cell:

$$k = \left(\frac{2b}{t} E_{pillar} \right) f + \left(\frac{2b}{t} E_{spacing} \right) (f - 1) = \left(\frac{2b}{t} E \right) f \quad (3)$$

Such formulation can be used within a general context, for instance including material variability (Maloney and Fleck, 2018; 2019). In the present study $E_{pillar} = E$, $E_{spacing} = 0$ and $f = d/(d + s)$. Thus, k defines a homogenized stiffness of the pillar region. Defining $E = mE^*$ where m is a constant, allows for adaptation of different stress-strain states (Heide-Jørgensen and Budzik, 2018). $m = 1$ for plane stress and $m = (1 - \nu^2)^{-1}$ for two-dimensional plane strain. Following the FEA, the latter assumption is used throughout the paper.

4.1.2. Unbonded domain

The unbonded domain spans from the load application point ($x = 0$) to the crack tip ($x = a$), with subscript $(\cdot)_1$ referring to quantities in this domain. Within the domain $k = 0$. With bending moment, $M = -Px$ and shear force, $V = -P$, integration of Eq. (2) yields:

$$\varphi_1 = \int -\frac{P}{EI_\beta} x dx = -\frac{P}{2EI_\beta} x^2 + A_1 \quad (4)$$

where A_1 is a constant of integration. Combining Eqs. (2) and (4) and integrating leads to:

$$w_1 = \int \frac{P}{\kappa GA_\beta} + \frac{P}{2EI_\beta} x^2 + A_1 dx = \frac{P}{6EI_\beta} x^3 + \frac{P}{\kappa GA_\beta} x + A_1 x + B_1 \quad (5)$$

where B_1 is an additional constant of integration. Both constants are found by imposing deflection and rotation continuity at the crack tip.

6

S. Heide-Jørgensen, M.K. Budzik and K.T. Turner / Journal of the Mechanics and Physics of Solids 137 (2020) 103825

4.1.3. Intact domain

The intact domain representing the interface region spans from the crack tip ($x = a$) to the end of the specimen ($x = L$) with $k \neq 0$.

The governing equation for a Timoshenko beam on an elastic foundation is:

$$\frac{d^4 w}{dx^4} - \frac{k}{\kappa G A_\beta} \frac{dw^2}{dx^2} + \frac{k}{EI_\beta} w = 0 \quad (6)$$

with a solution of the form:

$$w_2 = A_2 e^{-\gamma_1 x} + B_2 e^{\gamma_1 x} + C_2 e^{-\gamma_2 x} + D_2 e^{\gamma_2 x} \quad (7)$$

A_2, B_2, C_2 and D_2 are unknown constants. γ_1 and γ_2 are the roots of the eigenvalue problem Eq. (6) given by:

$$\gamma_1 = \lambda \sqrt{2(\varepsilon + \sqrt{\varepsilon^2 - 1})} \quad \gamma_2 = \lambda \sqrt{2(\varepsilon - \sqrt{\varepsilon^2 - 1})} \quad (8)$$

with λ and ε being phenomenological parameters related to the elastic process zone of the foundation's damping of the beam deflection (Heide-Jørgensen and Budzik, 2017) and to the modulation of the damping to either periodic or monotonic decay (Salem et al., 2013), respectively. They are expressed as:

$$\lambda = \sqrt[4]{\frac{k}{4EI_\beta}} \quad \varepsilon = \frac{\sqrt{kEI_\beta}}{2\kappa GA_\beta} \quad (9)$$

The rotation, obtained by combining Eqs. (2) and (7) and integrating, gives:

$$\phi_2 = -\psi_1 A_2 e^{-\gamma_1 x} + \psi_1 B_2 e^{\gamma_1 x} - \psi_2 C_2 e^{-\gamma_2 x} + \psi_2 D_2 e^{\gamma_2 x} \quad (10)$$

where ψ_1 and ψ_2 are constants depending on the geometry and the material of the specimen:

$$\psi_1 = \frac{\kappa GA_\beta \gamma_1^2 - k}{\kappa GA_\beta \gamma_1} \quad \psi_2 = \frac{\kappa GA_\beta \gamma_2^2 - k}{\kappa GA_\beta \gamma_2} \quad (11)$$

Constants A_2 and C_2 are determined through rotation and shear angle continuity between the two domains. The remaining constants, $B_2 = D_2 = 0$, are found by assuming the far field as intact ($w_2 = 0, \phi_2 = 0$ as $x \rightarrow \infty$).

4.1.4. Strain energy release rate

The compliance is calculated as ratio of the total displacement of the top and bottom beams to the applied force:

$$C = \frac{w_1(\beta = t) + w_1(\beta = b)}{P} \Big|_{x=0} \quad (12)$$

The strain energy release rate (SERR) for the macro-mechanical configuration is obtained by combining Eq. (12) and the Irwin-Kies equation, which states

$$\mathcal{G} = \frac{P^2}{2b} \frac{dC}{da} \quad (13)$$

Assuming that the crack grows once the Griffith fracture criterion (Griffith and Taylor, 1921) is satisfied, Eq. (13) is set equal to the critical strain energy release rate, \mathcal{G}_c , and an expression for the critical force, P_c , i.e. force necessary for crack onset, is obtained:

$$P_c = \sqrt{2b\mathcal{G}_c} \sqrt{\frac{da}{dC}} \quad (14)$$

Note, that the adhesion scaling law (Bartlett et al., 2012), in a generalized form Mojdehi et al. (2017), i.e. $P_c \propto \sqrt{\frac{da}{dC}}$ with $dA = bda$, is recovered.

Griffith's criterion requires the material to behave in an elastic-brittle manner, though small scale yielding is also allowed (Irwin, 1957). With the relatively small dimensions of the pillars (t, d) this can be questioned. The critical material length scale can be associated with the size of the crack tip plastic zone calculated as: $r_p = c \frac{\sigma_y E}{\sigma_f}$ where $c \in [\frac{1}{2\pi}; \frac{7}{8}]$ (Paris and Sih, 2009) depending on the assumed stress-strain conditions. For PMMA it equates to $r_p \approx 10^1 \mu\text{m}$. From dimensional analysis following non-dimensional groups are recognized: $\frac{r_p}{t}$; $\frac{r_p}{d}$; $\frac{r_p}{R}$. Here, $\frac{r_p}{R}$ is the largest with a magnitude on the order of 10^{-1} . The others are on the order of 10^{-2} or lower. We conclude, that in the present case the material can be regarded as brittle.

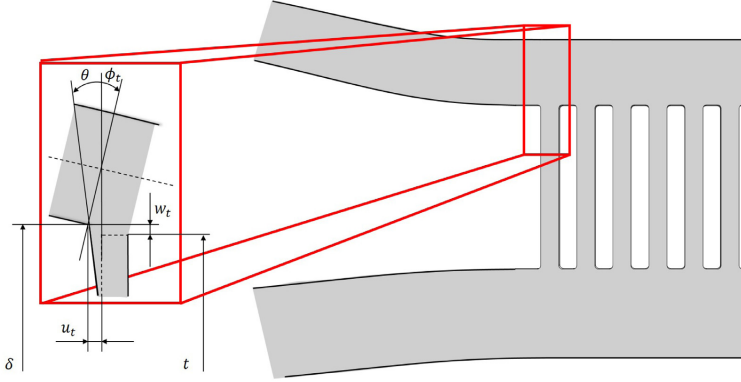


Fig. 4. Schematic representation of the kinematic field of the first pillar. Only the top pillar-beam transition is shown for clarity (denoted with index t).

4.2. Micro-mechanical concepts

In the previous section, the pillar region was treated as homogeneous, thus a dependence on pillar geometry was not obtained from the analysis. The geometrical realization of the concept of tunable toughness must be related to the distance between the pillars and the pillar aspect ratio. Additional, independent, non-dimensional groups could appear as important: $\frac{t}{d}$; $\frac{\delta}{d}$. The presence of a gap between the pillars alters the load transfer and introduces new mechanisms of failure. Fig. 4 shows a schematic view of the kinematic field experienced by pillars at the interface. Only the top adherend and the region near the adherend/first pillar is considered. In the general case, the adherends are of different bending rigidities, thus the top and bottom sections of the specimen will experience different rotations and displacements. The following assumptions are made: $\frac{1}{2}(\delta - t)/d = (\phi_t - \phi_b)t$ and $\lambda \cdot d \ll 1$. With the notation of Fig. 4, the loading distributed over the pillars can be separated into two distinct cases: (1) tension/compression of the pillars following $(\delta - t) = (w_t + w_b)$ (for the geometries studied compressive failure was not observed, however, for completeness analysis of the associated failure mode can be found in Appendix A2) and (2) shear through $u = (\phi_t - \phi_b)t$.

With the proposed load decomposition it is assumed that the failure mechanism of a single pillar is representative for the overall failure of the specimen.

4.2.1. Pillars under mode I loading

Tension of the pillar results in uniaxial force P_p and produces a moment M_p (with subscript p referring to the pillar). The mechanism of energy dissipation is through fracture caused by loads P_p and M_p . The change in elastic energy stored in the first pillar from P_p reads as:

$$\Delta U_p = \frac{1}{2} \sigma(x=a) \varepsilon \Delta V = \frac{1}{2} \frac{\sigma^2}{E} \Delta V \quad (15)$$

where we define $\sigma = \frac{P_p}{A_p}$ and $\varepsilon = \frac{\sigma}{E}$ assuming average values of both stress and strain. Here $A_p = bd$ is the cross sectional area of the pillar while ΔV is the volumetric change of the pillar between the loaded and the unloaded stages, i.e. $\Delta V = A_p \Delta \delta$. Combining previous equations we obtain:

$$\Delta U_p = \frac{1}{2} \frac{P_p^2}{A_p E} \Delta \delta \quad (16)$$

The displacement $\Delta \delta$ is eliminated using the axial stiffness of the pillar ($k_p = EA_p/t$), resulting in:

$$\Delta U_p = \frac{1}{2} \frac{P_p^3 t}{A_p^2 E^2} \Delta \delta \quad (17)$$

Following a similar approach the stored elastic energy due to the moment is:

$$\Delta U_m = \int_0^b \int_{-d/2}^{d/2} \frac{1}{2} \frac{\sigma^2}{E} dx dy \Delta \delta = \frac{6M_p^2 \Delta \delta}{Ed^3 b} \quad (18)$$

8

S. Heide-Jørgensen, M.K. Budzik and K.T. Turner / Journal of the Mechanics and Physics of Solids 137 (2020) 103825

where we define $\sigma = \kappa \frac{M_p}{I_p}$ with $I_p = d^3b/12$. Again, $\Delta\delta$ is eliminated using the stiffness of the pillar and Eq. (18) is rewritten as:

$$\Delta U_m = \frac{6M_p^2 P_p t}{d^3 b E^2 A_p} \quad (19)$$

With the elastic energy defined, the energy release rate is given as the change of elastic energy with the change of crack area:

$$\mathcal{G}_{tens} = \frac{(\Delta U_p + \Delta U_m)}{\Delta A_p} \quad (20)$$

Assuming that there exists a crack a_p such that $A_p = b(d - a_p)$ leads to:

$$\mathcal{G}_{tens} = \frac{1}{4} \frac{P_p^2 t}{(d - a_p)^3 b^3 E^2} + \frac{3M_p^2 P_p t}{d^3 b^3 E^2 (d - a_p)^2} = \mathcal{G}_p + \mathcal{G}_m \quad (21)$$

Within the limit of $a_p \rightarrow 0$, which sets up $P = P_c$ we obtain:

$$\mathcal{G}_{ctens} = \frac{1}{4} \frac{P_c^2 t}{d^3 b^3 E^2} + \frac{3M_p^2 P_c t}{d^5 b^3 E^2} \quad (22)$$

Moreover, taking $P_p = \sigma bd$ and $M_p \approx P_p(d + s)$ yields:

$$\mathcal{G}_{ctens} = \left[\frac{1}{4} \left(1 + \frac{s}{d}\right)^3 + 3 \left(1 + \frac{s}{d}\right)^5 \right] \left(\frac{t}{d}\right) \left(\frac{\sigma^3 d}{E^2}\right) \quad (23)$$

A complex relation between the pillars height, the width, the spacing and the SERR is revealed. The spacing-to-width ratio s/d increases the SERR while the aspect ratio t/d decreases the SERR.

4.2.2. Shear loading of pillars

Under the shear loading applied to the specimen, a single pillar can be treated as a cantilever beam under loading of the force $P_\tau = \int_0^d \tau(x) b dx$. Using Timoshenko beam theory, the compliance is:

$$C_p = \frac{u}{P_\tau} = \frac{t^3}{3EI_p} + \frac{2t}{\kappa A_p G} \quad (24)$$

where $I_p = \frac{1}{12} b d^3$. As in the previous case, consider a crack of length a_p inside a pillar so that: $I_p = \frac{1}{12} b (d - a_p)^3$ and $A_p = b(d - a_p)$. Using Irwin-Kies equation, Eq. (13), differentiating with respect to a_p results in:

$$\mathcal{G}_{sb} = 6 \frac{P_\tau^2 t^3}{b^2 E} (d - a_p)^{-4} + 2 \frac{P_\tau^2 t}{\kappa G b^2} (d - a_p)^{-2} \quad (25)$$

which contains both the bending (the first term on the right hand side) and the shear part (second term) of the SERR. At the onset of the failure, i.e. $a_p \rightarrow 0$, we write:

$$\mathcal{G}_{sb} = \mathcal{G}_{csb} = 6 \frac{P_\tau^2 t^3}{b^2 E} d^{-4} + 2 \frac{P_\tau^2 t}{\kappa G b^2} d^{-2} \quad (26)$$

Under the assumption $P_\tau = \tau bd$ yields bending:

$$\mathcal{G}_{cb} = 6 \frac{\tau^2 t^3}{E d^2} \quad (27)$$

and shear:

$$\mathcal{G}_{cs} = 2 \frac{\tau^2 t}{\kappa G} \quad (28)$$

parts of the energy release rate. Interestingly, in ref. Aghababaei et al. (2016) within a slightly different context and using calculations including coarse grained atomistic simulations, the existence of a critical length scale parameter agreeing perfectly with t , which controls failure of friction adhesive junction, was discovered. Eqs. (23), (27) and (28) summarize the results of the micro-mechanical analysis and will serve as a basis for the experimental and numerical investigations.

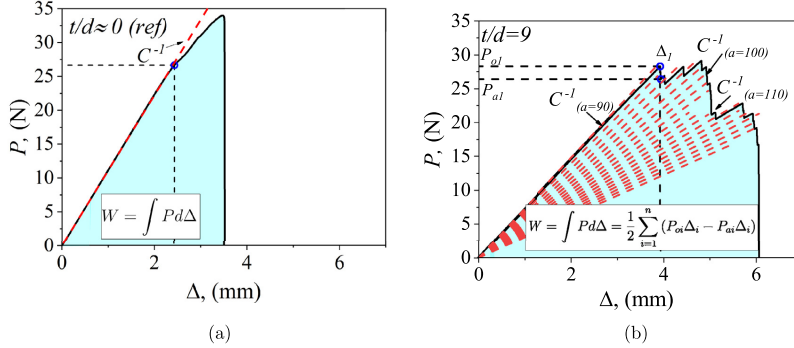


Fig. 5. Experimental force-displacement curves. a) Reference specimen where the dashed, red line showing the initial linear, loading path. b) Asymmetric specimen with pillars of $t/d = 9$. Red, dashed lines correspond to the compliance at specific crack lengths. The theoretical predictions agree very well with the positions of the pillars (2 mm separation). The cyan areas indicate the area used to evaluate the work of fracture - $W_{ref} = 0.067$ J and $W_{pillar} = 0.106$ J. (For interpretation of the references to color in this figure legend, the reader is referred to the web version of this article.)

4.2.3. Coupling between micro- and macro-mechanical models

A micro- and a macro-mechanical approach to describe the failure process of the configuration were developed in previous sections. In this section a coupling between them relating the macroscopic loading P to the resulting microscopic loading P_p and M_p is established. The pillars are assumed to act as linear springs with stiffness of the unit cell k . The traction, which acts on a pillar and is transferred to the beams, is equated as the extension of the pillar times the stiffness:

$$q(x) = k \cdot (w_t + w_b) \quad (29)$$

In the macro-mechanical configuration the single pillars are disregarded and a continuous, unit cell-based bondline is constructed. When shifting from the macroscopic to the microscopic configuration it is assumed that each pillar carries the loading of the corresponding unit cell. Furthermore, it is assumed that the overall failure of the structure is governed by the failure of the first pillar. Hence, the analysis is restricted to the first pillar only. The average stress acting on the first pillar is:

$$\sigma_p(x) = \frac{k}{(s+d)b} \int_a^{a+d+s} (w_t + w_b) dx \quad (30)$$

Assuming that the adherend thickness remains unchanged, the local pillar extension can be found from the global deflection as:

$$w_t = w_2(\beta = t) \quad \text{and} \quad w_b = w_2(\beta = b) \quad (31)$$

When combining Eqs. (30) and (31) the pillar stress becomes a function of the global loading P , hence, when inserted into Eq. (23) a coupling between the macroscopic loading and the microscopic failure is realized.

5. Results and discussion

5.1. Load response

Fig. 5 shows representative force-displacement curves for: (a) the reference specimen, and (b) the symmetric DCB with a pillar interface. Both specimens exhibit the same initial, linear loading up to crack onset, which is indicated by circular markers in the plots. For the reference specimens, Fig. 5(a), the initial linear loading path was replaced by another, almost linear, monotonically increasing in the present case. The deviation from the initial slope was caused by onset and propagation of the crack out from the initial plane defined by the pre-crack. In the experiments it was observed that the crack kinked out of the etched line and followed the shear band direction, resulting in catastrophic failure of the specimen.

A significantly different behavior is observed for the specimens with the pillar interface. In Fig. 5(b) a representative curve for the symmetric specimen is seen (specimen with aspect ratio $t/d = 9$). The initial loading persisted until the crack onset of the first pillar (marked by a circle). The failure of it led to a load drop (the second circle), however, load increased again after the crack reached the second pillar. Instead of catastrophic failure a new loading path is followed until the critical force for the next pillar is reached leading to its failure and a load drop, which is then recovered by the third pillar, and the process is repeated until the crack reached the last of the pillars. A non-steady state (effectively, the stick-slip) propagation

10

S. Heide-Jørgensen, M.K. Budzik and K.T. Turner / Journal of the Mechanics and Physics of Solids 137 (2020) 103825

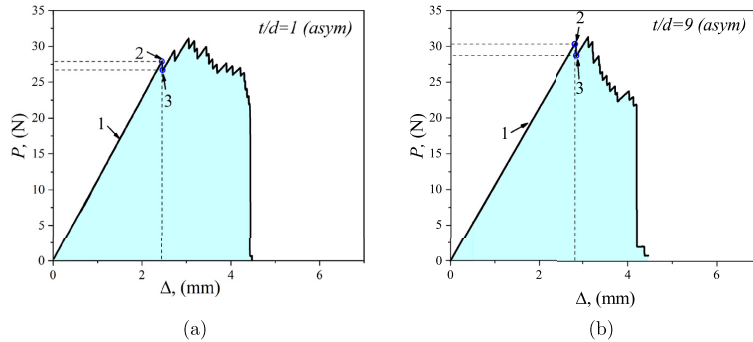


Fig. 6. Experimental force-displacement curves. a) Asymmetric DCB with a top adherend 1.5 times thicker than the bottom adherend. The pillars had an aspect ratio of $t/d = 1$. b) Asymmetric DCB with pillars of aspect ratio $t/d = 9$. The different marks indicate (1) initial loading path, (2) crack onset / loss of linearity, (3) point of crack arrest and beginning of new loading path. The cyan areas depict the work of $W_{t/d=1} = 0.090$ J and $W_{t/d=9} = 0.080$ J. (For interpretation of the references to color in this figure legend, the reader is referred to the web version of this article.)

is observed and is comprised of crack onsets and crack arrests. No kinking of the crack from the interface was observed in any of the experiments.

Together with the experimental data are depicted the theoretical loading paths (marked with dashed, red lines) obtained using Eq. (12). Each loading path was calculated with an initial crack length corresponding to a well defined pillar position. For example, the first loading path corresponds to a crack length of $a_{1p1} = a_0 = 90$ mm, the second path is calculated with $a_{1p2} = a_0 + (d + s) = 92$ mm, and so on. The theoretical predictions of the loading paths correspond very well with those of the experimental data. This supports the idea of each pillar failing individually followed by crack arrest at the next pillar. Furthermore, this result shows that crack propagation is the main source of energy dissipation and it gives confidence that the use of the Irwin-Kies assumption [Eq. (13)] is justified.

The crack propagation facilitated by multiple crack onsets and arrests gave the specimen a much larger extension range and associated work done i.e. $W = \int Pd\Delta = \frac{1}{2} \sum_{i=1}^n (P_{oi}\Delta_i - P_{ai}\Delta_i) \propto n$ where W , P_{oi} , P_{ai} , Δ_i , n denote the work done by structured interface, force at crack onset in pillar i , force at crack arrest position of pillar i , displacement at pillar i and the number of pillars, respectively, compared to the kinking crack, which in the present study always led to critical failure soon after onset.

For comparison, Fig. 6(a) and (b) show the exemplary load response for asymmetric specimens with the pillars of aspect ratios of $t/d = 1$ and $t/d = 9$, respectively. The same main features of the force-displacement curves are revealed viz. crack onset-arrest behavior visible from the characteristic jagged form (in Fig. 6 the numbers 1-3 denotes linear loading, crack onset and crack arrest stages respectively). It is noticed that introducing asymmetry to the configuration did not affect the load response significantly. Comparing the responses for different pillar heights, they are very similar in terms of qualitative behavior.

5.1.1. Compliance

Fig. 7 shows the compliance (normalized by the theoretical compliance of the reference geometry) as a function of the aspect ratio of the pillars obtained from the experiments, the analytical prediction in Eq. (12), and from the FEA.

The three approaches can be found in very good agreement. As anticipated, the thicker substrate (higher bending and shear rigidities) shifted the compliance to a lower state not affecting the overall trend of the curve. The compliance was expected to increase with increasing pillar aspect ratio as indicated by Eq. (3). This is also seen in Fig. 7. Both the analytical model and the FEA predict the compliances for both configuration in the tested range of pillar aspect ratios. However, the analytical model for the asymmetric configuration slightly underestimates the compliance of the specimen. It should be noticed that for the limiting case, where the aspect ratio tends toward zero the analytical model converges to the reference model. For a pillar aspect ratio of $t/d = 9$, the compliance is around 13% higher than for the reference DCB specimen. The good agreement between the FEA, which accounted for the structure of each pillar, and the analytical model, which homogenized the pillars and interface, supports the assumptions made for the latter.

5.1.2. Finite element analysis of load transfer

In Fig. 8(a-d) the normal stress, σ_{yy} , along the centreline of the interface region (as depicted in Fig. 3) of symmetric specimens with four different aspect ratios are shown. All of the four cases are presented as per unit of applied force.

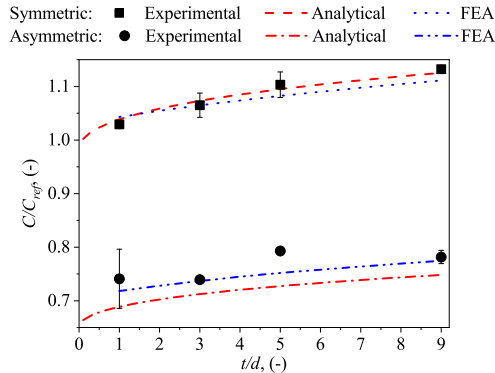


Fig. 7. Specimen compliance normalized with the theoretical reference geometry against aspect ratio of the interfacial pillars. The squares and circles show the mean values and accompanying standard deviations of the experimental compliances from the symmetric and asymmetric configuration, respectively. The red lines (dashed for symmetric and dashed-dotted for asymmetric) are the analytical model showing a very good agreement with the experimental data. The asymmetric configuration is slightly overestimated in terms of stiffness. The symmetrical configuration converges to the reference model in the limiting case where $t/d \rightarrow 0$. The FEA, depicted with blue lines (dotted for symmetric and dashed-dotted-dotted for asymmetric), also shows a very good agreement with both the analytical model and the experimental data. (For interpretation of the references to color in this figure legend, the reader is referred to the web version of this article.)

The red and blue regions depict the axial stress (tension and compression, respectively) in the pillars. For the lowest of the aspect ratios the stress distribution takes on a parabolic shape with largest magnitude in the middle of the pillar. This specific shape is due to the finite height of the pillar for which the center, $y = 0$, remains affected by the corner stress effects at $y = t/2$. The overall stress distribution resembles the shape predicted by the homogenized version of the elastic foundation model [Eq. (7)] plotted as a continuous black line. The peak stress, at the first pillar, i.e. governing failure load, is found to decrease significantly with increasing pillar aspect ratio. Increasing the aspect ratio from $t/d = 1$ to $t/d = 10$ reduces the peak stress on the first pillar by half.

A red, dashed line tracing the upper envelope of the stress in each pillar for the aspect ratio $t/d = 1$ in the first Fig. 8(a). The same dashed line is then plotted in the three, subsequent figures to visualize the effect of the pillar aspect ratio on the stress. This reveals an interesting trend where the stress in the first few pillars decrease as the aspect ratio goes up while more and more pillars are affected. Hence, larger aspect ratios prompt better stress distribution with the stress spread across more pillars. The distance from the crack tip to the end of the tensile zone (the process zone length) as obtained from the FE calculations is shown on the graphs as λ_{fe}^{-1} . This characteristic length increases by 1.5 times between $t/d = 1$ and $t/d = 10$ cases, resulting in two additional pillars carrying the load in the $t/d = 10$. This is in agreement with Eq. (9), which reveals that the elastic process zone increases with the aspect ratio of pillars. The failure of the specimen is assumed to be governed by the failure of the first pillar and the peak stress in it decreases with increasing aspect ratios, thus slender pillars should promote larger critical failure loads. Moreover, the product of $\lambda^{-1} \lambda_{fe} \rightarrow 1$ as $\frac{t}{d} \rightarrow \infty$, which indicates that the homogenized model may form a reference, asymptotic, solution. However, we expect the other non-dimensional interface parameter s/d to play an important role, which suggests a possible extension of the present work.

Let us briefly discuss consequences of the load distribution on the crack growth process by starting out with the unloaded configuration: $P = \Delta = 0$ in Fig. 5. Upon load application the stresses along the interface are distributed along λ^{-1} and the number of load sharing pillars is established. The stress level on the first pillar is below the critical value (recognized as critical force P_c). Once the critical stress on the first pillar is reached, the pillar breaks instantaneously. As reported for the homogeneous geometry (Appendix A1), due to the brittleness of the material and the finite (and small) width of the pillar, stable crack growth cannot be expected. The energy is released and the crack front position moves to the next pillar (i.e. $a_0 \rightarrow a_0 + d + s$). The process zone is re-established with the same number of pillars carrying the load as before, but the peak stress value (for the displacement controlled boundary conditions) is below the critical. Additional energy needs to be supplied to overcome the threshold value and propagate the crack further. The entire process is iterative as seen from Figs. 5 and 6. Due to the finite size of the pillars and the distance between them, the process is dominated by deterministic effects and can be related to lattice fracture models (Lawn, 1993). However, by increasing the number of pillars in the width direction or by reducing the gap s between the pillars, such that the stresses shared by two neighboring pillars will be of similar magnitude (Chung and Chaudhury, 2005), it can turn into a more stochastic process. Further analysis of such transition is beyond the scope of the present study.

12

S. Heide-Jørgensen, M.K. Budzik and K.T. Turner / Journal of the Mechanics and Physics of Solids 137 (2020) 103825

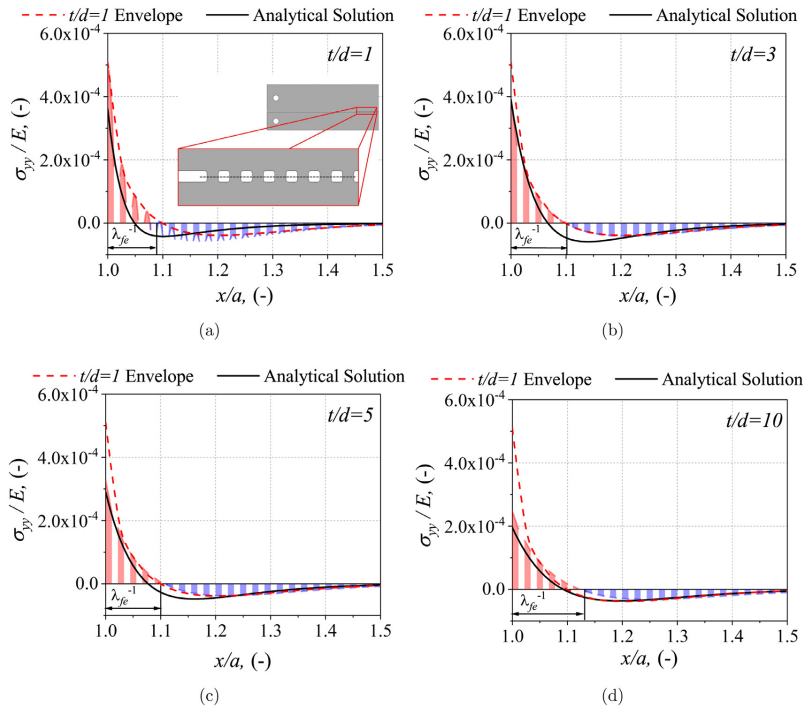


Fig. 8. FEA predictions of the stress σ_{yy} distribution in the pillars for the symmetric configuration. The red and blue regions depict the axial stress (tension and compression, respectively) in the pillars. The dashed, red lines show the upper envelope of the pillars with aspect ratios $t/d = 1$. The process zone λ_{fe}^{-1} spanning from the crack tip to the beginning of the compression zone is marked as well. The black lines show the analytical solution given by Eq. (7). (For interpretation of the references to color in this figure legend, the reader is referred to the web version of this article.)

To complete this section, in Fig. 9 the axial stress in the pillars for the asymmetric configurations are shown. The asymmetric specimen has a very similar trend to the symmetric specimen for both the stress distribution across a single pillar and the overall distribution across the interface. Both configurations stays in good agreement qualitatively and quantitatively, hence asymmetry, in the present case, does not seem to significantly affect the long-range distribution of the tensile component of the stress.

The asymmetric configuration results in additional shearing of the interface. In Fig. 10 the shear stress σ_{xy} distribution is shown. Common for all aspect ratios is that the shearing is largest in the middle of the pillars while it is zero near the edges (shear stress free). Like the axial stresses, the shear stresses decrease with increasing aspect ratio, however, the shear stresses are an order of magnitude smaller than the axial stresses. Recall, that peak axial stress decreased by a factor of 2 when the aspect ratio went from $t/d = 1$ to $t/d = 10$. The peak shear stress decreases by almost a factor of 30 for the same aspect ratio range. As expected from the macro-mechanical model, Eq. (26), the increased aspect ratio allows accommodation of the effects of specimen asymmetry, turning the shear dominated, stubby, geometry of the pillars ($t/d < 1$) to a more slender one ($t/d > 1$) in which bending prevails. While, in the present study the axial loading of the pillars is dominant and the shear stresses can be neglected from here on, the work also encourages further investigation of $t/d < 1$ cases under mixed mode conditions.

5.2. Micro-mechanics vs. macro-mechanics

In the following, the difference between the macroscopic and the microscopic approaches is described including the relation to the experimental observations.

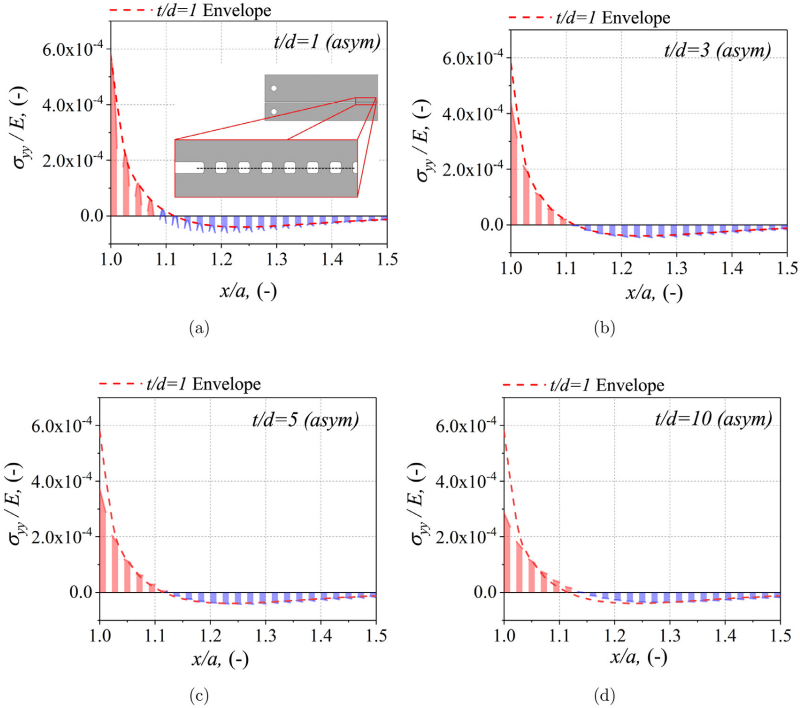


Fig. 9. FEA predictions of the distribution of axial stress σ_{yy} in the pillars for the asymmetric configuration. The red and blue pillars depict the tension and compression, respectively, in the pillars. The dashed, red lines are the upper envelope of the pillars with aspect ratio $t/d = 1$. (For interpretation of the references to color in this figure legend, the reader is referred to the web version of this article.)

5.2.1. Critical fracture force

As mentioned before, variations in the critical force, i.e. the force at crack onset, were determined for different specimen types and different pillar aspect ratios. The critical force for the symmetric and asymmetric specimens are shown by squares and circles, respectively, in Fig. 11. For comparison the critical forces are normalized with that of the reference specimens, $P_{c,ref}$. The results show that the onset force P_c decreases by around 20% relative to the reference specimen for aspect ratios up to $t/d = 1$. However, the critical force monotonically increases with increasing aspect ratios once $t/d > 1$. This supports the idea from the previous section of slender pillars aiding the stress distribution.

Recall, that within the present study the reference specimen broke abruptly, while the pillared specimen promoted crack propagation with multiple onsets and arrests. Introducing pillars at the interface increased work of fracture at the cost of a slightly lower onset force compared to the reference geometry, at least for the aspect ratios treated in this work. The trend of the data predicts that at certain aspect ratios $t/d > 9$ the critical force could be similar, even higher, than for the reference configuration. This observation suggests using fibril geometries $t/d \gg 1$, in agreement with the load sharing phenomena observed in fibrillar adhesives (Aksak et al., 2008; Bacca et al., 2016; Hui et al., 2004).

In Fig. 11 the predictions of the micro-mechanical and the macro-mechanical approaches are shown with dashed and dashed-dotted, and, dotted and dashed-dotted-dotted lines, respectively, with red color used for the symmetric and blue for the asymmetric specimens. Recall, that the macroscopic approach was based on the Irwin-Kies equation, Eq. (38), and the formulation treating the interface as homogeneous and continuous. The microscopic approach, Eq. (23), was based on an energetic analysis of the pillar taking its geometry into account. Importantly, even though the macro-mechanical model successfully captured the compliance of the configurations it failed to predict the critical force accurately. It underestimates the onset force while predicting a decreasing trend with increasing aspect ratio - the opposite of what is observed. The micro-mechanical approach, however, is in very good agreement with the experimental data both qualitatively and quantitatively.

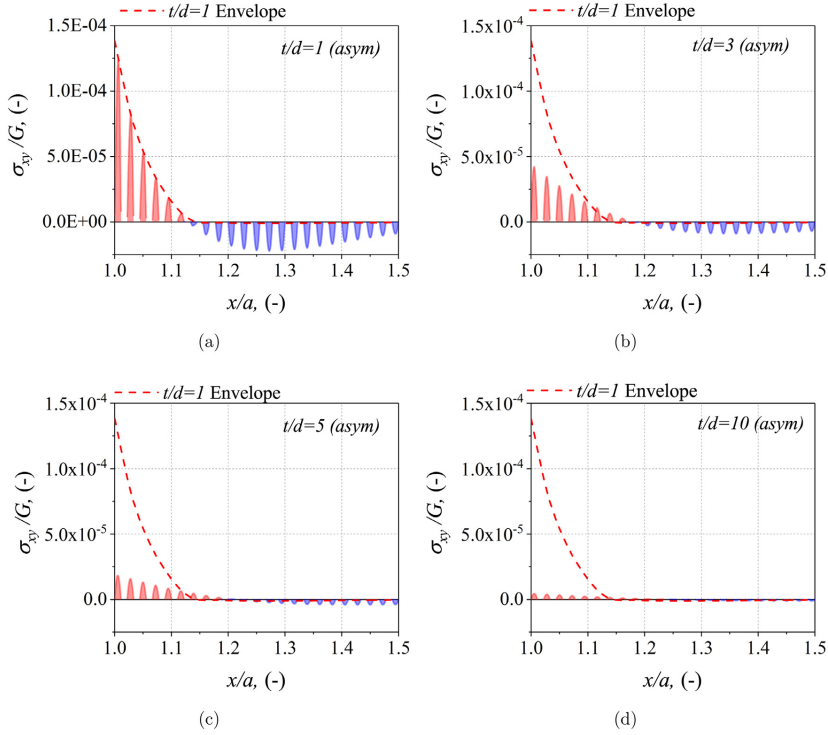


Fig. 10. Shear stress across the pillars in the asymmetric configuration. The red and blue pillars show the positive and negative shear stresses, respectively, obtained from FEA normalized with the shear modulus G . The dashed, red line is the upper envelope of the $t/d = 1$ specimen. (For interpretation of the references to color in this figure legend, the reader is referred to the web version of this article.)

This supports the concept of failure being governed by the micro-mechanical mechanisms and, thus, the macroscopic approach alone is insufficient.

Importantly, the macroscopic response of the material to applied load can be fully controlled through smaller scale geometrical manipulations being the core of mechanical metamaterials.

5.3. Interface material failure scaling law

The scaling law derived in Bartlett et al. (2012) suggests that the critical force of a bonded system is governed by the fracture energy \mathcal{G}_c , the contact area A , and, the compliance of the system C , i.e.:

$$P_c \sim \sqrt{\mathcal{G}_c} \sqrt{\frac{A}{C}} \quad (32)$$

In the present work, the area created during a single failure event is $b \cdot d = \text{const}$. However, Fig. 7 indicates that the compliance increased with the aspect ratio d/t such that the ratio $R_{AC} := \sqrt{A/C} \rightarrow 0$ as $t/d \rightarrow \infty$. Thus, the critical force was expected to decrease.

5.3.1. The effective load carrying area

In Fig. 12 the macro-mechanical and micro-mechanical approaches depict the relation between the normalized critical force and the compliance. The data are compared with experimental results. Both, the micro-mechanical approach and the

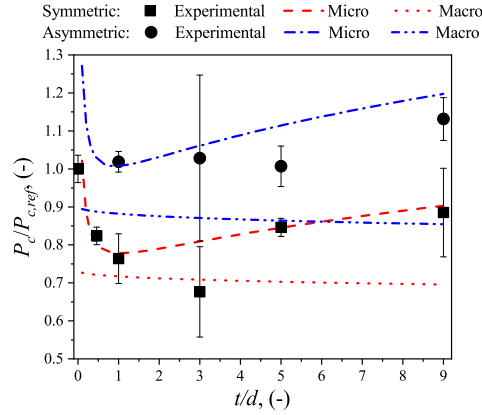


Fig. 11. Critical onset force normalized by the onset force of the reference specimen as function of the pillar aspect ratio. The squares and the circles show the experimental mean critical force and standard deviation for the symmetric and asymmetric configuration, respectively. The dotted and dashed-dotted lines show the predictions of the macro-mechanical approach and the dashed and dashed-dotted lines represent the micro-mechanical approach with red and blue lines for the symmetric and asymmetric configuration, respectively. Increasing critical force with increasing aspect ratio is observed. This was captured by the micro-mechanical approach while the macroscale approach fails to capture this trend. (For interpretation of the references to color in this figure legend, the reader is referred to the web version of this article.)

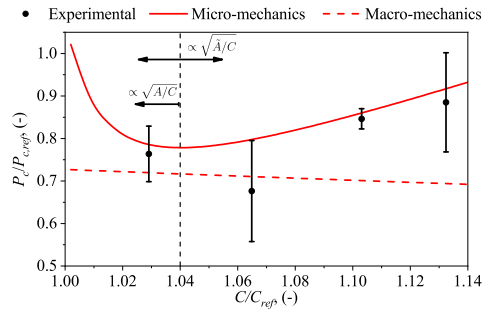


Fig. 12. Relation between the compliance and the critical force for the symmetric configuration. The global approach (dashed line) follows an inversely proportional relation that agrees with the scaling law proposed by Bartlett et al. (2012) when the surface area is kept constant. The experimental (circles) and the micro-mechanical approach (solid line), however, show proportionality between the critical force and the compliance.

experimental data display similar trend. Except at the very beginning, the critical force increased with increasing compliance, thereby contradicting the scaling in Eq. (32).

Assuming that the region responsible for load transfer ahead of the crack front is related to the elastic process zone of length λ^{-1} , the affected area can be defined by combining Eqs. (3) and (9):

$$\tilde{A} := \lambda^{-1} b f = (2I_\beta b^3)^{1/4} \left[\frac{d^4}{(d+s)^3} \right]^{1/4} \left(\frac{t}{d} \right)^{1/4} \tag{33}$$

The first term on the right-hand side represents the effect of the geometry of the substrates defining the ‘long range interactions’ length scale of the material. The second term expresses the characteristic, in-plane structure of the interface and is responsible for the efficiency of the load transfer between the long and short ranges. The third term reflects the smallest geometrical feature of the material, which in the present case is the pillar aspect ratio. Increasing either the dimensions of the substrate, the volume fraction of the pillars, or the pillar aspect ratio increases the load carrying area by extending the process zone. Since the compliance, Eq. (12), is proportional to the aspect ratio, the ratio $\sqrt{A/C}$ also decreases with the aspect ratio when the area is fixed.

16

S. Heide-Jørgensen, M.K. Budzik and K.T. Turner / Journal of the Mechanics and Physics of Solids 137 (2020) 103825

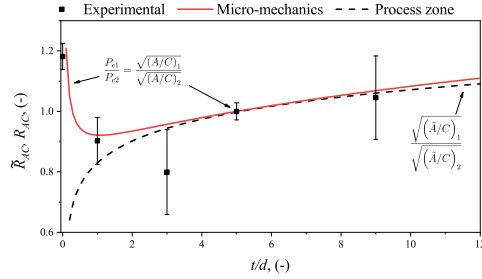


Fig. 13. Relation between the pillar aspect ratio t/d and normalized the surface area-compliance ratios \bar{R}_{AC} and R_{AC} . The dashed line shows the relation when only the load carrying surface area as stated in Eq. (33) is taken into account. The solid line represents the micro-mechanical model and the squares depict the experimental data. Both of them are calculated based on the scaling law Eq. (32) using the critical forces. An acceptable agreement between the different approaches and the experimental data is seen, especially for higher aspect ratios.

5.3.2. The surface area-compliance ratio

If the area increases, it is the competition between the growth of the area and that of the compliance, which determines if the ratio and, hereby, the critical force increases or decreases. The ratios R_{AC} for the experimental data and the analytical model are obtained using Eq. (32), the critical force and the fracture energy, hence:

$$R_{AC} := \frac{R_{AC1}}{R_{AC2}} = \frac{P_{c1}}{P_{c2}} = \frac{\sqrt{G_c} \left(\sqrt{\frac{A}{C}} \right)_1}{\sqrt{G_c} \left(\sqrt{\frac{A}{C}} \right)_2} \quad (34)$$

referred to as the 'force approach'. For comparison, a similar normalization is applied to $\bar{R}_{AC} = \sqrt{\bar{A}/C}$, referred to as the 'affected area' approach. In both cases $t/d = 5$ is used as reference (regarded as intermediate case). In Fig. 13 the three ratios are shown as functions of the pillar aspect ratio. A good agreement between the different approaches and the experimental data is observed. However, in the limit $\frac{t}{d} \rightarrow 0$, the interface region geometry translates to (flat) spots and both approaches diverge rapidly. Quantitatively minor discrepancies are revealed between the critical force approach and the affected area approach while qualitative resemblance is good. The dashed line representing the affected area approach increases with the aspect ratio, which means that the affected area grows faster than the compliance of the system. Both methods stay in good agreement with the experimental data. This indicates that the critical force scales with the load carrying interface area ahead of the crack, as stated by Eq. (33), and not the surface area of the pillar alone. This has two implications. Firstly, the scaling law is still valid for this configuration, however, instead of the geometrical interface area A , the load carrying area \bar{A} should be included:

$$P_c \sim \sqrt{G_c} \sqrt{\frac{\bar{A}}{C}} \quad (35)$$

Secondly, the critical force can be tuned without changing the geometrical interface area as shown in this study. From Eq. (33) it is seen that both the geometry, the composition of pillars and their spacing, and, the pillar aspect ratio influence the affected surface area and through it the critical force. This provides a powerful tool for understanding and designing materials with structured interfaces since these terms also affect the overall compliance allowing for tougher and more compliant structures.

6. Conclusions

We have investigated the use of geometry to engineer the fracture response of double cantilever beam specimens. Double cantilever beam reference specimens were laser cut from thin sheets of elastic-brittle PMMA and tested under mode I loading. Unstable crack growth and rapid catastrophic failure due to crack kinking were recorded in unstructured specimens. The introduction of geometrical features in the form of an array of pillars significantly altered the fracture response of the specimen. Thus, a new "material" is produced with properties depending on the intertwined length scales introduced by 'long range' beam and 'short range' pillar geometries. This led to a significant alteration of the load response of both quantitative and qualitative nature. The pillars caused a change from the single loading-critical failure event to a multiple failure event postponing the catastrophic failure, thus, significantly increasing the energy dissipated in fracture of the

specimens. For displacement-controlled experiments multiple failure events are guaranteed and independent of the pillar geometry. Importantly, the model provided can be used for designing interfaces maintaining such behavior under force controlled (unstable) loading. This can be achieved through the indicated parameters: thickness and width of the pillar, distance between the pillars, and the process zone size. The compliance and the critical fracture load were found to be affected by the geometrical features as well. Specifically, the compliance and failure load both increased with increasing pillar aspect ratio. Moreover we noted that the structured pillar interface, i.e. the micro-scale in our problem, were capable of absorbing a certain degree of imperfection, e.g. asymmetry. This provides a tool for increasing energy dissipation through interfaces but also for tuning structural properties.

While in this work the simplest geometrical modifications have been made, the observed phenomena and gains displayed a significant potential for geometric manipulation to achieve tougher or tuned properties.

Authors statement

The authors contributed equally to the present paper at all stages of paper preparation.

Declaration of Competing Interest

The authors declare that they have no known competing financial interests or personal relationships that could have appeared to influence the work reported in this paper.

Acknowledgments

Financial support from IDAs og Berg-Nielsens Studie- og Støttefond, Aage og Johanne Louis-Hansens Fond, Augustinus Fonden and Knud Højgaard's Fond are gratefully acknowledged. KIT acknowledges financial support for this work from the National Science Foundation under awards CMMI-1663037 and MRSEC DMR-1720530.

Appendix A. Reference specimens

To estimate the fracture toughness, G_c , without the steady-state crack propagation (usually, after the crack onset, the crack kinked out of the path that was pre-designed by etching) and the apparent bending rigidity EI , reference specimens with different initial crack lengths $a = 80, 100, 120$ mm were prepared. Two specimens for each of the crack lengths were manufactured and tested. The laser cutting process used for manufacturing the specimens including the pre-crack yielded a crack of approximately 300 μm in width.

A1. Apparent bending rigidity

Treating the specimens as cantilever beams, the compliance can be expressed with simple beam theory (ignoring the lower order Timoshenko beam effect, thus reflecting the apparent nature of estimated quantity), as:

$$C = \frac{a^3}{3EI} \quad (36)$$

From the experiments, the compliance of the specimens are measured as the tip displacement over the tip force $C_{\text{exp}} = \Delta/2P$. From Eq. (36) the apparent bending rigidity of the specimens are obtained as:

$$EI = \frac{a^3}{3C_{\text{exp}}} = \frac{2Pa^3}{3\Delta} \quad (37)$$

Fig. 14 shows the measured force-displacement curves for specimens with three different crack lengths. By analyzing the initial, linear loading part of this data, the bending rigidity was found to be approximately $EI \approx 5.35$ m² as an average value from all the experiments conducted.

A2. Fracture energy

To determine the fracture toughness of the material, the Irwin-Kies (Bonesteel et al., 1978) method is used together with Eq. (36) to obtain an expression for the energy release rate:

$$G = \frac{P^2}{2b} \frac{dC}{da} \quad (38)$$

Two parameters, namely, the critical force at the crack onset P_c and the rate at which compliance changes with respect to growing crack, dC/da , are required for obtaining the fracture energy. The critical force is determined as the point where the linearity of the initial loading is lost. The reported, average, values are: $P_{c80} = 36.1$ N, $P_{c100} = 27.6$ N, $P_{c120} = 19.8$ N. The second parameter is obtained by plotting the mean compliance for each of the crack lengths and fitting Eq. (36) as $C =$

18

S. Heide-Jørgensen, M.K. Budzik and K.T. Turner / Journal of the Mechanics and Physics of Solids 137 (2020) 103825

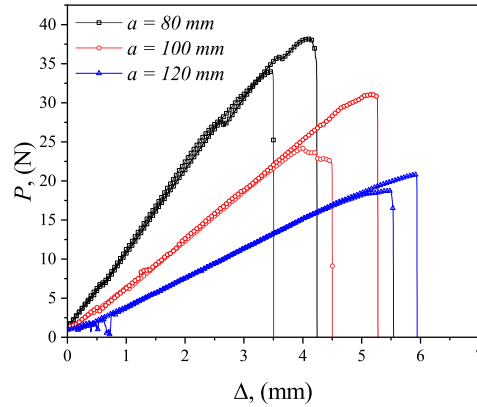


Fig. 14. Experimental load response for the reference DCB specimens. Where the gray, red and blue lines represent an initial crack length of 80 mm, 100 mm and 120 mm, respectively. (For interpretation of the references to color in this figure legend, the reader is referred to the web version of this article.)

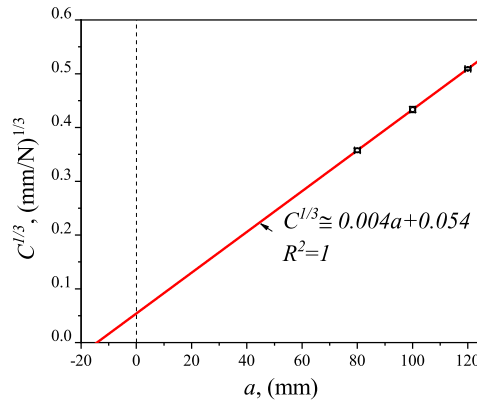


Fig. 15. The experimental compliance plotted against initial crack length. The red line is a fit, presenting Eq. (36), to the experimental data. (For interpretation of the references to color in this figure legend, the reader is referred to the web version of this article.)

$a_3 \cdot a^3$. In Fig. 15, the experimental data and the cubic fit are seen with the pre-factor $a_3 = 5.4787 \cdot 10^{-8}$. Note, that the intersection point with the ordinate axis yields a positive value; this is due to the finite stiffness of the loading system and tested specimens (e.g. due to the process zone, root rotation effects or similar.) Finally, $\frac{dC}{da} = 3 a_3 \cdot a^2$ which together with Eq. (38) and the critical forces yields a fracture energy $\mathcal{G}_c \approx 0.25 \text{ N mm}^{-1}$, which is found in a very good agreement with available literature, e.g. Gómez et al. (2000) and Ayatollahi et al. (2006).

Appendix B. Failure due to pillar compression

While failure due to pillar compression was not observed in this work, the macro-mechanical solution implies existence of a compressive zone ahead the crack. For specific geometries and materials, the compressive loading may lead to collapse of the pillar by exceeding the compression strength or critical buckling load. To keep the analysis relatively short we assume that a single pillar can be treated as a beam under fixed-fixed boundary conditions at $z = \pm \frac{t}{2}$. For such case, the boundary conditions reads as $u(\pm \frac{t}{2}) = 0 \wedge \frac{du}{dz}(\pm \frac{t}{2}) = 0$. Assuming the pillar behaves as a slender beam, the buckling solution

(Bažant and Cedolin, 2010), leads to the critical (Euler) load:

$$P_c = 4EI_p \left(\frac{\pi}{t} \right)^2 \quad (39)$$

Assuming:

$$\sigma_{comp} = \frac{P_c}{bd} = 4E \frac{I_p}{bd} \left(\frac{\pi}{t} \right)^2 \quad (40)$$

with the radius of gyration $r = \sqrt{\frac{I_p}{bd}}$ one obtains:

$$\sigma_{comp} = \frac{1}{4} E \pi^2 \left(\frac{t}{r} \right)^{-2} \quad (41)$$

Taking, to the first approximation, Eq. (23) we find:

$$\sigma_p = \sqrt[3]{4 \frac{G_c E^2}{t}} \quad (42)$$

which together with Eq. (40) readily equates to the following non-dimensional criterion for compressive failure:

$$\left(\frac{d}{t} \right)^2 = c_1 \sqrt[3]{\frac{G_c}{tE}} \quad (43)$$

with the non-dimensional constant $c_1 = \frac{\sqrt[3]{4}}{3\pi} \left(\frac{\sigma_{comp}}{\sigma_{cp}} \right)$ - index c corresponds to the failure stress. The structure fails in compression once the left hand side is greater than the right hand side. The buckling scenario could most likely take place once using brittle fibres and/or hair like structures. Such were not investigated here leaving place for the future exploration.

Supplementary material

Supplementary material associated with this article can be found, in the online version, at doi:[10.1016/j.jmps.2019.103825](https://doi.org/10.1016/j.jmps.2019.103825).

References

- Abid, N., Pro, J.W., Barthelat, F., 2019. Fracture mechanics of nacre-like materials using discrete-element models: effects of microstructure, interfaces and randomness. *J. Mech. Phys. Solids* 124, 350–365. doi:[10.1016/j.jmps.2018.10.012](https://doi.org/10.1016/j.jmps.2018.10.012).
- Aghababaei, R., Warner, D.H., Molinari, J.-F., 2016. Critical length scale controls adhesive wear mechanisms. *Nature Communications* 7 (1), 11816. doi:[10.1038/ncomms11816](https://doi.org/10.1038/ncomms11816). www.pubmedcentral.nih.gov/articlerender.fcgi?artid=3006164&tool=pmcentrez&rendertype=abstract.
- Aksak, B., Murphy, M.P., Sitti, M., 2008. Gecko inspired micro-fibrillar adhesives for wall climbing robots on micro/nanoscale rough surfaces. In: 2008 IEEE International Conference on Robotics and Automation, IEEE, pp. 3058–3063. doi:[10.1109/ROBOT.2008.4543675](https://doi.org/10.1109/ROBOT.2008.4543675).
- Ashby, M., Johnson, K., 2010. Materials and Design, second ed Butterworth-Heinemann, Canada doi:[10.1016/C2009-0-26530-5](https://doi.org/10.1016/C2009-0-26530-5).
- Autumn, K., Gravish, N., 2008. Gecko adhesion: evolutionary nanotechnology. *Philos. Trans. R. Soc. A* 366 (1870), 1575–1590. doi:[10.1098/rsta.2007.2173](https://doi.org/10.1098/rsta.2007.2173).
- Ayatollahi, M.R., Aliha, M.R., Hassani, M.M., 2006. Mixed mode brittle fracture in PMMA - an experimental study using SCB specimens. *Mater. Sci. Eng. A* 417 (1–2), 348–356. doi:[10.1016/j.msea.2005.11.002](https://doi.org/10.1016/j.msea.2005.11.002).
- Bacca, M., Booth, J.A., Turner, K.L., McMeeking, R.M., 2016. Load sharing in bioinspired fibrillar adhesives with backing layer interactions and interfacial misalignment. *J. Mech. Phys. Solids* 96, 428–444. doi:[10.1016/j.jmps.2016.04.008](https://doi.org/10.1016/j.jmps.2016.04.008).
- Bartlett, M.D., Croll, A.B., King, D.R., Paret, B.M., Irschick, D.J., Crosby, A.J., 2012. Looking beyond fibrillar features to scale gecko-like adhesion. *Adv. Mater.* 24 (8), 1078–1083. doi:[10.1002/adma.201104191](https://doi.org/10.1002/adma.201104191).
- Bažant, Z.P., Cedolin, L., 2010. Stability of structures: elastic, inelastic, fracture and damage theories. *Stabil. Struct.* 1–1012. doi:[10.1142/7828](https://doi.org/10.1142/7828).
- Bertoldi, K., Vitelli, V., Christensen, J., van Hecke, M., 2017. Flexible mechanical metamaterials. *Nat. Rev. Mater.* 2 (11), 17066. doi:[10.1038/natrevmats.2017.66](https://doi.org/10.1038/natrevmats.2017.66).
- Bonesteel, R.M., Piper, D.E., Davinroy, A.T., 1978. Compliance and KI calibration of double cantilever beam (DCB) specimens. *Eng. Fract. Mech.* 10 (2), 425–428. doi:[10.1016/0013-7944\(78\)90022-X](https://doi.org/10.1016/0013-7944(78)90022-X).
- Chaudhury, M.K., Chakrabarti, A., Ghatak, A., 2015. Adhesion-induced instabilities and pattern formation in thin films of elastomers and gels. *Eur. Phys. J. E* 38 (7), 82. doi:[10.1140/epje/i2015-15082-7](https://doi.org/10.1140/epje/i2015-15082-7).
- Chung, J.Y., Chaudhury, M.K., 2005. Roles of discontinuities in bio-inspired adhesive pads. *J. R. Soc. Interface* 2 (2), 55–61. doi:[10.1098/rsif.2004.0020](https://doi.org/10.1098/rsif.2004.0020).
- Deblieck, R.A., Van Beek, D.J., Remerie, K., Ward, I.M., 2011. Failure mechanisms in polyolefines: the role of crazing, shear yielding and the entanglement network. *Polymer* 52 (14), 2979–2990. doi:[10.1016/j.polymer.2011.03.055](https://doi.org/10.1016/j.polymer.2011.03.055).
- Del Campo, A., Greiner, C., Arzt, E., 2007. Contact shape controls adhesion of bioinspired fibrillar surfaces. *Langmuir* 23 (20), 10235–10243. doi:[10.1021/la7010502](https://doi.org/10.1021/la7010502).
- Dillard, D.A., Mukherjee, B., Karnal, P., Batra, R.C., Frechette, J., 2018. A review of Winkler's foundation and its profound influence on adhesion and soft matter applications. *Soft Matter* 14 (19), 3669–3683. doi:[10.1039/c7sm02062g](https://doi.org/10.1039/c7sm02062g).
- Geim, A.K., Dubonos, S.V., Grigorjeva, I.V., Novoselov, K.S., Zhukov, A.A., Shapoval, S.Y., 2003. Microfabricated adhesive mimicking gecko foot-hair. *Nat. Mater.* 2 (7), 461–463. doi:[10.1038/nmat917](https://doi.org/10.1038/nmat917).
- Glassmaker, N.J., Jagota, A., Hui, C.Y., Noderer, W.L., Chaudhury, M.K., 2007. Biologically inspired crack trapping for enhanced adhesion. *Proc. Natl. Aca. Sci. U.S.A.* 104 (26), 10786–10791. doi:[10.1073/pnas.0703762104](https://doi.org/10.1073/pnas.0703762104).
- Gómez, F.J., Elices, M., Valiente, A., 2000. Cracking in PMMA containing U-shaped notches. *Fatig. Fract. Eng. Mater. Struct.* 23 (9), 795–803. doi:[10.1046/j.1460-2695.2000.00264.x](https://doi.org/10.1046/j.1460-2695.2000.00264.x).
- Griffith, A.A., Taylor, G.I., 1921. VI. The phenomena of rupture and flow in solids. *Philosophical Transactions of the Royal Society of London, Series A, Containing Papers of a Mathematical or Physical Character* 221. doi:[10.1098/rsta.1921.0006](https://doi.org/10.1098/rsta.1921.0006).
- Grossman, M., Pivovarov, D., Bouville, F., Dransfeld, C., Masania, K., Studart, A.R., 2019. Hierarchical toughening of nacre-like composites. *Adv. Function. Mater.* 29 (9). doi:[10.1002/adfm.201806800](https://doi.org/10.1002/adfm.201806800).

20

S. Heide-Jørgensen, M.K. Budzik and K.T. Turner / *Journal of the Mechanics and Physics of Solids* 137 (2020) 103825

- Heide-Jørgensen, S., Budzik, M.K., 2017. Crack growth along heterogeneous interface during the DCB experiment. *Int. J. Solids Struct.* 120, 278–291. doi:10.1016/j.jsostr.2017.05.013.
- Heide-Jørgensen, S., Budzik, M.K., 2018. Effects of bondline discontinuity during growth of interface cracks including stability and kinetic considerations. *J. Mech. Phys. Solids* 117, 1–21. doi:10.1016/j.jmps.2018.04.002.
- Heide-Jørgensen, S., Møller, R.K., Buhl, K.B., Pedersen, S.U., Daasbjerg, K., Hinge, M., Budzik, M.K., 2018. Efficient bonding of ethylene-propylene-diene M-class rubber to stainless steel using polymer brushes as a nanoscale adhesive. *Int. J. Adhes. Adhes.* 87, 31–41. doi:10.1016/j.ijadh.2018.09.006.
- Heide-Jørgensen, S., Teixeira de Freitas, S., Budzik, M.K., 2018. On the fracture behaviour of CFRP bonded joints under mode I loading: effect of supporting carrier and interface contamination. *Compos. Sci. Technol.* 160, 97–110. doi:10.1016/j.compscitech.2018.03.024.
- Huang, Z., Li, X., 2013. Origin of flaw-tolerance in nacre. *Sci. Rep.* 3 (1), 1693. doi:10.1038/srep01693.
- Hui, C.Y., Glassmaker, N.J., Tang, T., Jagota, A., 2004. Design of biomimetic fibrillar interfaces: 2. Mechanics of enhanced adhesion. *J. R. Soc. Interface* 1 (1), 35–48. doi:10.1098/rsif.2004.0005.
- Hutchinson, R.G., Fleck, N.A., 2005. Microarchitected cellular solids - the hunt for statically determinate periodic trusses. *ZAMM* 85 (9), 607–617. doi:10.1002/zamm.200410208.
- Hutchinson, R.G., Fleck, N.A., 2006. The structural performance of the periodic truss. *J. Mech. Phys. Solids* 54 (4), 756–782. doi:10.1016/j.jmps.2005.10.008.
- Irwin, G., 1957. Analysis of Stresses and Strains Near the End of a Crack Traversing a Plate. no DOI
- Lawn, B., 1993. *Fracture of Brittle Solids*. Cambridge University Press, Cambridge doi:10.1017/CBO9780511623127.
- Maloney, K., Fleck, N., 2018. Damage tolerance of an architected adhesive joint. *Int. J. Solids Struct.* 132–133, 9–19. doi:10.1016/j.jsostr.2017.06.010.
- Maloney, K., Fleck, N., 2019. Toughening strategies in adhesive joints. *Int. J. Solids Struct.* 158, 66–75. doi:10.1016/j.jsostr.2018.08.028.
- Messner, M.C., 2016. Optimal lattice-structured materials. *J. Mech. Phys. Solids* 96, 162–183. doi:10.1016/j.jmps.2016.07.010.
- Minsky, H.K., Turner, K.T., 2017. Composite microposts with high dry adhesion strength. *ACS Appl. Mater. Interfaces* 9 (21), 18322–18327. doi:10.1021/acsami.7b01491.
- Mojdehi, A.R., Holmes, D.P., Dillard, D.A., 2017. Revisiting the generalized scaling law for adhesion: role of compliance and extension to progressive failure. *Soft Matter* 13 (41), 7529–7536. doi:10.1039/c7sm01098b.
- Murphy, M.P., Aksak, B., Sitti, M., 2009. Gecko-inspired directional and controllable adhesion. *Small* 5 (2), 170–175. doi:10.1002/sml.200801161.
- Negggers, J., Hoefnagels, J.P., Van Der Sluis, O., Geers, M.G., 2015. Multi-scale experimental analysis of rate dependent metal-elastomer interface mechanics. *J. Mech. Phys. Solids* 80, 26–36. doi:10.1016/j.jmps.2015.04.005.
- Ortiz, C., Boyce, M.C., 2008. Bioinspired structural materials. *Science* 319 (5866), 1053–1054. doi:10.1126/science.1154295.
- Ostoja-Starzewski, M., 2002. Lattice models in micromechanics. *Applied Mechanics Reviews* 55 (1), 35–60. doi:10.1115/1.1432990. 0042068663
- Paris, P., Sih, G., 2009. Stress analysis of cracks. *Fracture Toughness Testing and its Applications*. ASTM International, 100 Barr Harbor Drive, PO Box C700, West Conshohocken, PA 19428-2959 doi:10.1520/STP265845. 30–30–52
- Rayneau-Kirkhope, D., Dias, M.A., 2017. Embracing failure. *Phys. World* 30 (8), 25–28. doi:10.1088/2058-7058/30/8/39.
- Salem, N.B., Budzik, M.K., Jumel, J., Shanahan, M.E., Lavelle, F., 2013. Investigation of the crack front process zone in the double cantilever beam test with backface strain monitoring technique. *Eng. Fract. Mech.* 98 (1), 272–283. doi:10.1016/j.engfracmech.2012.09.028.
- Wadley, H.N., Fleck, N.A., Evans, A.G., 2003. Fabrication and structural performance of periodic cellular metal sandwich structures. *Compos. Sci. Technol.* 63 (16), 2331–2343. doi:10.1016/S0266-3538(03)00266-5.
- Walia, S., Shah, C.M., Gutruf, P., Nili, H., Chowdhury, D.R., Withayachumnankul, W., Bhaskaran, M., Srimam, S., 2015. Flexible metasurfaces and metamaterials: a review of materials and fabrication processes at micro- and nano-scales. *Appl. Phys. Rev.* 2 (1), 11303. doi:10.1063/1.4913751.
- Wegst, U.G., Bai, H., Saiz, E., Tomsia, A.P., Ritchie, R.O., 2015. Bioinspired structural materials. *Nat. Mater.* 14 (1), 23–36. doi:10.1038/nmat4089.
- Xue, L., Sanz, B., Luo, A., Turner, K.T., Wang, X., Tan, D., Zhang, R., Du, H., Steinhart, M., Mijangos, C., Guttman, M., Kappl, M., Del Campo, A., 2017. Hybrid surface patterns mimicking the design of the adhesive toe pad of tree frog. *ACS Nano* 11 (10), 9711–9719. doi:10.1021/acsnano.7b04994.
- Yang, Y., Dias, M.A., Holmes, D.P., 2018. Multistable kirigami for tunable architected materials. *Phys. Rev. Mater.* 2 (11), 110601. doi:10.1103/PhysRevMaterials.2.110601.
- Yao, H., Gao, H., 2006. Mechanics of robust and releasable adhesion in biology: bottom-up designed hierarchical structures of gecko. *J. Mech. Phys. Solids* 54 (6), 1120–1146. doi:10.1016/j.jmps.2006.01.002.
- Yao, L., Alderliesten, R.C., Benedictus, R., 2016. The effect of fibre bridging on the Paris relation for mode I fatigue delamination growth in composites. *Compos. Struct.* 140, 125–135. doi:10.1016/j.compstruct.2015.12.027.
- Yao, L., Alderliesten, R.C., Benedictus, R., 2016. The effect of fibre bridging on the Paris relation for mode I fatigue delamination growth in composites. *Compos. Struct.* 140, 125–135. doi:10.1016/j.compstruct.2015.12.027.
- Ye, J., 2003. *Laminated Composite Plates and Shells*. Springer London, London doi:10.1007/978-1-4471-0095-9.
- Zhao, N., Wang, Z., Cai, C., Shen, H., Liang, F., Wang, D., Wang, C., Zhu, T., Guo, J., Wang, Y., Liu, X., Duan, C., Wang, H., Mao, Y., Jia, X., Dong, H., Zhang, X., Xu, J., 2014. Bioinspired materials: from low to high dimensional structure. *Adv. Mater.* 26 (41), 6994–7017. doi:10.1002/adma.201401718.

Chapter 7

Summary and Outlook

The dissertation deals with structured interfaces and their effects on joint behavior. Several research questions are identified during the initial work on nano-adhesives for rubber-metal bonding (Chapter 2). The questions are broken down into smaller pieces and treated individually. Early on, structuring of the interface region is restricted to the surface (Chapters 3-5), later a metamaterial-inspired approach is taken where the bondline is structured as well (Chapter 6). The studies cover both analytical and numerical work supported by systematic experiments.

In Chapter 2 bonding between EPDM rubber and stainless steel through a polymer brush-based nano-adhesive is investigated. It is concluded that using poly(glycidyl methacrylate) brushes modified with benzoyl peroxide provides similar adhesion strength and quality as a common, commercial primer-and-binder solution. However, with a bondline three orders of magnitude thinner. The custom-made peel specimen containing distinct bonded zones raises several questions such as what are the consequences of having these zones and how the crack velocity and the load response are related for structured interfaces. These are pursued in the remaining chapters.

In Chapter 3 the first question is pursued. Structured interfaces containing regions of weak adhesion running perpendicular to the crack growth direction is studied using the DCB configuration. It is found that the weak zones cause the apparent critical fracture energy, and thereby load carrying capacity, to drop. This effect is more dominant for many small zones compared to few large zones and is reflected in the load response as oscillations. The apparent critical fracture energy is accurately described as a function of the critical fracture energies of the strong and the weak zones and their volume fractions within the elastic process zone. This introduces a new length scale - the elastic process zone size, λ^{-1} .

This is further pursued in Chapter 4 where the stability consequences and rate effects of a single weak zone are investigated. The study shows that as the crack approaches the weak zone it is destabilized by it. This causes an acceleration of the crack propagation and, eventually, a snap-down. Both are captured in the load response. The rate-form ERR reveals a kinetic term depending on loading rate and crack velocity, which is normally not included. The kinetic term is found to lower the effective ERR with up to 15% during crack onset and then diminishes during crack growth. The raising R-curve trend observed experimentally could be related to the kinetic contribution.

Through a collaboration with Delft University the research questions are pursued in the direction of bonded composite joints and kissing-bonds as described in Chapter 5. However, the support carrier included in the bondline is found to trigger an unexpected bridging effect significantly increasing the apparent critical fracture energy and damage tolerance of the joint. As such, this phenomenon is pursued as well. An effective description of the ERR contribution from the bridging is formulated. Similar observations as those of the two previous chapters are made indicating that the phenomena remain independent across three orders of magnitude in stiffness of both adherend and adhesive.

While, in the previous chapters the structuring is limited to the surface, Chapter 6 introduces spatial structuring to the bondline as well. By introducing pillars spanning both adherends, the failure mechanisms of the joint are changed and the dissipation increased. This leads to a higher critical fracture load and a slightly increased global compliance. Increasing the aspect ratio of the pillars increases this effect.

7.1 Contributions to the Field

The main contributions to the field provide by the present dissertation are as follows.

- Chemical formulations and bench-marking of nano-scale, polymer brush-based adhesives for bonding EPDM rubber and stainless steel.
- Extensive experimental exploration of interfacial heterogeneities containing zones of weak adhesion, similar to kissing bonds, and their effects on joint mechanics and failure in particular the load response, fracture energy and crack kinetics.

- Theoretical description and prediction of joint mechanics and failure in term of load response and effective critical fracture energy for structured interfaces containing bands of weak adhesion running perpendicular to the crack growth direction.
- Insight into the interaction between the elastic fracture process zone in front the crack and interfacial heterogeneities, which introduces a new length scale parameter.
- Knowledge on how failure of bonded joints and the concept of critical fracture energy are dependent on rates, i.e. loading rate and crack velocity, and how it changes during crack growth, e.g. rises in the R-curve as an inherent property of testing.
- Quantitative and qualitative descriptions of the effects of a bridging phenomenon triggered by the support carrier within the bondline on critical fracture energy and crack propagation.
- Theoretical and experimental investigation of how including pillars in the bondline region can significantly increase the critical fracture load, improve damage tolerance by postponing catastrophic failure and increase joint compliance.

The following analytical models were developed and validated experimentally during the project. Figure 7.1 shows the contributions to the DCB framework made within this project.

- An analytical unit pattern model of an interfacial heterogeneity used to investigate the load response and the ERR in regard to heterogeneity size. The model is based on beam theory, LFM and the elastic foundation formulation.
- A multi-pattern semi-analytical version of the unit pattern model allowing for multiple zones of weak adhesion with varying sizes and positions is established based.
- A rule of mixtures predicting the effective critical fracture energy as a function of the critical fracture energies of the strong and the weak zones and their volume fraction in the elastic fracture process zone.
- A rate-form of the ERR for the DCB configuration able of decomposing the ERR into a static and a kinetic part, which depends on the

loading rate and the crack velocity. This is based on Griffith's generalized theory.

- Macro- and micro-mechanical models of a pillar structured interface coupling both the global response of the joint, in terms of load response, and the micro-mechanical failure of the pillars. The models are based on Timoshenko beam theory, the Winkler foundation and LFM.
- A FE model of the pillared interface incorporating VCCT to predict failure.

7.2 Perspective

The novel nano-scale adhesive proves promising in bonding metal and rubber where chemical migration is a concern such as food and drinking water applications. This method significantly reduces the amount of chemistry used by decreasing the bondline thickness by three orders of magnitude: from μm to nm .

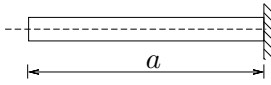
The development of the unit pattern and multi-pattern models can make it possible to describe joints with structured interfaces, e.g. kissing bonds or zones with varying adhesion. It is almost impossible to avoid any defects in bonded joints or composite materials. Trapped air, kissing bonds or zones of weak adhesion will always be present. With these models and the proposed rule of mixtures it can be possible to assess what impact the specific defect will have on the joint and, ultimately, if the part should be kept or discarded. Especially for very small defects, which cause minimal fluctuations in the load response but significantly lower the critical fracture load, these models can be very helpful in predicting the actual strength of the joint.

The rate-form ERR shows that kinetic effects play a vital role especially at crack onset and early propagation. This means that experimentally measured critical fracture energies could be unnecessary conservative. Identifying the contribution of the kinetics and subtracting it from the measured ERR could provide more accurate results of the critical fracture energy. With the effects identified experimental methods and data reduction could be tuned.

The support carrier, which is used to control the bondline thickness, is normally regarded as a weakening factor. However, it was found to cause a bridging phenomenon under the right circumstances. This substantially increased the energy dissipation and the critical fracture load. Introducing this in real life applications, e.g. composite materials or load-carrying adhesive joints, could be a way of enhancing reliability. The support carrier should act as a secondary load-carrier hence taking over if the part would fail preventing catastrophic failure. Essentially, this is another dissipative mechanism to be added.

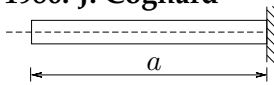
Finally, structured interfaces with pillars have great potentials since they enhance the critical fracture load and increase damage tolerance. In fact, this method could be implemented to increase reliability of joints since

1956: J.J. Benbow and F.C. Roesler



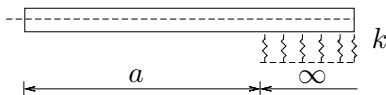
$$0 < x < a : EI \frac{d^4 w}{dx^4} = 0$$

1986: J. Cognard



$$0 < x < a : EI \frac{d^4 w}{dx^4} = q - \frac{EI}{\kappa AG} \frac{d^2 q}{dx^2}$$

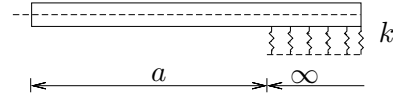
2012: N.B. Salem et al.



$$0 < x < a : EI \frac{d^4 w}{dx^4} = q - \frac{EI}{\kappa AG} \frac{d^2 q}{dx^2}$$

$$a < x < \infty : EI \frac{d^4 w}{dx^4} - \frac{kEI}{\kappa GS} \frac{d^2 w}{dx^2} + kw = q$$

1973: M.F. Kanninen



$$0 < x < a : EI \frac{d^4 w}{dx^4} = q$$

$$a < x < \infty : EI \frac{d^4 w}{dx^4} + kw = q$$

$$k = \left(\frac{2Eb}{t} \right)$$

1992: F.E. Penado



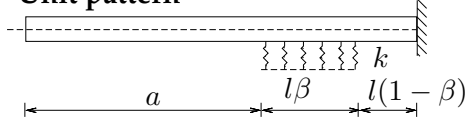
$$0 < x < a : EI \frac{d^4 w}{dx^4} = q$$

$$a < x < \infty : EI \frac{d^4 w}{dx^4} + kw = q$$

$$k = \frac{1}{\frac{1}{k_{adherent}} + \frac{1}{k_{adhesive}}}$$

$$k_{adherent} = \frac{4Eb}{t}$$

$$k_{adhesive} = \frac{b}{t} \frac{E}{1 - \nu^2}$$

Unit pattern

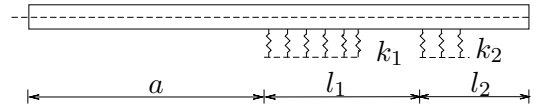
$$0 \leq x \leq a : EI \frac{d^4 w}{dx^4} = q$$

$$a \leq x \leq l\beta : EI \frac{d^4 w}{dx^4} + kw = q$$

$$l\beta \leq x \leq l : EI \frac{d^4 w}{dx^4} = q$$

$$k = \left(\frac{2Eb}{t} \right)$$

$$0 < \beta < 1$$

Multi-pattern

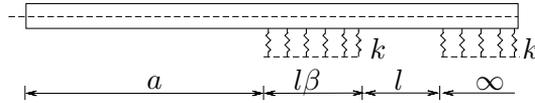
$$0 \leq x \leq a : EI \frac{d^4 w}{dx^4} = q$$

$$a, l_{n-1} \leq x \leq l_n \beta : EI \frac{d^4 w}{dx^4} + kw = q$$

$$l_n \beta \leq x \leq l_n : EI \frac{d^4 w}{dx^4} = q$$

$$k_n = \left(\frac{2E_n b}{t_n} \right)$$

$$0 < \beta < 1, 1 \leq n < \infty$$

Single defect model

$$0 \leq x \leq a : EI \frac{d^4 w}{dx^4} = q$$

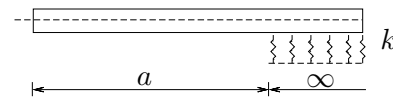
$$a \leq x \leq l\beta : EI \frac{d^4 w}{dx^4} + kw = q$$

$$l\beta \leq x \leq l : EI \frac{d^4 w}{dx^4} = q$$

$$l \leq x < \infty : EI \frac{d^4 w}{dx^4} + kw = q$$

$$k_n = \left(\frac{2E_n b}{t_n} \right)$$

$$0 < \beta < 1$$

Pillar interface model

$$0 \leq x \leq a : EI \frac{d^4 w}{dx^4} = q - \frac{EI}{\kappa AG} \frac{d^2 q}{dx^2}$$

$$a \leq x < \infty : EI \frac{d^4 w}{dx^4} - \frac{kEI}{\kappa GS} \frac{d^2 w}{dx^2} + kw = q$$

$$k = \left(\frac{2E_{pillar} b}{t} \right) f + \left(\frac{2E_{spacing} b}{t} \right) (1 - f)$$

FIGURE 7.1: Contributions made to the theoretical DCB framework.

it is rather simple and easy to achieve while has a huge impact. Another aspect is the increased compliance which comes with the pillars. In some applications with very high stiffness, e.g silicon chips used in MEMS, where more compliance and a larger fracture toughness are desired, this method could be used to obtain both at the same time.

7.3 Recommendation for Further Work

The nano-scale adhesive developed in Chapter 2 is tested on EPDM rubber and stainless steel and bench-marked against a commercial solution. However, only the adhesion strength and quality are tested. Environmental treatment in terms of heat, moisture, shock and chemical resistance could be implemented to further bench-mark the new solution. Other combinations of rubber and metal could be investigated as well to identify the working range of the adhesive.

In Chapters 3-5 the zones of weak adhesion span across the full width of the specimen. To follow up on that investigation, zones of varying shapes and widths could be studied. It could be beneficial to investigate if the models developed also apply for these scenarios. This is essential for assessing real life defects. Furthermore, the model could be extended with material and geometrical nonlinearities to get closer to the questions raised in Chapter 2. In fact, at the time of writing the model has been extended with an elastica formulation allowing the free part to experience large geometrical deformations. The aim is to investigate the transition from cleavage to peel as the adherend becomes more and more flexible. The would show if the phenomena observed in Chapter 3-5 are affected by the type of loading (DCB vs. peel) or if they are independent. It is a crucial step to explaining the behavior of the peel specimen from Chapter 2. The work is ongoing and is expected to be published within the year.

Finally, the structured interface investigated in Chapter 6 is two-dimensional as it is cut with a laser. A natural extension would be to investigate three-dimensional structured interfaces, e.g. rows of pillars both parallel and perpendicular to the crack growth direction. Also, the shape of pillars could be varied or even optimized using algorithms to find the most suitable configuration. Since the results are very promising, it could be interesting to include structured interfaces in real applications to see if it is beneficial.

Bibliography

- [1] S. Heide-Jørgensen, R. K. Møller, K. B. Buhl, S. U. Pedersen, K. Daasbjerg, M. Hinge, and M. K. Budzik, "Efficient bonding of ethylene-propylene-diene M-class rubber to stainless steel using polymer brushes as a nanoscale adhesive," *Int. J. Adhes. Adhes.*, vol. 87, no. September, pp. 31–41, 2018.
- [2] S. Heide-Jørgensen and M. K. Budzik, "Crack growth along heterogeneous interface during the DCB experiment," *Int. J. Solids Struct.*, vol. 120, pp. 278–291, 2017.
- [3] S. Heide-Jørgensen and M. K. Budzik, "Effects of bondline discontinuity during growth of interface cracks including stability and kinetic considerations," *J. Mech. Phys. Solids*, vol. 117, pp. 1–21, 2018.
- [4] S. Heide-Jørgensen, S. Teixeira de Freitas, and M. K. Budzik, "On the fracture behaviour of CFRP bonded joints under mode I loading: Effect of supporting carrier and interface contamination," *Compos. Sci. Technol.*, vol. 160, pp. 97–110, 2018.
- [5] S. Heide-Jørgensen, M. K. Budzik, and K. T. Turner, "Mechanics and fracture of structured pillar interfaces," *Journal of the Mechanics and Physics of Solids*, p. 103825, 2019.
- [6] M. K. Budzik and S. Heide-Jørgensen, "Branching and softening of loading path during onset of crack at elastic-brittle interface," *Mech. Mater.*, vol. 127, pp. 1–13, aug 2018.
- [7] K. B. Buhl, R. K. Møller, S. Heide-Jørgensen, A. N. Kolding, M. Kongsfelt, M. K. Budzik, M. Hinge, S. U. Pedersen, and K. Daasbjerg, "Highly efficient rubber-to-stainless steel bonding by nanometer-thin cross-linked polymer brushes," *ACS omega*, vol. 3, no. 12, pp. 17511–17519, 2018.

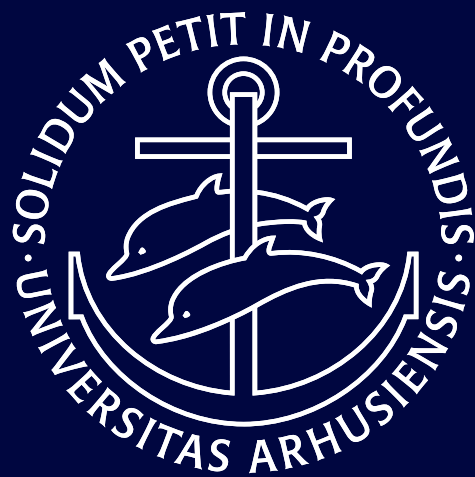
- [8] R. Røjkjær, E. Andersen, S. Heide-Jørgensen, C. Ciallella, R. Mikkelsen, S. Kristiansen, and M. Hinge, "Straight forward approach for obtaining relaxation-recovery data.," 2018.
- [9] R. Z. Wang, Z. Suo, A. G. Evans, N. Yao, and I. A. Aksay, "Deformation mechanisms in nacre," *J. Mater. Res.*, vol. 16, no. 9, pp. 2485–2493, 2001.
- [10] K. Autumn, "Gecko Adhesion: Structure, Function, and Applications," *MRS Bull.*, vol. 32, no. 6, pp. 473–478, 2007.
- [11] P. P. A. Mazza, F. Martini, B. Sala, M. Magi, M. P. Colombini, G. Giachi, F. Landucci, C. Lemorini, F. Modugno, and E. Ribechini, "A new Palaeolithic discovery: tar-hafted stone tools in a European Mid-Pleistocene bone-bearing bed," *J. Archaeol. Sci.*, vol. 33, no. 9, pp. 1310–1318, 2006.
- [12] H. Lowood and I. McNeil, "An Encyclopaedia of the History of Technology," *Technol. Cult.*, vol. 33, no. 1, p. 183, 2006.
- [13] R. D. Adams, *Adhesive bonding: Science, technology and applications*. 2005.
- [14] S. P. Skovsgaard and H. M. Jensen, "Constitutive model for imperfectly bonded fibre-reinforced composites," *Compos. Struct.*, vol. 192, pp. 82–92, 2018.
- [15] S. P. Skovsgaard and H. M. Jensen, "Three-dimensional constitutive model for elastic-plastic behaviour of fibre-reinforced composites," *Int. J. Solids Struct.*, vol. 139-140, pp. 150–162, 2018.
- [16] S. P. Skovsgaard and H. M. Jensen, "A general approach for the study of kink band broadening in fibre composites and layered materials," *Eur. J. Mech. A/Solids*, vol. 74, pp. 394–402, 2019.
- [17] S. Peters, *Handbook of Composites*. 2012.
- [18] R. Zhou, P. Zhu, and Z. Li, "The shielding effect of the plastic zone at mode-II crack tip," *Int. J. Fract.*, vol. 171, no. 2, pp. 195–200, 2011.
- [19] O. Volkersen, "Die Nietkraftverteilung in zugbeanspruchten Nietverbindungen mit konstanten Laschenquerschnitten," *Luftfahrtforschung*, vol. 15, no. 1/2, pp. 41–47, 1938.

- [20] R. Quispe Rodríguez, W. P. De Paiva, P. Sollero, M. R. Bertoni Rodrigues, and É. L. De Albuquerque, "Failure criteria for adhesively bonded joints," in *Int. J. Adhes. Adhes.*, vol. 37, pp. 26–36, 2012.
- [21] M. Goland and E. Reissner, "The Stresses in Cemented Joints," *J. Appl. Mech.*, vol. 11, no. 1, pp. A17–A27, 1944.
- [22] L. J. Hart-Smith, *Adhesive-bonded single-lap joints*. Citeseer, 1973.
- [23] J. J. Benbow and F. C. Roesler, "Experiments on controlled fractures," *Proc. Phys. Soc. Sect. B*, vol. 70, no. 2, pp. 201–211, 1957.
- [24] L. Fryba, "History of Winkler foundation," *Veh. Syst. Dyn.*, vol. 24, no. sup1, p. 7, 1995.
- [25] D. A. Dillard, B. Mukherjee, P. Karnal, R. C. Batra, and J. Frechette, "A review of Winkler's foundation and its profound influence on adhesion and soft matter applications," 2018.
- [26] N. B. Salem, M. K. Budzik, J. Jumel, M. E. Shanahan, and F. Lavelle, "Investigation of the crack front process zone in the double cantilever beam test with backface strain monitoring technique," *Eng. Fract. Mech.*, vol. 98, no. 1, pp. 272–283, 2013.
- [27] J. Cognard, "The mechanics of the wedge test," *J. Adhes.*, vol. 20, no. 1, pp. 1–13, 1986.
- [28] F. E. Penado, "A Closed Form Solution for the Energy Release Rate of the Double Cantilever Beam Specimen with an Adhesive Layer," *J. Compos. Mater.*, vol. 27, no. 4, pp. 383–407, 1993.
- [29] R. S. Rivlin, "The Effective Work of Adhesion," in *Collect. Pap. R.S. Rivlin*, pp. 2611–2614, Springer, 2013.
- [30] K. Kendall, "The adhesion and surface energy of elastic solids," *J. Phys. D. Appl. Phys.*, vol. 4, no. 8, pp. 1186–1195, 1971.
- [31] J. W. Cook, S. Edge, and D. E. Packham, "The adhesion of natural rubber to steel and the use of the peel test to study its nature," *Int. J. Adhes. Adhes.*, vol. 17, no. 4, pp. 333–337, 1997.
- [32] M. Barquins and M. Ciccotti, "On the kinetics of peeling of an adhesive tape under a constant imposed load," *Int. J. Adhes. Adhes.*, vol. 17, no. 1, pp. 65–68, 1997.

- [33] J. M. Piau, C. Ravilly, and C. Verdier, "Peeling of polydimethylsiloxane adhesives at low velocities: Cohesive failure," *J. Polym. Sci. Part B Polym. Phys.*, vol. 43, no. 2, pp. 146–157, 2005.
- [34] K. Kendall, M. Kendall, and F. Rehfeldt, *Adhesion of cells, viruses and nanoparticles*. 2011.
- [35] Z. Gu, S. Li, F. Zhang, and S. Wang, "Understanding surface adhesion in nature: A peeling model," 2016.
- [36] L. F. da Silva and R. D. Campilho, "Advances in numerical modelling of adhesive joints," in *SpringerBriefs Appl. Sci. Technol.*, no. 9783642236075, pp. 1–93, 2012.
- [37] N. A. Adams, R. D., Peppiatt, "Stress analysis of adhesively-bonded lap joints," *Compos. Struct.*, vol. 47, no. 1-4, pp. 673–678, 1999.
- [38] B. N. Legarath, "Debonding of particles in anisotropic materials," *Int. J. Mech. Sci.*, 2003.
- [39] K. N. Shivakumar, P. W. Tan, and J. C. Newman, "A virtual crack-closure technique for calculating stress intensity factors for cracked three dimensional bodies," *Int. J. Fract.*, 1988.
- [40] C. V. Nielsen, B. N. Legarath, and C. F. Niordson, "Extended FEM modeling of crack paths near inclusions," *Int. J. Numer. Methods Eng.*, 2012.
- [41] G. Fajdiga, Z. Ren, and J. Kramar, "Comparison of virtual crack extension and strain energy density methods applied to contact surface crack growth," *Eng. Fract. Mech.*, 2007.
- [42] L. F. M. Da Silva and A. Öchsner, *Modeling of adhesively bonded joints*. 2008.
- [43] S. G. Hong and F. J. Boerio, "Adhesive Bonding of Oil-Contaminated Steel Substrates," *J. Adhes.*, vol. 32, no. 2-3, pp. 67–88, 1990.
- [44] M. Olia and J. N. Rossettos, "Analysis of adhesively bonded joints with gaps subjected to bending," *Int. J. Solids Struct.*, vol. 33, no. 18, pp. 2681–2693, 1996.
- [45] K. Kendall, "Control of Cracks by Interfaces in Composites," *Proc. R. Soc. A Math. Phys. Eng. Sci.*, vol. 341, no. 1627, pp. 409–428, 2006.

- [46] P. J. Das Neves, L. F. Da Silva, and R. D. Adams, "Analysis of mixed adhesive bonded joints part II: Parametric study," *J. Adhes. Sci. Technol.*, vol. 23, no. 1, pp. 35–61, 2009.
- [47] M. K. Budzik, J. Jumel, and M. E. Shanahan, "Impact of interface heterogeneity on joint fracture," *J. Adhes.*, vol. 88, no. 11-12, pp. 885–902, 2012.
- [48] S. M. Xia, L. Ponson, G. Ravichandran, and K. Bhattacharya, "Adhesion of heterogeneous thin films - I: Elastic heterogeneity," *J. Mech. Phys. Solids*, vol. 61, no. 3, pp. 838–851, 2013.
- [49] S. M. Xia, L. Ponson, G. Ravichandran, and K. Bhattacharya, "Adhesion of heterogeneous thin films II: Adhesive heterogeneity," *J. Mech. Phys. Solids*, vol. 83, pp. 88–103, 2015.
- [50] C. Cuminatto, G. Parry, and M. Braccini, "A model for patterned interfaces debonding - Application to adhesion tests," *Int. J. Solids Struct.*, vol. 75-76, no. august, pp. 122–133, 2015.
- [51] F. A. Cordisco, P. D. Zavattieri, L. G. Hector, and B. E. Carlson, "Mode I fracture along adhesively bonded sinusoidal interfaces," *Int. J. Solids Struct.*, vol. 83, pp. 45–64, 2016.
- [52] H. K. Minsky and K. T. Turner, "Composite Microposts with High Dry Adhesion Strength," *ACS Appl. Mater. Interfaces*, vol. 9, no. 21, pp. 18322–18327, 2017.
- [53] S. R. Ranade, Y. Guan, R. B. Moore, J. G. Dillard, R. C. Batra, and D. A. Dillard, "Characterizing fracture performance and the interaction of propagating cracks with locally weakened interfaces in adhesive joints," *Int. J. Adhes. Adhes.*, vol. 82, pp. 196–205, 2018.
- [54] M. A. Dias, L. H. Dudte, L. Mahadevan, and C. D. Santangelo, "Geometric mechanics of curved crease origami," *Phys. Rev. Lett.*, vol. 109, no. 11, 2012.
- [55] Y. Yang, M. A. Dias, and D. P. Holmes, "Multistable kirigami for tunable architected materials," *Phys. Rev. Mater.*, vol. 2, no. 11, pp. 1–6, 2018.

-
- [56] D. G. Hwang, K. Trent, and M. D. Bartlett, "Kirigami-Inspired Structures for Smart Adhesion," *ACS Appl. Mater. Interfaces*, vol. 10, no. 7, pp. 6747–6754, 2018.
- [57] A. T. Nguyen, M. Brandt, A. C. Orifici, and S. Feih, "Hierarchical surface features for improved bonding and fracture toughness of metal-metal and metal-composite bonded joints," *Int. J. Adhes. Adhes.*, vol. 66, pp. 81–92, 2016.
- [58] C. M. Landis, T. Pardoen, and J. W. Hutchinson, "Crack velocity dependent toughness in rate dependent materials," *Mech. Mater.*, vol. 32, no. 11, pp. 663–678, 2000.
- [59] B. Mukherjee, D. A. Dillard, R. B. Moore, and R. C. Batra, "Debonding of confined elastomeric layer using cohesive zone model," *Int. J. Adhes. Adhes.*, vol. 66, pp. 114–127, 2016.
- [60] M. Taleb Ali, J. Jumel, and M. E. Shanahan, "Effect of adhesion defects on crack propagation in double cantilever beam test," *Int. J. Adhes. Adhes.*, vol. 84, pp. 420–430, 2018.
- [61] T. Pardoen, T. Ferracin, C. M. Landis, and F. Delannay, "Constraint effects in adhesive joint fracture," *J. Mech. Phys. Solids*, vol. 53, no. 9, pp. 1951–1983, 2005.



PhD Dissertation

Author: Simon Heide-Jørgensen

Supervisor: Michal K. Budzik

Department of Engineering

Aarhus University, Denmark